Doctoral theses at NTNU, 2023:371

Abdulla Shaikh Abdul Qader Bin Afif

Design of *in situ* Atomic Layer Deposition Systems and Exploring Applications based on Characteristic Nucleation and Growth Behaviour

Doctoral thesis

NTNU
Norwegian University of Science and Technology
Thesis for the Degree of
Philosophiae Doctor
Faculty of Engineering
Department of Mechanical and Industrial
Engineering

Norwegian University of
Science and Technology

Abdulla Shaikh Abdul Qader Bin Afif

Design of *in situ* Atomic Layer Deposition Systems and Exploring Applications based on Characteristic Nucleation and Growth Behaviour

Thesis for the Degree of Philosophiae Doctor

Trondheim, November 2023

Norwegian University of Science and Technology
Faculty of Engineering
Department of Mechanical and Industrial Engineering

Norwegian University of
Science and Technology

NTNU
Norwegian University of Science and Technology

Thesis for the Degree of Philosophiae Doctor

Faculty of Engineering
Department of Mechanical and Industrial Engineering

© Abdulla Shaikh Abdul Qader Bin Afif

ISBN 978-82-326-7442-8 (printed ver.)
ISBN 978-82-326-7441-1 (electronic ver.)
ISSN 1503-8181 (printed ver.)
ISSN 2703-8084 (online ver.)

Doctoral theses at NTNU, 2023:371

Printed by NTNU Grafisk senter

Preface

This thesis has been submitted to NTNU, Norwegian University of Science and Technology, in partial fulfillment of the requirements for the academic degree of Philosophiae Doctor.

The work included in this thesis has been performed at NTNU between October 2018 and August 2022, including a 1-week beam time at the SLAC synchrotron facility (March 2020), Stanford University. This work has been supervised by Professor Jan Torgersen (main advisor), NTNU, and Professor Peter Köllensperger (co-advisor), NTNU.

The thesis was completed and submitted under Professor Nuria Espallargas's (NTNU) supervision.

Abdulla Shaikh Abdul Qader Bin Afif was supported by NTNU's Enabling technologies: Nanotechnology and the Norwegian micro and nano fabrication Facility, NorFab, project 245963/F50. In addition, the Research Council of Norway (Norges Forskningsråd) is acknowledged for its support under project 274459, Trånslate.

This page is intentionally left blank

Acknowledgments

In 2018, when I was actively looking for a Ph.D. opportunity in micro-nano fabrication, I received two Ph.D. offers simultaneously, and it was a difficult decision to choose one. However, after four years, I am grateful that I made the right decision, and it was possible due to the nice and open conversation with my supervisor Jan Torgersen, which made me realize that NTNU is where I want to learn, conduct research, and collaborate.

First and foremost, I would like to express my sincere gratitude to my main supervisor, Jan Torgersen, for believing in me, providing me with this opportunity, and guiding me throughout my Ph.D. journey. I am grateful for all the valuable scientific discussions, knowledge sharing, and support you have provided me. Your positive attitude and responsiveness to all my queries and doubts were truly remarkable. I am grateful for the motivation and encouragement you gave me.

I would like to thank my co-supervisor, Peter Köllensperger for giving me the opportunity to be part of NTNU's "Enabling technologies" and to conduct my duty work at NTNU's Nano lab related to my research.

I am also thankful to my new main supervisor, Nuria Espallargas, for motivating me during the final stage of my Ph.D. and for handling the transition smoothly. The guidance and support you provided me during this critical stage were invaluable.

I would like to express my appreciation to Prof. Andreas Erbe and Johannes Ofstad at the materials science and engineering department NTNU for their help and support.

I am thankful to Mirco Peron and Alaa Faid for their collaborations, which allowed me to use my skills effectively.

I am fortunate to have worked in a wonderful research environment, and I would like to thank all my colleagues in my group for their scientific discussions and collaborations. I am grateful to Anup Dadlani for his warm welcome and humility during the beginning of my Ph.D. Andreas Flaten's assistance was highly appreciated, and I am grateful for all the collaborations with Stephanie Burgmann, Markus Joakim Lid, Kristin Ødegård, and Kjetil Baglo.

Naresh Kumar Veldurthi's motivation and valuable experience sharing were truly valuable. I also appreciate the discussions with Håkon Jarand Dugstad Johnsen and Marco Sauermoser.

I would like to express my gratitude to my friend Mohammed Nazeer Khan, who was already working at NTNU when I started, especially for his help during my first months in Norway.

I am especially thankful to my friends, Sohail Shah, Shafi Khurieshi Mohammed, Waseem Hassan, Ahfaz Ahmed, Shareq Mohd Nazir, Chaitanya Dhoke, Ali Shafqat and Mohammed Rizwan for making my stay joyful.

I am deeply grateful to my family, who played a crucial role in my journey. My parents provided an exceptional home environment, education, and guidance that enabled me to pursue my dream of obtaining a PhD. Without my mother's hard work and dedication, none of this would have been possible. My brother Salem Bin Afif was a constant source of motivation throughout my journey, and my twin brother Mohammed Bin Afif provided unwavering support. I also want to thank my sisters for their invaluable help with schoolwork and for being role models of hard work and dedication to education. I am grateful to my wife for her unwavering support and patience throughout my PhD journey. Her humor and encouragement made my journey much easier. Finally, a special thanks to my sweet little daughter, who joined me in the last stage of my PhD journey and brought joy and laughter to my everyday life with her smile.

Abstract

The atomic layer deposition (ALD) technique is a subclass of chemical vapor deposition (CVD) using a sequential gas phase chemical process to deposit ultrathin films with uniformity and conformality on 3D surfaces. The sequential process gives it a unique position in the field of micro and nanofabrication since the chemical precursors are used to react with the surface of a material one at a time in a self-limiting manner. ALD thus plays an increasingly important role in modern semiconductors and energy applications. Among the available thin film deposition techniques, ALD stands out in terms of thickness control and conformality on 3D surfaces. Moreover, the resulting films are dense and of high quality.

The work presented in this Ph.D. thesis can be broadly classified into two parts,

In the first part of my Ph.D. research, diffrent applications of ALD using diverse materials that exhibit distinct nucleation behaviors were studied. We leveraged the variation in nucleation and growth differences to explore different applications. Furthermore, the obstacles that come with growing ultra-thin conformal films or using new and complex materials were emphasized, which underlined the significance of designing in situ ALD systems in the second phase of my research.

1. **ALD as a protective coating**: The atomic layer deposition (ALD) of oxides is a widely used method for producing conformal and uniform thin films. This work utilizes the nucleation and growth aspects of common oxides such as HfO_2, TiO_2, and ZrO_2 to address the challenge of corrosion-assisted cracking in magnesium alloys, which are being investigated for use as temporary implant devices. High corrosion rates and premature deformation due to stress corrosion cracking (SCC) limit the clinical applications of these devices. To investigate the effectiveness of ALD coatings for corrosion protection, 100 nm thick TiO_2 and ZrO_2 coatings were deposited, and their effects on the SCC susceptibility of an AZ31 Mg alloy were studied. Both coatings showed improved performance against stress corrosion cracking for AZ31 alloy.

Furthermore, a comparison study of the corrosion protection performance of ALD and sputtered biocompatible TiO_2 coatings was carried out. The results showed that both sputtering and ALD coating improved the corrosion resistance of the AZ31 alloy, but the ALD-coated surface exhibited the lowest corrosion rates, regardless of the surface conditions. The difference in coating performance was attributed to the line of sight limitation of sputtering, which was apparent in 3D samples.

Finally, the corrosion behavior and cytotoxicity of the AZ31 Mg alloy were studied after the deposition of 100 nm thick TiO_2, ZrO_2, and HfO_2 ALD coatings. The results revealed that the ALD TiO_2 coating led to a notable improvement in the corrosion performance of AZ31 alloy, while ZrO_2 and HfO_2 ALD coatings demonstrated even higher corrosion resistance. This superior performance was attributed to the coatings lower wettability, greater electrochemical stability, and superior surface integrity, characterized by fewer cracks and pores. Furthermore, the higher corrosion resistance provided by the coatings led to an improvement in the cytotoxicity performance of AZ31 alloy.

2. **ALD for catalyst design**: High surface area materials have been shown to exhibit low overpotential and improved activity as oxygen evolution reaction (OER) catalysts compared to planar surfaces. In addition to using low-cost materials, the ability to deposit catalyst material uniformly on 3D surfaces using atomic layer deposition (ALD) can be advantageous in controlling particle size and surface coverage, thus creating a potential process property relationship. Here, we study the use of ALD to deposit Cu on Ti and Ni mesh as OER catalysts, uniformly distributed Cu islands were formed on Ti substrate, whereas Cu clusters were seen in the case of Ni substrate. Results from linear sweep voltammetry in 1 M KOH solution show that that the Ni mesh outperformed the Ti mesh in terms of overpotential, with the lowest overpotential of 320 mV observed for both the pristine Ni mesh and Ni mesh with 1500 cycles of ALD Cu. The study also revealed a correlation between island density and OER performance in the case of Ti mesh. The Ti mesh with 500 ALD Cu cycles exhibited the highest Cu island density and, consequently, delivered the best performance with an overpotential of 345 mV.

3. **ALD of perovskites**: This review examines the growth process of ALD perovskites to gain insights into the challenges associated with such processes and the steps required to tackle them. The combination of the functionality of perovskites and the deposition advantages of ALD has led to new endeavors in diverse applications. ALD offers high conformality, uniformity, and control over the growth and stoichiometry of these films, making it advantageous compared with other deposition processes. Modern-day devices with novel designs and high efficiencies require materials with controlled stoichiometries and complex device designs. Four applications were reviewed and discussed: high-k dielectrics, piezoelectrics, optoelectronics, and solar-to-energy conversion devices. In addition, interfacial effects and the impact of different process parameters were reviewed.

In the second part *in situ* ALD systems were designed, as for new precursors and complex process there is still a lack of clear understanding of the reaction mechanisms occurring during the ALD process and there are other challenges associated with nucleation of thin films restricting growth of ultrathin films. Conducting *in situ* studies can help achieve optimized ALD growth by providing continuous chemical and physical information during the process.

1. ***In situ* FTIR ALD***:* In this work, a compact and flexible *in situ* transmission FTIR spectroscopy ALD system has been designed and built, allowing to detect surface organometallic species from the first reactant half-cycle and mapping out ligand exchange reactions in the subsequent half-cycles. The integrity and functionality of the system to track the nucleation stage are validated by conducting *in situ* FTIR absorption measurements of Al_2O_3 using Tri-methyl Aluminum (TMA) and H_2O. Thus, with Potassium Bromide (KBr) as substrate, this instrument can enable straightforward ALD nucleation studies using a DTGS detector having sufficient signal without additional optical setup and modifications to off-the-shelf FTIR systems that allow low wavenumber experiments.
2. ***In situ* XAS ALD**: Although the general principle of the ALD Cu process is known, the nucleation phase has limited experimental studies, due to the lack of a characterization techniques that are sensitive enough to probe minute quantities of material deposited per half-cycle. However, synchrotron-based X-ray absorption techniques have the capability to do so. X-ray absorption spectra of materials are

characterized by a sharp increase in absorption at specific photon energies, depending on the absorbing element. Structural information can be deduced from the measured absorption spectra.

Before conducting *in situ* studies for Cu growth using X-ray Absorption Spectroscopy (XAS), preliminary experiments were performed to develop the ALD process and confirm growth on different substrates.

The *in situ* XAS ALD was designed and built to conduct absorbtion spectroscopy studies at the Stanford synchrotron radiation light source (SLAC national accelerator, California). Unfortunately, the study was incomplete due to X-ray beam alignment difficulties, limited beam time, and Covid-related restrictions.

Contributions

The work in this Ph.D. thesis was carried out at the Department of Mechanical and Industrial Engineering at NTNU in Trondheim, Norway. The work was supervised by Professor Jan Torgersen and co-supervised by Professor Peter Köllensperger.

This work was carried out as part of the Micro and Nanoscale Design group. Abdulla Shaikh Abdul Qader Bin Afif was supported by NTNU's Enabling technologies: Nanotechnology. The Research Council of Norway (Norges Forskningsråd) is acknowledged for its support under project 274459, Trånslate, and the Norwegian micro-and nano-fabrication Facility, NorFab, project 245963/F50.

Publications

The following publications constitute parts of the thesis, and the illustration below represents the thesis's structure and timeline.

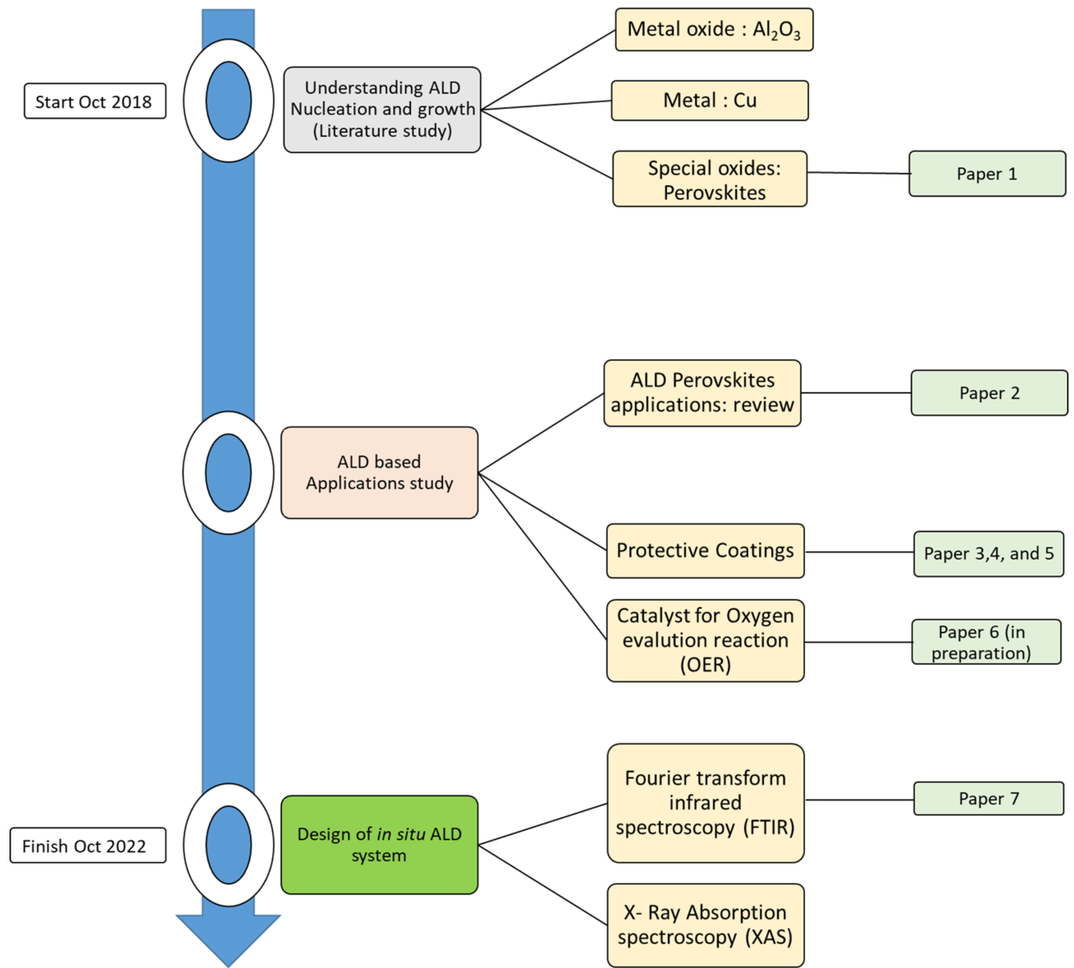
Start Oct 2018
Understanding ALD Nucleation and growth (Literature study)
Metal oxide : Al_2O_3
Metal : Cu
Special oxides: Perovskites
Paper 1
ALD Perovskites applications: review
Paper 2
ALD based Applications study
Protective Coatings
Paper 3,4, and 5
Catalyst for Oxygen evalution reaction (OER)
Paper 6 (in preparation)
Fourier transform infrared spectroscopy (FTIR)
Paper 7
Finish Oct 2022
Design of *in situ* ALD system
X- Ray Absorption spectroscopy (XAS)

1. **Paper 1**

Abdulla Bin Afif, Anup L. Dadlani, Stephanie Burgmann, Peter Köllensperger, and Jan Torgersen. "Atomic layer deposition of perovskites—**Part 1**: Fundamentals of nucleation and growth". *Material Design & Processing Communications* 2(1) (2020) p.e114.

**Contribution: Conceptualization, Methodology, Preparing the figures, Writing - original draft, review & editing.*

As part of my contribution to this review work, I performed the conceptualization and writing of the entire draft of the article, including the preparation of original figures. Additionally, I curated the data related ALD growth of perovskites.

2. **Paper 2**

Abdulla Bin Afif, Anup L. Dadlani, Stephanie Burgmann, Peter Köllensperger, Jan Torgersen. "Atomic layer deposition of perovskites **part 2**: Designing next generation electronic applications". *Material Design & Processing Communications* 2(1) (2020) p.e115.

**Contribution: Conceptualization, Methodology, Preparing the figures, Writing - original draft, review & editing.*

In this review work, I performed the conceptutalization and data curation for ALD based perovskites application. I was also responsible for complete writing of the draft.

3. **Paper 3**

Mirco Peron, **Abdulla Bin Afif**, Anup L. Dadlani, Filippo Berto, and Jan Torgersen. "Improving stress corrosion cracking behavior of AZ31 alloy with conformal thin titania and zirconia coatings for biomedical applications." *Journal of the Mechanical Behavior of Biomedical Materials* 111 (2020): 104005.

**My experimental contribution to the research project included ALD deposition of Titania an Zirconia, as well as using Spectroscopic Ellipsometry for thickness measurement. Additionally, I performed XPS measurements and analysis to determine the chemical composition of the ALD Titania.*

In addition to this experimental work, I also contributed to writing the specific sections of the research article related to mentioned experimental methods.

4. **Paper 4**

Mirco Peron, **Abdulla Bin Afif**, Anup L. Dadlani, Filippo Berto, and Jan Torgersen. “Comparing physiologically relevant corrosion performances of Mg AZ31 alloy protected by ALD and sputter coated TiO_2.” *Surface and Coatings Technology, p.125922*.

**My experimental contribution to the research project included conducting both ALD and sputter deposition of Titania, as well as using Spectroscopic Ellipsometry for thickness measurement, and Profilometry to measure surface roughness. Additionally, I performed XPS measurements and analysis to determine the chemical composition of the ALD Titania.*

In addition to this experimental work, I also contributed to writing the specific sections of the research article related to mentioned experimental methods.

5. **Paper 5**

Mirco Peron, Susanna Cogo, Maria Bjelland, **Abdulla Bin Afif**, Anup L. Dadlani, Elisa Greggio Filippo Berto, and Jan Torgersen. “On the evaluation of ALD TiO_2, ZrO_2 and HfO_2 coatings on corrosion and cytotoxicity performances.” *Journal of Magnesium and Alloys*, *9*(5), pp.1806-1819.

**My experimental contribution to the research project included ALD deposition of Titania, Zirconia, and Hafnia,as well as using Spectroscopic Ellipsometry for thickness measurement. Additionally, I performed XPS measurements and analysis to determine the chemical composition of the ALD Titania.*

In addition to this experimental work, I also contributed to writing the specific sections of the research article related to mentioned experimental methods

6. **Paper 6**

In preparation: **Abdulla Bin Afif**, Alaa Faid, Anup L. Dadlani, Andreas Flaten, Peter Köllensperger Svein Sunde, and Jan Torgersen. "Studying high surface area Atomic layer deposited Cu islands on Ti and Ni Mesh as an Electro-catalyst for Oxygen Evolution Reaction (OER)."

**Contribution: Conceptualization, Data curation, Investigation, Methodology, Validation, Visualization, Writing - original draft, Writing -review & editing.*

In addition to contributing to the conceptualization and writing of the complete draft, I performed experimental work in this project, which includes, ALD of Copper (Cu) on Titanium (Ti) and Nickel (Ni) mesh substrates, performing Scanning Electron Microscopy (SEM) imaging of the catalyst, and conducting X-ray Photoelectron Spectroscopy (XPS).

Also, I conducted data analysis for all the characterization mentioned, including the electrochemical Oxygen Evolution Reaction (OER) characterization, as well as for XPS measurements.

7. **Paper 7**

Abdulla Bin Afif, Anup L. Dadlani, Andreas Flaten, Markus Joakim Lid, Johannes Ofstad, Andreas Erbe, Peter Köllensperger, Jan Torgersen. "A toolbox for easy entry low wavenumber in situ atomic layer deposition transmission FTIR spectroscopy studies." *Review of Scientific Instruments* 93.8 (2022): 085107.

**Contribution: Conceptualization, Methodology, Acquiring analyzing and interpreting the experimental data, Preparing the figures, Writing - original draft, review & editing*

In addition to contributing to the conceptualization and writing of the complete draft, I performed the experimental work in this project, which includes design and setup of the in situ ALD FTIR system, and conducting in situ FTIR experiments. Apart from experimental work, my contribution also includes data analysis for all the in situ and ex situ characterizations carried out in this work.

Other Contributions included in the thesis but not in research article form

1. Chapter 9: Experimental study- Design of in situ ALD XAS system

   Abdulla Bin Afif, Anup L. Dadlani, Andreas Flaten, Peter Köllensperger, Jan Torgersen

**Contribution: Conceptualization, Methodology, Acquiring analyzing and interpreting the experimental data, Preparing the figures*

In addition to contributing to the conceptualization of the in situ XAS ALD work, I performed the experimental work in this project, which includes, preliminary ex situ ALD Cu growth study, design and setup of the in situ ALD XAS system, and conducting in situ XAS experiments at

synchrotron beamline. Apart from experimental work, my contribution also includes data analysis of ex situ characterizations.

Other Contributions not included in the thesis

1. **Paper 1**

Mohammed Bin Afif, **Abdulla Bin Afif**, Harry Apostoleris, Krishiv Gandhi, Anup L. Dadlani, Amal Al Ghaferi, Jan Torgersen, and Matteo Chiesa. "Ultra-Cheap Renewable Energy as an Enabling Technology for Deep Industrial De-carbonization via Capture and Utilization of Process CO_2 Emissions". *Energies* 2022, 15, 5181.

**Contribution: Conceptualization, Methodology, Investigation, Writing - original draft, review & editing*

2. **Paper 2**

Markus Joakim Lid, **Abdulla Bin Afif**, Jan Torgersen, Fritz B. Prinz. "Finish-pass strategy to improve sidewall angle and processing time in FIB milled structures." *Procedia Structural Integrity* 34 (2021): 266-273.

**Contribution: E-beam evaporation deposition of thin films.*

3. **Paper 3**

Kristin Sirnes Ødegaard, Marita Westhrin, **Abdulla Bin Afif,** Qianli Ma, Therese Standal, Christer Westum Elverum. “The effects of surface treatments on electron beam melted Ti-6Al-4V disks on osteogenesis of human mesenchymal stromal cells.” *Biomaterials Advances* 147 (2023): 213327.

**Contribution: ALD deposition and XPS measurement and analysis for determining the chemical composition*

4. **Paper 4**

Kjetil Baglo, Marco Sauermoser, Markus Lid, Thomas Paschke, **Abdulla Bin Afif**, Markus Lunzer, Andreas Flaten, Martin Steinert, Robert Bock, and Jan Torgersen. “Overcoming the transport limitations of photopolymer-derived, architected carbon.” *Advanced Materials Technologies* (2023): 2300092.

**Contribution: FTIR characterization of the photopolymer*

Other dissemination

In addition to the papers listed above, the work was disseminated in the following ways:

1. **Abdulla Bin Afif**, Anup L. Dadlani, Andreas Flaten, Markus Joakim Lid, Peter Köllensperger, and Jan Torgersen. "Design of Adaptive ALD Reactor for In-Situ FTIR Spectroscopy Studies using DTGS Detector." NKS-FUM (Functional Inorganic Materials) meeting 2021. (**Oral presentation**)

2. **Abdulla Bin Afif**, Anup L. Dadlani, Stephanie Burgmann, Peter Köllensperger, and Jan Torgersen. "Understanding Nucleation phenomenon of ALD Deposited Ultra-Thin Functional Films." NTNU Nano Symposium 2018. (**Poster presentation**)

This page is intentionally left blank

Contents

PREFACE .... **I**

ACKNOWLEDGMENTS .... **III**

ABSTRACT .... **V**

CONTRIBUTIONS .... **IX**

CONTENTS .... **XVII**

ABBREVIATIONS .... **XXI**

LIST OF TABLES .... **XXIII**

LIST OF FIGURES .... **XXIV**

1. CHAPTER 1: INTRODUCTION AND OVERVIEW **1**

1.1 ALD GROWTH MODES 1
1.1.1 Surface interaction *1*
1.1.2 High aspect ratio structures *4*
1.2 MOTIVATION 5
1.2.1 Exploring ALD-based application *5*
1.2.1.1 ALD of oxides as a protective coating 5
1.2.1.2 ALD Cu as a catalyst for oxygen evolution reaction (OER) 5
1.2.1.3 ALD perovskite applications 7
1.2.2 Challenges in ALD growth *9*
1.2.3 In situ ALD studies *10*
1.2.3.1 *In situ* FTIR ALD 10
1.2.3.2 *In situ* XAS ALD 11
1.3 THESIS OBJECTIVE 13
1.3.1 Research questions this Ph.D. thesis is answering *13*
1.4 THESIS STRUCTURE 16

2. CHAPTER 2: LITERATURE REVIEW **19**

2.1 ATOMIC LAYER DEPOSITION (ALD) 19
2.1.1 Background *19*
2.1.2 Principle *19*
2.1.3 Process characteristics *21*
2.1.4 Type of ALD *23*
2.1.5 Materials range *24*
2.1.6 Precursor selection *24*
2.2 ALD VS. OTHER DEPOSITION TECHNIQUES AND ITS LIMITATIONS 25
2.3 CURRENT ALD BASED APPLICATIONS 27
2.4 ALD PEROVSKITE FOR NOVEL APPLICATIONS 31
2.4.1 Growth process *31*
2.4.2 ALD perovskite applications *31*
2.4.2.1 High K dielectrics for DRAM capacitors 31
2.4.2.2 Piezoelectric 32
2.4.2.3 Optoelectronics 33
2.4.2.4 Solar to energy conversion (thermo-chemical process) 34
2.4.3 Challenges in ALD of perovskites *35*

2.4.3.1 Differential growth at the interface 35
2.4.3.2 Effect of process parameters on growth 36
2.4.4 Summary 37
2.5 WHY *IN SITU* STUDIES ARE REQUIRED 38
2.5.1 Introduction 38
2.5.2 Motivation for in situ studies 40
2.5.2.1 New precursors 40
2.5.2.2 Miniaturization 40
2.5.2.3 Complex ALD process and process property relationship 40
2.6 *IN SITU* ALD CHARACTERIZATION METHODS 41
2.6.1 In situ spectroscopic ellipsometry 41
2.6.2 In situ Infrared spectroscopy 43
2.6.3 Quartz crystal microbalance 44
2.6.4 Quadrupole mass spectrometry 45
2.6.5 Optical emission spectroscopy 46
2.7 *IN SITU* ALD SYNCHROTRON TECHNIQUES 47
2.7.1 X-ray absorption spectroscopy (XAS) 48
2.7.2 X-ray reflectivity (XRR) 50
2.7.3 X-ray diffraction (XRD) 51
2.7.4 Grazing incidence small angle X-ray scattering (GISAXS) 52
2.7.5 X-ray photoelectron spectroscopy (XPS) 53

3. CHAPTER 3: EXPERIMENTAL TECHNIQUES 55

3.1 FTIR 55
3.2 XAS 57
3.3 XPS 58
3.4 SEM AND EDS 58
3.5 ELLIPSOMETRY 58
3.6 ELECTROCHEMICAL MEASUREMENTS 58

4. CHAPTER 4: EXPERIMENTAL STUDY – ALD OF OXIDES AS PROTECTIVE COATINGS 61

4.1 BACKGROUND: ALD METAL OXIDES FOR CORROSION PROTECTION 61
4.2 ADVANTAGE OF ALD VS OTHER TECHNIQUES FOR PROTECTION APPLICATION 62
4.3 STUDY: IMPROVING STRESS CORROSION CRACKING BEHAVIOR OF AZ31 ALLOY WITH CONFORMAL THIN TITANIA AND ZIRCONIA COATINGS FOR BIOMEDICAL APPLICATIONS 63
4.3.1 ALD deposition process 64
4.3.2 Results 66
4.3.2.1 Ellipsometery 66
4.3.2.2 Chemical composition 66
4.3.3 Summary 68
4.4 STUDY: COMPARING PHYSIOLOGICALLY RELEVANT CORROSION PERFORMANCES OF MG AZ31 ALLOY PROTECTED BY ALD AND SPUTTER COATED TiO_2 72
4.4.1 ALD and sputter deposition process 72
4.4.2 Results 74
4.4.2.1 Roughness measurement 74
4.4.2.2 Chemical composition 75
4.4.3 Summary 76
4.5 STUDY: ON THE EVALUATION OF ALD TiO_2, ZrO_2, AND HfO_2 COATINGS ON CORROSION AND CYTOTOXICITY PERFORMANCES 81
4.5.1 ALD deposition process 81
4.5.2 Results 83
4.5.2.1 Chemical composition 83
4.5.3 Summary 85

5. CHAPTER 5: EXPERIMENTAL STUDY – ALD OF CU AS A CATALYST FOR OXYGEN EVOLUTION REACTION (OER) 89

5.1 BACKGROUND 89
5.2 EXPERIMENTAL 90
5.3 RESULTS AND DISCUSSION 91
5.4 SUMMARY 97

6. CHAPTER 6: EXPERIMENTAL STUDY - DESIGN OF *IN SITU* ALD FTIR SYSTEM 99

6.1 *IN SITU* FTIR 99
6.2 STATE OF THE ART 100
6.3 DESIGN OF *IN SITU* FTIR ALD SYSTEM 101
6.4 METHODS 103
6.4.1 Substrate selection for FTIR studies 103
6.4.2 Windows protection 104
6.4.3 Detector for FTIR spectroscopy measurements 105
6.5 MAIN RESULTS 105
6.6 SUMMARY 107

7. CHAPTER 7: EXPERIMENTAL STUDY - DESIGN OF *IN SITU* ALD XAS SYSTEM 109

7.1 X-RAY ABSORPTION SPECTROSCOPY 109
7.2 WHY *IN SITU* XAS ALD 110
7.3 STATE OF THE ART 111
7.4 DESIGN OF *IN SITU* XAS ALD SYSTEM 113
7.4.1 System design 113
7.4.2 Sample holder 113
7.4.3 Optical windows 114
7.4.4 Support frame 114
7.4.5 Beam allignment 115
7.4.6 System overview 115
7.5 METHODS 116
7.5.1 Substrate preparation 116
7.5.2 Cu precursor boosting 116
7.6 EXPERIMENT: 117
7.6.1 Preliminary ex situ experimental study 117
7.6.2 In situ XAS characterization 118
7.7 RESULTS AND DISCUSSION 119
7.7.1 Preliminary ex situ ALD Cu study 119
7.7.1.1 Background 119
7.7.1.2 Literature: Nucleation and growth 119
7.7.1.3 Literature: Selective growth 121
7.7.1.4 *Ex situ* experimental study : Results and discussion 121
7.7.2 Overview of in situ XAS experiments 124
7.7.2.1 Practical challenges during the experiments 125
7.7.3 Improvements in the system design 126
7.8 SUMMARY 126

8. CHAPTER 8: CONCLUSIONS AND FUTURE WORK 129

8.1 CONCLUSIONS 129
8.2 FUTURE WORK 131

9. REFERENCES 135

10. FULL-TEXT PAPERS INCLUDED IN THESIS 155

PAPER 1........ 155
PAPER 2.... 162
PAPER 3... 173
PAPER 4.. 185
PAPER 5.. 199
PAPER 6.. 213
PAPER 7.. 237

Abbreviations

ALD	Atomic layer deposition
AlN	Aluminum Nitride
ALE	Atomic layer epitaxy
BST	Barium strontium titanate
BTO	Barium titanate
Cp	Cyclopentadienyl
CSP	Concentrated solar power
CVD	Chemical vapor deposition
DRAM	Dynamic random access memory
DTGS	Deuterated L-alanine doped triglycine sulfate
EELS	Electron energy loss spectroscopy
EIS	Electrochemical impedance spectroscopy
D33	Piezoelectric coefficient
EOT	Equivalent oxide thickness
EXAFS	Extended x-ray absorption fine structure
FTIR	Fourier transform infrared
GPC	Growth per cycle
HQ	Hydroquinone
IR	Infrared
ITRS	International technology roadmap for semiconductors
KBr	Potassium Bromide
LSV	Linear sweep voltammetry
MCT	Mercury cadmium telluride
MEMS	Micro-electromechanical system
MFC	Mass flow controller
NEMS	Nano-electromechanical systems
NRR	Nitrogen reduction reaction
OER	Oxygen evolution reaction
PBS	Lead sulfide
PBZ	Lead zirconium titanate
PZT	Lead zirconate titanate
RBS	Rutherford backscattering
RHE	Reversible hydrogen electrode
RMS	Root Mean Square

RMDS	Reactive molecular dynamic study
SALD	Spatial atomic layer deposition
SCC	Stress corrosion cracking
SEM	Scanning electron microscope
SMSI	Strong metal-support interaction
S/N	Signal to noise
STO	Strontium titanate
TMA	Tri-methyl Aluminum
XAS	X-ray absorption spectroscopy
XANES	X-ray absorption near edge spectroscopy
XPS	X-ray photoelectron spectroscopy

List of tables

Table 1: Dielectric constant of perovskite-based thin films synthesized by ALD [39] 32
Table 2: Effect of interface condition on the ALD growth [34]. 36
Table 3: Synchrotron based in situ characterization methods used for ALD research [127]. 48
Table 4: Chemical composition of Mg Alloy AZ31 [139]. 63
Table 5: Crack density of coated samples [133]. 68
Table 6: Corrosion potentials (E_{CORR}) and corrosion current densities (I_{CORR}) [133]. 69
Table 7: Electrochemical corrosion data extrapolated from potentiodynamic polarization for rough and smooth samples [134]. 77
Table 8: Corrosion potentials (E_{CORR}) and corrosion current densities (I_{CORR}) values for bare and coated samples [135]. 87
Table 9: Different ALD Cu precursors and their characteristics. 120

List of figures

FIGURE 1: SCHEMATIC ILLUSTRATION OF SELECTED GROWTH MODES POSSIBLE IN ALD: TWO DIMENSIONAL GROWTH OR LAYER BY LAYER GROWTH, ISLAND GROWTH WITHOUT DIFFUSION AND RANDOM DEPOSITION DUE TO ISLAND GROWTH WITH DIFFUSION [12]. 2

FIGURE 2: SCHEMATIC REPRESENTATION OF UNSATURATED THICKNESS PROFILES: (A) DIFFUSION LIMITED, (B)REACTION LIMITED AND, (C) RECOMBINATION LIMITED GROWTH TYPE [1]. 4

FIGURE 3: ALD GROWTH OF ABO_3 COMPOUNDS [34] 8

FIGURE 4: SCHEMTIC REPRESENATION OF THE INTEGRATION OF ALD REACTOR AND FTIR SYSTEM. 11

FIGURE 5: DESCRIPTION OF THE X-RAY BEAM INCIDENT ON THE SAMPLE SURFACE IN THE IN SITU XAS REACTOR ASSEMBLY. 12

FIGURE 6: SIMPLIFIED SCHMEATIC OF ALD SYSTEM WITH MAJOR COMPONENTS. 20

FIGURE 7: SCHEMATIC REPRESENTATION OF THE CHEMISTRY INVOLVED IN THE CYCLIC ALD PROCESS OF Al_2O_3 USING TMA AND H_2O [52] 21

FIGURE 8: CLASSIFICATION FOR THE ALD PROCESSES BASED ON THE GROWTH MODES: (A) LINEAR MODE: WHERE THERE IS A LINEAR INCREASE IN GROWTH WITH NUMBER OF ALD CYCLES USED, (B) SUBSTRATE-ENHANCED MODE; THE SUBSTRATE SURFACE PROVIDES FAVOURABLE CONDITIONS FOR THE REACTION TO TAKE PLACE THUS RESULTING IN ENHANCED GROWTH , (C) SUBSTRATE-INHIBITED MODE OF TYPE 1 RESULTING IN NO FURTHER GROWTH IN THICKNES AFTER CERTAIN NUMBER OF CYCLES, AND (D) SUBSTRATE-INHIBITED MODE OF TYPE 2, WHERE THERE IS INCREASE FOLLOWED BY DIP IN THICKNESS OF THE THIN FILM [10] 22

FIGURE 9: ALD GPC VERSUS TEMPERATURE SHOWING ALD WINDOW [5]. 23

FIGURE 10: OVERVIEW OF MATERIALS GROWN BY ALD, THE ALD GROWTH OF PURE ELEMENTS AND COMPOUNDS REPRESENTED THROUGH SHADING AND COLORS [34] *(SOURCE: HTTPS://WWW.ATOMICLIMITS.COM/ALDDATABASE/* [64]*).* 24

FIGURE 11: SCHEMATIC REPRESENATION OF DIRECTIONALITY IN DIFFERENT DEPOSITION METHODS [69]. 27

FIGURE 12: SIMPLIFIED SCHEMATIC DIAGRAM OF A DRAM CAPACITOR WITH ALD DEPOSITED DIELECTRIC [49]. 28

FIGURE 13: STRUCTURE OF OLED ENCAPSULATION [17] 29

FIGURE 14: ALD COATED PT ANODE ON SOLID OXIDE FUEL CELL (SOFC) FOR ENERGY STARGE AND CONVERSION APPLICATION [80] 30

FIGURE 15: ZNO MICROFILTRATION MEMBRANES FOR DESALINATION BY ALD [82]. 30

FIGURE 16: BANDGAP ENERGY AND SPECIFIC PERMITTIVITY OF VARIOUS DIELECTRIC FILMS [88] 32

FIGURE 17:(A) SCHEMATIC OF THE 2-STEP THERMOCHEMICAL SOLAR-TO-FUEL CONVERSION PROCESS [99]*. (B) CERIA SAMPLE WITH DUAL-SCALE POROSITY* [100]. 35

FIGURE 18: EFFECT OF DIFFERENT PROCESS PARAMETERS ON PEROVSKITES PROPERTIES [34]. 37

FIGURE 19: . (A) SCHEMATIC REPRESENTATION OF A SINGLE-WAFER ALD REACTOR INTEGRATED WITH ROTATING COMPENSATOR ELLIPSOMETE. (B) PHOTOGRAPH OF A JAWOOLLAM CO., INC., M2000 SPECTROSCOPIC ELLIPSOMETER FITTED ON AN OXFORD INSTRUMENTS FLEXAL™ ALD REACTOR [115] 42

FIGURE 20: SCHEMATIC OF THE ALD REACTOR CONNECTED TO AN IR SPECTROPHOTOMETER FOR INS SITU ALD STUDIES WITH SAMPLE POSITIONED IN TRANSMISSION MODE [123]. 44

FIGURE 21: SCHEMATIC OF INGRATED QCM FIXTURE [124]. 45

FIGURE 22: THE IN SITU QMS DEPICTED IN AN SCHEMATIC OF OXFORD INSTRUMENTS FLEXALD REACTOR [125]. 46

FIGURE 23: SCHEMATIC REPRESENTATION OF THE OXFORD INSTRUMENTS FLEXAL REACTOR INTEGRATED WITH OES COMPONENT [126]. 47

FIGURE 24: EXAMPLE X-RAY ABSORPTION SPECTRUM IRON– SULFUR–LITHIUM [128] WITH DIFFERENT REGIONS NUMBERED AS 1: BACKGROUND REGION, 2: EDGE,3: XANES AND,4: EXAFS. 49

FIGURE 25: SCHEMATIC OF THE IN SITU XRD CHAMBER [127]. 52

FIGURE 26: DRAWING OF THE ALD SYSTEM INTEGRATED WITH THE FTIR SPECTROMETER. 55

FIGURE 27: COMPARISON OF IR TRANSMISION AT WAVENUMBER 1000 CM^{-1} FOR DIFFERENT SUBSTRATES, (A) SI S AND (B) KBR. .. 56

FIGURE 28: COMPARISON OF DETECTOR SIGNAL OF INCIDENT IR BEAM FOR SI AND KBR SUBSTRATE 56

FIGURE 29: SCHEMATIC SHOWING THE SETUP OF IN SITU XAS ALD REACTOR AND X-RAY BEAM. 57

FIGURE 30: COATING UNIFORMITY ON 3D SUBSTRATES WITH DIFFERENT DEPOSITION TECHNIQUES [139]. 62

FIGURE 31: SCHEMATIC OF SAVANNAH ALD SYSTEM USED FOR THE ALD OF ZrO_2 AND TiO_2 65
FIGURE 32: XPS SPECTRA FOR ALD DEPOSITED TIO2 (A) TI 2P REGIONAL PEAK AND (B) O 1S REGIONAL PEAK [133]. 67
FIGURE 33: XPS SPECTRA FOR ALD ZrO_2 ,(A) ZR 3D REGIONAL PEAK AND (B) O 1S REGIONAL PEAK [133] 68
FIGURE 34: SEM IMAGES OF ALD (A) TiO_2 AND, (B) ZrO_2 COATED AZ31 SURFACES WITH SURFACE CRACKS [133]. 69
FIGURE 35: POTENTIODYNAMIC POLARIZATION CURVES OF BARE (BLUE), TiO_2 COATED (RED) AND ZrO_2 COATED (GREEN) AZ31 ALLOY IN SBF [133]. 69
FIGURE 36: SSC INDICES FOR THE BARE AND COATED AZ31 SAMPLE [133]. 70
FIGURE 37: HYDROGEN EVOLVED FROM THE IMMERSION OF BARE (BLUE), TiO_2 COATED (RED) AND ZrO_2 COATED (GREEN) AZ31 ALLOY IN SBF [133]. 71
FIGURE 38: SEM FRACTOGRAPHIES OF THE GAUGE SECTION OF (A) BARE, (B) TiO_2 COATED AND (B) ZrO_2 COATED SAMPLES [133]. 71
FIGURE 39: 3D REPRESENTATION OF SUBSTRATES IN DIFFERENT SHAPES, (A) DISCS, (B) PLATES AND (C) 3D STRUCTURES USED IN THE HYDROGEN EVOLUTION EXPERIMENTS [134] 72
FIGURE 40: PURGE TIME OPTIMIZATION OF ALD TiO_2 FOR A SPECIALIZED BIG LID ON THE SVANNAH ALD SYSTEM........ 74
FIGURE 41: : XPS SPECTRA FOR ALD TiO_2 (A) TI 2P (B) O 1S AND SPUTTER DEPOSITED TiO_2 (C) TI 2P AND (D) O 1S [134]. 76
FIGURE 42: HYDROGEN EVOLUTION OF (A) ROUGH SAMPLES, (B) SMOOTH SAMPLES AND, (C) 3D SAMPLES [134]. 77
FIGURE 43: MACRO-MORPHOLOGIES OF (A),SMOOTH AND (B) ROUGH (BARE, SPUTTER AND ALD TIO2 COATED SAMPLES) BEFORE AND AFTER CORROSION [134]. 78
FIGURE 44: MACRO-MORPHOLOGIES OF SMOOTH BARE, SPUTTER AND ALD TiO_2 COATED 3D SAMPLES BEFORE AND AFTER CORROSION [134]. 79
FIGURE 45: SEM IMAGE OF SLICED CROSS-SECTION (A) BARE, (B) SPUTTER COATED AND, (C) ALD COATED 3D SAMPLES [134]. 80
FIGURE 46: XPS SPECTRA FOR ALD TIO2 (A) TI 2P AND (B) O 1S [135]. 84
FIGURE 47: XPS SPECTRA FOR ALD DEPOSITED ZRO2 (A) ZR 3D AND (B) O 1S [135]. 84
FIGURE 48: XPS SPECTRA OF ALD DEPOSITED HfO_2 (A) HF 4F AND (B) O 1S [135]. 85
FIGURE 49: MICRO-MORPHOLOGIES OF (A) BARE, (B) TiO_2, (C) ZrO_2, AND (D), HfO_2 COATED SAMPLES AFTER CORROSION [135]. 86
FIGURE 50:MACRO-MORPHOLOGIES OF BARE, TiO_2 , ZrO_2 AND HfO_2 COATED SAMPLES BEFORE AND AFTER CORROSION [135]. 86
FIGURE 51: HYDROGEN EVOLVED FROM THE IMMERSION OF BARE AND COATED AZ31 ALLOY IN SBF [135]. 87
FIGURE 52: SCHEMATIC OF THE ALD SYSTEM DESIGN USED FOR THE ALD DEPOSITION OF CU. 90
FIGURE 53: SCHEMATIC REPRESENTATION OF THE REACTION MECHANISM OF THERMAL ALD OF CU USING $Cu(acac)_2$ AND H_2 91
FIGURE 54: SEM IMAGES OF THE ALD DEPOSITED CU FOR DIFFERENT NUMBERS OF CYCLES SHOWING SEPARATE ISLAND TI (A-C) MESH AS COMPARED TO CLUSTER FORMATION ON NI (D-F) MESH. 92
FIGURE 55: OER PERFORMANCE OF DIFFERENT CU COATED AND PRISTINE SAMPLE TI AND NI MESH SAMPLES IN 1 M KOH, (A) AND (B) LINEAR SWEEP VOLTAMMOGRAM OF THE OXYGEN EVALUATION REACTION, (C) POTENTIAL AT CONSTANT CURRENT DENSITIES FOR DIFFERENT SAMPLES, AND (D) STABILITY TEST FOR NI WITH 500 CYCLES OF CU. 96
FIGURE 56: (A) 3D REPRESENTATION OF THE IN SITU ALD REACTOR, (B) FRONT-VIEW CROSS-SECTIONAL DIAGRAM OF THE ALD REACTOR (DIMENSIONS IN MM). 102
FIGURE 57: 3D REPRESENTATION OF THE MANIFOLD DESIGN WITH THE ALD VALVES AND PRECURSOR. 102
FIGURE 58: 3D REPRESENTATION OF SAMPLE HOLDER ASSEMBLY. 103
FIGURE 59: ABSORBANCE SPECTRA FOR SI AT NORMAL INCIDENCE VS. AT BREWSTER ANGLE WITH NO SAMPLE AS BACKGROUND [52]. 104
FIGURE 60: (A) ABSORBANCE SPECTRA (1000 - 4000 cm^{-1}) AFTER 1st, 2nd TMA, AND WATER PULSE, RESPECTIVELY, WITH 5 NM SI/KBR SUBSTRATE AS BACKGROUND FOR 1st TMA PULSE MEASUREMENT. PREVIOUS MEASUREMENTS ARE THE BACKGROUND FOR REMAINING SUBSEQUENT MEASUREMENTS (B) ABSORBANCE SPECTRA FROM (500-1500 cm^{-1}) [52]. 106
FIGURE 61: X-RAY ABSORPTION SPECTRUM OF AN ELECTRODE INCORPORATING THE IRON–SULFUR–LITHIUM NANOCOMPOSITE [128]. 110
FIGURE 62: IN SITU XAS ALD REACTOR MOUNTED ON THE SUPPORT FRAME. 115
FIGURE 63: OVERVIEW OF X-RAY BEAM DIRECTION AND SAMPLE POSITION 116
FIGURE 64: PRECURSOR BOOSTING SETUP FOR LOW VAPOUR PRESSURE PRECURSORS. 117
FIGURE 65: SEM MICROGRAPHS OF ALD CU NUCLEATION ON (A) TI, (B) SI, AND (C) RU SUBSTRATES. 122
FIGURE 66: SEM MICROGRAPHS OF ALD CU ON TI SUBSTRATE WITH DIFFERENT NUMBER OF CYCLES. 122
FIGURE 67: ISLAND GROWTH OF ALD CU ON TI SUBSTRATE. 123
FIGURE 68: STUDYING THE EFFECT OF SUBSTRATE TEMPERATURE OF ALD CU ON TI SUBSTRATE. 123

FIGURE 69: STUDYING THE EFFECT OF H_2 EXPOSURE OF ALD CU ON TI SUBSTRATE....124
FIGURE 70: STUDYING THE EFFECT OF AR FLOW FOR BOOSTING OF THE CU PRECURSOR.....124

1. Chapter 1: Introduction and overview

Atomic layer deposition (ALD) occupies a unique position in both research and industry due to its ability to deposit materials with nanoscale precision, high uniformity, conformality, and excellent stoichiometry control [1]. This technique has revolutionized the fabrication of commercial devices with film thickness below 5 nm [2] . In addition, ALD enables the deposition of complex materials, such as doped, ternary, quaternary, and multi-component materials, in a single process [3] . With the increasing demand for downsizing and the use of more economical materials, ALD has become the benchmark and ultimate limit for miniaturization in manufacturing [4]. As a result, the ALD materials library is rapidly expanding to include metals, insulators, and semiconductors in both crystalline and amorphous phases [5]. ALD is now an essential process in emerging research and industrial applications, particularly in the development of novel semiconductors, energy conversion technologies, and protective coatings [6].

1.1 ALD growth modes

1.1.1 Surface interaction

In terms of growth, by definition ALD growth takes place with an atom-by-atom arrangement in the form of monolayer growth, but in reality, less than a monolayer growth is observed for most of the processes [7]. The two important factors for such behavior are steric hindrance, where the precursor molecule is prevented from interacting with the active sites on the surface, and the other is the lack of active species on the substrate [8].

The growth mode can be categorized into three types based on the interaction forces between the adsorbed atoms and both the underlying substrate and the deposited substrate [9] (*Figure 1*). The first type represents an ideal scenario, where one monolayer is grown per cycle, resulting in 2D growth. This growth mode is also referred to as Frank-van der Merwe growth or bi-dimensional growth. In terms of surface forces, the adhesive force on the surface surpasses the cohesive force between atoms of the precursor molecule, facilitating a layer-

by-layer growth on the substrate. In other words, the atoms fully cover the surface, forming a complete monolayer before the subsequent layer is deposited on top.

In the second type of growth, known as Volmer-Weber growth [10], growth occurs in the form of islands due to substrate dependence or inhibition. This island growth is facilitated by the preferential absorption of precursor molecules on the deposited surface. In this mode, the initial nucleation of small clusters or islands takes place on the surface. The formation of these islands is attributed to the fact that the interaction between the adsorbed atoms is stronger among themselves compared to their interaction with the substrate. In terms of energy or force, the cohesive force among the atoms surpasses the surface adhesive force, causing the atoms to accumulate. Subsequently, these small clusters grow into larger three-dimensional structures and eventually merge to cover the entire surface.

Lastly, the third type of growth, known as Stranski-Krastanov growth [11], is characterized by random deposition. In this growth mode, molecules have an equal probability of attaching to any surface, resulting in much smoother films when compared to island growth.

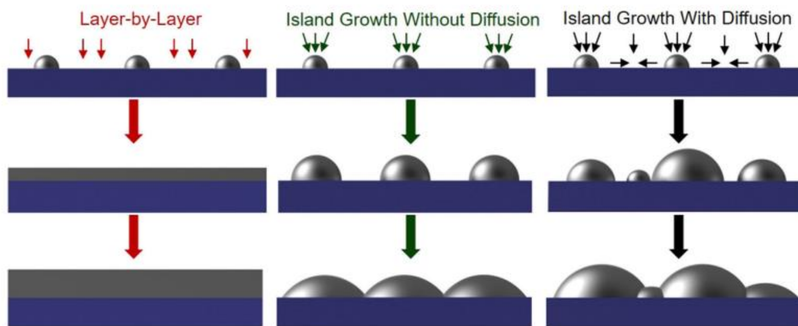

Figure 1: Schematic illustration of selected growth modes possible in ALD: two dimensional growth or layer by layer growth, island growth without diffusion and random deposition due to island growth with diffusion [12].

The nucleation phenomenon and the types of growth can also be understood in the context of wetting behavior, which can be described using Young's equation [13] . In this scenario, the initial nanoparticles or clusters formed on the substrate can be thought of as liquid droplets on a solid surface. This perspective provides insights into the relationship between surface energies and wetting behavior [14].

Young's equation, represented as eq.(1):

$$\gamma_S = +\gamma_L(\cos\ \theta) + \gamma_{SL} \qquad (1)$$

where, S represents the substrate, L denotes a liquid droplet on the substrate, SL stands for the substrate-liquid interface, and θ represents the contact angle. γ_S represents the surface energy of the substrate, γ_L is the surface energy of the nanocluster "droplet," and γ_{SL} is the interfacial energy between the substrate and the nanocluster "droplet."

In the case of ideal wetting behavior, θ approaches approximately 0, and cos θ approaches approximately 1. Under these conditions, Young's equation simplifies to $\gamma_S = \gamma_L + \gamma_{SL}$. Assuming there is finite interfacial energy, wetting requires that $\gamma_S > \gamma_L$. Consequently, the underlying substrate must have a higher surface energy than the liquid "droplet" on the substrate for uniform nucleation and the formation of ultra-thin films.

The growth modes discussed above can be influenced by process parameter, such as the precursor purge time, which affects the self-limiting behavior. Self-limiting behavior is a fundamental characteristic of ALD [1], setting it apart from closely related thin-film deposition techniques like CVD. In the ALD process, each cycle comprises two half-reactions. In the first half-reaction, a precursor molecule is introduced to the substrate and reacts with the surface, forming the first half-layer. Followed by removal of unreacted gas.Then, the second half-reaction involves a second precursor, which reacts with the surface to form the monolayer, again followed by removal of unreacted precursor molecules. Notably, these half-reactions are self-terminating, meaning that surface saturation occurs during each half-reaction. Once the surface is saturated, additional precursor molecules do not readily react, leading to the self-limiting behavior. Saturation takes place when all available reaction sites on the surface are occupied by precursor molecules, preventing further reactions

In other words, as the exposure of the precursor increases, the surface reaches a point of saturation, rendering it non-reactive. In cases where only a fraction of the substrate's surface is covered, achieved by reducing the duration of the precursor pulse and purge, the surface retains limited reactivity. This may occur due to the short purge duration, which can leave unreacted precursor molecules. Subsequently, when the co-reactant is introduced, it can lead to gas-phase reactions, resembling CVD growth. To achieve pure ALD growth, it is crucial to

provide a sufficient precursor pulse to fully saturate the surface and an adequate purge to completely remove any unreacted gases.

1.1.2 High aspect ratio structures

The trend toward miniaturization in semiconductor devices has led to the development of increasingly complex 3D structures with a high aspect ratio (HAR), characterized by significant differences in depth and width. When dealing with HAR structures, the growth behavior of ALD within narrow features in the molecular flow regime can be categorized as either diffusion-limited or reaction-limited. It's important to note that the type of ALD growth is influenced by both the aspect ratio (AR) of the feature and the sticking probability of the ALD reactants. The aspect ratio (AR) of a structure is conventionally expressed as AR = L/w, where 'L' (in meters) represents the depth of the structure, and 'w' (in meters) represents its width.

Three distinct growth types can be identified (*Figure 2*). The first, diffusion-limited growth, is influenced by the geometry of the feature, which significantly impacts the coating process. During deposition, the most readily accessible surface sites are the initial ones to be covered, resulting in a distinct boundary between the coated (accessible) and as-yet-uncoated (less accessible) regions. This boundary gradually extends deeper into the feature as deposition proceeds. In the second type, known as reaction-limited growth, the primary characteristic is a notably low sticking probability of the reactant molecules. In such scenarios, the division between the coated and uncoated sections of the feature is less distinct and less sharply defined, ultimately leading to a more conformal deposition. The third type is recombination-limited growth, where saturation is not primarily influenced by diffusion rates or sticking probabilities but is instead determined by the loss of radicals due to recombination during collisions with the feature's side-walls.

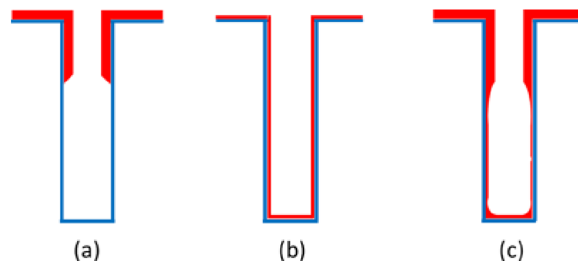

Figure 2: Schematic representation of unsaturated thickness profiles: (a) diffusion limited, (b)reaction limited and, (c) recombination limited growth type [1].

1.2 Motivation

1.2.1 Exploring ALD-based application

1.2.1.1 ALD of oxides as a protective coating

1.2.1.1.1 ALD of oxides

The ALD of oxides have been widely implemented in the semiconductor industry [2] due to the development of efficient growth process that allows conformal and uniform thin films [15]. Also, compared to the ALD of metals, the nucleation and growth aspect of most common oxides such as Al_2O_3, HfO_2, TiO_2, and ZrO_2 has been conformal and uniform [16]. This is due to the availability of stable precursors, the presence of suitable reactive sites on the deposition surface, and, most importantly, efficient self-terminating surface reactions [16].

1.2.1.1.2 Protective coating application

The ability of ALD to deposit of uniform and conformal coatings has been incomparable. Its exceptional performance in prolonging the operational lifespan and enhancing the performance of organic light emitting diodes (OLEDs) is well studied and implemented [17]. OLEDs are vulnerable to environmental factors, such as moisture and oxygen, which can lead to performance degradation and reduced longevity. In recent years, researchers are actively exploring a multitude of applications where ALD's unique capability for uniform surface coating has yielded promising results [18]. Notably, ALD has demonstrated its effectiveness in corrosion protection for steel through the deposition of metal oxide coatings. This underscores the versatility and reliability of ALD in a wide range of protective coating applications [19].

1.2.1.2 ALD Cu as a catalyst for oxygen evolution reaction (OER)

1.2.1.2.1 ALD of Cu

Copper (Cu) has long been favored as an interconnect material [20] in the microelectronics industry due to its low electrical resistivity, high electro-migration resistance, high thermal conductivity, and favorable chemical and thermodynamic properties [21].

To deposit Cu thin films, several techniques such as electrochemical deposition, physical vapor deposition (PVD), chemical vapor deposition (CVD), and atomic layer deposition (ALD)

can be used. However, with the increasing demand for downsizing and designing high aspect ratio structures, where "downsizing" here refers to the trend in the microelectronics industry where there is a demand for making electronic devices smaller and more compact. This typically involves reducing the size of individual components, features, and structures on semiconductor devices, for higher performance and greater integration of components into smaller spaces to improve device performance and efficiency. As a result, new challenges have arisen, such as decreased cross-sectional area leading to increased resistance and non-uniform deposition.

The microelectronics industry often utilizes ALD alongside PVD despite ALD being more expensive for the deposited thickness [22]. In general for common metal oxides, such as Al_2O_3, HfO_2, TiO_2, ZrO_2 etc. ALD provides precise and conformal coating, making it suitable for manufacturing ultra-thin films and complex multilayers, as well as achieving consistent thickness even in complex structures. It also offers control over material properties, electrical properties, and the creation of effective barrier layers, which are essential for next-generation devices and improved device reliability. While PVD is more economical, the unique capabilities of ALD are essential for meeting the increasingly stringent requirements of advanced semiconductor manufacturing, justifying its use despite higher costs.

Among the various deposition techniques, PVD methods like thermal evaporation and sputtering have been widely employed in the industry [23] . However, ALD has recently gained significant attention as a seed layer for subsequent electrolytic and electroless deposition methods [24], especially for the deposition of Cu on arbitrary substrates. Despite this interest, preferential growth on metallic surfaces like Ti, Pt, and Ru has been observed, leading to non-uniform and rough thin films due to island growth and contamination from precursor decomposition. Moreover, growth studies for different precursors and substrate combinations are limited.

While thermal ALD of Cu suffers from a slow growth rate, high temperature requirement (>240°C), and incorporation of impurities, plasma-based processes have been explored to address these limitations [25]. However, these processes have resulted in high roughness and agglomeration of Cu thin films [26], making it difficult to deposit conformal films on high aspect ratio structures [27].

Apart from microelectronics, Cu-based materials have also garnered significant interest in catalysis [28] and gas sensing applications [29], making it imperative to address these challenges to explore the full potential of Cu in various fields.

1.2.1.2.2 Oxygen evolution reaction (OER) catalyst application

Due to the instability in the supply of conventional fossil fuels for energy generation and growing concerns about the effects of global warming resulting from ever-increasing greenhouse gas (GHG) emissions, there is a pressing need to find sustainable energy solutions. One approach is to convert water to chemical energy by splitting it into oxygen and hydrogen, but the anodic oxygen evolution reaction (OER), which is essential for this process, is a complex and slow process that requires high energy inputs [30].

To facilitate the OER, an ideal catalyst should promote the reaction rate, reduce the over-potential, and have low activation energy. While noble metal-based catalysts such as RuO_2, IrO_2, and Pt have shown high OER performance, their limited availability and high cost makes them unsuitable for large-scale implementation [31]. Therefore, there is a need for stable, active, and cost-effective electro-catalysts, for which different materials and strategies must be explored.

Recently, Copper based materials has emerged as a promising catalyst due to its numerous advantages, such as low cost, low toxicity, high electrical conductivity, and high strength compared to other transition metals [32]. Additionally, Copper has demonstrated remarkable electrocatalytic activity and stability, making it a viable candidate as a replacement material for noble metals in OER applications [33]. As such, there has been growing interest in exploring Copper-based catalysts as a potential solution for sustainable energy generation.

1.2.1.3 ALD perovskite applications

1.2.1.3.1 ALD of perovskites

Perovskites are a type of ternary oxide that typically have a cubic structure. When using Atomic Layer Deposition (ALD) to deposit perovskites, a sequential reaction occurs where binary oxides AO and BO_2 are formed (Figure 3). The growth rate of AO on BO_2, or vice versa, differs due to differences in bonding site density and chemisorption rates provided by the surfaces. A perovskite structure is typically formed by intermixing these binary layers [34].

Therefore, for successful ALD deposition, the diffusion length of atomic species should be higher than the thickness of each binary layer, which should be less than 2 Å. This allows for the mobility of atoms and results in a uniform composition. If the binary layer thickness is greater than 2 Å, atomic species diffusion is restricted, resulting in phase segregation [3]. In such cases, a higher deposition temperature or a post-deposition annealing process is required to increase the diffusion of atomic species [3]. Therefore, to develop perovskites with a specific composition, it is crucial to understand the interaction of materials with different surfaces.

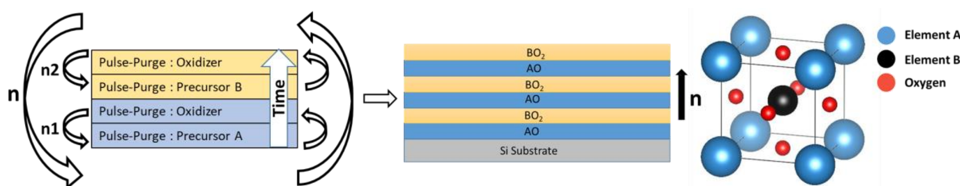

Figure 3: ALD growth of ABO_3 compounds [34]

1.2.1.3.2 Applications

Perovskites deposited using atomic layer deposition (ALD) offer several advantages that make them a promising choice for various applications. Research on ALD deposition of perovskites for dynamic random access memory (DRAM) applications [35] has shown that thin films of strontium titanate (STO) and barium titanate (BTO) [36–38] with high dielectric constants (over 146) are ideal candidates, resulting in an equivalent oxide thickness (EOT) below 0.5 nm [39].

Perovskite-based piezoelectric materials have recently gained attention for their use in nano-electromechanical systems (NEMS) and micro-electromechanical system (MEMS) based applications. Barium titanate (BTO) based perovskites with high piezoelectric coefficient d33 of 500 pC/N [40], comparable with lead zirconate titanate (PZT) [41], are a promising lead (Pb) free alternative for piezoelectric materials [39].

In addition, perovskite-based solar cells have been successfully developed using methylammonium lead iodide ($CH_3NH_3PbI_3$), achieving more than 20% efficiency and thus becoming competitive with silicon-based solar PV technologies [42] . Moreover, a novel hybrid ALD process that combines ALD lead sulfide (PbS) [43] with further processing can be implemented to fabricate light-emitting diodes[44].

ALD provides the feasibility of working at lower temperatures with controlled conformal growth for these applications. Furthermore, lanthanum-based perovskite compounds are used for thermo-chemical processes where oxidation and reduction reactions are leveraged for the production of H_2 and CO in solar energy conversion [45]. ALD deposition of perovskites enables conformal deposition on high surface area structures, ultimately improving the fuel yield. Additionally, perovskite redox materials allow for lower temperatures (1200˚C) compared to conventional cerium oxide, which generally requires higher temperatures (1500 ˚C), resulting in an unpractical thermal load to the system [39].

These applications demonstrate the potential of ALD-deposited perovskites to enhance performance and provide novel solutions for various industries.

1.2.2 Challenges in ALD growth

With new and novel applications and materials comes new challenges. In recent years, there has been significant development and experimentation with new precursors containing various organometallic compounds for ALD [46]. Despite these efforts, however, there is still a lack of clear understanding regarding the reaction mechanisms occurring during the ALD process for many of these precursors [47].

It is important to note that the initial nucleation phase of ALD can differ significantly from the later stages, where self-limiting chemical vapor exposure governs the growth process [5]. This early stage can vary across different material systems, and the chemical and physical mechanisms behind the nucleation phenomena are still not fully understood. This phase is crucial in determining the properties of future thin films. Therefore, a deeper understanding of this phase is essential for successful miniaturization. In addition to this, the topological and morphological studies at atomic scale resolutions are currently insufficient [48], indicating a need for further research in this area.

Moreover, perovskite materials deposited through ALD are multi-component materials that require a combination of binary cycles to deposit them, known as a super cycle. This complex deposition process requires a detailed understanding of the growth mechanism and precursor interaction to achieve controlled growth and tunable functionalities [49].

Thus, conducting *in situ* studies can help achieve optimized ALD growth by providing continuous chemical and physical information during the process [50]. This will enable a better understanding of the complex interactions and mechanisms involved in the deposition process, leading to more efficient and effective use of new precursors and improved thin film properties.

1.2.3 *In situ* ALD studies

In situ ALD studies provide a direct way to observe the surface chemistry, physical and structural properties of the ALD process. These studies offer valuable insights into the nucleation and growth of thin films, surface chemistry and defects, and the effects of process parameters on film properties [51]. By analyzing this information, process control can be improved, new precursors can be designed, and reaction conditions can be tailored to achieve desired material properties. *In situ* studies also allow real-time measurements of film thickness and facilitate the optimization of process parameters for the desired material properties. However, challenges with *in situ* techniques include the need for specialized equipment, limited characterization techniques, and higher costs and time requirements for initial experiments.

1.2.3.1 *In situ* FTIR ALD

One of the analytical techniques that can be used is infrared (IR) spectroscopy, which offers the advantage of flexibility in the variety of sample types to be analysed (e.g., liquids, powders, gases, thin films, and solid surfaces). In addition, *in situ* FTIR systems allow us to detect surface organometallic species from the first reactant half-cycle and thus help us to map out ligand exchange reactions in the subsequent half-cycles [52].

FTIR spectroscopy is a powerful tool for analyzing the surface chemistry of materials when integrated with an ALD reactor (Figure 4), allowing us to conduct real-time analysis of film growth and surface chemistry during the deposition process.

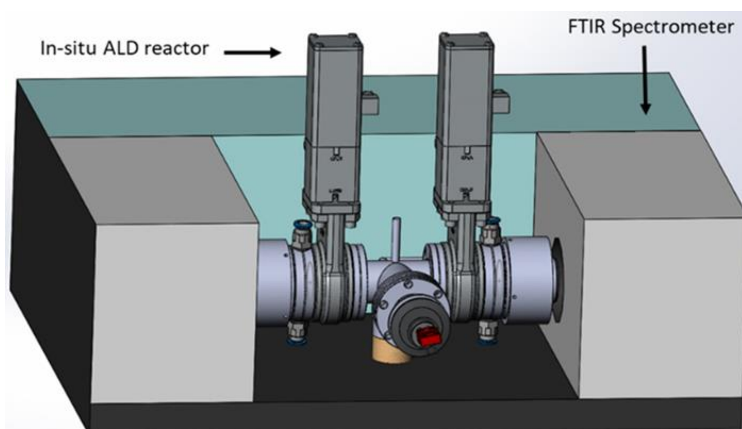

Figure 4: Schemtic represenation of the integration of ALD reactor and FTIR system.

The principle of ALD involves sequential exposure of a substrate to two or more precursor gases, which react with the substrate surface to form a monolayer of the desired material. After each exposure, the substrate is purged with an inert gas to remove any unreacted precursor and reaction by-products. In *in situ* FTIR ALD, the FTIR spectrometer is used to analyze the surface species of the substrate before and after each precursor exposure. This allows for the identification of the formation of the desired material and any unwanted by-products. This technique is particularly useful in detecting surface organometallic species from the first reactant half-cycle and mapping out the ligand exchange reaction in subsequent half-cycles.

Moreover, FTIR spectroscopy is an inexpensive and widely available tool in different labs, with a high signal-to-noise (S/N) ratio and low data acquisition time [52].

1.2.3.2 *In situ* XAS ALD

X-ray absorption spectroscopy (XAS) is an element-specific technique that can provide valuable information about local electronic and geometric structures of materials. XAS has several key advantages [31]. *In situ* XAS ALD system (*Figure 5*) at a synchrotron can probe a much wider range of elemental edges and has a much higher signal-to-noise (S/N) ratio due to orders of magnitude higher flux, allowing for the detection of even trace elements.

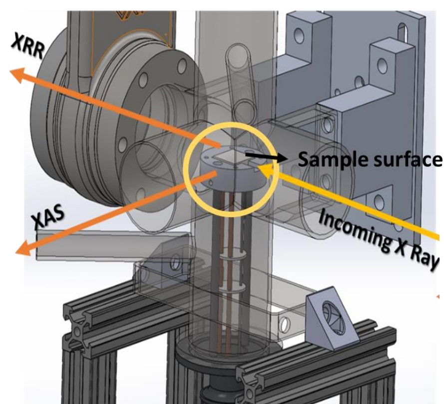

Figure 5: Description of the X-ray beam incident on the sample surface in the in situ XAS reactor assembly.

XAS can be divided into three main regions: the pre-edge, X-ray absorption near edge spectroscopy (XANES) region, and extended x-ray absorption fine structure (EXAFS). Each region provides valuable information about the material. The pre-edge region can estimate ligand-field, spin-state, and centrosymmetric. The XANES region can be used to obtain local geometric structure and metal-ligand overlap via shakedown transitions, ligand arrangement, oxidation state, and density of states. The EXAFS region can obtain bond distances, coordination numbers, and Debeye-Waller factors [32].

1.3 Thesis objective

The objective of this Ph.D. thesis is to investigate and evaluate the potential of atomic layer deposition (ALD) for various applications, leveraging its unique growth behavior. With the increasing demand for new materials and complex processes in emerging applications, there are growing challenges in the growth of ALD thin films. Therefore, it is crucial to develop a comprehensive understanding of the growth process. Furthermore, the thesis aims to design and develop *in situ* ALD systems that can monitor the growth process for new or intricate procedures, especially for ultra-thin films in the expanding field of novel applications. Through these efforts, the thesis seeks to advance the knowledge and capabilities of ALD technology and enable its broader use in cutting-edge applications

1.3.1 Research questions this Ph.D. thesis is answering

Question 1. What is the scope of ALD based applications beyond microelectronics, and what are their potential benefits?

- ALD for Catalyst design
  High surface area materials have found interest due to low over-potentials and enhanced activity as an oxygen evolution reaction (OER) catalyst compared to planar surface forms. ALD deposited Cu on Ti and Ni mesh as a catalyst for OER will be investigated.

- ALD for protective coatings
  Investigating the corrosion behaviour of ALD-coated AZ31 magnesium alloy for use in biomedical applications

Question 2. Can ALD be adapted to deposit new materials and complex structures?

- Review: ALD of perovskites
  A literature study is conducted, and the growth of ALD perovskites is discussed, with an application-centered overview of the characteristics of perovskite processing in the ultrathin films regime.

Question 3. What are the major difficulties in developing new ALD materials and processes?

- Review: ALD of perovskites
  The different challenges associated with complex and new process are highlighted, such as unknown chemistry, abnormal growth behavior, differential growth at interface and process parameters optimization requirements thus revealing importance of growth studies.

<u>Question 4.</u> How can we optimize the growth of ALD thin films for new materials and processes?

ALD growth studies can be conducted by both *ex situ* and *in situ* means, but the degree of understanding of the process property relationhip varies.

- <u>*Ex situ* study</u>
  In this work, preliminary *ex situ* study was conducted for ALD Cu (Ch. : 9), where the effect of process parmeters on the nucleation and growth was evaluated and discussed.

- <u>*In situ* study</u>
  In situ ALD studies provide a direct way to observe the surface chemistry, physical and structural properties of the ALD process. Thus, in this work *in situ* ALD systems will be designed which will enable in situ studies.

<u>Question 5.</u> Can we develop an *in situ* ALD system that can enable real-time monitoring and control of the deposition process?

- <u>*In situ* FTIR</u>
  In this work, a flexible and compact *in situ* transmission FTIR spectroscopy ALD system is designed and built, allowing us to detect surface organometallic species from the first half-cycle and map out ligand exchange reactions in the subsequent half-cycles.

- <u>*In situ* XAS</u>
  In this work, an *in situ* XAS ALD system was designed to investigate the ALD growth of Cu, a process whose general principle is well-known, but the nucleation phase has not been explored experimentally due to the challenge of characterizing the minute quantities of material deposited in each half-cycle.

<u>Question 6.</u> What are the critical differences between the designed *in situ* ALD system and state-of-the-art *in situ* ALD systems , and how can we leverage these differences to advance the field?

In this work, a detailed description of the system design and important aspects related to it are discussed. It is anticipated this work will be valuable knowledge for a wider community working on material growth and characterization.

Certain aspects are highlighted that are critical for successful implementation of *in situ* ALD studies such as, reactor heating, minimum reactor volume, protection of optical window, direct integration of the characterization equipment, detector selection in the case of *in situ* FTIR studies, portable system design and substrate selection

<u>Question 7.</u> What are the technical and practical challenges in building an *in situ* ALD system and what are the potential solutions and trade-offs?

This work emphasizes the practical challenges that arise in the design of *in situ* systems. The most critical of these challenges is the integration of the characterization tool and ALD system. This integration is often hindered by limited space, which is a common observation. In addition, the modular design and numerous vacuum components can make leak detection a significant challenge, consuming a considerable amount of time and resources.

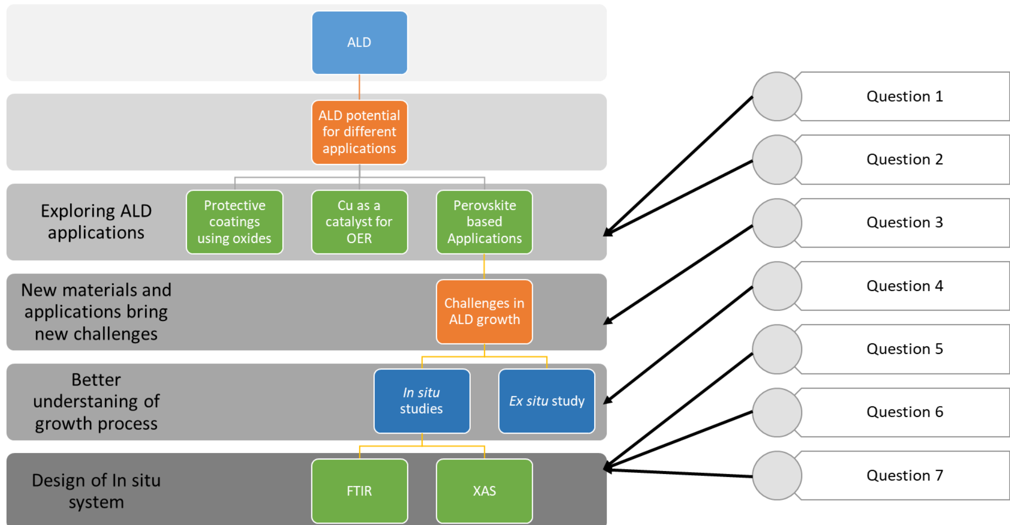

1.4 Thesis structure

This thesis consists of 9 chapters, an outline and summary of each chapter is presented here,

<u>Chapter 1</u>*: *Introduction and overview

This chapter serves as a background to the research work, which aims to explore the use of atomic layer deposition (ALD) for various applications and to develop *in situ* ALD systems to address the challenges associated with new materials and future applications. It includes the motivation behind the research, as well as the objectives and key research questions answerred in the thesis.

<u>Chapter 2</u>*: *Literature review

This chapter provides an overview and introduction to the atomic layer deposition (ALD) process and highlights its unique capabilities in comparison to other deposition techniques. It also gives a brief overview of different applications that use ALD. Furthermore, the section highlights various characterization tools that have been utilized in *in situ* ALD studies.

A section is assigned to ALD perovskite for novel applications, the use of more complex materials with Atomic Layer Deposition (ALD), such as perovskites, has been explored for novel applications. To better understand the potential of ALD technique for deposition of these materials, a literature review was conducted, which discusses various perovskite-based applications. Additionally, the review includes an examination of the growth process for Strontium Titanate (STO), in order to gain insights into the challenges associated with such processes and the steps required to tackle them.

Finally a section in this chapter is dedicated to a discussion on “Why *in situ* studies are required?” In this section, we will briefly introduce various in situ techniques and emphasize why in situ studies are important. Subsequently, we will discuss the main reasons for conducting such studies. This discussion will help us understand how in *situ* systems contribute to and improve the ALD process.

<u>Chapter 3</u>*: *Experimental techniques

This chapter provides an overview of the various characterization methods employed in this study. It includes system details of fourier transform infrared spectroscopy (FTIR), X-ray

absorption spectroscopy (XAS), X-ray photoelectron spectroscopy (XPS), scanning electron microscopy (SEM), energy-dispersive X-ray spectroscopy (EDS), ellipsometry, and electrochemical measurements equipment used in this research.

<u>Chapter 4</u>*: *Experimental study – ALD of oxides as protective coatings

This chapter presents a summary of experimental work on the use of atomic layer deposition (ALD) as a protective coating. It begins with a discussion on the benefits of ALD of metal oxides for corrosion protection, highlighting the advantages over other deposition methods. The chapter then describes the results of my contribution to this collaborative work, which involved conducting ALD and sputter deposition of thin films, using spectroscopic ellipsometry to measure film thickness, profilometry to assess surface roughness, and X-ray photoelectron spectroscopy (XPS) to determine the materials chemical composition. A complete set of results for this section is provided in the research articles included in the Appendix.

<u>Chapter 5</u>: Experimental study – ALD of Cu as a catalyst for Oxygen evolution reaction(OER)

This chapter presents the experimental study on the use of atomic layer deposition (ALD) of copper on high surface area 3D structures as a catalyst for the oxygen evolution reaction.

<u>Chapter 6</u>: Experimental study – Design of in situ ALD FTIR system

This chapter focuses on the experimental work conducted to design an *in situ* ALD FTIR system, based on our published research article. The chapter begins with a discussion on the *in situ* FTIR technique, followed by a review of the current state of the art. Subsequent sections describe the design of the *in situ* FTIR system, along with details of the validation process. By presenting this experimental work, the chapter aims to contribute to the ongoing efforts to improve the ALD process through the development of effective *in situ* system.

<u>Chapter 7</u>: Experimental study – Design of in situ ALD XAS system

This chapter builds upon previous work on the design of *in situ* Atomic Layer Deposition (ALD) systems, focusing specifically on the design of an *in situ* X-ray Absorption Spectroscopy (XAS) system. The chapter begins with an introduction to XAS and an explanation of why *in situ* XAS is a useful characterization strategy for ALD processes. The design of the *in situ* XAS system is then discussed, followed by a description of the preliminary *ex situ* experiments carried out

to develop an initial ALD Copper (Cu) process and gain an understanding of the growth process. Finally, a discussion of the *in situ* XAS experiments is presented, including the challenges faced during measurement and subsequent improvements made to the system.

***Chapter 8*: Conclusion and future work**

This chapter serves as the conclusion for the entire body of work conducted during this Ph.D. research. Based on the results obtained and the current status of the work, the chapter also includes a discussion of future directions for research.

***Chapter 9*: References**

This chapter serves as a comprehensive list of all references cited throughout the thesis.

2. Chapter 2: Literature review

2.1 Atomic Layer Deposition (ALD)

2.1.1 Background

ALD is a thin-film deposition method, often regarded as a variation of the chemical vapor deposition (CVD) technique. However, a crucial conceptual distinction exists between ALD and CVD. In CVD, the process is steady-state, meaning that growth continues at a consistent rate as a function of time, maintaining a constant growth rate over time. In contrast, ALD is based on the principle of self-limited interactions between species and the substrate surface. This means that molecules can only react with a finite number of available surface sites. Once these sites are consumed, the growth process terminates. This unique characteristic of ALD results in inherently conformal deposition, as it ensures that the growth precisely conforms to the contours and features of the substrate.

There has been a dispute on the claims of the invention of the ALD technique. However, the consensus is that it was independently invented twice [53]. The well-known origin of ALD, named initially “atomic layer epitaxy” (ALE), was in Finland in the 1970s by Prof. Suntola [54]. However, ALD was also studied earlier in the form of “molecular layering” in the former soviet union in the 1960s by Prof. Aleskovskii and Kolt’sov [55].

2.1.2 Principle

ALD deposition process works on the principle of self-limiting sequential interaction of precursor and co-reactant. Generally, a single precursor and co-reactant are used for binary compounds. Whereas, complex compounds or multi-component materials are deposited by combining binary cycles [3]. The distinctive self-limiting characteristics of ALD allow comparatively better conformal growth behavior and control over the thickness compared to CVD process. The thickness of the deposition is controlled by the number of cycles defined in the process. *Figure 6* describes a typical ALD system with major components.

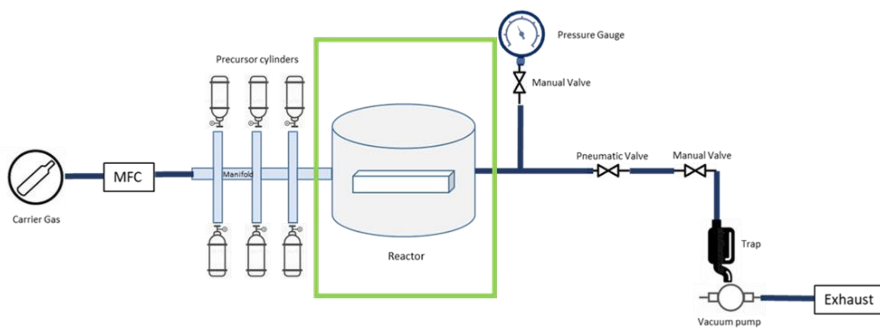

Figure 6: Simplified schmeatic of ALD system with major components.

To better understand the ALD growth process, we will review the Al_2O_3 growth mechanism [52]. The ALD Al_2O_3 growth on -OH terminated SiO_2/Si substrate mainly involves –CH_3 and –OH groups. The chemistry can be illustrated schematically, as shown in *Figure 7*. The ALD cycle starts with an -OH terminated surface. In the 1st half-cycle, trimethyl aluminum (TMA) vapor is pulsed in a controlled way to chemisorb the -OH groups present on the surface. TMA presence initiates a ligand exchange reaction (eq. 2), where the metal component of the precursor attaches with oxygen and simultaneously forms a -CH_3 terminated surface. This results in CH_4 (g) molecules forming as a reaction product. This is followed by a system purge using inert gas to remove the unreacted precursor and reaction by-products, which gives the ALD process itself a limiting characteristic behavior. The 2nd half-cycle consists of an H_2O vapor pulse which reacts with a –CH_3 terminated surface, initiating ligand exchange reaction, resulting in the formation of a –OH terminated surface, followed by a similar inert gas purge of the reactor (eq. 3). The reactions ((eq. 2 and eq. 3)) are summarized in the equations below (with the surface represented as ǁ), and we obtain the required thickness of the thin film by specifying the number of cycles in the ALD process. This enables us to achieve precise control over the deposition of conformal and uniform thin films [52].

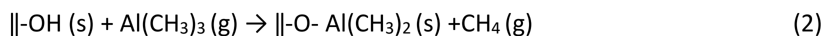

$$\| \text{-OH (s)} + Al(CH_3)_3 \text{ (g)} \rightarrow \| \text{-O-} Al(CH_3)_2 \text{ (s)} + CH_4 \text{ (g)} \qquad (2)$$

$$\| \text{-O-} Al(CH_3)_2 \text{ (s)} + H_2O \text{ (g)} \rightarrow \| \text{-O-} Al(CH_3)OH \text{ (s)} + CH_4 \text{ (g)} \qquad (3)$$

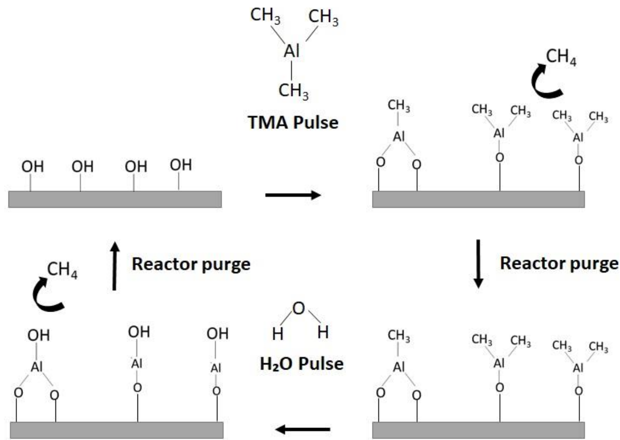

Figure 7: Schematic representation of the chemistry involved in the cyclic ALD process of Al_2O_3 using TMA and H_2O [52]

2.1.3 Process characteristics

The defining feature of ALD is saturated growth. For each ALD cycle, the reaction between the precursor molecule and the surface should be self-limiting, and the presence of excess precursor should not result in an increased growth rate. Thus, for an ideal ALD process, saturated growth is expected.

For ALD processes, the growth rate is defined in terms of growth per cycle (GPC). The GPC can be linear or non-linear depending on multiple factors; as shown in *Figure 8*, for a substrate-independent process, linear growth is observed, and for a substrate-dependent growth, the growth could be either enhanced or inhibited in the first few cycles, thus affecting the initial linearity of the growth.

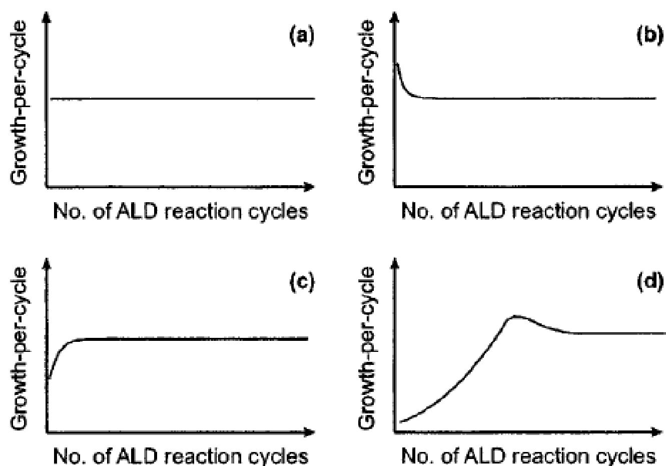

Figure 8: Classification for the ALD processes based on the growth modes: (a) linear mode: where there is a linear increase in growth with number of ALD cycles used, (b) substrate-enhanced mode; the substrate surface provides favourable conditions for the reaction to take place thus resulting in enhanced growth , (c) substrate-inhibited mode of type 1 resulting in no further growth in thicknes after certain number of cycles, and (d) substrate-inhibited mode of type 2, where there is increase followed by dip in thickness of the thin film [10] .

The substrate temperature influences the deposition process (*Figure 9*). Generally, ALD precursor molecules interact differently at different temperatures. It is typically observed that, at low temperatures, a low growth rate could be due to physisorption, as there are a low number of active sites. At the same time, precursor condensation is also possible to result in high growth. In the latter case of condensation, the thin films have a large amount of contamination from the condensed precursor molecule. A similar growth rate is observed at a slightly higher temperature range, called the ALD temperature window; in this temperature window or range, the deposited thin film is expected to be free from contamination. Whereas heating the substrate above the ALD temperature window can either cause precursor decomposition, resulting in a higher growth rate due to contamination, or lower growth due to desorption of the precursor molecules attached to the substrate surface.

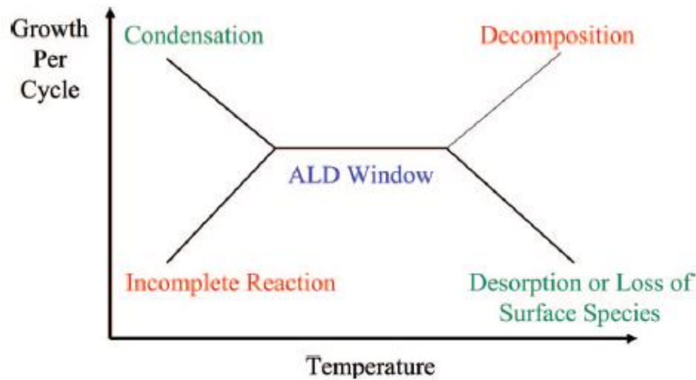

Figure 9: ALD GPC versus temperature showing ALD window [5].

The volatility of an ALD precursor is a critical parameter that impacts film thickness control, uniformity, self-limiting behavior, deposition rate [56], and the potential for thermal decomposition [57]. Precursors with the appropriate level of volatility need to be carefully selected to ensure the success of the ALD process and the desired film properties. The volatility will be further dicussed in the coming precursor selection section.

2.1.4 Type of ALD

The interaction of the precursor molecules with the substrate surface can be driven by different modes. The most used and straightforward approach is thermal ALD, where the reaction is assisted by the thermal energy supplied through continuous substrate heating at a defined temperature, depending on the precursor requirements. This approach has been widely used for depositing ceramics and metals; substrate temperature ranges from 50 °C to 500 °C [58]. In terms of system design, one of the advantages of thermal ALD is simplified reactor design, allowing flexibility in the system setup. Concerning the deposited layer, thermal ALD works well on high aspect ratio structures. The other extensively studied approach is plasma-enhanced ALD [25], which is especially suitable for thermally sensitive substrates that cannot handle high temperatures, such as polymers. The reaction process, in this case, is driven by energetic ions produced inside the reactor. However, plasma ALD limits its use in high aspect ratio structures due to ion recombination [59]. Due to the requirement of attaching additional components to the reactor for plasma generation, the system design is much more complex and less flexible.

2.1.5 Materials range

Advancements in ALD technology have led to the development of new precursors and processes, broadening the range of materials that can be deposited [60]. This range includes pure elements as well as compounds containing Te, F, N, O, S, Se, and other elements, as illustrated in *Figure 10*. While the complexity and efficiency of ALD vary for different materials, binary oxides like HfO_2, Al_2O_3, and ZrO_2 have been widely studied and implemented as high K materials in DRAM capacitors. Ternary compounds, such as $BaTiO_3$ (BTO), which have a perovskite structure [61], are being explored for superior properties in the same application. For microelectronics applications, ALD-based nitrides such as Titanium nitride (TiN) and Tungsten nitride (WN) have been studied as barrier layers [62]. For a comprehensive list of materials studied for the ALD process, please refer to the detailed review [63].

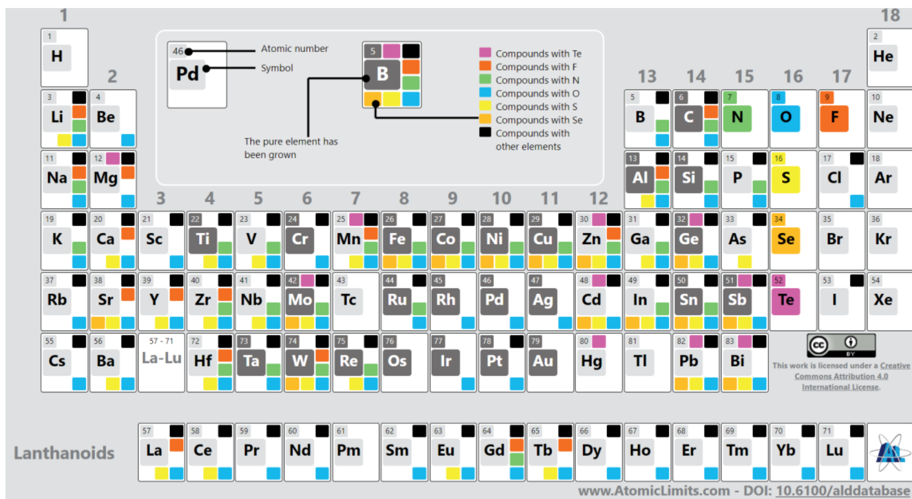

Figure 10: Overview of materials grown by ALD, the ALD growth of pure elements and compounds represented through shading and colors [34] *(source: https://www.atomiclimits.com/alddatabase/* [64]*).*

2.1.6 Precursor selection

When selecting a precursor for a material deposition, it is important to consider the specific process requirements, as there is possibility of multiple precursors for the same material type [34]. Thus, precursors are classified based on their thermal stability, reactivity, and volatility. Ideally, an efficient precursor will react quickly with the substrate surface groups and reach

the surface saturation stage as rapidly as possible. Precursors are typically classified based on their ligands, which includes halides, β-diketonates, alkoxides, alkylamides, alkyls, cyclopentadienyls, and amidinates. Based on the type of ligands the properties of the precursors can be tuned thus helping meet the process requirements [46].

The volatility of an ALD precursor is a critical factor in the ALD process. Volatility refers to how quickly a precursor can transform into a vapor (gas) under specific conditions like temperature and pressure. Highly volatile precursors readily become vapor, while less volatile ones do so more slowly. In ALD, precursors must vaporize to interact with the substrate and create thin films, making their volatility a key determinant of process efficiency. Achieving the right balance of volatility is essential for precise and controlled film deposition. For example, ALD at low temperatures benefits from highly volatile precursors, while less volatile ones require higher vaporization temperatures. However, excessive heating can lead to thermal decomposition before the precursor reaches the substrate, underscoring the importance of an optimal volatility level for successful ALD [65].

2.2 ALD vs. other deposition techniques and its limitations

ALD stands out in terms of thickness control and conformality on 3D surfaces and complex geometries when compared to other available thin film deposition techniques, such as physical vapor deposition (PVD), electrochemical deposition, chemical vapor deposition (CVD), and its variants, including metalorganic chemical vapor deposition (MOCVD). In addition to that, ALD films are versatile, dense, and of high quality [66].

However, the saturated ALD growth comes at the cost of a slow growth rate compared to other deposition process. Nevertheless, this limitation can be compensated by large batch processing, resulting in increased film volume produced in unit time [2].

ALD works efficiently in a defined temperature window, depending on the precursor chemistry. A stable sample temperature is advantageous; inefficient and non-uniform heating can cause cold spots in the reactor, resulting in precursor condensation and subsequent desorption, thus resulting in non-uniform and contaminated thin films.

The ALD process typically consists of a sequence of alternating precursor pulses, each followed by a purge step, rather than a continuous flow of precursor gases as seen in CVD.

Thus, ALD is characterized by the sequential, self-limiting adsorption of precursors. In each ALD cycle, a precursor is pulsed into the chamber for a specific duration, allowing it to react with the substrate surface.

Although ALD is inherently a self-saturating process, designed to limit each precursor pulse to ideally deposit one monolayer of material on the substrate, the pulse duration still holds significance within this framework. In an ideally self-saturating ALD process, the reaction between the precursor and the substrate should conclude in a very short time. An excessively long pulse duration can lead to overexposure, causing more precursor molecules to adsorb than necessary for a single monolayer. This may result in non-ideal film properties and limted thickness control [67]. Conversely, a too-short pulse duration may not provide sufficient time for all reactive sites on the substrate to interact with the precursor, leading to incomplete surface reactions and incomplete monolayer coverage.However, In specific cases, especially when employing less reactive precursors, longer pulse durations might be necessary to ensure adequate surface reactions at lower temperatures. Therefore, optimizing pulse durations is crucial to strike a balance between achieving complete surface reactions, uniform coverage, and efficient precursor usage while adhering to the self-limiting nature of ALD. The optimal pulse duration can also vary depending on the specific ALD process and the desired properties of the thin film [68].

There are limited standardized ALD processes with defined conditions and working windows; new precursor chemistries and processes must be studied and optimized for individual ALD system designs.

PVD techniques (e.g., sputtering, evaporation, and electron beam deposition) are highly directional in terms of deposition direction (*Figure 11*). They rely on the line of sight from the target source to the substrate, resulting in a directional deposition pattern. PVD is susceptible to shadowing effects, where certain areas of a substrate may not receive direct deposition due to obstructed line-of-sight paths. This can lead to non-uniform coverage on complex or deep structures. Also, achieving uniformity with PVD can be challenging on surfaces with complex topographies, It may require substrate rotation or multiple deposition angles to improve uniformity. In contrast, ALD is known for its exceptional uniformity and conformality, making it ideal for complex 3D substrates and high-aspect-ratio structures. It ensures precise

and uniform coverage even on intricate and irregular surfaces which is a distinct characteristic that sets ALD apart.

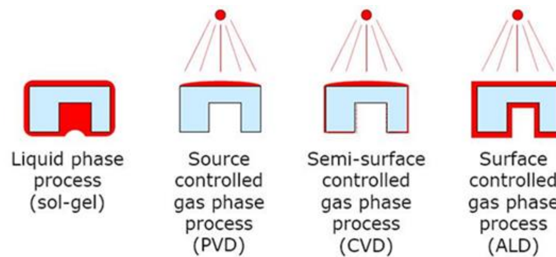

Figure 11: Schematic represenation of directionality in different deposition methods [69].

In terms of cost, commercial ALD systems are comparatively more expensive than other vacuum deposition systems. The cost of maintenance of the different components and high precursor costs add to overall costs in the long run. In recent years, home-built ALD systems have been designed and built to study new processes at a much lower cost [70]. They also give researchers more flexibility in experimentation and process optimization than commercial systems.

In the case of industrial implementation, the cost-effectiveness of the ALD process in terms of deposition rate is a major challenge, for which different approaches are being explored. One interesting strategy to tackle this challenge is using spatial ALD (SALD) [71]. In a spatial ALD process, the substrate moves over precursor zones or gaseous volumes, thus building up layers, whereas in the normal ALD process, the substrate is static, and the precursor is pulsed and purged from the reactor volume. Thus, in spatial ALD, avoiding the pulse and purge step makes the process faster, resulting in high throughput at a lower cost.

2.3 Current ALD based applications

Microelectronics industry has been the most important user of the ALD , obviously because of the scaling down requirements of new devices, there has been a lot of research and discussion on the use of ALD in these fields in academia, but very little or negligible information is revealed by the companies on the actual implementation due to strategic reasons [2].

ALD plays a critical role in microelectronics industry due to increasingly more complex designs requirements for 3D capacitor structures along with high accuracy in deposition thickness, uniformity, conformality on 3D surfaces. One of the most widely studied and implemented application is deposition of high k dielectrics for dynamic random access memory (DRAM) capacitor (*Figure 12*)and metal oxide field effect transistor (MOSFET). From the insutrial implementaion point of view, Samsung has developed 10 nm DRAM with 8 billion cells for an 8 gb chip [72]. The other possible use of ALD in microelectronics industry is for interconnects with the deposition of ALD tungsten (W), ruthenium (Ru) and copper (Cu) [73].

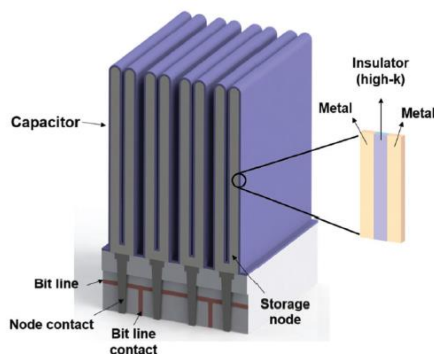

Figure 12: Simplified schematic diagram of a DRAM capacitor with ALD deposited dielectric [49].

Magnetic heads used to read and write in hard disks found the use of ALD Al_2O_3 in commercial applications, the insulting gap layers deposited using ALD were found to be very effective for downscaled 3D structures [2].

Apart from electronics, ALD has found use as protective coating or barrier coating [74]. In the OLED technology, the utilization of ALD coatings as protective layers assumes critical importance. OLED devices are particularly vulnerable to environmental factors, namely moisture and oxygen, which has shown to deteriorate device performance and reduce its operational lifespan. Among the key technologies influencing the lifetime and reliability of OLEDs, encapsulation plays an important role. Thin film encapsulation (TFE) has emerged as one of the most critical approaches for protection against the penetration of moisture and oxygen.

Metal oxide thin films, including aluminum oxide (Al_2O3), zirconium oxide (ZrO_2), and titanium oxide (TiO_2), grown via ALD, have emerged as preferred choices for TFE materials. These ALD

coatings function as effective barriers, shielding OLED devices from the adverse effects of environmental factors (*Figure 13*). Beyond their moisture and oxygen resistance, ALD coatings also find utility in enhancing the optical and electrical characteristics of OLED devices. Furthermore, they offer a long-term encapsulation solution, shielding the devices for extended protection and improved performance [17].

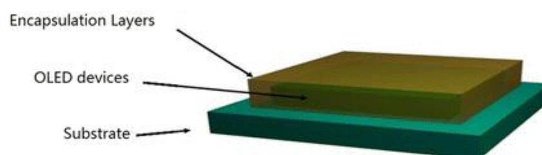

Figure 13: Structure of OLED encapsulation [17]

Within the domain of solar photovoltaics, ALD has emerged as a prominent technology with widespread applications, particularly in silicon solar cells [75] . ALD's role is most notably seen in the deposition of metal oxide layers, serving as both passivation layers and passivating contacts for crystalline silicon (c-Si) solar cells [76]. These thin ALD films play a vital role in reducing surface recombination and electronic losses, thereby resulting in substantial enhancements in solar cell efficiency. Moreover, ALD can also used to deposit reflective coatings of the solar cells. These coatings are useful in mitigating sunlight reflection, thereby ensuring that a larger fraction of incident light is absorbed by the solar cell, which results in improved efficiency.

Other applications were ALD is still being explored and a great potential is seen is in energy storage and conversion applications [77], such as for the design of efficient catalyst for fuel cell, this would help in design high surface area catalyst and also address the problem of material loading as seen in the case of Pt [78](*Figure 14*).

ALD has also found use in lithium based Batteries , for enhancing the conductivity of cathode materials, the adoption of Carbon/Sulfur (C/S) composite electrodes has emerged as a conventional choice for use in Lithium-Sulfur (Li-S) systems. These composite electrodes are designed to encapsulate sulfur within a porous carbon structure, effectively reducing the diffusion of polysulfides and concurrently improving electronic conductivity. However, this approach alone does not comprehensively address the underlying challenges. To tackle the issue of polysulfide dissolution, incorporation of metal oxide (Al_2O3 and TiO_2) and porous oxide nanoparticles is found to be useful strategy, which function as adsorption and

absorption agents. In this context, ALD emerges as a valuable technique for engineering cathodes with these protective layers [79].

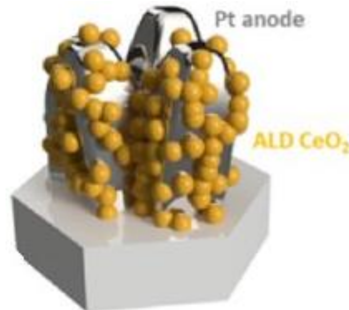

Figure 14: ALD coated Pt anode on Solid oxide fuel cell (SOFC) for energy starge and conversion application [80]

Desalination [81] is another interesting application where problems faced in membrane design such as slow water transportation and a high energy cost can addressed with the used of ALD (*Figure 15*), the strategy adapted to tackle this challenge is design of biomimetic membranes which uses flexible supports along with corrosion protection and mechanical stability [22]. The potential and possibilities of using is ALD is enormous as it offers high quality thin films, thus there is no doubt there will more commercial application which will rely on unique abilities which ALD has to offer.

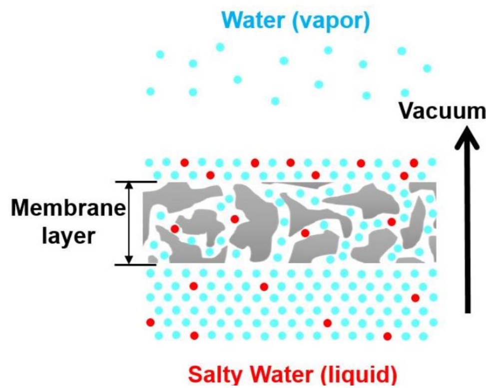

Figure 15: ZnO Microfiltration Membranes for desalination by ALD [82].

2.4 ALD perovskite for novel applications

This section is based on Research article 1 [34] and 2 [39]. This work was conducted in the initial stage of the Ph.D. work to gain a deeper insight into the ALD perovskites process and different challenges, and also to have an overview of different perovskite based applications that are possible using the ALD process. The complete details of this chapter can be found in the research articles included in the appendix.

2.4.1 Growth process

This section provides an overview of the atomic layer deposition (ALD) process for depositing perovskite thin films, using strontium titanate (STO) as a model system [30]. Of particular interest is the use of cyclo-pentadienyl (Cp)-based precursors due to their high reactivity and low carbon contamination [83]. Similar to the conventional ALD process, the deposition of STO thin films involves four surface reactions in a super-cycle [84,85]. Firstly, the surface is hydroxylated with H_2O pulses, followed by a reactor purge. Next, the Sr precursor reacts with the hydroxylated surface, protonating one of the ligands with H while the other ligand leaves the reaction chamber in the vapor phase carried by an inert process gas. In the second step, the remaining Cp ligands are protonated and removed by pulsing with H_2O, forming an -OH terminated surface of Sr in preparation for the following binary layer deposition. The deposition of titanium oxide (TiO_2) binary layers follows a similar reaction mechanism [86], but the energetics of growth differ from those of binary compounds alone [30] due to the ternary compound's unique behavior [34].

2.4.2 ALD perovskite applications

2.4.2.1 High K dielectrics for DRAM capacitors

ALD is widely used in the micro and nanoelectronics industry because of its ability to deposit conformal and uniform layers, especially for high-k dielectric materials used in DRAM capacitors. The benchmark for evaluating dielectric materials for DRAM applications is the EOT, which is determined by the dielectric constants and thickness of the material. High-k dielectric materials with ultra-low thickness and high uniformity can achieve the EOT target of 0.3 nm [35]. However, depositing ultra-thin layers using ALD can result in high leakage currents due to post-deposition annealing-induced cracks [87]. Additionally, decreasing the thickness can increase the leakage current and lead to direct electron tunneling, which affects

device performance. To achieve high-performance dynamic random access memory (DRAM), it is crucial to have an optimized thickness with a high dielectric constant. Several materials have been studied as high-k dielectrics , and among them, strontium titanate (STO) and barium strontium titanate (BST) exhibit high dielectric constants [36–38]. These thin films are ideal candidates for future DRAM applications due to their high dielectric constants, as shown in (*Figure 16*). However, interfacial dead layer effects can cause a reduction in the dielectric constant when the thickness of the film is reduced below 50 nm. Table 1 provides a overview of the dielectric properties of perovskite thin films and the factors that affect their properties [34].

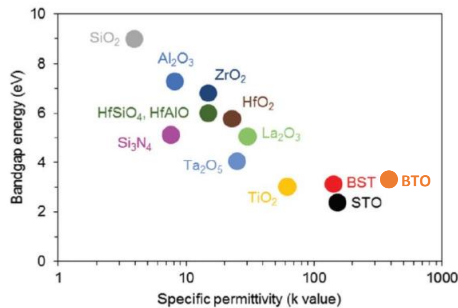

Figure 16: Bandgap energy and specific permittivity of various dielectric films [88] .

Table 1: Dielectric constant of perovskite-based thin films synthesized by ALD [39]

Material	Thickness (nm)	K	EOT	Remarks	Year	Ref.
$BaTiO_3$	32	73	1.8	permitivity increase with postdeposition annealing at 600˚C	2007	[89]
$SrTiO_3$	10	146	0.57	Change in K with composition Ti/(Ti+Sr)= 32% - 61%	2011	[90]
$SrHfO_3$	4.6	17	1	Growth on Ge substrate with postdeposition annealing	2014	[91]
BaTiO3	5	122	0.38	Postdeposition plasma treatment improves the EOT	2014	[92]
$BaTiO_3$	20	35	2.2	Low temp. deposition (180˚C) with pyrrole-based precursor.	2015	[93]
$SrZrO_3$	11.5	31	0.8	Epitaxial growth on pre-treated Ge Substrate	2018	[94]

2.4.2.2 Piezoelectric

Thin films based on piezoelectric materials have become increasingly important for micromechanical systems (MEMS) [39]. These films work on the principle of converting

applied strain energy to an electric signal and vice versa. While lead zirconate titanate (PZT) has exceptional piezoelectric properties, its hazardous nature has led to interest in finding new piezoelectric materials to replace it [41]. However, PZT remains the preferred material for microactuators, microphones, and energy harvesting devices. With the growing interest in nanoelectromechanical systems (NEMS) and MEMS technologies, atomic layer deposition (ALD) can play a vital role in depositing ultra-thin films. ALD-deposited barium-based perovskites with ideal piezoelectric properties and a proven deposition process of barium oxide and barium titanate are promising candidates. Barium-based perovskites have a piezoelectric coefficient comparable to PZT. For example, 100 nm thick PZT perovskite films have been used as a piezoelectric material for low voltage actuators using sputtering and sol-gel deposition methods, while sputter-deposited aluminum nitride (AlN) films of a similar thickness have been used for logical nano-switching [95].

2.4.2.3 Optoelectronics

Perovskite-based solar cells are an important application of perovskite-based compounds [42] . These solar cells have achieved efficiencies of over 20%, making them competitive with Si-based PV technology in terms of efficiency [96] . Methyl-ammonium lead bromide/iodide ($CH_3NH_3PbI_3$), a lead organo-halide perovskite, has excellent optoelectronic properties, including an optical band gap of 1.55 eV in the near-infrared region and high absorption per unit length of 104 cm-1 just above the band gap [43] . These properties have also been used in other applications, such as light-emitting diodes and lasers [97].

ALD is a promising technique for developing organometallic perovskites due to its advantages over solution-based processes, including the ability to work at lower temperatures, provide conformal growth on larger areas, and not require a very low vacuum, making it suitable for industrial implementation [39]. Recently, a hybrid deposition method has been adopted that combines ALD deposition of PbS with sublimation of iodine chips in a sealed environment and dipping in CH_3NH_3I and IPA [145]. This approach has been used to fabricate light-emitting diodes based on direct bandgap semiconductors, with ALD providing the feasibility of working at lower temperatures with controlled conformal growth. The perovskite layer thickness in this structure is 15 nm, which is ideal for ALD deposition.

2.4.2.4 Solar to energy conversion (thermo-chemical process)

The field of renewable energy is constantly evolving, with new technologies and devices being explored for higher efficiency and environmental sustainability. One promising technology in this regard is "solar to fuel," which converts H_2O and CO_2 into H_2 and CO gas using perovskite materials through thermochemical reaction cycles [39]. This process involves concentrated light providing the heat for the endothermic reaction at the perovskite surface, followed by an exothermic reaction with H_2O and CO_2 that produces H_2 and CO, as shown in *Figure 17* (a).

Ceria is currently the preferred material for this application due to its high efficiency and thermal and chemical stability. However, the higher working temperature required for ceria is a concern, as it creates excess thermal load on the system. Therefore, researchers are exploring perovskites as an alternate family of materials. Perovskites have an energetically stable electronic system, which allows for fine-tuning of stoichiometry and electrochemical properties, and a wide range of stoichiometries can be achieved to fit the exchange reactions occurring at the surface [98].

Most perovskites studied for this application are complex quaternary oxides based on elements such as La, Sr, Mn, Cr, Fe, Co, and Al [98]. With the development of new atomic layer deposition (ALD) precursors and a wider range of materials, it is now possible to grow complex compounds with reasonable control over composition and stoichiometry. Lanthanum-based perovskites deposited using ALD have been extensively studied for different applications [99]. Recently, ALD-deposited Pd-doped lanthanum ferrite ($LaFeO_3$) was studied as a smart catalyst that undergoes efficient redox cycling. ALD was instrumental in depositing highly conformal layers on high surface area supports [100], such as porous structures, opening new avenues for research and development in the field of thermo-chemical splitting of CO_2 [39,45].

However, perovskites still face challenges, including chemical stability and low enthalpies, which must be addressed [101]. Lower enthalpies are favorable for the reduction reaction but result in lower hydrogen yield or fuel formation during oxidation. Despite these challenges, perovskites show great promise as a sustainable and efficient material for "solar to fuel" technology. Further research and development can help overcome the remaining obstacles and bring this technology closer to commercialization [102,103].

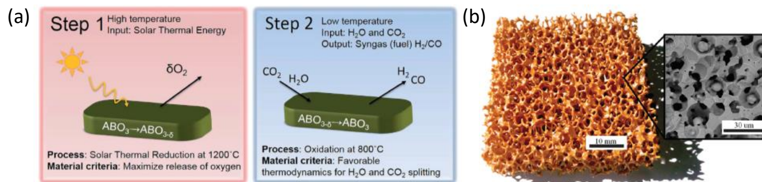

Figure 17:(a) Schematic of the 2-step thermochemical solar-to-fuel conversion process [99]*. (b) Ceria sample with dual-scale porosity* [100]*.*

2.4.3 Challenges in ALD of perovskites

2.4.3.1 Differential growth at the interface

The growth rate of ternary compounds cannot be simply calculated by combining the growth rate of binary compounds. This is because the surface reactivity between precursor ligands and interfacial functional groups can be higher than expected, resulting in a faster growth rate [104] . To understand how interfaces affect growth, the nucleation/wetting aspect of binaries on different substrates needs to be understood. This is particularly important for ternaries, as each binary deposited becomes the substrate for the next binary. summarizes the results of different studies on the growth of SrO on different surfaces. In a typical ALD growth process of STO, sub-cycles of TiO_2 and SrO are deposited. The growth of SrO on SrO and SrO on TiO_2 surfaces differ; for example, Rahtu et al. found that SrO grows faster on TiO_2 than on itself due to higher adsorption of the Sr precursor [84] . The growth of SrO in the first few cycles is also enhanced on the hydroxylated SiO_2 surface, which has a higher reactivity and OH density than SrO [85]. Also, the growth process of ternary compounds is complex due to multiple interdependencies, and several other parameters affecting the process [34].

The growth of ternary compounds is a complex process that cannot be easily calculated by combining the growth rates of binary compounds. This is because the surface reactivity between precursor ligands and interfacial functional groups can be higher than expected, resulting in a faster growth rate. To understand how interfaces affect growth, it is important to comprehend the nucleation/wetting aspect of binaries on different substrates, especially for ternaries, as each binary deposited becomes the substrate for the next binary. summarizes the results of various studies on the growth of SrO on different surfaces. The growth process of ternary compounds is complex, with multiple interdependencies and several other parameters affecting the process.

Table 2: Effect of interface condition on the ALD growth [34]

Material	Binary A/B	Reactant / Co reactant A	Reactant B / Co reactant B	Temp. (˚C)	Year	Ref.	Growth Remark
STO	SrO/ TiO_2	$Sr(iPr_3Cp)_2$ /H20	$Ti[OCH(CH_3)_2]_4$ / D_2O	325 ˚C	2001	[84]	Higher SrO growth on TiO_2 surface
STO	SrO/ TiO_2	$Sr(tBu_3Cp)_2$ /H20	$Ti(OMe)_4$ /H_2O	250˚C	2009	[83]	Higher Ti incorporation due to increased Strontium pulse
STO	SrO/ TiO_2	$Sr(iPr_3Cp)_2$ /H20	Ti (O-iPr)$_2$(tmhd)$_2$ / O_3	370 ˚C	2011	[90]	Higher SrO growth on TiO_2 surface

2.4.3.2 Effect of process parameters on growth

To start with, precursor selection is crucial for perovskite thin film development, with Sr and Ba-based perovskites commonly deposited using diketonates [105] and Cp-based precursors [85][106]. The bonding energy between the ligand and the metal atom affects the growth process, with Cp-based precursors found to be ideal due to weaker bonding with the metal and lower carbon contamination [107]. The energy required for breaking the bond between the metal and the first ligand in the Sr(iPr3Cp) precursor is 2.58 eV, while diketonate-based precursors require a higher energy at 4.94 eV, making Cp-based precursors more stable [107].

Subsequently, co-reactants used, such as H_2O, O_2 plasma, or ozone, affect growth rates and usable reactor temperatures [8] [27]. The use of plasma sources offers advantages such as lower deposition temperatures, which allows deposition on fragile substrates or those with thermal limitations. For instance, plasma is essential for space defined double patterning method in the fabrication of logic devices that require lower working temperatures due to the use of temperature-sensitive photo resist. HfO_2 dielectric films with higher interface quality and density, along with lower impurity levels, can be formed using O_2 plasma [108], and low-temperature deposition can also prevent the formation of unwanted oxide layers at the interface [109].

PEALD has certain advantages, such as higher growth rates due to increased surface reactivity, leading to enhanced growth per cycle [110]. However, these advantages are limited to specific applications and processes. PEALD can result in limited conformality on high aspect ratio structures due to surface collisions [59]. Moreover, plasma-induced damage from high-energy ion bombardment can cause defects on the substrate surface and undesirable

oxidation and nitration when using O_2 or N_2, NH_3-based plasmas. Despite these limitations, the advantages of plasma processing for STO and BTO perovskites often outweigh its drawbacks since growth and crystal structure are affected. Perovskite crystallinity is critical for obtaining the desired structural properties, as many of the material functionalities depend on their crystalline structure [34].

Also during ALD process, incomplete removal of precursor ligands can lead to carbon and hydroxide contamination, which reduces thin film performance. Thus, it's essential to optimize process parameters to achieve optimum ligand interaction during the cyclic process [89] . *Figure 18* summarizes the various deposition process variations and post-deposition treatments that need to be optimized for obtaining perovskites with desired properties [34].

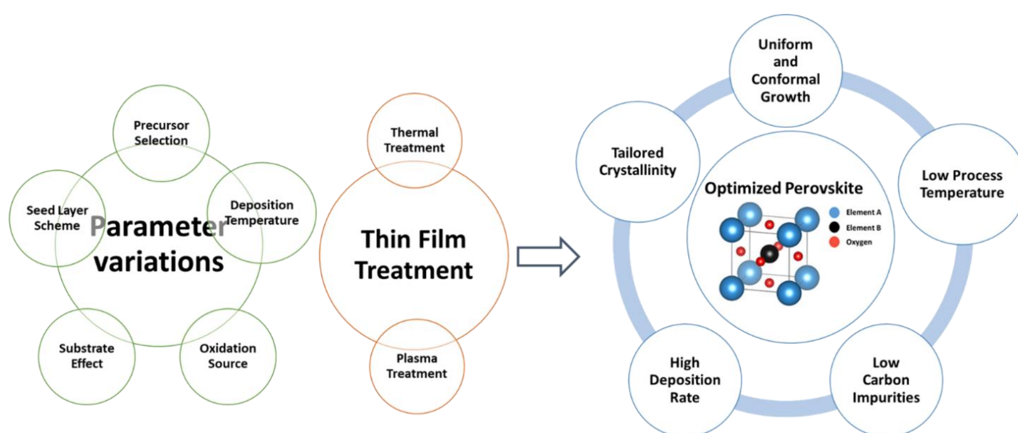

Figure 18: Effect of different process parameters on perovskites properties [34].

2.4.4 Summary

In conclusion, this study investigated the growth mechanism and interfacial effects of ALD deposited perovskites, and explored their potential applications. We found that the use of ALD for synthesizing perovskites offers several advantages over other deposition processes, including high conformality, uniformity, and control over the growth and stoichiometry of the films. The research also reviewed a range of perovskite-based applications to highlight the capability of ALD. In summary, this lireature study provides an understanding of the growth of ALD perovskites and highlights their potential for various applications in the ultrathin films

regime [34]. In addition to this , this work stresses the need for *in situ* studies to have better understanding of new and complex processes.

2.5 Why *in situ* studies are required

2.5.1 Introduction

In situ ALD studies provide a direct observation of the surface chemistry and reaction mechanisms involved in the ALD process. By monitoring the surface and gas-phase species during deposition, we can gain valuable insights into the nucleation and growth of thin films, the role of surface chemistry and defects, and the effects of process parameters on film properties [50]. This allows us to understand the role of surface chemistry and defects on film growth and properties.

Surface-sensitive technique such as reflection high-Energy electron diffraction (RHEED) has been used for the study of ALD growth [111]. This technique has been utilized for *in situ* analysis of crystal growth in systems such as pulsed laser deposition (PLD) and molecular beam epitaxy (MBE). In RHEED, a beam of high-energy electrons, typically in the range of 5–35 keV, is directed towards the sample surface at grazing incident angles, often at approximately 1°–3° with respect to the wafer's surface. The short wavelength of these high-energy electrons (approximately 0.070 Å) is significantly smaller than the spacing between scattering centers, which are typically atoms on or near the surface of the material. By analyzing the diffraction spots and intensity oscillations of the reflected beam, valuable information related to the growth mechanism can extracted, such as crystallographic phase, crystal orientation, and lattice constant of the material under study.

Techniques such as X-ray photoelectron spectroscopy (XPS) [112] and Fourier transform infrared spectroscopy (FTIR) [52], can be used to probe the surface chemistry of the substrate and film during deposition. These techniques provide information about the formation of surface oxides, surface functional groups, and surface reactions, which can further help researchers to improve the quality, uniformity, and reproducibility of ALD thin films.

Quadrupole mass spectrometry (QMS) has been widely used for *in situ* ALD studies [113], this method involves the ionization of gases and the subsequent measurement of the mass-to-

charge ratio (m/z) [114], which allows for the identification of the composition of gases or reaction products.

Moreover, this information can be used to design new precursors, tailor reaction conditions, and improve process control. *In situ* studies can also provide insights into the nucleation and growth of thin films, as well as the evolution of surface morphology and crystal structure during the deposition process [48].

One of the significant advantages of *in situ* ALD studies is that they can provide real-time measurements of the film thickness such as, refractive index using techniques such as quartz crystal microbalance (QCM) [114] and spectroscopic ellipsometry [115]. These measurements can help to optimize process parameters such as precursor pulse times and purge times, which can affect the film growth rate and quality. Thus helping us to achieve the desired material properties, such as high uniformity, high purity, and improved electrical and mechanical properties.

Overall, *in situ* ALD studies are a powerful tool for understanding and optimizing the ALD process. They enable us to gain insights into the fundamental surface chemistry and reaction mechanisms involved, and provide a means to develop new materials and applications. Besides fundamental research, *in situ* ALD studies are also useful for industrial applications such as the fabrication of electronic devices, solar cells, batteries, and catalytic systems. *In situ* ALD studies can help optimize the deposition process, reduce defects, and improve the yield and performance of these devices.

However, while *in situ* growth studies have advantages there certain challenges. Firstly, these techniques may require specialized equipment and sample preparation, which can limit the size and type of samples that can be studied. Secondly, there are limited characterization techniques compared to *ex situ* techniques, which can limit the types of measurements that can be made. Finally, *in situ* techniques can be more expensive and time-consuming for the initial experiments compared to *ex situ* techniques, due to specialized system designs.

2.5.2 Motivation for *in situ* studies

2.5.2.1 New precursors

In recent years, there has been continuous development and experimentation with new precursors containing various organometallic compounds for ALD [116]. However, despite these efforts, there is still a lack of clear understanding of the reaction mechanisms occurring during the ALD process for many of these precursors. Conducting in situ studies can help achieve optimized ALD growth by providing continuous chemical information during the process. This will enable us to gain a better understanding of the complex interactions and mechanisms involved in the deposition process, leading to more efficient and effective use of new precursors and improved thin film properties.

2.5.2.2 Miniaturization

The initial nucleation phase of ALD can differ significantly from the later stages, where self-limiting chemical vapor exposure governs the growth process. This early stage can vary significantly across different material systems, and the chemical and physical mechanisms behind the nucleation phenomena are still not fully understood. Current and future thin films will be determined by the nucleation phase [117]. Hence, whether the topography following the initial cycles may or may not be beneficial, miniaturization will rely on understanding this phase[118]. Topological and morphological studies at atomic scale resolutions are missing signifying our insufficient knowledge of ALD processes in key emerging applications. Thus, with the implementation of *in situ* studies at lowest possible scale, significant understanding and knowledge can be achieved, thus helping us reach the goal of miniaturization for different applications.

2.5.2.3 Complex ALD process and process property relationship

For example, perovskite materials deposited through ALD are multi-component materials that require the combination of binary cycles, referred to as a super cycle, to deposit them [43]. The deposition of functional thin films using ALD requires a comprehensive understanding of the growth mechanism and precursor interactions to achieve precise control over film composition and tunable functionalities. This understanding can be gained through a range of *in situ* studies that provide insight into the evolution of the thin film structure and properties during the deposition process. By adjusting various deposition

parameters, different thin films properties can be controlled and the functionality be tailored to specific applications, such as the composition of the materials, the concentration of point defects, lattice strain, and crystal structure. This process-property relationship would allow for the exploration of new, high-performance materials with novel applications, making ALD a powerful tool for advancing materials science research.

2.6 *In situ* ALD characterization methods

There are several methods for characterizing materials *in situ* during ALD [50], but the most commonly used techniques are spectroscopic ellipsometry, gas phase and surface infrared spectroscopy, quartz crystal microbalance (QCM), quadrupole mass spectrometry (QMS), and optical emission spectroscopy. Classifying these methods based on their adequacy, feasibility, complexity, and cost provides a good overview of the possibilities and perspectives for choosing the appropriate technique for specific materials study [119] .

Each technique has its own advantages and limitations, so it is essential to understand what information is needed to improve a particular ALD thin film. In this section, we briefly summarize the each method.

2.6.1 *In situ* spectroscopic ellipsometry

We begin the discussion with spectroscopic ellipsometry (SE) [115] , which measures the change in polarization of light reflected from the growth surface (*Figure 19*). SE offers several advantages, including rapid measurement of film thickness, providing valuable insights into the optical and electrical properties of materials. To summarise, it allows for the calculation of growth rate per cycle by monitoring thickness increase, it is possible to investigate the nucleation behavior on diverse substrates by capturing data after each ALD cycle during initial growth, and is capabale of probing of submonolayer-level changes following precursor and reactant steps by collecting data after each ALD half-cycle.

Ellipsometry data is typically represented through the amplitude ratio (ψ) and phase angle (Δ) as shown in eq. 4, which are linked to the complex Fresnel reflection coefficients (R_p and R_s) for p- and s-polarized light. This relationship is expressed as,

$$\rho = R_p/R_s = \tan(\psi)e^{i\Delta} \qquad (4)$$

The polarization change is determined across a range of wavelengths within a specific photon energy spectrum. From the gathered ellipsometric data, it is possible to deduce both the thickness of the film and the dispersion relation of optical constants across this photon energy spectrum. These optical constants are expressed as the refractive index (n) and extinction coefficient (k), and are represented in terms of the real (ε_1) and imaginary (ε_2) components of the complex dielectric function ε.

The relationship between these components is defined as eq. 5,

$$\varepsilon_1 = n^2 - k^2 \text{ and } \varepsilon_2 = 2nk \text{ [115]} \qquad (5)$$

Leveraging these optical constants, various material properties of thin films can be derived, including the determination of the optical band gap for dielectric materials.

The sensitivity of SE is capable to detect changes in the thickness of surface layers equivalent to 0.01 monolayer [120]. However, the method can be complex due to optical modeling, and expensive ellipsometry equipment and the requirement of optical ports on the ALD reactor.

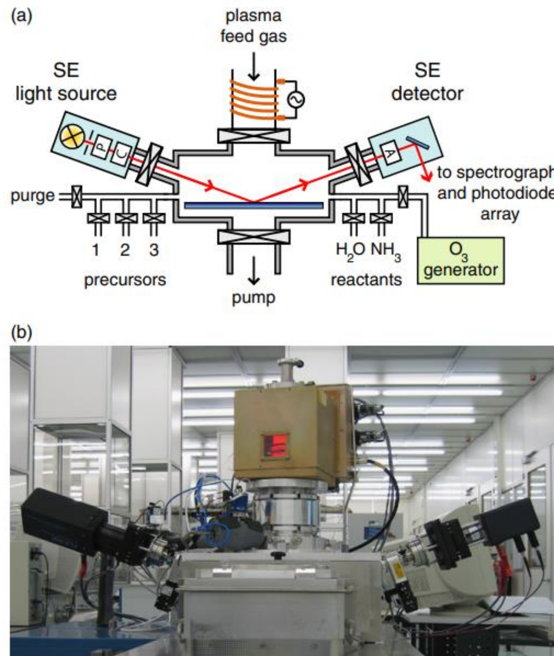

Figure 19: . (a) Schematic representation of a single-wafer ALD reactor integrated with rotating compensator ellipsomete. (b) Photograph of a JAWoollam Co., Inc., M2000 spectroscopic ellipsometer fitted on an Oxford Instruments FlexAL™ ALD reactor [115] .

2.6.2 *In situ* Infrared spectroscopy

Now, let's discuss another technique that relies on the absorption of infrared light. Infrared spectroscopy plays a crucial role in *in situ* FTIR ALD studies. This approach utilizes an FTIR spectrometer to examine the molecular species present on the substrate and within the reactor volume before and after each exposure to precursor molecules.This enables the identification of both the desired material formation and any undesired by-products. The absorbance value is calculated using the formula eq.6 ,

$$absorbance = -\log10(I_{sample}/I_{reference}) \qquad (6)$$

where I_{sample} represents the intensity of transmitted infrared (IR) radiation through the sample, and $I_{reference}$ represents the IR intensity without the sample (Figure 20). Typically, spectroscopy data is collected within the range of 400 to 4000 cm^{-1} at a resolution of 4 cm^{-1}, averaging 200 scans across all measured spectra.

This technique proves especially valuable in detecting surface organometallic species during the first reactant half-cycle and elucidating the ligand exchange reaction in subsequent cycles. It can be employed in two ways: by detecting molecules in the gas phase or by studying their interaction on the surface. While the gas-phase approach provides accurate calibration, its sensitivity can vary for different species, making it challenging to detect certain substances. Additionally, gas-phase measurements capture all species present, not just those on the substrate. In contrast, surface infrared spectroscopy detects surface groups formed or removed during the ALD process [52], offering a deeper understanding of the reaction mechanism. Also, in surface infrared spectroscopy, the utilization of high-surface-area nanoparticles has shown to enhance the signal intensity in *in situ* ALD studies [121]. Zirconium dioxide (ZrO_2) nanopowder substrates [122], with high surface area, contribute significantly to this improvement. By expanding the available surface area for the loading of precursor molecules, ZrO_2 substrates ensure that even the smallest quantities of these molecules can generate a satisfactory signal intensity, ultimately enhancing the sensitivity and reliability of surface infrared spectroscopy.

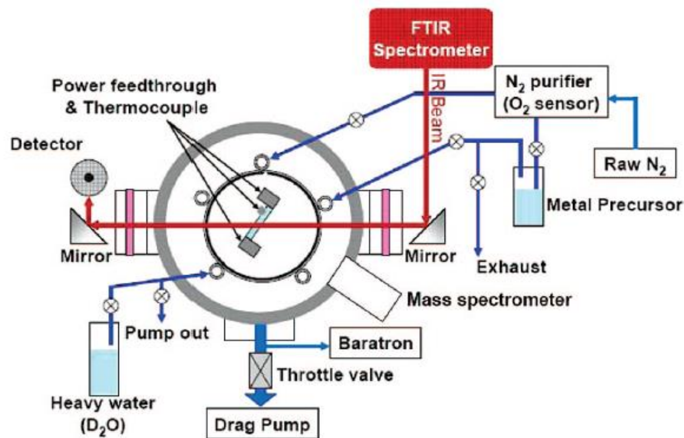

Figure 20: Schematic of the ALD reactor connected to an IR spectrophotometer for ins situ ALD studies with sample positioned in transmission mode [123].

2.6.3 Quartz crystal microbalance

The quartz crystal microbalance (QCM) is a widely employed and cost-effective technique for quantifying mass variations. While this method offers simplicity and quantitative measurement of mass gain and loss, it does exhibit sensitivity to fluctuations in ALD process parameters, such as gas flows and system temperature. The QCM, serving as a highly sensitive mass sensor, operates by applying alternating current to a quartz crystal, inducing oscillations linked to the crystal's thickness. As mass is deposited or removed from the crystal's surface, it causes noticeable oscillation frequency changes. These frequency shifts can be accurately quantified using the Sauerbrey equation, establishing a connection between frequency alterations and mass variations. Notably, the QCM's high sensitivity enables the detection of mass changes at submonolayer resolutions, rendering it invaluable in growth studies for precise mass measurements and monitoring.

QCMs find routine application in traditional vacuum deposition processes where in situ thickness measurements hold significance, such as in thermal evaporation. In ALD studies, QCM measurements have emerged as a useful in situ method for assessing growth rates, and optimizing processing conditions. Nevertheless, obtaining accurate mass measurements during ALD presents challenges, primarily because QCM measurements are typically conducted at room temperature. To address these limitations, a novel wall-mounted integral QCM has been developed and tested under various ALD conditions [124] (*Figure 21*). In this

work, an Inficon SQM160 multi-film rate/thickness monitor was utilized to track the QCM's frequency, providing a frequency resolution of 0.03 Hz at 10 readings per second. This resolution corresponds to a mass resolution of approximately 0.375 ng/cm^2.

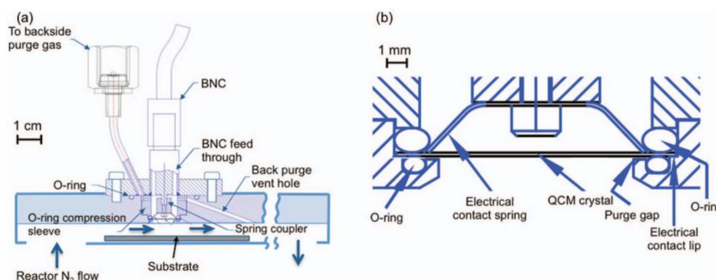

Figure 21: Schematic of ingrated QCM fixture [124].

2.6.4 Quadrupole mass spectrometry

Quadrupole mass spectrometry (QMS) is a widely adopted method that involves the ionization of gases and the subsequent measurement of the mass-to-charge ratio (m/z) [114]. This allows for the identification of the composition of gases or reaction products. While this technique is relatively straightforward and cost-effective, it can be challenging to distinguish between products originating from the substrate and those originating from the reactor walls. In in situ QMS studies [121], the analysis are conducted by incorporating a 200 atomic mass unit (amu) quadrupole mass spectrometer which are equipped with a pressure reduction system (Eg. PPR200, SRS Inc., Sunnyvale, CA) into the reactor setup. During the exposure to reactants, the QMS performs the scans across the mass range from 1 to 75 m/z with a resolution of 0.1 m/z. A Faraday cup is employed as the detector, without the use of an electron multiplier. With these settings, approximately 5 seconds are required to complete a scan across the entire mass range. *Figure 22* shows a schematic diagram illustrating the integration of QMS with an ALD system.

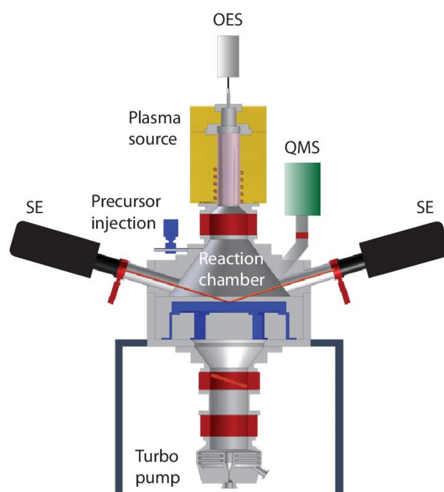

Figure 22: The in situ QMS depicted in an schematic of Oxford Instruments FlexALD reactor [125].

2.6.5 Optical emission spectroscopy

Optical emission spectroscopy is useful during plasma exposure for plasma-enhanced ALD (PEALD) studies [126]. Because in plasma-assisted ALD one of the two main steps is the exposure of the surface to a plasma for surface ligand exchange, the unique possibility exist to study the light emitted by the plasma (*Figure 23*). This plasma emission contains information about the species present in the plasma and with the method of optical emission spectroscopy (OES) reactant species delivered to the surface by the plasma can be identified.

This method measures the radiation emitted by excited species as they decay to lower energy levels, enabling identification of the excited species present in the plasma. In ionizing plasmas, the excitation of species primarily occurs through electron impact. This excitation process involves the transition of a species from one energy level (q) to another (p), followed by possible decay to a lower energy level (k) through spontaneous emission. Consequently, the wavelength (λ) of an emission line corresponds to the energy difference (Ep - Ek) between these levels, as described by eq. 7,

$$\lambda = hc / (E_p - E_k) \qquad (7)$$

where h and c represent Planck's constant and the speed of light, respectively. The emission intensity (I_{pk}) in terms of the number of photons per unit volume per second is determined

by the product of the transition probability (Einstein coefficient, A_k) for spontaneous emission and the population density (n_p) of the excited level as eq.8,

$$I_{pk} = n_p A_{pk} \qquad (8)$$

This relationship underscores that emission intensity is proportional to the density of electronically excited species, assuming self-absorption can be neglected in OES measurements.

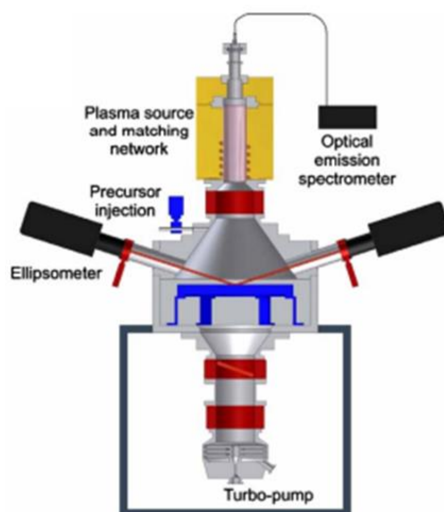

Figure 23: Schematic representation of the Oxford Instruments FlexAL reactor integrated with OES component [126].

2.7 *In situ* ALD synchrotron techniques

The utilization of a synchrotron radiation source for *in situ* studies offers substantial advantages when compared to the use of conventional commercial x-ray tube sources. The most important advantage is the elevated photon flux attainable from a synchrotron source in contrast to commercial x-ray tubes. This heightened photon flux not only amplifies the signal-to-noise ratio but also reduces measurement time. Furthermore, synchrotron sources permit the use of higher energy x-ray radiation, a distinct advantage when compared to the typical 8.04 keV Cu Kα emission characteristic of commercial x-ray tubes. This extended energy range expands the experimental capabilities. A practical consideration that underlines the adoption of synchrotron radiation pertains to spatial constraints. Compact commercial x-

ray instruments may lack the necessary physical space and flexibility to seamlessly integrate to ALD system within the instrument itself. In contrast, synchrotron beam line end stations are traditionally designed on a larger scale, affording the requisite room and adaptability to house an ALD setup effectively [127] .

The Table 3 shows different synchrotron based technqiues which has been used for ALD studies.

Table 3: Synchrotron based in situ characterization methods used for ALD research [127].

Technique	Accessible information
XRR	Thickness
	Roughness
	Electron density
GISAXS	Morphology
	Roughness
XRD	Phase and size of crystalline grains
EXAFS (*in vacuo*)	Local atomic environment
XPS (*in vacuo*)	Chemical state

2.7.1 X-ray absorption spectroscopy (XAS)

XAS involves measurement of X-ray absorption by a material while varying the X-ray energy, which offers valuable insights into the material's structural and electronic properties. In the context of *in situ* studies during ALD, when investigating thin films, the conventional method of absorption measurement reveals minimal alterations in transmission due to the limited amount of absorbing material within the film, leading to a suboptimal signal-to-noise ratio. Conversely, fluorescence signals remain detectable even when the quantity of material is quite limited. For XAS studies during ALD, the sample of interest can be prepared as as a thin film, powder, or liquid. It must exhibit stability under the X-ray beam and compatibility with the experimental setup [48].

In the course of the measurement, an incident X-ray beam is directed towards the sample, leading to two processes. Firstly, photoelectric absorption occurs, whereby X-rays are absorbed by atoms in the sample, resulting in the ejection of inner-shell electrons. The probability of this absorption depends on the energy of the incident X-rays and the atomic

properties of the absorbing element. Secondly, Scattering processes can take place, encompassing elastic or inelastic interactions between X-rays and the sample's electrons or nuclei without absorption. However, XAS primarily centers on the absorption process. Detecting equipment is employed to capture the transmitted or fluorescent X-rays emanating from this absorption process. During the analysis, the energy of the X-ray beam is systematically scanned across a defined range, effectively encompassing the X-ray absorption edge specific to the element of interest. The resultant absorption spectrum is then recorded as a function of X-ray energy as illustrated in *Figure 24*.

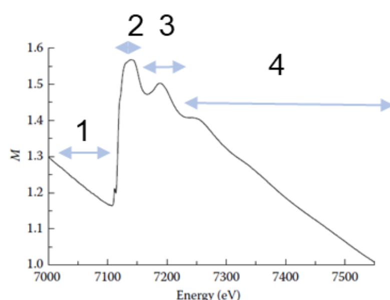

Figure 24: Example X-ray absorption spectrum iron– sulfur–lithium [128] *with different regions numbered as 1: background region, 2: Edge,3: XANES and,4: EXAFS.*

The XANES region constitutes the low-energy range situated just above the absorption edge (*Figure 24*). Within this range lies crucial information concerning the electronic structure and chemical state of the absorbing element. It gives insights into oxidation state, coordination environment, and bonding characteristics. The EXAFS region encompasses the high-energy range that follows the XANES region. This region is instrumental in providing details about the local atomic structure surrounding the absorbing element. Within the EXAFS spectrum, oscillations are due to the constructive and destructive interference of X-rays scattered by neighboring atoms. Analyzing these oscillations allows for the determination of parameters such as atomic distances, coordination numbers, and the degree of disorder in the atomic arrangement.

The relationship between absorption and the intensity of secondary X-rays in XAS is directly proportional and is given by eq. 9. Essentially, as the sample's X-ray absorption increases, the intensity of the resulting fluorescent X-rays also increases. This higher level of X-ray

absorption leads to greater electron excitation and, subsequently, elevated emission of fluorescent X-rays, resulting in a stronger fluorescent signal.

$$k=\frac{\sqrt{2m_e(E-E_0)}}{\hbar} \qquad (9)$$

here 'K' represents the wavenumber of the photoelectron, 'E' is the energy of the incident X-ray, and 'E_0' represents the energy required to remove the electron.

The probability of absorption (χ) is related to the cosine function as eq.10,

$$\chi \propto \cos(2kD) \qquad (10)$$

where 'χ' represents the probability of absorption, and 'D' is the distance between the atoms.

The absorption spectrum obtained is analysed using theoretical models and advanced data processing techniques. By conducting theoretical calculations and making comparisons with reference materials, the X-ray Absorption Spectroscopy (XAS) data can be effectively interpreted.

2.7.2 X-ray reflectivity (XRR)

In situ XRR is a highly effective technique employed in ALD studies conducted at synchrotron facilities. XRR revolves around the controlled incidence of X-rays upon a thin film or substrate at a shallow angle relative to the surface. It serves as a valuable tool for exploring various aspects of thin film growth, encompassing the precise determination of film thickness, assessment of surface roughness, and evaluation of film density [129].

By measuring the intensity of reflected X-rays across different incident angles, researchers gain the ability to monitor alterations in film thickness and roughness as ALD cycles progress. Furthermore, the utilization of synchrotron radiation enhances the intensity of both incident and reflected X-rays, broadening the range of accessible incident angles by a few degrees when compared to conventional laboratory-based systems. The fundamental principle underlying XRR involves the interaction of X-rays with the thin film. These incident X-rays penetrate the film and are subsequently reflected at the interface between the film and the underlying substrate. Simultaneously, X-rays are also reflected at the interface between the film and the surrounding air. These interactions generate an interference pattern, characterized by periodic oscillations within the XRR pattern, analysis of these fringes enables

the precise determination of film thickness [127].In addition to film thickness, XRR facilitates the assessment of surface roughness and the determination of film density. Typically, this involves fitting the experimentally measured XRR curve to a well-defined theoretical model, allowing for the extraction of these key parameters [48].

2.7.3 X-ray diffraction (XRD)

Utilizing XRD is critical in the investigation of crystalline materials. However, the application of *in situ* XRD during ALD is somewhat constrained since most materials deposited through ALD exhibit an amorphous structure during the deposition process. Nonetheless, certain ALD processes, such as the deposition of ZnO, are notable exceptions as they yield crystalline materials during deposition [130]. Furthermore, XRD proves particularly advantageous when exploring metallic materials, making it a valuable tool for ALD studies [127].

In this context, synchrotron-based XRD offers a distinct edge over laboratory-based XRD. The primary advantage comes from its heightened sensitivity and detection capabilities. By harnessing the intense photon flux generated by synchrotron sources, even minute quantities of crystalline material can be detected.

When the crystallites within a film exhibit random orientation, the intensity of the diffraction peaks becomes a valuable metric for assessing the deposited material's quantity. The analysis involving the Scherrer equation applied to peak widths in the XRD pattern enables the determination of grain sizes within the deposited film.

The mean size (τ) of ordered crystalline domains can be calculated using the formula (eq.11):

$$\tau = K \lambda / \beta \cos(\Theta) \qquad (11)$$

In this equation, K represents a dimensionless shape factor, typically close to unity and dependent on the crystallite shape, λ denotes the x-ray wavelength, β signifies the line broadening at half the maximum intensity in radians, and Θ corresponds to the Bragg angle.

Incorporating XRD as an *in situ* technique during ALD enables investigation of phenomena nucleation of metals, the dynamic changes in grain sizes throughout the growth process, the impact of growth parameters on crystallinity, and the influence of the substrate, including epitaxial growth. However, it's crucial to consider that synchrotron X-ray sources remain stationary. Therefore, the ALD chamber needs to possess the adaptability to align itself

accurately with the Bragg condition for the specific diffraction peak of interest (*Figure 25*). This approach of collecting *in situ* data offers a unique advantage as it allows for the continuous monitoring of a single ALD film's growth process, spanning from its initial nucleation phase through to the eventual coalescence of the film [127].

Grazing incidence X-ray diffraction (GIXRD) allows for assessing the orientation and composition of thin films. By employing a grazing angle for the incident x-ray beam, the technique effectively limits its penetration into the substrate. This aspect is particularly essential when examining ultra-thin films, such as those encountered during the initial nucleation stages of ALD growth. The minimized interaction with the substrate reduces background interference [127].

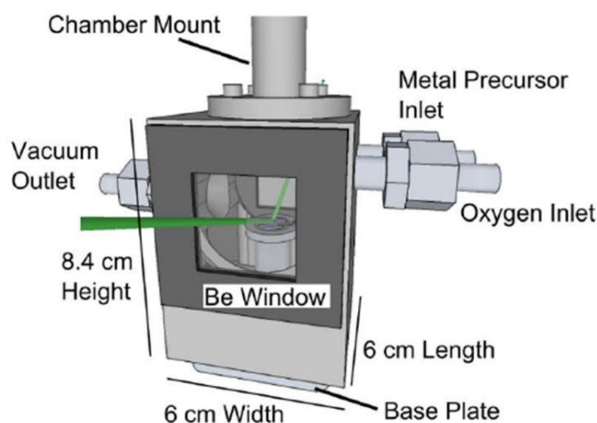

Figure 25: Schematic of the in situ XRD chamber [127].

2.7.4 Grazing incidence small angle X-ray scattering (GISAXS)

GISAXS is found to be useful method for characterizing the morphology of nanoscale entities such as particles and pores. In the context ALD, GISAXS helps in determining the size of islands formed in the early stages of growth before the film's consolidation. A GISAXS experiment primarily involves the measurement of diffuse scattering surrounding the beam that's specularly reflected from the sample. To minimize undesired bulk scattering originating from the substrate and enhance the near-surface scattering, an extremely small angle of incidence is employed, maintaining a close proximity to the sample surface. In this configuration, any form of surface roughness or variation in electron density within the subsurface region results in scattering in non-specular directions. The scattered intensity is typically captured using a

two-dimensional detector, and data is collected as a function of both the out-of-plane and in-plane angles. Thorough analysis of the resulting 2D GISAXS spectra offers insights into the geometry, size distribution, and spatial correlation of the scattering features, contributing significantly to the study of ALD processes [127].

2.7.5 X-ray photoelectron spectroscopy (XPS)

XPS is a powerful technique utilized for investigating the composition and chemical state of elements within a material. Operating based on the principles of the photoelectric effect, XPS involves illuminating the material with x-rays at a fixed energy (E_{photon}). These x-rays interact with electrons within the shells of the atoms being irradiated. When the energy of E_{photon} surpasses the binding energy of the electrons ($E_{binding}$), these electrons are emitted and acquire kinetic energy ($E_{kinetic}$) equal to the energy surplus. Subsequently, these photoelectrons can be collected and subjected to analysis. This process is described by eq.12:

$$E_{binding} = E_{photon} - (E_{kinetic} - \phi) \qquad (12)$$

where ϕ represents the work function of the spectrometer. Each element exhibits a unique set of peaks at specific $E_{binding}$ values, enabling elemental analysis of the sample. Moreover, since $E_{binding}$ is also contingent upon the chemical state of the involved atoms, XPS proves invaluable in determining the local bonding configurations of the atoms.

XPS relies on the collection of electrons, necessitating ultra-high vacuum (UHV) conditions. This requirement poses a substantial challenge when considering the integration of XPS as an *in situ* technique. Incorporation of ALD within an XPS chamber, achieving and maintaining UHV conditions is challenging, and extensive precautions are required to protect the detector against the effects of the ALD process [127]. However, XPS has been used as an *in vacuo* technique [131], signifying that the sample is transferred from an ALD chamber to an XPS analysis chamber under UHV conditions.

3. Chapter 3: Experimental techniques

3.1 FTIR

In this work, we used a Bruker vertex 80V spectrometer to perform FTIR spectroscopy. The spectroscopy data was collected between 400 to 4000 cm^{-1} at a resolution of 4 cm^{-1}, with an average of 200 scans for all the measured spectra. We utilized the sample compartment volume of the spectrometer, and designed the reactor with limited space availability in mind (*Figure 26*). Provisions were made for the reactor outlet and inlet to reduce interference with the spectrometer. To ensure accurate measurements, the infrared beam from the spectrometer was aligned to pass through the center of the sample holder[52].

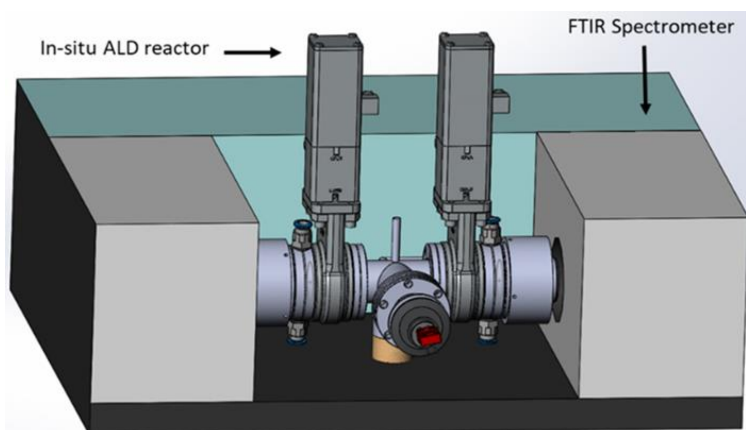

Figure 26: Drawing of the ALD system Integrated with the FTIR spectrometer

The absorbance was calculated using the relation eq.13,

$$\text{Absorbance} = -\log_{10}(I_{sample} / I_{reference}) \qquad (13)$$

where I_{sample} and $I_{reference}$ are IR intensity of transmitted radiation.

The substrate consisted of a 4 mm thick KBr (potassium bromide) with a 5 nm Si (silicon) layer sputtered onto it. KBr possesses a refractive index of approximately 1.533 in the IR spectrum, making it highly transparent to IR light, KBr was placed normal to the incident IR beam with an optical transmittance of 90% over the IR spectrum, by using a material with a lower

refractive index like KBr, it helps minimize reflection losses to ~10% at normal incidence, thus enhancing the efficiency of IR measurements (*Figure 27*). This choice of substrate offers superior IR transmissivity compared to a typical p-doped Si wafer.

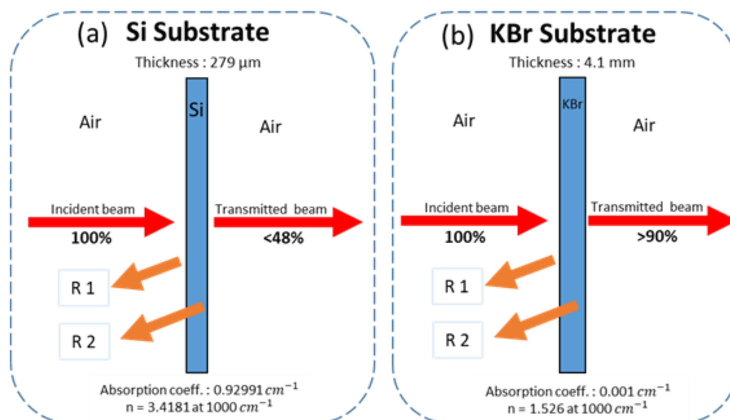

Figure 27: Comparison of IR transmision at wavenumber 1000 cm^{-1} for different substrates, (a) Si s and (b) KBr.

More IR beam intensity at the detector results in a better signal-to-noise (S/N) ratio of the obtained spectra. For comparison of the two substrates (Si and KBr) the signal amplitude of the incident beam on the detector was measured (*Figure 28*), for Si Wafer the signal was 1605 units, compared to 18600 units with the use of 5nm Si/KBr substrate. For systems, where high sensitivity is required for very small absorption's higher S/N ratio allows us to have a clearer and distinguishable spectrum. If surface studies, i.e. the nucleation of ALD films (or in our case TMA) with the Si surface are of interest, we believe that the approach of depositing a thin Si layer on the surface only can yield much better insight into the underlying chemistry during nucleation.

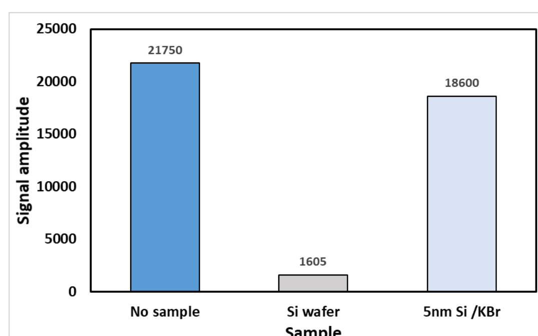

Figure 28: Comparison of detector signal of incident IR beam for SI and KBr substrate

3.2 XAS

For conducting XAS experiments, the samples were positioned at a grazing angle relative to the incident x-ray beam and detector at SSRL BL 11-2, a wiggler side station with a range of 2.4 keV – 11 keV unfocused energy. The energy x-ray slits were adjusted to a size of 1 mm x 10 mm. Total Fluorescence Yield (TFY) data at the Cu K-edge were collected using a Passivated Implanted Planar Silicon (PIPS) detector. A low grazing angle of incidence was chosen to limit the X-ray beam's interaction with the surface and to track the growth cycle of the ALD process for evaluation of the structural evolution of the formed thin film. Additionally, the low incidence angle helped reduce scattering loss from the substrate.

In the X-ray analysis setup, alignment is crucial for accurate measurements. The incoming X-ray beam is centered on the beam inlet flange, ensuring precise targeting of the sample (Figure 29). Detector alignment is maintained, with the detector center aligned with the centerline of the detector flange. To ensure optimal sample positioning, the sample holder is placed in a manner that aligns the sample surface with the lowest point of the beryllium windows aperture, allowing for the passage of X-rays.

The alignment is further refined through the use of stage movement and a fluorescent strip-camera setup. However, it's worth noting that alignment with the fluorescent strip and camera is not feasible when beryllium windows are in use; in such cases, quartz windows are employed for alignment.

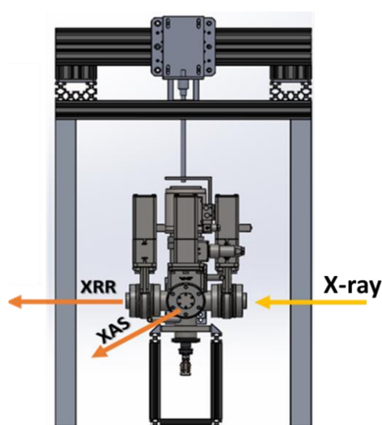

Figure 29: Schematic showing the setup of in situ XAS ALD reactor and X-ray beam.

3.3 XPS

To determine the chemical composition of the ALD TiO_2, HfO_2, and ZrO_2 thin films for protective coating applications and ALD Cu on Ti and Ni Mesh for Cu catalyst for OER application, X-ray photoluminescence spectroscopy (XPS) measurements were performed. The Kratos Analytical XPS Microprobe, which utilizes Al (Kα) radiation of 1486 eV in a vacuum environment of $5x10^{-9}$ Torr, was utilized for this purpose. The XPS data were analyzed using Casa XPS software.

3.4 SEM and EDS

The SU9000 Hitachi High-Tech electron microscope was used to capture Scanning Electron Microscopy (SEM) images with an acceleration voltage of 3 kV. Energy dispersive spectroscopy (EDS) was also performed using the Oxford Ultim Extreme 120 mm2 attached to the same SEM.

3.5 Ellipsometry

The thickness of ALD TiO_2, HfO_2, ZrO_2 and Al_2O_3 thin films on Si substrate was measured using a Woollam M2000 ellipsometer. This ellipsometer model which we used has a fixed angle base that is at an incident angle of 65 degrees [132] . To extract the thickness, the optical layer stack (OLS) technique was employed with completeEASE software provided by the same company. The software's inbuilt library of optical parameters and absorption coefficient of different materials was used to determine the thickness.

3.6 Electrochemical measurements

The catalysts electrochemical investigation was done using (Ivium-n-Stat) potentiostat in a three-electrode cell where sputtered catalyst, Hg/HgO electrode (Pine Research), and carbon rod were used as working, reference, and counter electrodes, respectively. The KOH

electrolytes were N_2 saturated. The OER catalyst was activated by cycling for 10 cycles at a scan rate of 100 mV/s between 1.1 V and 1.8 V vs. reversible hydrogen electrode (RHE). The linear sweep voltammetry (LSV) polarization curves were carried out in a (1.2 – 1.8 V vs. RHE) potential range at a 1 mV/s scan rate. Electrochemical impedance spectroscopy (EIS) is conducted at an amplitude of 10 mV root mean square (RMS) alternating current (AC) perturbation in a 0.1– 10^5 Hz frequency range. The ohmic (iR) resistance was compensated at 100 % of the high-frequency resistance (HFR) collected by EIS at 1.7 V vs. RHE. The stability testing was carried out at 1.8 V vs. RHE in 1 M KOH for a Ni sample with 500 cycles of copper.

The reference electrode (Hg/HgO) was calibrated in a hydrogen-saturated electrolyte using a Pt counter and working electrodes. By determining the potential in which current is zero in the polarization curve, the (Hg/HgO) reference electrode is assessed versus RHE. The Hg/HgO electrode is calibrated versus RHE in 1 M KOH:

$$E_{vs\mathrm{RHE}} = E_{\mathrm{vsHg/HgO}} + 0.9 \qquad (14)$$

The over-potential (η) is calculated, considering $E_{O2/H2O}$ = 1.23 V versus RHE, as follows:

$$\eta = E_{vs\mathrm{RHE}} - 1.23 \qquad (15)$$

This page is intentionally left blank

4. Chapter 4: Experimental study – ALD of oxides as protective coatings

This section is a summary based on the published findings from research article 3 [133], 4 [134], and 5 [135]. Through this collaborative effort, a potential application based on the ALD process was studied. The contributions performed by me are highlighted and discussed in this chapter along with other relevant results required for understanding the outcome of the work. A comprehensive set of results and discussion for this section can be found in the research articles included in the Appendix.

I contributed in this collaborative work by conducting ALD and sputter deposition of thin films, performing spectroscopic ellipsometry to measure film thickness, using profilometry to measure surface roughness, and conducting XPS analysis to determine the material's chemical composition.

4.1 Background: ALD metal oxides for corrosion protection

ALD is a unique and promising technique for developing protection layers, thanks to its ability to deposit ultra-thin films with uniformity on 3D surfaces and high aspect ratio structures. Recent studies have shown promising results in the corrosion protection of metals, with the use of Al_2O_3, TiO_2, ZnO, HfO_2, and ZrO_2 [85]. Using ALD, a decrease in corrosion rate for most surfaces has been achieved, although the degree of protection varies depending on the interface type and process conditions [86]. Furthermore, the use of protective layers with ALD has been extended to various other applications, such as TiO_2 protection layers for electrodes in water splitting [87], corrosion protection of photoelectrochemical cells [88], and protection of next-generation lithium-ion batteries [89]. As such, the scope and potential of the ALD technique is broad, making it a relevant and valuable tool for various industrial applications.

4.2 Advantage of ALD vs other techniques for protection application

Coatings have become the go-to approach for surface protection and functionalization in both industry and academia [136]. While there are many deposition methods available that follow the surface texture and add the possibility of tailoring the surface porosity, physical vapor deposition (PVD), sol-gel methods, and anodization have had varying degrees of success in improving corrosion resistance [137]. However, these methods have also had limitations such as cracking of thin films, limited control over deposition thickness, and undesirable porosity. Sputtering has shown good results, but its use is limited to flat surfaces due to line-of-sight deposition [134]. The "line of sight" limitation in thin film deposition techniques refers to the constraint that these techniques operate based on a direct line of sight between the deposition source and the substrate surface. This means that only the portions of the substrate surface that are directly exposed to the deposition source can receive material, and those areas that are obstructed or shadowed from the source will not receive deposition. This limitation can be particularly relevant in techniques such as physical vapor deposition (PVD) methods like sputtering and evaporation, as well as some chemical vapor deposition (CVD) processes. As a result, complex three-dimensional structures, recessed areas, or features hidden from the direct line of sight may not receive uniform or complete coverage, leading to issues like incomplete coatings, uneven film thickness, and shadowing effects (Figure 30).

To overcome this challenge, chemical vapor deposition (CVD) has emerged as a viable alternative, with ALD being particularly well-suited due to its best-in-class conformality, thin film density, and composition control [138].

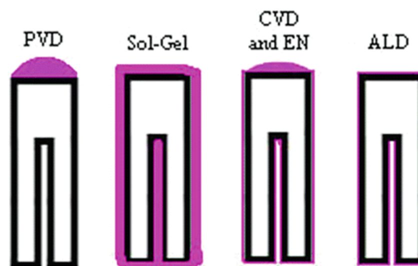

Figure 30: Coating uniformity on 3D substrates with different deposition techniques [139].

4.3 Study: Improving stress corrosion cracking behavior of AZ31 alloy with conformal thin titania and zirconia coatings for biomedical applications

In this study, we investigate the susceptibility of stress corrosion cracking (SCC) in AZ31 alloy coated with a 100 nm thick layer of ALD ZrO_2 and TiO_2. ZrO_2 and TiO_2 were selected as coating materials due to their known biocompatibility [133].

AZ31 is a magnesium alloy that belongs to the broader class of magnesium-aluminum (Mg-Al) alloys. It is one of the most commonly used magnesium alloys and is known for its good combination of properties, including low density, high strength-to-weight ratio, and good corrosion resistance. AZ31 is primarily composed of magnesium (Mg), aluminum (Al), and amount of zinc (Zn) (Table 4) [140]. AZ31 finds use in a wide range of applications, including aerospace [141] and marine components[142], automotive parts, medical devices, and sporting goods [143]. Its lightweight and corrosion-resistant properties make it valuable in industries where weight savings and durability are essential.

Table 4: Chemical composition of Mg Alloy AZ31 [140].

Alloy	**Chemical composition (wt%)**							
AZ31	Al	Zn	Mn	Cu	Ni	Si	Fe	Mg
	2.45	0.92	0.31	0.006	0.002	0.07	0.002	**Balance**

In this work, AZ31 magnesium-aluminum (Mg-Al) alloy has been considered for medical applications, i.e. bone implants and transplants, for several reasons:

1. Biocompatibility: Magnesium is an essential element in the human body, and its alloys like AZ31 are generally biocompatible [144]. This means that they are well-tolerated by the body and do not elicit harmful immune responses or allergic reactions when used as implants. This biocompatibility makes AZ31 suitable for medical applications.
2. Low Density: AZ31 is a lightweight material with a low density, similar to that of natural bone. This characteristic can reduce the overall weight of implants, making them more comfortable for patients and potentially reducing the risk of complications during and after surgery [145].

3. Mechanical Properties: While not as strong as some other implant materials like titanium alloys, AZ31 offers a balance of mechanical properties that can be suitable for certain medical applications. It has adequate strength and stiffness for bone implants and can provide the necessary support while allowing for some flexibility [146].
4. Degradability: One of the unique advantages of magnesium alloys like AZ31 is their potential to degrade in the body over time. This property can be beneficial for temporary implants, such as bone fixation devices or scaffolds for bone regeneration. As the implant gradually degrades, it can be replaced by newly formed bone tissue, reducing the need for additional surgeries to remove the implant [147].

The use of magnesium alloys in medical applications is an area of ongoing research and development. While AZ31 and similar alloys have shown promise, researchers are continuously working to optimize their properties and performance for specific medical applications.

4.3.1 ALD deposition process

The ALD coating process was conducted using the Savannah S200 ALD system (*Figure 31*) (Veeco Instruments Inc., USA). The deposition of a 100 nm thickness of zirconium oxide (ZrO2) was achieved through a series of successive cycles at 160 ◦C using Tetrakis (dimethylamino) zirconium (TDMAZ) and deionized water (H_2O) as reactants. The pulse and purge durations of the precursor and co-reactant, as well as the thermal conditions of the system, were determined according to the standard recipes provided by the manufacturer of the ALD system. These standard processes did not require further optimization, as the measured growth rates, as confirmed by the ellipsometer, were consistent with the expected values. Each cycle consisted of two stages: a 250 ms TDMAZ precursor pulse, followed by a 10 s N_2 purge to eliminate residual reactants and by-products, and a 150 ms H_2O precursor pulse, followed by a 15 s N_2 purge. The TDMAZ precursor and delivery lines were heated to 75 ◦C and 160 ◦C, respectively, while the H_2O precursor was maintained at room temperature. The deposition rate of the ZrO2 layer was determined through ellipsometry, yielding a rate of approximately 1.08 Å/cycle. Given that the deposition was conducted using standard ALD precursors within the ALD Savannah system, which has a well-defined growth process, there

was no need for cross-verification of thickness using SEM. Consequently, the measured growth rate closely aligned with the expected rate [133].

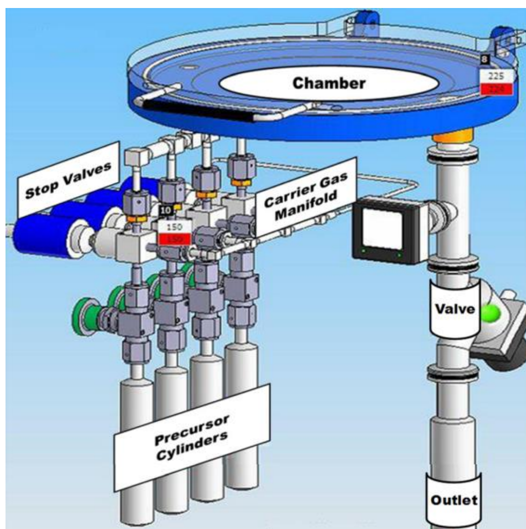

Figure 31: Schematic of Savannah ALD system used for the ALD of ZrO_2 and TiO_2 .

In thermal atomic layer deposition (ALD) of ZrO_2, the process with the use of $Zr(NMe_2)_4$ as the zirconium source and H_2O as the oxygen source. This reaction mechanism can be represented by two distinct reactions [148]:

Here, **--I** denotes the surface and an asterisk (*) denotes a surface species.

Step 1: TDMAZ precursor pulse : $Zr(NMe_2)_4$

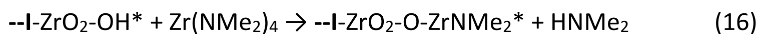

$$\text{--I-}ZrO_2\text{-OH}^* + Zr(NMe_2)_4 \rightarrow \text{--I-}ZrO_2\text{-O-}ZrNMe_2^* + HNMe_2 \quad (16)$$

Step 2 : Purge of the reactor for the evacuation of unreacted TDMAZ precursor.

Step 3: H_2O pulse.

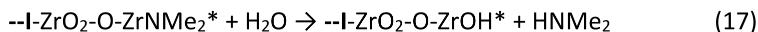

$$\text{--I-}ZrO_2\text{-O-}ZrNMe_2^* + H_2O \rightarrow \text{--I-}ZrO_2\text{-O-}ZrOH^* + HNMe_2 \quad (17)$$

Step 4 : Purge of the reactor for the evacuation of unreacted H_2O.

For TiO_2, Tetrakis (dimethylamido) titanium (IV) (TDMA-Ti) was used as a precursor, heated to 75 ◦C. Each cycle involved a 0.1 s TDMA-Ti precursor pulse, followed by a 5 s N_2 purge with a flow rate of 20 sccm, and a 0.015 s H_2O precursor pulse, followed by a 5 s N_2 purge. The deposition rate of the TiO_2 layer was measured to be 0.5 Å/cycle [133].

This reaction mechanism can be represented by the below reactions steps [149],

Here, **--I** denotes the surface and an asterisk (*) denotes a surface species.

Step 1: TDMAT precursor pulse:

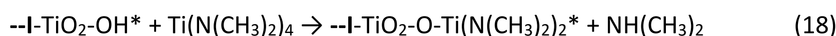

$$\text{--I-}TiO_2\text{-}OH^* + Ti(N(CH_3)_2)_4 \rightarrow \text{--I-}TiO_2\text{-}O\text{-}Ti(N(CH_3)_2)_2^* + NH(CH_3)_2 \quad (18)$$

Step 2: Purge of the reactor for the evacuation of unreacted TDMAT precursor.

Step 3: H_2O pulse:

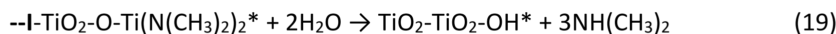

$$\text{--I-}TiO_2\text{-}O\text{-}Ti(N(CH_3)_2)_2^* + 2H_2O \rightarrow TiO_2\text{-}TiO_2\text{-}OH^* + 3NH(CH_3)_2 \quad (19)$$

Step 4: Purge of the reactor for the evacuation of unreacted H_2O.

4.3.2 Results

4.3.2.1 Ellipsometery

The thickness of the film was determined using spectroscopic ellipsometry at a fixed angle of incidence of 65◦, using a J.A. Woollam M2000U instrument. The measurements were carried out on thin films deposited on p-doped <100> 500 µm thick Si wafers. The ellipsometry data were analyzed using a B-spline model, which accounted for the Si substrate, native oxide layer, and the ALD layer of the relevant material. The measured thickness for the TiO_2 and ZrO_2 deposition was 100.98 and 100.97 nm thick, respectively [133].

4.3.2.2 Chemical composition

We conducted X-ray photoelectron spectroscopy (XPS) measurements to analyze the chemical composition of the TiO_2 and ZrO_2 coating deposited through ALD. Kratos Analytical XPS system, which employs Al (Kα) radiation of 1486 eV in a vacuum environment of $5*10^{-9}$ Torr, was used for this purpose. The XPS data were analyzed using CasaXPS software [133].

First, the surface was etched for 180 s at an energy of 2 KeV to remove environmental contamination and surface oxidation. High-resolution regional scans were then conducted on TiO_2 substrates for Ti 2p, O 1s, and C 1s to assess the chemical composition. Negligible amounts of C were observed, indicating a contamination-free deposition. The regional scans of Ti 2p and O 1s (shown in *Figure 32* a and b, respectively) revealed peaks at binding energies of 459 eV and 464 eV for Ti $2p_{3/2}$ and Ti $2p_{1/2}$, respectively, corresponding to the Ti^{4+} oxidation state in TiO_2. A shoulder around 456 eV was also observed, which is due to the presence of Ti^{3+} caused by the argon etching step. The O peak at 531 eV corresponds to O atoms in the TiO_2 phase, while the small shoulder at higher energy is due to O in OH groups present as impurities. The composition of the TiO_2 thin film was found to be approximately 60% oxygen and 40% titanium, indicating an oxygen-deficient deposition [133].

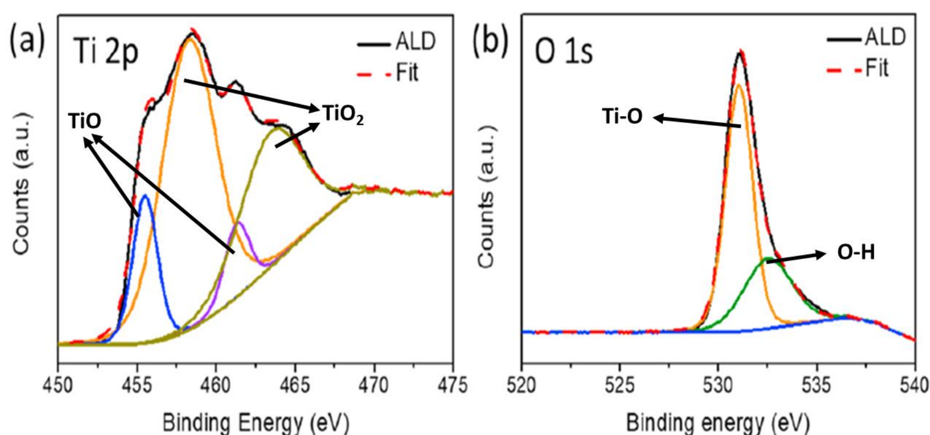

Figure 32: XPS spectra for ALD deposited TiO2 (a) Ti 2p regional peak and (b) O 1s regional peak [133].

For ZrO_2 coated samples, high-resolution regional scans of Zr 3d, O 1s, and C 1s were conducted. No peak was observed in the high-resolution scan for elemental carbon, indicating a carbon-free ALD deposition. The Zr 3d high-resolution spectra (shown in Figure 33 (a)) displayed two peaks at binding energy 182 eV and 184 eV, which correspond to Zr $3d_{5/2}$ and Zr $3d_{3/2}$, respectively. The The deconculation of peaks were in accordance with the values reported in literature . The O 1s scan revealed (*Figure 33* (b))a peak at 530 eV, which belongs to ZrO_2, while the shoulder on the higher energy side is due to the oxidation of metal in air forming ZrO. Quantification calculations using CASA XPS software showed a composition of 40% Zr and 60% O, indicating an oxygen-deficient ZrO_2 thin film [133].

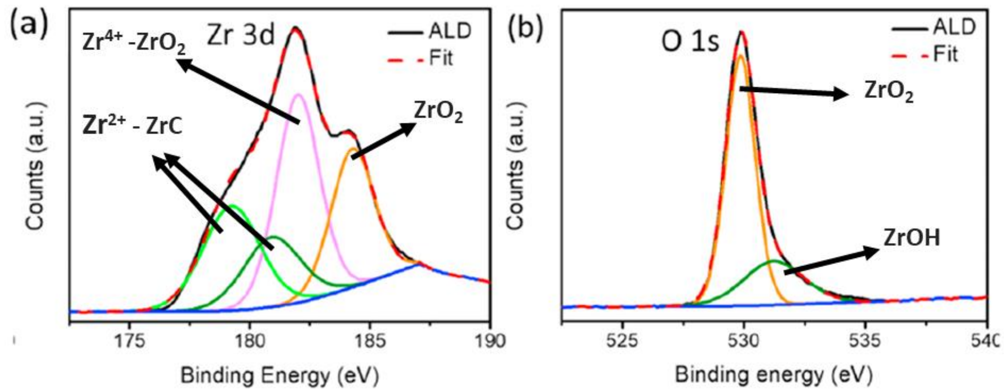

Figure 33: XPS spectra for ALD ZrO_2 ,(a) Zr 3d regional peak and (b) O 1s regional peak [133] .

4.3.3 Summary

Both the coatings showed improved performance against stress corrosion cracking (SSC) for AZ31 alloy. TiO_2 reduced the I_{UTS} and the $I\varepsilon$ to 6% and 40%, respectively, while for ZrO_2 the reduction was 70% and 76%, respectively, (I_{UTS} and the $I\varepsilon$ are the susceptibility indices, UTS (ultimate tensile strength) and ε (elongation)). The difference in the performance of the two coating could be due key parameters, such as cohesive energy, wettability, thermal expansion, and elongation of the coating [133]. The details of the improved performance are highlighted below.

Surface Analysis

SEM analysis of the ALD coated samples revealed the presence of cracks, as depicted in (*Figure 34*). Notably, the number of cracks (referred to as crack density in Table 5) and their respective lengths exhibited an increase when transitioning from ZrO_2 to TiO_2 coated samples. The integrity of the coating is a crucial factor, as defects like pores and cracks serve as pathways for the of fluids to reach the substrate, thus contributing to the difference in their corrosion behavior[133].

Table 5: Crack density of coated samples [133].

	TiO_2	ZrO_2
Crack length (μm)	4.54 ± 3.05	3.14 ± 2.41
Density (n° cracks/cm²)	0.87 ± 0.37	0.61 ± 0.28

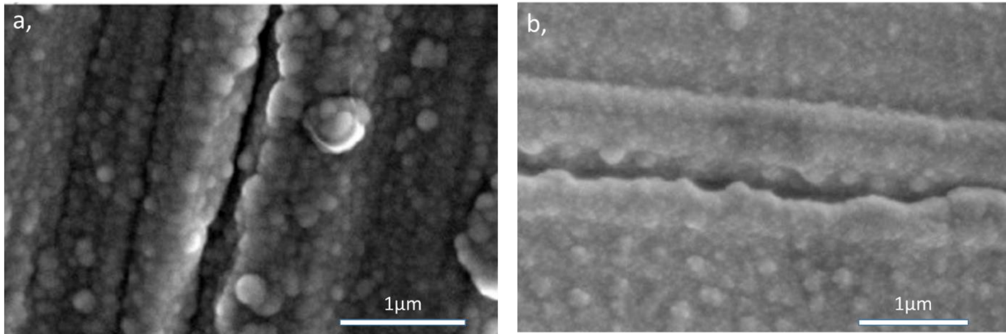

Figure 34: SEM images of ALD (a) TiO_2 and, (b) ZrO_2 coated AZ31 surfaces with surface cracks [133].

Potentiodynamic polarization curves

To assess corrosion, the potentiodynamic polarization curves were detrmined. The curves for both the TiO_2 and ZrO_2-coated samples, as well as the uncoated ones, are presented in *Figure 35*. The corrosion potential (E_{corr}) and corrosion current density (i_{corr}), and the results are summarized in Table 6. Compared to the uncoated alloy, the coated samples showed a reduction in corrosion current density, with the ZrO_2 coating demonstrating a more significant reduction than the TiO_2 coating. A lower corrosion current density signifies a slower corrosion rate, indicating that these coatings effectively shield the Mg alloys from corrosion, particularly the ZrO_2 coating, which showed superior barrier properties[133].

Table 6: Corrosion potentials (E_{corr}) and corrosion current densities (i_{corr}) [133].

	Bare	TiO_2 coating	ZrO_2 coating
E_{corr} (V)	-2.00 ± 0.02	-1.90 ± 0.01	-2.02 ± 0.01
i_{corr} (A/cm^2)	$3.0\ 10^{-3} \pm 0.4$	$2.5\ 10^{-5} \pm 0.6$	$1.2\ 10^{-6} \pm 0.3$

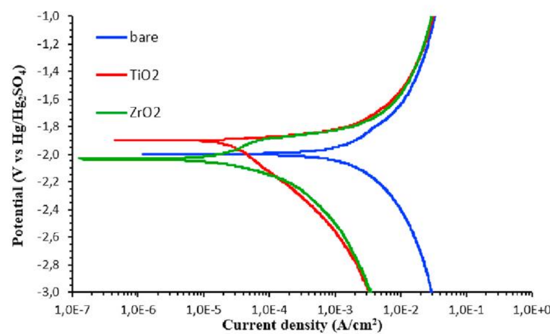

Figure 35: Potentiodynamic polarization curves of bare (blue), TiO_2 coated (red) and ZrO_2 coated (green) AZ31 alloy in SBF [133].

Stress corrosion cracking

The susceptibility to stress corrosion cracking (SCC) of AZ31 samples was evaluated, both uncoated and coated with TiO_2 and ZrO_2, under test conditions in air and simulated body fluid (SBF) [133] .

The susceptibility indices I_{UTS} and I_{ε} were calculated according to Eq. (20) and Eq. (21),

$$I_{UTS} = (UTS_{air} - UTS_{SBF})/ UTS_{air} \qquad (20)$$

$$I_{\varepsilon} = (\varepsilon_{air} - \varepsilon_{SBF})/\varepsilon_{air} \qquad (21)$$

where UTS is the Ultimate Tensile Strength and ε the elongation at failure. A lower index value indicates higher resistance to SCC. Our assessment in both air and SBF revealed that both coatings significantly enhance the SCC resistance of AZ31 alloy. Notably, the 100 nm thick ZrO_2 coating exhibited more effective reduction in SCC susceptibility compared to the TiO_2 coating. Specifically, I_{ε} was reduced from 75.1 to 43.2 with TiO_2 and to 18.3 with ZrO_2, while I_{UTS} decreased from 8.97 to 8.42 with TiO_2 and to 2.68 with ZrO_2 (*Figure 36*) [133].

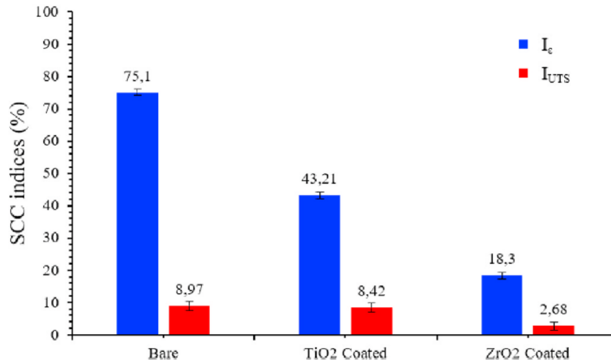

Fig. 10. SCC indices for the bare and coated AZ31 samples.

Figure 36: SSC indices for the bare and coated AZ31 sample [133].

Hydrogen evolution test

Hydrogen evolution test was conducted to evaluate the corrosion behavior of AZ31 alloy in a simulated body fluid (SBF), comparing samples with and without ALD coatings. The objective of this test was to gauge the corrosion resistance and overall performance of AZ31 alloy in an environment that replicates physiological conditions. The hydrogen evolution curves for both uncoated and coated samples are presented in *Figure 37*, with the results indicating that the

application of coatings effectively shields AZ31 alloy from degradation. Notably, the 100 nm thick ZrO_2 coating outperforms the TiO_2 coating, reducing hydrogen evolution by 93% compared to the bare sample, while the TiO_2 coating reduces it by 52%. This demonstrates the superior protective properties of the ZrO_2 coating in preventing corrosion [133].

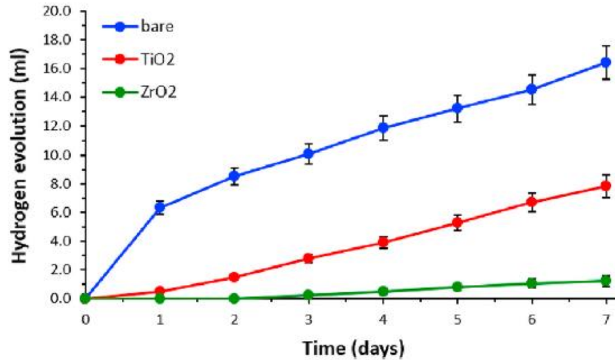

Figure 37: Hydrogen evolved from the immersion of bare (blue), TiO_2 coated (red) and ZrO_2 coated (green) AZ31 alloy in SBF [133].

Fractography

The improved corrosion performance observed in the coated samples when tested in SBF in contrast to the bare sample, is further validated by examining the tilted views of the gauge section. A comparison of these views between the bare sample and the coated samples (as shown in *Figure 38*) reveals clear differences. The bare samples exhibit deep secondary cracks and some pits, whereas the coated sample displays an absence of deep secondary cracks and pits. Moreover, the ZrO2 coated samples exhibit necking, which serves as confirmation of increased ductility [133].

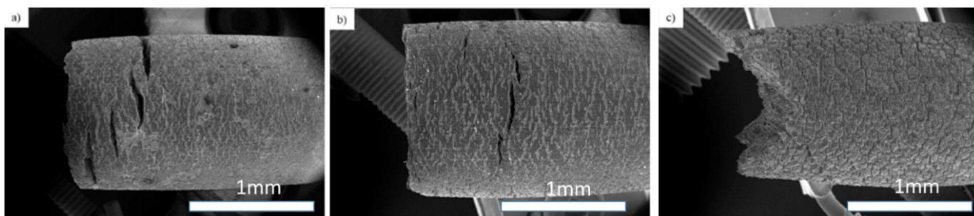

Figure 38: SEM fractographies of the gauge section of (a) bare, (b) TiO_2 coated and (b) ZrO_2 coated samples [133].

4.4 Study: Comparing physiologically relevant corrosion performances of Mg AZ31 alloy protected by ALD and sputter coated TiO_2

This study focuses on evaluating the effectiveness of Atomic Layer Deposition (ALD) coatings in reducing corrosion on AZ31 alloy implant surfaces, and comparing the results with those obtained using the sputtering technique [134]. To achieve this, we used both ALD and sputtering to coat specimens with varying surface roughness and 3D topologies, creating a 40 nm layer of TiO_2. TiO_2 was chosen as the coating material due to its high biocompatibility and its ability to bond quickly and directly with living bone after implantation, making it a promising material in the biomedical field. We analyzed the chemical composition of the TiO_2 layer using X-ray photoelectron spectroscopy (XPS) both before and after a 24-hour corrosion period in simulated body fluid (SBF) [134].

4.4.1 ALD and sputter deposition process

These samples or substrates were AZ31 alloy material, included flat discs, used for potentiodynamic polarization curves, and plates for hydrogen evolution tests. Additionally, small cubes with pass-through holes were created to mimic the porosity seen in actual implants. The flat discs had a 29 mm diameter and were 2 mm thick (as shown in Figure 39 a), while the plates were 2 mm thick, 60 mm long, and 25 mm wide (as seen in Figure 39 b). To achieve different surface textures, the samples were grounded. The "rough" group was treated with 40 grit silicon carbide papers, resulting in a rough surface, while the "smooth" group underwent grinding up to 4000 grit silicon carbide papers, achieving a smooth surface [134].

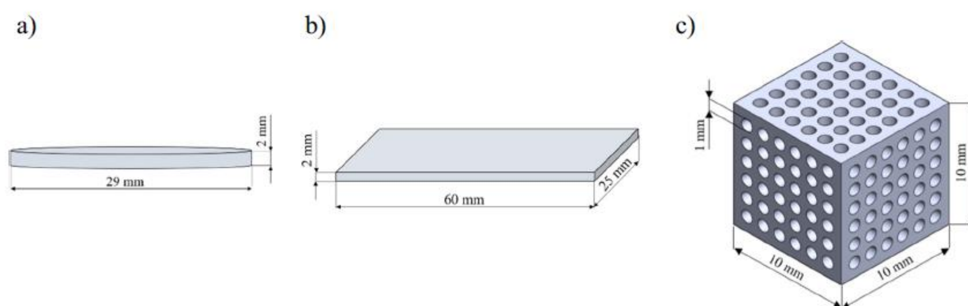

Figure 39: 3D representation of substrates in different shapes, (a) discs, (b) plates and (c) 3D structures used in the hydrogen evolution experiments [134] .

To deposit a thin film of TiO_2, we used the AJA ATC-2200 V magnetron-sputtering tool from AJA International Inc. USA, with a 99.99% pure 2" TiO_2 target as the source material. The sputtering chamber was evacuated to a base pressure below $2e^{-7}$ Torr, and we used an RF power of 63 W, a pressure of 3 mtorr, and an Argon gas flow rate of 63 sccm for deposition. To determine the deposition rate, we conducted preliminary depositions and measured the deposition rate using quartz crystal monitor (QCM), which resulted in a deposition rate of 0.21 nm/min [134].

For ALD growth of the TiO_2 thin film, we used a Savannah S200 system operating on thermal mode at a reactor temperature of 160 °C. We used Tetrakis (dimethyl amido) titanium (IV) or TDMATi as the metal organic precursor, heated to 75 °C, and deionized water as an oxidizer. A constant flow rate of 20 sccm of Nitrogen was used as a carrier gas. The oxidant and precursor were pulsed in the following sequence: a 0.015 s water pulse, a 5 s purge, a 0.1 s TDMA-Ti precursor pulse, and another 5 s purge. To determine the growth rate, we also coated Si wafers and used spectroscopic ellipsometry (Woollam M2000, USA), which showed a growth rate of 0.5 Å /cycle [134].

The deposition process on 3D cube samples necessitated a specialized lid, resulting in an expansion of the reactor volume. Initially, with the standard 5-second purge time, a notably high growth rate of 0.70 Å per cycle was recorded. Consequently, various purge times were tested in an attempt to achieve a growth rate similar to that observed with the standard lid.

It was observed that as the purge time was extended, a consistent reduction in the growth rate occurred, gradually approaching the standard rate (*Figure 40*). Subsequently, when a 20-second purge time was implemented, a growth rate of 0.54 Å per cycle was measured, closely aligning with the standard rate. Further extending the purge time to 30 seconds did not yield any significant change in the growth rate.

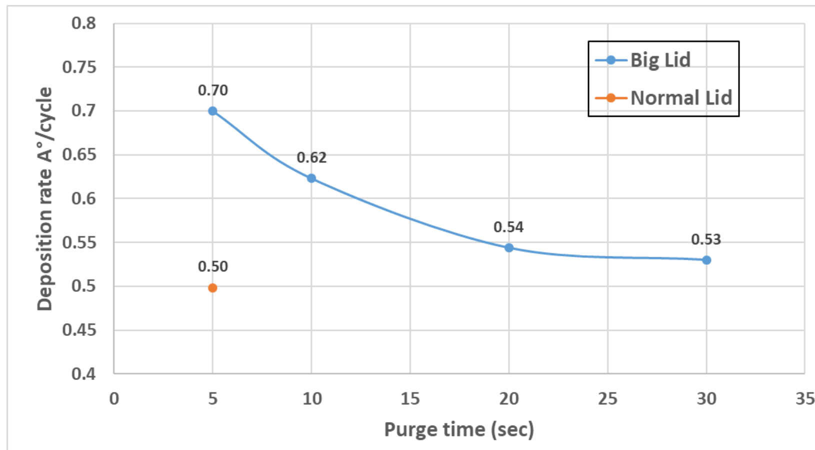

Figure 40: Purge time optimization of ALD TiO_2 for a specialized big lid on the Svannah ALD system.

The reaction mechanism for the ALD TiO_2 can be represented by the below reactions steps [149],

Here, **--I** denotes the surface and an asterisk (*) denotes a surface species.

Step 1: TDMAT precursor pulse:

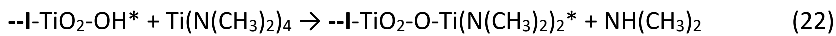

$$\text{--I-}TiO_2\text{-}OH^* + Ti(N(CH_3)_2)_4 \rightarrow \text{--I-}TiO_2\text{-}O\text{-}Ti(N(CH_3)_2)_2^* + NH(CH_3)_2 \quad (22)$$

Step 2: Purge of the reactor for the evacuation of unreacted TDMAT precursor.

Step 3: H_2O pulse:

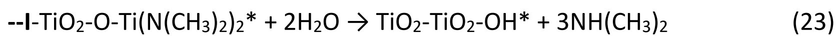

$$\text{--I-}TiO_2\text{-}O\text{-}Ti(N(CH_3)_2)_2^* + 2H_2O \rightarrow TiO_2\text{-}TiO_2\text{-}OH^* + 3NH(CH_3)_2 \quad (23)$$

Step 4: Purge of the reactor for the evacuation of unreacted H_2O.

4.4.2 Results

4.4.2.1 Roughness measurement

We used a Dektak 150 Profilometer (Veeco, USA) to measure the roughness values of both smooth and rough discs. To calculate the Roughness Average (Ra), we defined an assessment length of 300 µm, where we calculated the arithmetic average deviation from the mean line. We carried out measurements at multiple points on each sample and calculated the average

value. The results showed that the average surface roughness of the smooth bare samples was 118.6 ± 5.1 nm, while that of the rough bare samples was 4794.3 ± 49.4 nm [134].

4.4.2.2 Chemical composition

X-ray photoelectron spectroscopy (XPS) was utilized to assess the chemical composition of the samples coated with sputter and ALD techniques. Furthermore, the chemical composition of the smooth samples coated with sputter and ALD after immersion in SBF for 24 hours was evaluated using XPS. The measurements were conducted using a Kratos Analytical XPS Microprobe, which uses Al (Kα) radiation of 1486 eV in a vacuum environment of 5×10^{-9} Torr. The XPS data was analyzed using CasaXPS software [134].

To eliminate the effects of environmental contamination and surface oxidation, etching was conducted on the surface before conducting the measurements. The surface was etched for 180 seconds with an ion beam energy of 2 KeV. High-resolution regional scans for titanium, oxygen, and carbon were performed, and negligible amounts of carbon were observed, indicating an ideal deposition without any process contamination [134].

The regional scans (*Figure 41*) of titanium for ALD and sputter deposition techniques showed very similar peaks, corresponding to the core level binding energies of Ti $2p_{3/2}$ and Ti $2p_{1/2}$, which is due to Ti^{4+} oxidation state in TiO_2. The shoulder at lower energy around 456 eV was observed due to the presence of Ti^{3+} caused by the argon-etching step. Regional scans of oxygen in both ALD and sputter-coated samples showed a peak at 531 eV, which is due to oxygen atoms in TiO_2 phase, while a small shoulder at higher energy is due to O in –OH groups present as impurities. The composition of the TiO_2 thin films was found to be around 60% for O and 40% Ti, indicating an O deficient deposition in both cases [134].

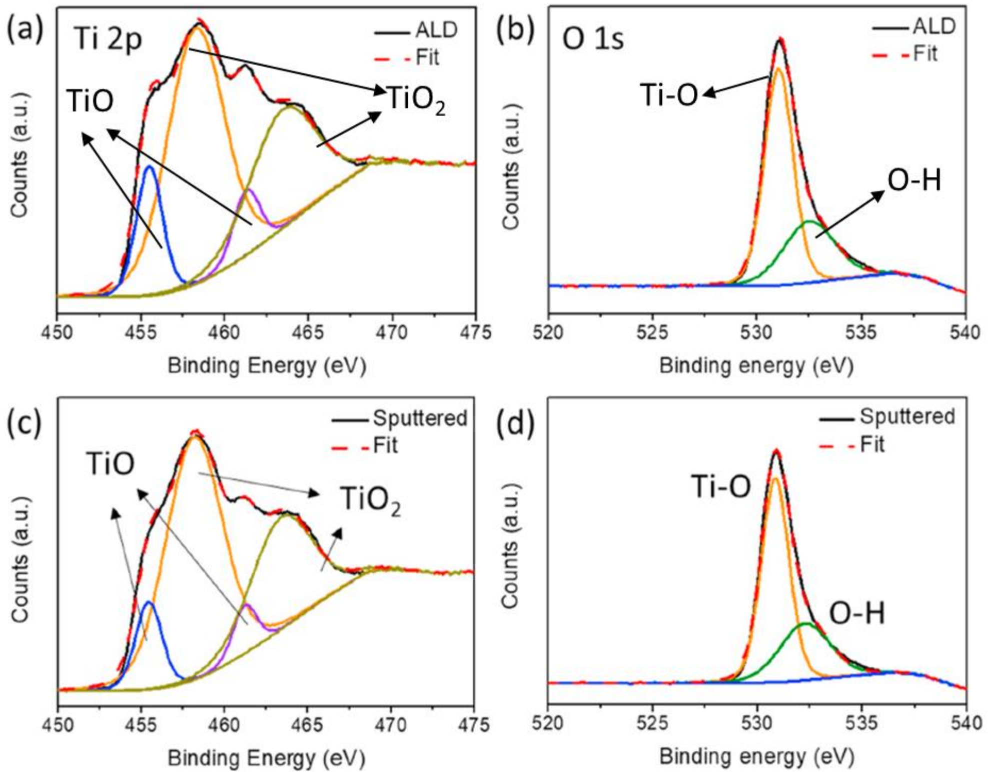

Figure 41: : XPS spectra for ALD TiO_2 (a) Ti 2p (b) O 1s and sputter deposited TiO_2 (c) Ti 2p and (d) O 1s [134].

4.4.3 Summary

In this study, the corrosion performance of AZ31 Mg alloy coated with ALD was evaluated, as well as the effectiveness of sputtered and ALD-coated biocompatible TiO_2 coatings were compared. The corrosion properties of substrates with varying surface roughness and complex 3D architectures were also investigated. A 40 nm layer of TiO_2 was deposited to all samples through sputter deposition and ALD techniques. These samples or substrates included flat discs, used for potentiodynamic polarization curves, plates for hydrogen evolution tests, and small cubes with pass-through holes to mimic the porosity seen in actual implants. To achieve different surface textures, the samples were grounded and smoothened with different grit papers [134].

Analyzing the data (Table 7) derived from the potentiodynamic polarization curves, significant improvements in corrosion resistance for both rough and smooth samples was observed with the TiO_2 coatings. This improvement is characterized by an increase in the corrosion potential (E_{corr}) and a reduction in corrosion current density (i_{corr}), by over an order of magnitude. Notably, ALD coatings were particularly effective in protecting against corrosion, especially when dealing with surfaces of high roughness [134].

Table 7: Electrochemical corrosion data extrapolated from potentiodynamic polarization for rough and smooth samples [134].

Rough samples	Ecorr (V)	icorr (μA/cm²)
Bare	−1.97 ± 0.025	1500 ± 40
Sputter coated	−1.95 ± 0.035	600 ± 10
ALD coated	−1.90 ± 0.015	102 ± 4
Smooth samples	**Ecorr (V)**	**icorr (μA/cm²)**
Bare	−1.91 ± 0.02	1400 ± 25
Sputter coated	−1.79 ± 0.033	220 ± 15
ALD coated	−1.83 ± 0.016	84 ± 6

The outcomes from the hydrogen evolution tests (*Figure 42*) align closely with the observations made in the potentiodynamic polarization curves. The coating application slows down the corrosion process, regardless of the surface roughness under consideration. Moreover, the distinction in effectiveness between the sputter and ALD coatings is particularly evident in the case of rough samples, which is in line with the findings of the potentiodynamic polarization curves. This superior corrosion protection offered by ALD, when compared to sputtering, is further validated by the results of hydrogen evolution tests conducted on 3D structures [134].

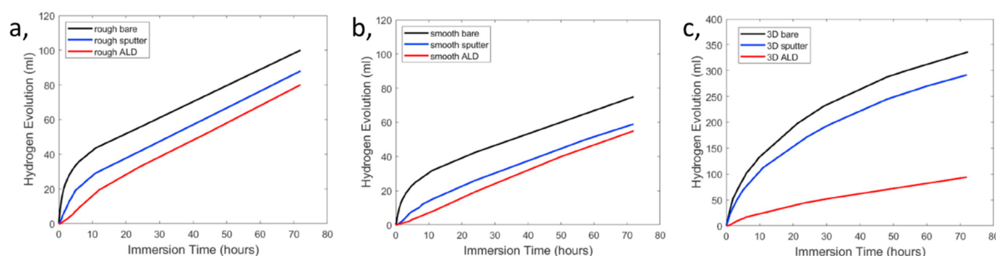

Figure 42: Hydrogen evolution of (a) rough samples, (b) smooth samples and, (c) 3D samples [134].

Figure 43 illustrates the overall appearances of cylindrical samples coated via sputter and ALD methods, both before and after one day of immersion in SBF, for both smooth and rough

samples. An evident reduction in the extent of corrosion damage is observed in all cases where coatings were applied. Notably, the protective effectiveness of the ALD coating stands out. In both smooth and rough samples, the majority of the TiO_2 coating remains intact. In contrast, sputter-coated samples reveal several areas where the Mg substrate is exposed, especially in the case of rough specimens [134].

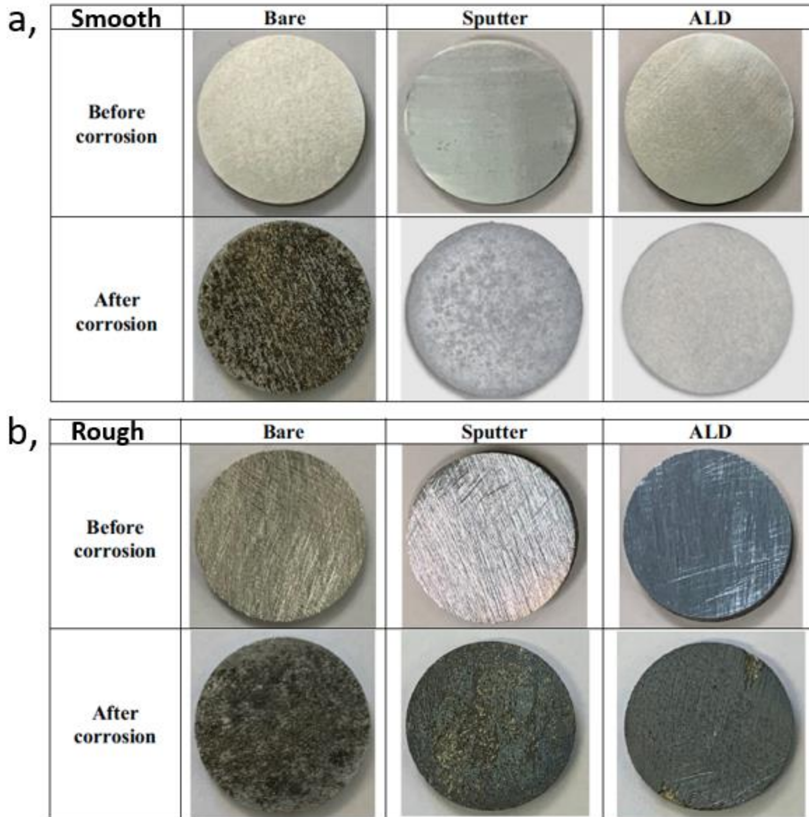

Figure 43: Macro-morphologies of (a),smooth and (b) rough (bare, sputter and ALD TiO2 coated samples) before and after corrosion [134].

Figure 44 provides an overview of the visual changes in the 3D samples, both in their pristine state and following a one-day immersion in SBF, for bare, sputter-coated, and ALD-coated samples. The bare samples exhibit extensive corrosion, obscuring their original form to a significant degree. Notably, the application of coatings leads to a noticeable reduction in corrosion, with the ALD-coated sample standing out as particularly effective in preserving the sample's original shape [134].

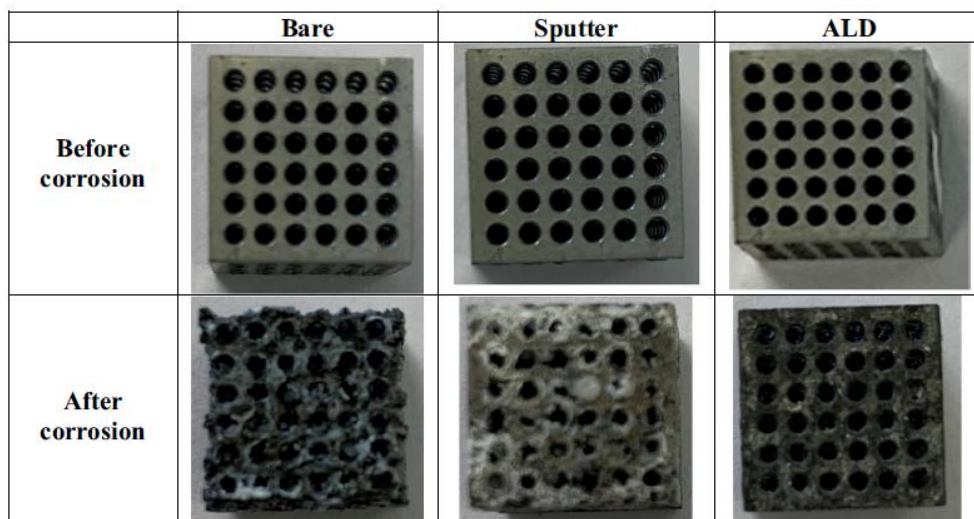

Figure 44: Macro-morphologies of smooth bare, sputter and ALD TiO_2 coated 3D samples before and after corrosion [134].

To summarise the results showed that both sputtering and ALD coating improved the corrosion resistance of the AZ31 alloy, but the ALD-coated surface exhibited the lowest corrosion rates, regardless of the surface conditions. This makes the ALD technique a promising approach for developing biodegradable implants with increased durability inside the human body [134].

ALD-grown TiO_2 films are characterized by their fine-grained structure [150], which results in a uniform coating. This is advantageous for corrosion protection because smaller grains contribute to a continuous and uniform barrier, minimizing pathways for corrosive agents to penetrate the substrate. Moreover, ALD produces highly dense [151] and conformal films that effectively blocks corrosive substances from reaching the underlying substrate. In both cases, the key to effective corrosion protection lies in the creation of a dense, pinhole-free, and defect-free coating.

The variation in coating performance can be attributed to the constraints posed by the line of sight during the sputtering process, which became particularly evident in the case of 3D samples. Interestingly, when we examined the SEM micrograph of the undercuts and shadowed areas within the sliced 3D structures (*Figure 45*), it became apparent that the sputter-coated samples exhibited a similar morphology to the bare samples. This suggests that these regions were either not covered at all or were only partially coated to begin with.

In contrast, ALD coatings are conformal in nature, meaning they conform to and effectively cover the inner areas of the structure. Our hypothesis is that this conformal coverage of the internal structure is the primary factor contributing to the significant differences observed in degradation when the internal structure is exposed to SBF [134].

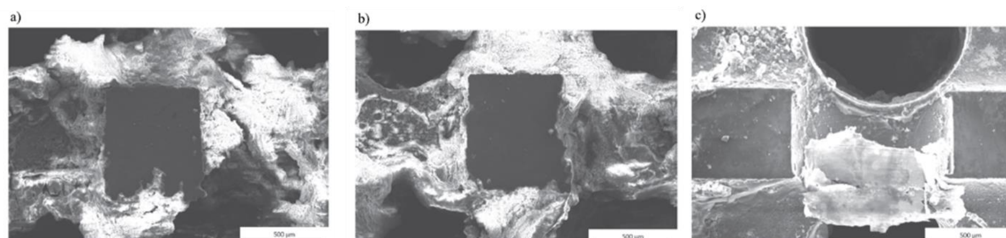

Figure 45: SEM image of sliced cross-section (a) bare, (b) sputter coated and, (c) ALD coated 3D samples [134].

4.5 Study: On the evaluation of ALD TiO_2, ZrO_2, and HfO_2 coatings on corrosion and cytotoxicity performances

In this study, we investigate the effect of TiO_2, ZrO_2, and HfO_2 ALD coatings on both the corrosion resistance and cell viability of AZ31 alloys in bone-implant applications [135]. We also conducted various tests on 100 nm thick coated AZ31 samples to understand their corrosion resistance. ALD HfO_2 coatings shown to reduce the corrosion current density of AZ31 alloys by up to three orders of magnitude, but little information is available on its effects on cell viability. To fill this gap, we evaluate the effects of ALD HfO_2 coatings on cell viability using 100 nm thick ALD HfO_2 coated AZ31 samples [135].

4.5.1 ALD deposition process

A commercial ALD reactor (Savannah S200, USA) was used to deposit the ALD coatings in our study. For the deposition of 100 nm of ZrO_2, we employed successive cyclic reactions of Tetrakis dimethylamino zirconium (TDMAZ) and deionized water (H_2O) at 160 °C. Each cycle consisted of two parts: a 250 ms TDMAZ precursor pulse followed by a 10 s N_2 purge with a flow rate of 20 sccm, and a 150 ms H_2O precursor pulse followed by a 10 s N_2 purge. The TDMAZ precursor was heated at 75 °C, while the H_2O precursor and the delivery lines were kept at 25 °C and 160 °C, respectively. The N_2 purge was utilized to remove residual reactants and by-products from the chamber to prevent additional chemical vapor deposition reactions. We determined the deposition rate to be around 1.08 A°/cycle [135].

This reaction mechanism of ALD ZrO_2 can be represented by the below reaction steps [148]:

Here, **--I** denotes the surface and an asterisk (*) denotes a surface species.

Step 1: TDMAZ precursor pulse : $Zr(NMe_2)_4$

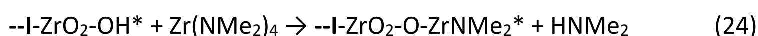

$$\text{--I-}ZrO_2\text{-}OH^* + Zr(NMe_2)_4 \rightarrow \text{--I-}ZrO_2\text{-}O\text{-}ZrNMe_2^* + HNMe_2 \quad (24)$$

Step 2 : Purge of the reactor for the evacuation of unreacted TDMAZ precursor.

Step 3: H_2O pulse.

$$\text{--I-}ZrO_2\text{-}O\text{-}ZrNMe_2^* + H_2O \rightarrow \text{--I-}ZrO_2\text{-}O\text{-}ZrOH^* + HNMe_2 \quad (25)$$

Step 4 : Purge of the reactor for the evacuation of unreacted H_2O.

For ALD TiO_2, we used Tetrakis dimethylamino titanium (IV) or TDMA-Ti heated at 75 °C. Each cycle comprised of a 0.1 s TDMA-Ti precursor pulse followed by a 5 s N_2 purge with a flow rate of 20 sccm, and a 0.015 s H_2O precursor pulse followed by a 5 s N_2 purge. The deposition rate was measured to be 0.5 A ˚/cycle [135].

This reaction mechanism of ALD TiO_2 can be represented by the below reactions steps [149],

Here, **--I** denotes the surface and an asterisk (*) denotes a surface species.

Step 1: TDMAT precursor pulse:

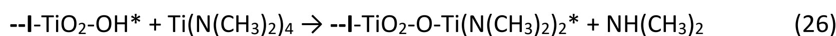

$$\text{--I-}TiO_2\text{-}OH^* + Ti(N(CH_3)_2)_4 \rightarrow \text{--I-}TiO_2\text{-}O\text{-}Ti(N(CH_3)_2)_2^* + NH(CH_3)_2 \qquad (26)$$

Step 2: Purge of the reactor for the evacuation of unreacted TDMAT precursor.

Step 3: H_2O pulse:

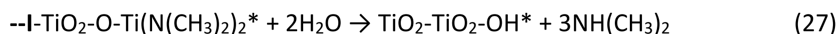

$$\text{--I-}TiO_2\text{-}O\text{-}Ti(N(CH_3)_2)_2^* + 2H_2O \rightarrow TiO_2\text{-}TiO_2\text{-}OH^* + 3NH(CH_3)_2 \qquad (27)$$

Step 4: Purge of the reactor for the evacuation of unreacted H_2O.

Finally, for HfO_2 deposition, we utilized Tetrakis dimethylamino Hafnium (TDMAH) and deionized water (H_2O) at 160 °C. Each cycle comprised of a 200 ms TDMAZ precursor pulse followed by a 10 s N_2 purge with a flow rate of 20 sccm, and a 150 ms H_2O precursor pulse followed by a 10 s purge. The TDMAZ precursor was heated at 75 °C, while the H_2O precursor and the delivery lines were kept at 25 °C and 160 °C, respectively. The deposition rate was determined to be 1.3 A°/cycle [135].

This reaction mechanism of ALD HfO_2 can be represented by the below reactions steps [152],

Here, **--I** denotes the surface and an asterisk (*) denotes a surface species.

Step 1: TDMAT precursor pulse:

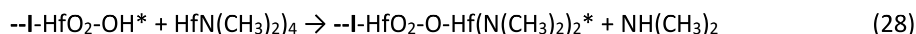

$$\text{--I-}HfO_2\text{-}OH^* + HfN(CH_3)_2)_4 \rightarrow \text{--I-}HfO_2\text{-}O\text{-}Hf(N(CH_3)_2)_2^* + NH(CH_3)_2 \qquad (28)$$

Step 2: Purge of the reactor for the evacuation of unreacted TDMAT precursor.

Step 3: H_2O pulse:

$$\text{--I-}HfO_2\text{-O-}Hf(N(CH_3)_2)_2^* + 2H_2O \rightarrow HfO_2\text{-}HfO_2\text{-}OH^* + 3NH(CH_3)_2 \quad (29)$$

Step 4: Purge of the reactor for the evacuation of unreacted H_2O.

4.5.2 Results

4.5.2.1 Chemical composition

The chemical composition of TiO_2, ZrO_2, and HfO_2 ALD coatings was assessed using X-ray photoluminescence (XPS) measurements. A Kratos Analytical XPS system was used to conduct the measurements in a vacuum environment of 5×10^{-9} Torr, using Al (K α) radiation of 1486 eV. CasaXPS software was used to analyze the XPS data [135].

To minimize the effect of the underlying substrate, the measurements were carried out on thin films deposited on Si wafers. Prior to chemical characterization, the effect of environmental contamination and surface oxidation were removed by etching the surface for three minutes with an energy of 2 KeV [135].

For TiO_2, high resolution regional scans were conducted for titanium and oxygen *(Figure 46)*. The negligible amount of carbon detected excluded the presence of any process contamination, thus indicating an ideal deposition. Regional scans of titanium and oxygen showed peaks corresponding to the core level binding energies of Ti $2p_{3/2}$ and Ti $2p_{1/2}$, respectively, indicating the presence of Ti^{4+} oxidation state in TiO_2. The presence of Ti^{3+} due to the argon etching step caused a shoulder at lower energy. Oxygen atoms in TiO_2 phase lead to the peak at 531 eV, while oxygen in hydroxyl groups present in the form of impurities induces the small shoulder at higher energy. The composition was found to be oxygen deficient with 60% of oxygen and 40% of titanium, while the stoichiometric composition should be 66.7% oxygen and 33.3% titanium [135].

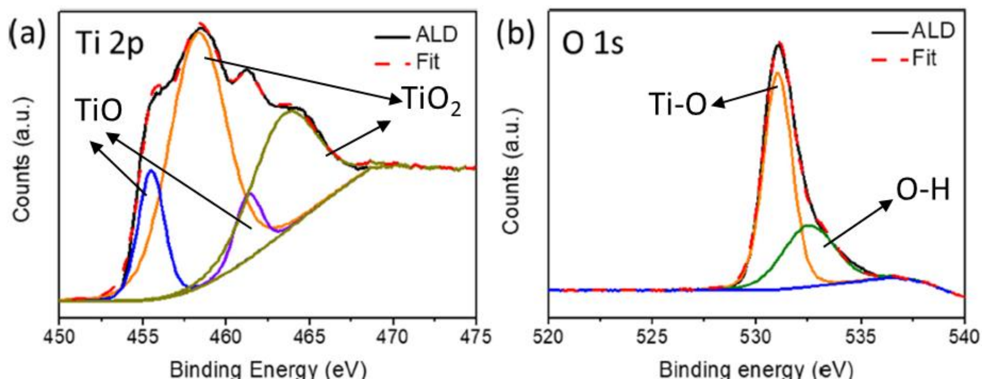

Figure 46: XPS spectra for ALD TiO2 (a) Ti 2p and (b) O 1s [135].

For ZrO_2, high resolution regional scans were also carried out for zirconium, oxygen, and carbon (*Figure 47*). No peak was observed in the high resolution scan for the element carbon, indicating a nearly carbon-free ALD deposition. The high-resolution spectra of Zr 3d showed two peaks at binding energy 182 eV and 184 eV, corresponding to Zr $3d_{5/2}$ and Zr $3d_{3/2}$, respectively. The scan conducted for O 1s showed a peak at 530 eV, which belongs to ZrO_2, and the shoulder on the higher energy side is due to the oxidation of metal in air forming ZrO. The quantification calculation using CASAXPS software showed a composition of 40% Zr and 60% O, indicating an oxygen deficient zirconia thin film [135].

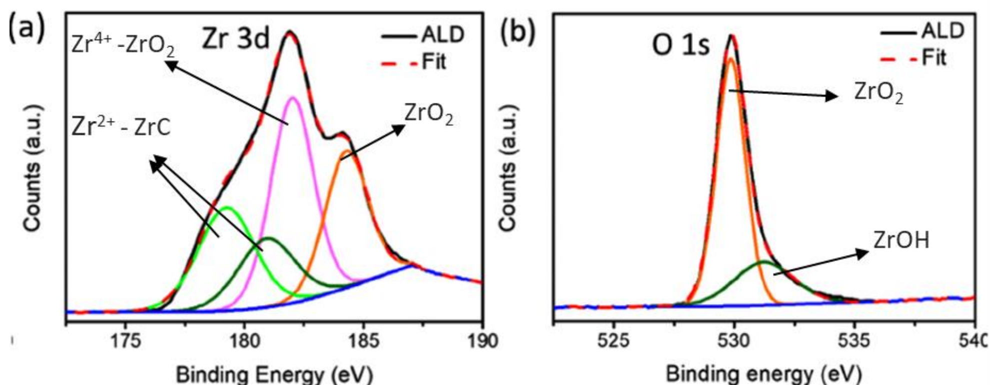

Figure 47: XPS spectra for ALD deposited ZrO2 (a) Zr 3d and (b) O 1s [135].

For HfO_2, high resolution regional scans for hafnium and oxygen were conducted (*Figure 48*). An ideal deposition without any contaminants was highlighted by the negligible amount of carbon detected. The core level spectra of O 1s associated with HfO_2 showed a shoulder at higher energy above the peak at 531 eV due to the presence of a small amount of contamination, likely carbon or moisture. In the regional scan of element Hf 4f, peak positions at 18.5 eV and 20.7 eV correspond to Hf $4f_{7/2}$ and Hf $4f_{5/2}$ in HfO_2 [153]. The shoulders at lower energies below 18.5 eV are due to Hf interstitials and oxygen vacancies. Again, the deposition was observed to be oxygen deficient, with a composition of 63% oxygen and 37% hafnium, while the stoichiometric composition of HfO_2 should have Hf and O in 1:2 ratio i.e. 66.7% oxygen and 33.3% hafnium [135].

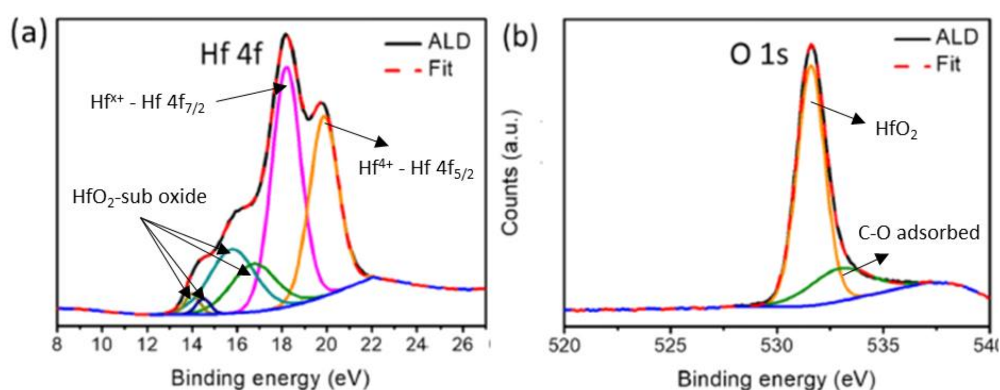

Figure 48: XPS spectra of ALD deposited HfO_2 (a) HF 4f and (b) O 1s [135].

4.5.3 Summary

In this work, the impact of a 100 nm thick TiO_2, ZrO_2, and HfO_2 atomic layer deposition (ALD) coating on both the corrosion behavior and cytotoxicity of the AZ31 magnesium alloy was studied. Results revealed ALD TiO_2 coating led to a notable improvement in the corrosion performance of AZ31 alloy, while ZrO_2 and HfO_2 ALD coatings demonstrated even higher corrosion resistance. This superior performance can be attributed to the coatings lower wettability [154], greater electrochemical stability [155], and superior surface integrity characterized by fewer cracks and pores (Figure 49).

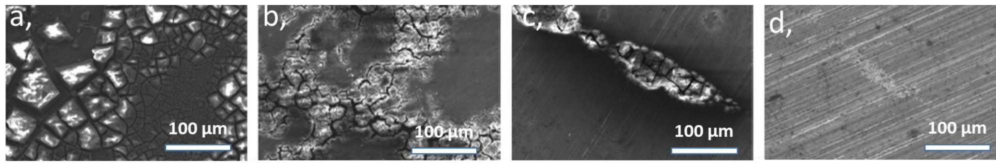

Figure 49: Micro-morphologies of (a) bare, (b) TiO_2, (c) ZrO_2, and (d), HfO_2 coated samples after corrosion [135].

Moreover, the enhanced corrosion resistance imparted by these coatings contributed to improved cytotoxicity performance of the AZ31 alloy [135]. Cytotoxicity was evaluated using the MTS cell proliferation assay (Promega) with L929 murine fibroblasts. The application of these coatings effectively mitigated the pH increase associated with the uncoated alloy. Specifically, the pH was reduced by 15.5% when a 100 nm ALD TiO_2 coating was applied. Even greater enhancements were achieved when ZrO_2 and, particularly, HfO_2 were employed: the former resulted in a pH reduction of 27.1%, while the latter led to an impressive reduction of 29.7% [135].

Figure 50 provides a visual representation of the macro-morphologies of coated samples both before and after a one-day immersion in SBF, with the uncoated AZ31 sample serving as a control. The figure illustrates the corrosion-reducing effects of the coatings. Notably, in the case of HfO_2-coated samples, corrosion damage became nearly non-existent. The extensively corroded surface observed on the bare samples, marked by the presence of pits, was notably reduced by the application of a TiO_2 layer. In the macro-morphologies of ZrO2-coated samples, there was scarcely any observable corrosion, save for some small areas of corrosion in the center, revealed more prominently in micro-morphological analysis. While the macro-morphologies of HfO_2-coated samples appeared entirely free of corrosion, closer examination via micro-morphological analysis disclosed the presence of small areas where early-stage corrosion products were forming [135].

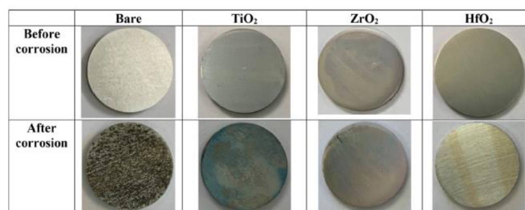

Figure 50:Macro-morphologies of bare, TiO_2 , ZrO_2 and HfO_2 coated samples before and after corrosion [135].

The average corrosion potential (E_{corr}) and corrosion current density (i_{corr}) values for both uncoated and coated samples were extracted from the potentiodynamic polarization curves and are presented in Table 8. Notably, the presence of coatings significantly enhances the material's corrosion resistance. Specifically, the HfO_2 coating stands out, exhibiting the lowest corrosion current density, which is only half of that offered by ZrO_2 and a 40 times lower than that of TiO_2 [135].

Table 8: Corrosion potentials (E_{corr}) and corrosion current densities (i_{corr}) values for bare and coated samples [135].

	Bare	TiO_2 coating	ZrO_2 coating	HfO_2 coating
E_{corr} (V)	-2.0 ± 0.02	-1.90 ± 0.01	-2.02 ± 0.01	-2.09 ± 0.02
i_{corr} (A/cm^2)	$3.0\ 10^{-3} \pm 0.4$	$24.9\ 10^{-6} \pm 0.6$	$1.2\ 10^{-6} \pm 0.3$	$0.6\ 10^{-6} \pm 0.4$

The hydrogen evolution test (*Figure 51*) clearly demonstrates the protective effect of the coatings on AZ31 alloy. Notably, after 7 days, the amount of hydrogen evolved from the uncoated samples is reduced by 52% when a 100 nm ALD TiO_2 coating is applied. Even more significant enhancements were achieved when employing ZrO_2 and, especially, HfO_2: the former results in a 92.5% reduction in hydrogen evolution, while the latter achieves an impressive reduction of 95% [135].

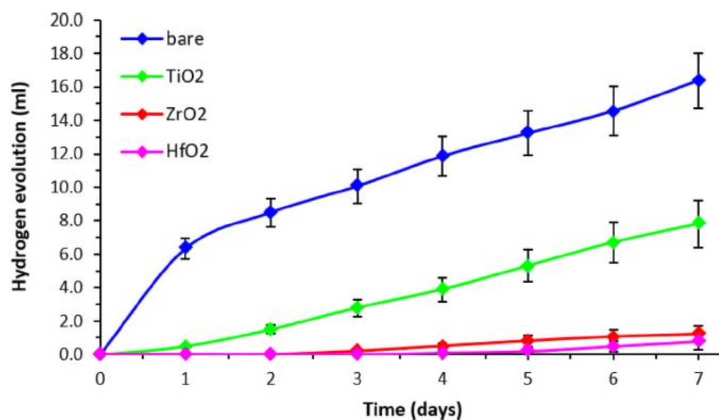

Figure 51: Hydrogen evolved from the immersion of bare and coated AZ31 alloy in SBF [135].

This page is intentionally left blank

5. Chapter 5: Experimental study – ALD of Cu as a catalyst for oxygen evolution reaction (OER)

This chapter investigates the use of atomic layer deposition (ALD) of copper on high surface area 3D structures as a catalyst for the oxygen evolution reaction (OER). A comprehensive set of results for this chapter can be found in the research article 6 (manuscript) included in the appendix.

5.1 Background

Water splitting, which converts water into chemical energy, is an important reaction that has been identified as a potential solution to the world's energy crisis and is crucial for enabling hydrogen-based renewable energy technologies [156]. However, the anodic oxygen evolution reaction (OER) involved in the process is complex and slow [30], requiring high-energy inputs, and effective and efficient catalysts are needed for large-scale implementation [157]. Currently, noble metal-based catalysts like RuO_2, IrO_2, and Pt have high OER performance but are limited by their high cost and limited material availability [31].

As a solution, researchers are exploring copper-based catalysts, which have gained attention in recent years due to their low cost, low toxicity, high strength, and resistance to erosion and abrasion compared to other transition metals [32]. Among copper-based catalysts, oxides, hydroxides, sulfides, selenides, tellurides, and phosphides are being studied, with each type having its own advantages and limitations. Copper oxides are particularly advantageous due to their simplicity and abundance in the earth's crust, which is critical for large-scale implementation. They also have a well-defined coordination chemistry and remain stable at high potentials, unlike other compounds that can undergo chemical transformation, affecting their chemical activity[158].

5.2 Experimental

Cu was deposited on Ti and Ni mesh (thickness 500 µm) with consistent diameters (~Ti: 30 µm and ~Ni: 35µm) and high porosity, giving us a high surface area substrate. The mesh was purchased from BEKAERT, Belgium, the porosity of Ti and Ni mesh was 56% and 66% respectively.

A custom-built ALD system was employed for depositing copper islands, utilizing nitrogen (AGA 5.0) as a carrier gas for the copper precursor. *Figure 52* describes the design of the ALD system. The ALD reactor used in this system was similar to the one utilized for *in situ* XAS studies of copper, with the exception of gate valve and optical window replacement by blank flanges. The base pressure of the system was 20 mtorr. The solid precursor copper(II) acetylacetonate ($Cu(acac)_2$) was sourced from Gelest (USA). The sublimation of $Cu(acac)_2$ was carried out at 145°C, with high purity molecular hydrogen produced on demand by using a generator from Peak Scientific (Scotland, UK) serving as the co-reactant.

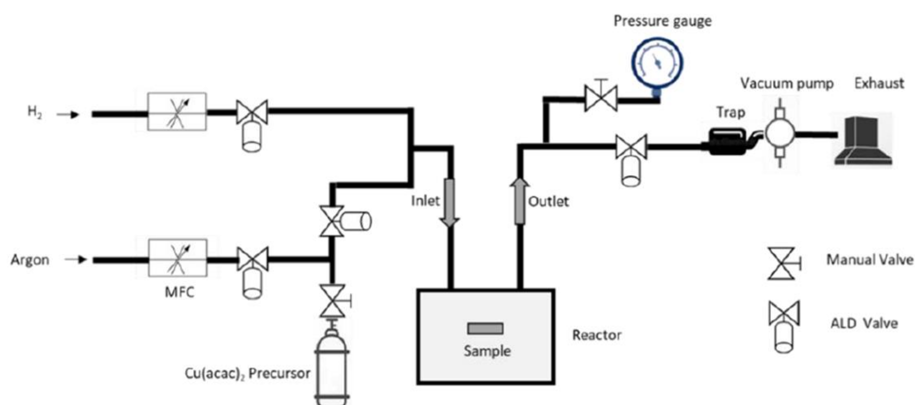

Figure 52: Schematic of the ALD system design used for the ALD deposition of Cu.

The deposition of Cu islands is performed through successive cyclic reactions between $Cu(acac)_2$ and H_2 at 245 °C, the substrate is directly mounted above the ceramic cartridge heater. Each ALD cycle is composed of two parts. The first part consists of a 5 s copper precursor boost [159] using Ar gas flowing at 200 sccm, which is an effective strategy to deliver low vapour pressure precursors. This is followed by precursor pulse of 3 s under exposure mode with the exhaust valve closed, which allows more time for the precursor to react with the substrate surface [160]. Finally sytem evacuation is carried out for 10 s to

complete the first step . The second part consists of a 5 s H_2 pulse under exposure mode followed by a similar system evacuation.

The reaction mechanism of ALD Cu, utilizing $Cu(acac)_2$ and H_2, is anticipated to follow a conventional redox reaction [161]. In this mechanism, "M" represents the substrate which is metal surface, "g" and "s" indicates the gaseous solid state's respectively as shown in eq. 30 and eq.31.

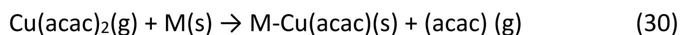

$$Cu(acac)_2(g) + M(s) \rightarrow M\text{-}Cu(acac)(s) + (acac)\ (g) \quad (30)$$

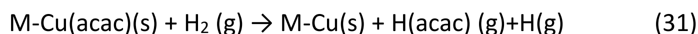

$$M\text{-}Cu(acac)(s) + H_2\ (g) \rightarrow M\text{-}Cu(s) + H(acac)\ (g) + H(g) \quad (31)$$

This equation elucidates the transition of $Cu(acac)_2$ in the gaseous state reacting intially with the metal surface and thus breaking down half of the attached precursor ligand. In the subsequent H_2 pulse, the remaning acac ligand attached to the surface via the metal centre is removed to form solid copper (M) along with the production of gaseous H(acac) and atomic H.

This reaction can also be comprehended through the following schematic representation (*Figure* 53):

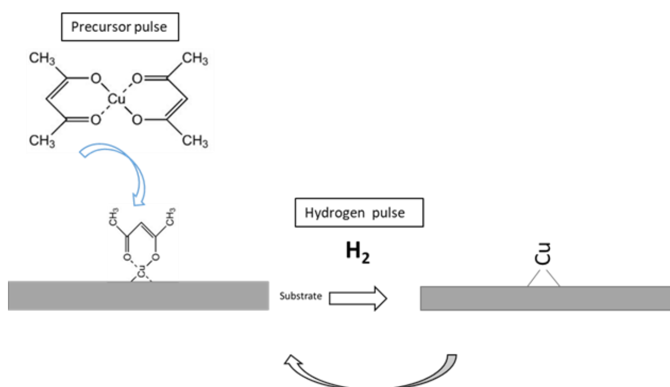

Figure 53: Schematic representation of the reaction mechanism of thermal ALD of Cu using $Cu(acac)_2$ and H_2

5.3 Results and discussion

The ALD deposition of Cu on Ti Mesh is in the form of islands, it is found that with the increase in the number of cycles the size of the island increased (*Figure 54* (a-c)). This type of growth behavior of Cu on TiO_2 has been described before as self-limiting island growth [162]. The

island growth behavior is typically observed in ALD of metals and is a result of agglomeration [163]. Copper is known for its tendency to agglomerate or form clusters. The precursor molecules may adsorb and diffuse to form clusters before reaching adjacent sites, contributing to island growth. Theoretical study conducted on the Cu agglomeration [164] has shown formation of copper clusters on the WN(001) surface which is energetically favorable, and the energy barriers for this cluster formation are not very high. It implies that the copper atoms on the substrate have a tendency to group together and form clusters rather than spreading out evenly to create a conformal monolayer. In other words, the natural preference of copper atoms on this specific substrate is to aggregate into clusters rather than forming a smooth, continuous monolayer. Thus, the tendency for copper to form clusters is in competition with the formation of a uniform monolayer, and the formation of clusters is the more competitive process. Furthermore, investigations have shown that surface defects or roughness play a role in promoting the preferential nucleation of copper islands in these areas [162].

The average diameter of the Cu islands is 10 nm, 24 nm, and 54 nm for 100, 500, and 1500 cycles respectively. Whereas in the case of Ni Mesh, the growth is seen in the form of clusters of Cu (*Figure 54* (d-f)) with much bigger islands representing a collection of Cu particles very close to each other. Visibly, the surface coverage of ALD Cu is higher on Ni mesh when compared to Ti mesh.

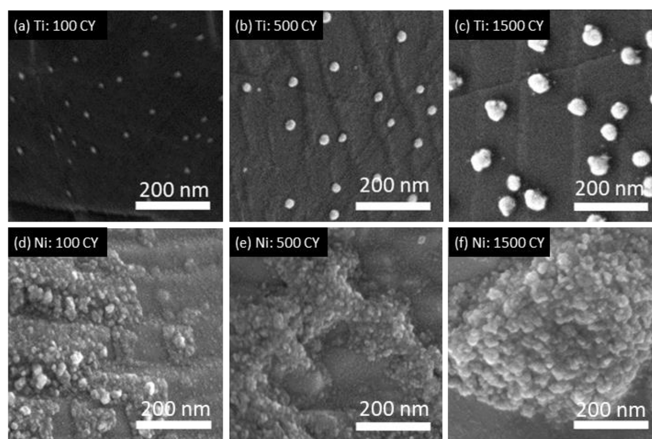

Figure 54: SEM images of the ALD deposited Cu for different numbers of cycles showing separate island Ti (a-c) mesh as compared to cluster formation on Ni (d-f) mesh.

The results of the electrochemical OER performance in terms of onset potential and potential required to reach 10 mA cm^{-2} for Ni and Ti substrates coated with ALD Cu for different number of cycles is presented in *Figure 55*. *Figure 55* (a) shows the linear sweep voltammetry of ALD Cu coated Ti substrates and reveals that the Ti substrate with 500 cycles showed the best performance compared to the bare Ti substrate. The island density was found to be related to the OER performance; with the sample having 500 ALD Cu cycles and the highest Cu Island density (58 islands per μm^2) performing the best with an overpotential of 345 mV among the different Ti mesh samples. The other two samples with 100 and 1500 cycles performed lower but had approximately similar island density and OER performance. It is noteworthy that the Ti mesh with no Cu deposition performed slightly better than the samples with 100 and 1500 ALD Cu cycles. This indicates that a lower number of Cu islands 36 and 39 per μm^2 (100 and 1500 cycles respectively) lowers the OER performance indicating a possible synergistic effects [165] as seen in other transition metal oxide combinations [166]. Additionally, transition metal oxide-based catalysts on Ti substrates have exhibited surface deactivation and stability loss due to mixed mechanisms [166]. Firstly, there could be catalyst dissolution and detachment, which results in a rapid change in catalyst performance. Moreover, the gradual formation of a thicker oxide layer can lead to the loss of electrical conductivity, hindering performance in the form of surface passivation. Lastly, a change in surface chemical composition can have an adverse effect on the catalyst's performance [167]. It might be interesting to note here, the native oxide layer on Ni mesh should be less than 0.8 nm [168], whereas a comparatively thicker native oxide layer is expected on the Ti (thickness of native TiO_2 ~10 nm [169]).

For Ni substrates with ALD Cu, *Figure 55* (b) shows the linear sweep voltammetry data. The best performance was observed in the Ni substrate coated with 1500 cycles, with a trend of improved OER performance in terms of lower overpotential with increasing number of ALD Cu deposition cycles. However, it was also noted that the bare Ni mesh performed similarly to the best-performing ALD Cu on Ni mesh sample.

In *Figure 55* (c), the potentials at a current density of 10 mA cm^{-2} were evaluated. Overpotential, which is the standard metric used for water splitting studies and calculated as $\eta = E_{vsRHE} - 1.23$, is measured at 10 mA cm^{-2}. Results showed that the Ni mesh samples performed better than the Ti substrates, interestingly with the lowest overpotential of 320

mV recorded for both the pristine Ni mesh and Ni mesh with 1500 cycles of ALD Cu. The Ni substrate with 100 and 500 cycles of ALD Cu had an overpotential of 390 and 370 mV respectively.

In order to investigate the effect of the number of ALD Cu cycles on the Ni mesh substrates, we studied the ALD Cu nucleation and growth using SEM images (*Figure 54*). The results showed that the nucleation of ALD Cu was observed throughout the surface even with lowest deposition cycles. However, with the increase in cycles formation of Cu clusters was observed with an increasing size. The size of the Cu clusters increased, ranging from 30-60 nm for 100 cycles, 200-300 nm for 500 cycles, and 400-600 nm for 1500 cycles. It was observed that the surface area on Ni mesh is higher with 1500 ALD Cu cycles due to the presence of larger clusters with a higher number of particles, followed by 500 and 100 ALD Cu cycles samples. For an approximation, assuming the islands are hemispheres and are uniformly distributed ALD Cu hemispheres on Ni surface the surface area of Cu per μm^2 is evaluated as 1.53, 1.57, and 1.57 μm^2 for 100, 500, and 1500 cycles, respectively. A recent study [170] discusses the correlation between the OER performance of Cu catalysts and their structural forms, indicating that the presence of Cu nanoclusters enhances the catalyst performance. It is possible that the increase in Cu loading and surface area with the number of deposition cycles along with better adhesion when compared on Ti mesh could explain why the 1500 cycles sample exhibited better performance compared with lower numbers of cycles.

Furthermore, our observations also revealed that there was similar performance between the pristine Ni mesh and the Ni mesh with 1500 cycles of ALD Cu. This can be a result of the formation of $Ni(OH)_2$ on the pristine Ni surface. Previous studies have shown that $Ni(OH)_2$ enhances OER activity [171]. When pristine Ni is immersed in an alkaline media, such as 1M KOH, it immediately forms a layer of $Ni(OH)_2$ above the NiO layer. These layers tend to grow with increasing electrochemical cycles, resulting in increased surface roughness and increased electrochemically active sites. Therefore, the formation of $Ni(OH)_2$ on the pristine Ni surface may explain why it exhibited similar OER activity to the Ni mesh with 1500 cycles of ALD Cu.

For the Ti mesh samples, the best performance was achieved by the substrate coated with 500 cycles of ALD Cu, with an overpotential of 345 mV. In comparison, the pristine Ti mesh, 100 cycles Cu, and 1500 cycles Cu sample had overpotentials of 490 mV, 550 mV, and 540 mV respectively.

SEM images (*Figure 54* (a-c)) of Ti mesh samples showed that the ALD growth of Cu resulted in island formation. With an increase in the number of Cu deposition cycles (100, 500, and 1500), the size of the islands increased. The average size of the islands in terms of diameter was 10 nm, 24 nm, and 54 nm for 100, 500, and 1500 cycles, respectively. The Cu island density was 36, 58, and 39 particles/islands per μm^2 for 100, 500, and 1500 cycles, respectively. The number of islands increased from 100 cycles to 500 cycles, but decreased with 1500 cycles, possibly due to coalescence of smaller islands to form larger ones.

The island density was found to be related to the OER performance, with the sample having 500 ALD Cu cycles and the highest Cu island density (58 islands per μm^2) performing the best with an overpotential of 345 mV among the different Ti mesh samples. The other two samples with 100 and 1500 cycles performed lower, but had similar island density and OER performance. It is noteworthy that the Ti mesh with no Cu deposition performed better than the samples with 100 and 1500 ALD Cu cycles. This indicates that a lower number of Cu islands 36 and 39 per μm^2 (100 and 1500 cycles respectively, poor surface adhesion of the islands and in addition to blocking the active sites on the pristine Ti mesh substrate, lowers the OER performance.

When we compare the OER performance of our samples with catalyst to similar mesh designs, foils or other 3D structures, the results are found to be comparable to literature values. For example, Ni foams underwent electro oxidation to yield a NiO_x/Ni type surface, which resulted in an OER overpotential of 390 mV (j = 10 mA cm^{-2}) along with high stability (20000 sec in 1 M KOH) [172]. The high stability was linked to interface effect of NiO_x/Ni, where the interface enhances the intrinsic catalytic activity and stability by optimizing the surface atomic and chemical structures [173]. Similarly, the OER activity of cobalt sulphite nano-sheets electrodeposited on Ti foil required an overpotential of 361 mV to achieve a current density of j = 10 mA cm^{-2} [174].

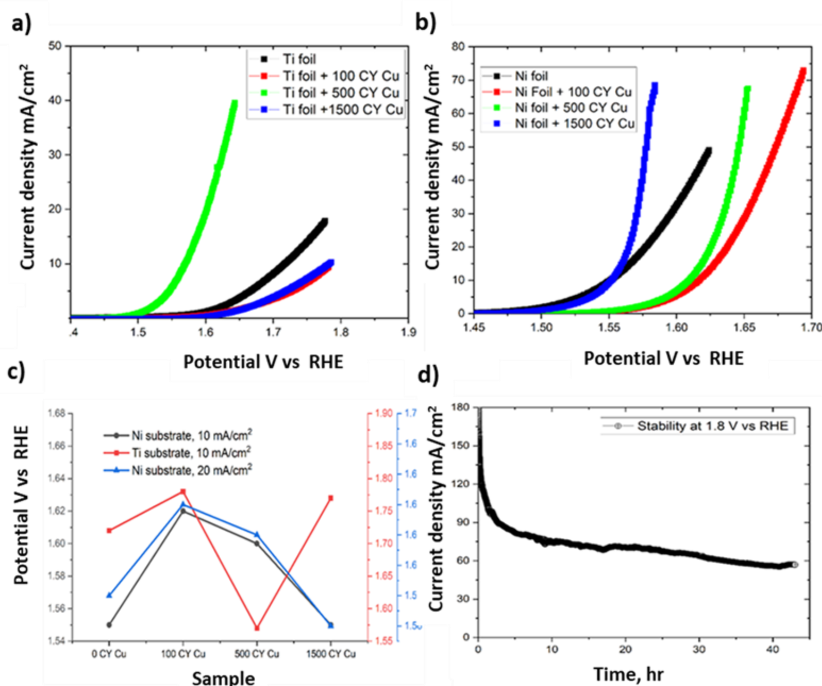

Figure 55: OER performance of different Cu coated and pristine sample Ti and Ni mesh samples in 1 M KOH, (a) and (b) Linear sweep voltammogram of the oxygen evaluation reaction, (c) Potential at constant current densities for different samples, and (d) Stability test for Ni with 500 cycles of Cu.

The stability of the sample (Ni 500 ALD cycles of Cu) was evaluated for 43 hours in 1 M KOH at 1.8 V vs RHE, as shown in *Figure 55* (d). The catalyst showed a performance loss within the first 3 hours, indicating a possibility of detachment/dissolution of the catalyst coating. Also, dissolution of copper has also been reported in the case of a 30% nickel-copper alloy during the OER process [175], indicating a possible effect on adhesion behavior on Ni mesh substrates during extended durations.

In comparison with state of art of noble metal-free bifunctional catalysts [176] and other complex catalysts [177], the overpotential measured at 10 mA cm^{-2} for our ALD Cu coated Ni (1500 cycles) and Ti (1500 cycles) mesh samples are found to be 320 mV and 345 mV, respectively. In addition, there is less complexity involved in our case for the fabrication of islands on highly porous 3D substrates with the use of ALD. A recent review [178] on Cu based catalyst for OER helps us to compare performance in terms of overpotential required to achieve 10 mA cm^{-2} for OER. However, we argue that the preparation route for the catalyst fabrication presented here is facile i.e. striaghforward and implementable, requiring the

pristine substrate to undergo one automated deposition cycle only with no further processing. Also, with regards to the cost, the economic advantage of ALD over sputtering or CVD hinges on the specific context and application requirements. ALD demonstrates cost-effectiveness in scenarios where precision, uniformity, and the unique capabilities it offers for intricate 3D surfaces are essential. In such cases, ALD is often the sole feasible choice, given its unmatched ability to fulfill these requirements. Whereas, sputtering is favored for its higher deposition rates and with lower equipment costs, particularly when applied to flat substrates. Thus, the choice of the most economically viable method relies on the distinct demands of the application and the need to strike a balance between the factors at play.

It has to be noted, however, that the OER activity decreases faster than with the published counterparts, which we argue being a matter of poor adhesion. In future studies, the latter could be enhanced by increasing the process complexity through a removal of the surface oxide prior to the deposition, through a plasma cleaning process [179] or a wet chemical etching routine [180]. Further, a graphene conductive layer [181] or a variation in stoichiometry may be strategies to employ.

5.4 Summary

We investigated the potential of ALD Cu deposited on Ti and Ni mesh as cost-effective electrocatalysts for the oxygen evolution reaction (OER). Our results showed that Ni mesh substrates had lower overpotential than Ti substrates, with the lowest overpotential of 320 mV recorded for both pristine Ni mesh and Ni mesh with 1500 cycles of ALD Cu. The SEM images showed that an increase in Cu loading and surface area with the number of deposition cycles could explain the better performance of the Ni 1500 cycles sample. Moreover, the formation of $Ni(OH)_2$ on the pristine Ni surface may explain why it exhibited similar OER activity to the Ni mesh with 1500 cycles of ALD Cu. For Ti mesh substrates, the best performance was achieved by the substrate coated with 500 cycles of ALD Cu, with an overpotential of 345 mV. The island density of Cu was found to be related to the OER performance, with the sample having 500 ALD Cu cycles and the highest Cu island density performing the best. The Ti mesh with no Cu deposition performed better than the samples with 100 and 1500 ALD Cu cycles, indicating that a low presence of Cu islands along with poor surface adhesion could negatively affect the performance. The SEM and XPS analyses

provided insights into the surface morphology and oxidation state of the ALD Cu catalysts on both substrates, confirming the presence of CuO and Cu_2O. However, the durability test revealed limited adhesion of the best performing sample, with performance reduction observed within the first three hours. The SEM and EDS analysis of the adhesion test samples further revealed detachment and modifications of the ALD Cu layer indicating the need for further investigation to improve the adhesion and stability of the catalyst surface.

Furthermore, the overpotentials measured at 10 mA cm^{-2} for our ALD Cu coated Ni and Ti mesh samples are comparable to state-of-the-art noble metal-free bifunctional catalysts, and our approach offers less complexity in fabricating islands on highly porous 3D substrates with the use of ALD.

6. Chapter 6: Experimental study - Design of *in situ* ALD FTIR system

In this chapter, a summary of the design of an *in situ* FTIR system based on research article 7 [52] is provided. A comprehensive set of results for this chapter can be found in the research article 7 included in the appendix.

6.1 *In situ* FTIR

FTIR spectroscopy is a powerful tool for analysing the surface chemistry of materials. In *in situ* FTIR ALD, the FTIR instrument is integrated with the ALD reactor to allow for real-time analysis of film growth and surface chemistry during the deposition process.

The principle of ALD is based on exposing a substrate sequentially to two or more precursor gases, which react with the substrate surface to form a monolayer of the desired material. After each exposure, the substrate is purged with an inert gas to remove any unreacted precursor and reaction by-products. In *in situ* FTIR ALD, the FTIR spectrometer is used to analyse the surface species of the substrate before and after each precursor exposure. This allows for identification of the formation of the desired material and any unwanted by-products. This technique is especially useful in detecting surface organometallic species from the first reactant half-cycle and mapping out the ligand exchange reaction in subsequent half-cycles.

The flexibility of *in situ* ALD growth studies using infrared (IR) spectroscopy is a significant advantage as different sampling techniques such as transmission measurements, attenuated total reflection (ATR), and diffuse reflectance infrared Fourier transform spectroscopy (DRIFTS) can be used for various sample types including liquids, powders, gases, thin films, and solid surfaces [52].

FTIR offers several advantages as a characterization tool, including high signal-to-noise (S/N) ratio, low data-acquisition time, and flexibility in sample preparation. Additionally, FTIR systems are inexpensive and widely available in different labs [52].

6.2 State of the art

In situ ALD FTIR studies have been conducted using home-built reactors, which have demonstrated the potential to carry out *in situ* studies [182]. However, the system design of these reactors poses particular challenges that can have an impact on the ALD process and characterization capability. Previous studies have shown that the use of a cold-wall reactor is one such challenge, as it can lead to precursor condensation that is difficult to remove even with system purging [183]. Although a cold wall reactor may be suitable for certain processes using reactive precursors and chemistries at low temperatures, it can result in slow desorption of the precursor over time, creating a virtual leak that can react with the surface under study. To mitigate this issue, it is recommended to heat the reactor wall and design the reactor with the smallest volume possible, which would enable a comparatively more straightforward system evacuation, thereby reducing the possibility of CVD growth [184]. However, most reported ALD systems have been designed for multiple in situ characterization capabilities, resulting in large reactor volumes with multiple ports [52].

The contamination of optical windows in the IR beam path is another critical issue that needs to be addressed in ALD reactors since the windows must remain clean. If the precursor pulse is introduced into the reactor without covering the windows, it can result in the condensation of precursor molecules, contaminating the window surface [183]. Although this configuration has been used before, the contamination problem can be partly resolved by conducting a background measurement immediately before each pulse. However, even with this solution, the measured absorption spectrum can still be misleading as it will also consider the formation and removal of molecules on the window's surface, which can differ depending on the temperature difference between the window and substrate. To address this issue, gate valves must be used to shield the windows during the precursor pulse [52].

The integration of the reactor and characterization tool in in situ ALD systems has proven to be challenging. Typically, the IR source, detector, and ALD reactor are integrated using multiple mirrors in an optics compartment, adding complexity to the system design and

causing optical losses [121,184,185]. To avoid these issues, it is beneficial to directly integrate the ALD system with a FTIR spectrometer, eliminating the need for additional components [52].

However, even in situ ALD reactors with optical flanges on tubes for diagnostic access can pose problems due to stagnant volumes that result in the mixing of reactive gases, limiting the system's in situ characterization capability. To address this issue, the reactor should be designed with diagnostic access in the form of optical flanges directly on the reactor wall to avoid unwept volumes and ensure efficient evacuation [52].

In situ ALD FTIR studies require high sensitivity due to optical losses. Most previous studies have used mercury cadmium telluride (MCT) detectors, which have limitations such as a lower wavenumber limit of around 600 cm^{-1} and variations in response depending on the composition of the detector [186]. However, narrowband MCT detectors with higher sensitivity and a lower spectral window are commercially available, indicating that 600 cm^{-1} is not the absolute limit of MCT [52].

In contrast, the wide bandgap deuterated L-alanine doped triglycine sulfate (DTGS) detector used in this work can measure down to 30-50 cm^{-1}, but the use of KBr in the beam path limits the spectral range to 400 cm^{-1}. The DTGS detector offers higher stability and lower drift than MCTs, making it an ideal choice for capturing weak signals below 600 cm^{-1}. In this study, we aim to evaluate the *in situ* system's capability to track the chemistry during Al_2O_3 ALD half-cycles using the DTGS detector [187].

6.3 Design of *in situ* FTIR ALD system

In this section, a summary of the design and components of the *in situ* FTIR ALD system is provided (Figure 56). The reactor has a T-shape design with three flanges, CF-40 type, welded directly on the center T-piece. The center flange is for mounting the sample holder, and the other two flanges are for optical diagnostic purposes. The reactor body is made of stainless steel AISI304 and has a compact size with a small reactor volume for efficient precursor delivery and purging. Electrical heating tapes heat the reactor walls, and precursor gases are introduced through an inlet port on the front side of the reactor [52].

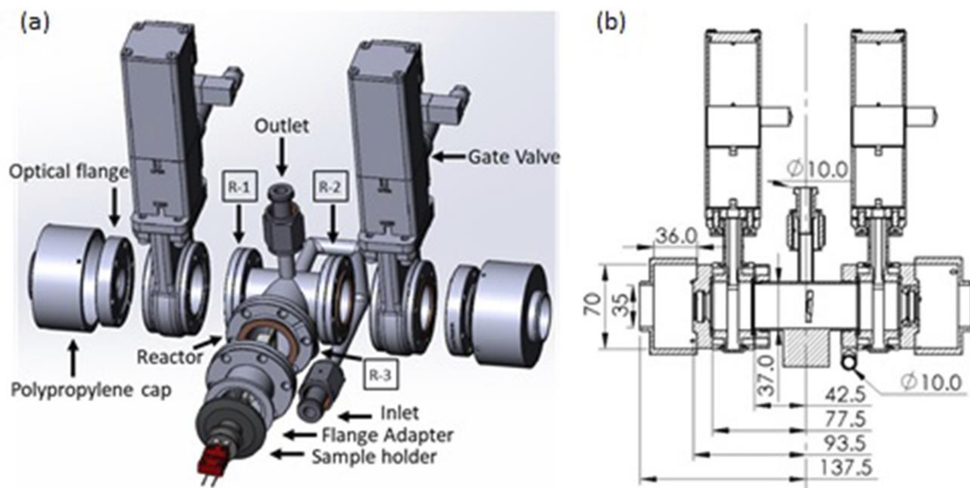

Figure 56: (a) 3D representation of the in situ ALD reactor, (b) front-view cross-sectional diagram of the ALD reactor (dimensions in mm).

The system's manifold is designed (*Figure 57*) with 316L stainless steel VCR components from Swagelok and is equipped with pneumatic controlled diaphragm valves, referred to as ALD valves, which are used for pulsing the precursors. The introduction of the carrier gas into the system is controlled by a mass flow controller from Alicat scientific. The manifold, inlet, and outlet are heated using electrical heating tapes from Omega Engineering [52].

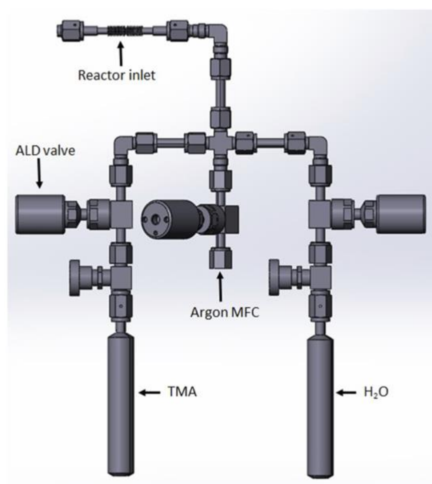

Figure 57: 3D representation of the manifold design with the ALD valves and precursor.

The sample holder assembly (*Figure 58*) is centered around a thermocouple feedthrough that consists of a ceramic holder, ceramic heater, and 316L Stainless steel (SS) sample holder. The sample holder is heated with a 20 mm x 20 mm x 2.5 mm advanced ceramic heater (Ultramic 600, Watlow) with a power rating of 200 W, mounted on a specially designed ceramic holder. The sample is mounted on the sample holder using SEM clips (Ted Pella), and a hole is drilled in the center of the sample holder to allow the infrared light beam to pass through, ensuring homogeneous heating of the sample [52].

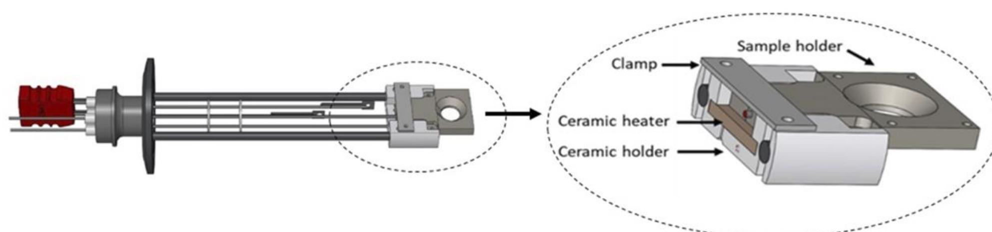

Figure 58: 3D representation of sample holder assembly.

The vacuum system uses an RV5 rotary vane vacuum pump from Edwards to achieve an ultimate pressure of 6 mtorr in the reactor system. A molecular sieve trap with zeolite particles is installed in the exhaust line to remove hydrocarbons, water vapor, and other gases from the outlet gas stream. A Pirani gauge from Pfeiffer vacuum is used to measure vacuum, and an ALD valve is installed to protect the pressure gauge during reactant pulse [52].

The control system comprises an Arduino Mega 2560 Rev.3 and a MOSFET shield, along with a custom Python-based software running on a PC for communication and control of the Arduino. The self-developed PC software provides systematic valve control, allowing users to load, edit, and execute ALD recipes [52].

6.4 Methods

6.4.1 Substrate selection for FTIR studies

The suitability of single-side polished p-type Si wafers as substrates for *in situ* ALD studies in transmission mode was assessed. The thickness of the silicon wafer was measured at 279 ± 25 µm. The reflectivity of p-polarised light has a characteristic minimum at the Brewster angle, which minimizes reflection losses in transmission geometry and ensures a well-defined polarisation of both reflected and transmitted beams. This increases the sensitivity to

absorption from adsorbed species. Our *ex situ* FTIR experiments revealed that for a p-Type Si (resistivity: 1-10 Ω cm, crystal orientation: <100>±1°) at normal incidence and Brewster angle, the absorbance of the observed peaks was similar (*Figure 59*). The two prominent peaks at ~1100 cm^{-1} and ~610 cm^{-1} are typically observed in the absorption spectra of silicon. However, using silicon as a substrate results in significant reflection losses of approximately 40%, due to its high refractive index with a complex refractive index of ~3.4 + *i*2.12e^{-7} (n+ *i*k) at wavelength of 3.333 µm (corresponds to 3000 cm^{-1}), where n is the refractive index and k is the extinction coefficient. In addition, free carrier absorption may contribute to sufficiently low wavenumbers. To minimize reflection losses, the IR transparent KBr, with a refractive index of ~1.5 and almost zero extinction coefficient in the IR light, was used as a substrate. Consequently, the reflection loss is minimized to approximately 10% at normal incidence [52].

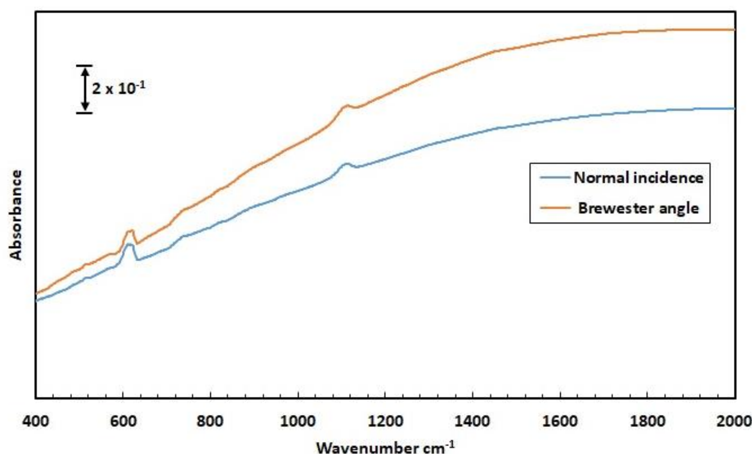

Figure 59: Absorbance spectra for Si at normal incidence vs. at Brewster angle with no sample as background [52].

6.4.2 Windows protection

In situ ALD spectroscopic studies rely on accurately tracking changes in absorption spectra, but contamination can lead to misleading data that is difficult to analyze. One common source of contamination is the condensation of precursor molecules on window surfaces during introduction into the reactor. Even conducting a background measurement before each pulse may not fully resolve this issue, as it also considers the formation and removal of molecules

on the window surface, and the reaction mechanism can be affected by different temperatures between the window and substrate [52].

To minimize window contamination, several strategies should be implemented. The first and most critical step is installing pneumatically controlled gate valves on the reactor, which close during the precursor and oxidant pulses to protect the windows. Reactor purging is also necessary, with at least 100 seconds of evacuation after the reactant pulse and prior to opening the gate valves, to prevent contamination from residual gases. Heating all vacuum components is another important step to avoid cold spots and desorption of molecules, which can cause contamination and shift ALD processes outside the self-limiting regime [52].

6.4.3 Detector for FTIR spectroscopy measurements

DTGS and MCT [186] detectors are commonly used in FTIR spectroscopy, each with its advantages and limitations. MCT detectors have a faster response time and higher sensitivity, making them useful for applications with low light intensity and weak absorption signals. However, MCT detectors are limited to a minimum wavenumber of 600 cm^{-1}, and detecting OH-related modes can be challenging due to ice condensation on the detector windows, which causes ice peaks to appear in the spectra. In contrast, DTGS detectors can detect wavenumbers down to the far-IR and are beneficial in detecting vibrational bands and coordination bonds in metal complexes. However, the available spectral range is often limited by the optical window materials used [52].

In *in situ* ALD FTIR studies, MCT [187] detectors are commonly used due to their high sensitivity requirements. However, the wide bandgap DTGS detector can measure down to 30-50 cm^{-1}, and its higher stability and lower drift make it a good alternative for capturing weak signals below 600 cm^{-1}[52].

6.5 Main results

In situ FTIR experiments were conducted to track the reaction mechanism. The first $Al(CH_3)_3$ (TMA) pulse, which is the first half-cycle, produced positive peaks at 3016 cm^{-1} and 1306 cm^{-1} (*Figure 60* (a)). These peaks indicate the presence of CH_4, which is formed as a reaction product during TMA adsorption. This behavior has been previously reported when excess TMA precursor was used and a gas phase IR spectrum was measured with the exhaust valve

closed. However, detecting the rotational-vibrational fine structure of the CH_4 spectrum in the absorption spectrum, specifically in the spectral region with the CH stretching modes (2800- 3000 cm^{-1}) of adsorbed methyl groups, was difficult [52].

After the subsequent H_2O pulse, the peaks flipped at the same position, indicating the removal of molecular species. With the second TMA pulse, the formation of peaks was observed and their removal with the next H_2O pulse confirmed the cyclic ALD process [178]. Negative peaks were observed from 1400 – 1800 cm^{-1} and 3500 – 3900 cm^{-1} after the first TMA pulse, explaining the presence of a rotationally resolved vibrational spectrum of water vapor. The presence of peaks from CO_2 (2300-2400 cm^{-1}) suggested that at least part of the water vapor contribution originated from residual atmospheric gases in the beam path and slight partial pressure differences between sample and reference measurements [52].

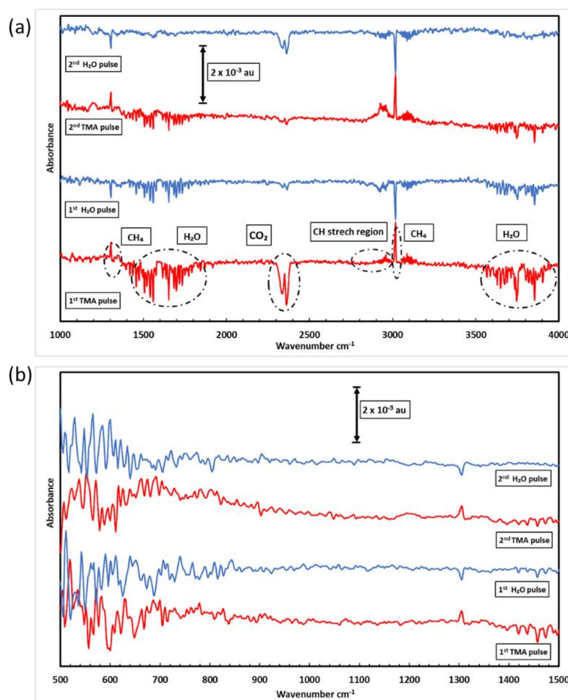

Figure 60: (a) Absorbance spectra (1000 - 4000 cm^{-1}) after 1st, 2nd TMA, and water pulse, respectively, with 5 nm Si/KBr substrate as background for 1st TMA pulse measurement. Previous measurements are the background for remaining subsequent measurements (b) Absorbance spectra from (500-1500 cm^{-1}) [52].

6.6 Summary

An *in situ* ALD-FTIR system is developed within an existing FTIR characterization instrument. The approach employs a mechanical design suitable for most conventional spectroscopy compartments, which has been successfully validated in a Bruker Vertex 80 FTIR spectrometer. Off-the-shelf electronic equipment, vacuum components, and electric heaters were employed, but a specially designed sample holder was used to ensure uniform substrate heating. This holder allowed us to use a 4 mm thick KBr disc with sputtered 5 nm Si as a substrate, which increased the IR transmissivity compared to a conventional p-doped Si wafer [52].

Insights on the significance of purging and proper vacuum base level are provided to establish self-limiting ALD conditions, which is essential for studying the nucleation chemistry. The reactor windows are successfully shielded from cross-contamination using pneumatic gate valves, uniform reactor heating, and an extended argon purge of the system. It is suggested that an argon window shield and a turbopump could provide further protection and reduced purge time [52].

The MCT vs. DTGS detectors with *ex situ* studies are compared, to show how they can be instrumental in investigating metal complexes during the early stages of ALD nucleation. Finally, the system's capability to conduct in-situ studies is demonstrated by successfully tracking the ligand exchange reaction for the ALD growth of Al_2O_3 using an FTIR spectrometer [52].

7. Chapter 7: Experimental study - Design of *in situ* ALD XAS system

This chapter focuses on the design of *in situ* X-ray absorption spectroscopy (XAS) system, as well as the initial *ex situ* experiments that were conducted to investigate the growth of atomic layer deposition (ALD) Cu. The *in situ* XAS system was designed and the first round of *in situ* experiments was carried out. However, the study could not yield conclusive results regarding ALD Cu growth due to some challenges, including beam alignment issues and limited beam time.

7.1 X-ray absorption spectroscopy

X-Ray absorption spectroscopy is an inner shell spectroscopy technique where the x-ray interacts predominantly with the deep core electrons [188]. The deep core electron moves to the unoccupied state above the fermi energy, resulting in a core hole. Subsequently, this causes the decay of higher electrons into the core hole, causing the emission of a photon. However, the decay of higher electrons can also cause the emission of Auger electrons.

The XAS spectra of any material are characterized by a sharp increase in absorption at specific photon energy, depending on the absorbing element. The sudden increase in absorption is defined as absorption edges related to the energy required to remove a deep core electron. *Figure 61* shows the absorption spectrum of iron-sulphur-lithium nanocomposite, a sharp rise in absorption can be seen at around 7100 eV; this is the energy required to remove an electron from 1s orbital; this is called iron K edge. The peaks and other features near or on edge are known as x-ray absorption near edge structure (XANES). The features above the edge in gradual oscillations are called extended X-Ray absorption fine structure (EXAFS). From the measured absorption spectra, deducing structural information is of most interest. However, directly obtaining information for an unknown material is not possible. In order to obtain information, the absorption spectrum of the most probable structures is theoretically

calculated and compared with the measured spectrum, thus systematically narrowing it down to a specific structure. After having a good idea about the structure, other properties like bond length, symmetry, and density of states can be obtained [128].

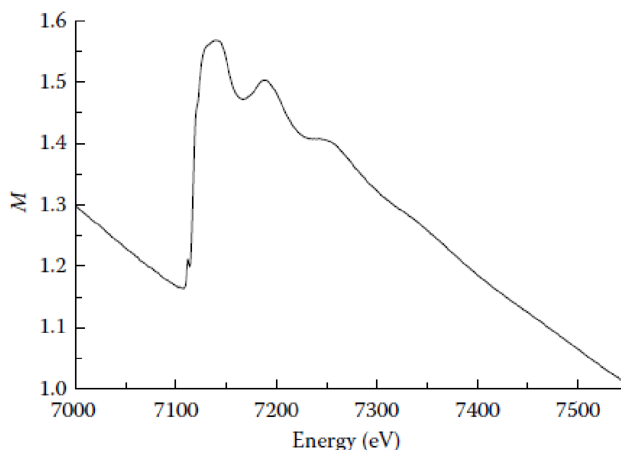

Figure 61: X-ray absorption spectrum of an electrode incorporating the iron–sulfur–lithium nanocomposite [128].

7.2 Why *in situ* XAS ALD

The fundamental question that arises when considering the merits of conducting *in situ* X-ray absorption spectroscopy (XAS) studies is why one would opt for such an approach when simpler and more readily available characterization techniques such as X-ray photoelectron spectroscopy (XPS), X-ray reflectivity, and scanning probe microscopy (SPM) are capable of providing atomic scale structural and chemical information. However, the use of these techniques for *in situ* atomic layer deposition (ALD) studies poses a significant challenge due to the requirement of high vacuum conditions for successful measurements. As the ALD process is carried out at low vacuum, a pressure gap emerges, necessitating the internal transfer of the sample from the reactor to a separate characterization compartment. This transfer can result in significant delays, leading to deviations from continuous ALD growth and making *in situ* XAS studies a more viable and informative alternative for examining ALD processes.

In situ X-ray absorption spectroscopy (XAS) studies during atomic layer deposition (ALD) can provide valuable insights into the chemical and electronic structure of thin films as they grow [48]. By analyzing changes in the XAS spectra at different stages of the ALD cycle, we can track the chemical evolution of the thin films and gain insights into the reaction mechanism and kinetics of the ALD process. Specifically, in situ XAS ALD studies can reveal the oxidation state of the metal in the thin film by measuring the energy and intensity of the metal K-edge absorption edge. Moreover, it can provide information about the coordination geometry of the metal atoms in the thin films by analyzing changes in the shape and intensity of the pre-edge feature in the XAS spectra. Furthermore, in situ XAS ALD studies can detect the presence of impurities or defects that can impact the optical, electrical, and mechanical properties of the films. Overall, in situ XAS ALD studies are a powerful tool for characterizing the chemical and structural properties of thin films, which can help optimize the ALD process and design functional materials for various applications.

In this study, our focus was on designing an in situ XAS ALD system to investigate the ALD growth of Cu, a process whose general principle is well-known, but the nucleation phase has not been explored experimentally due to the challenge of characterizing the minute quantities of material deposited in each half-cycle. However, synchrotron-based X-ray absorption techniques are capable of probing these small quantities of material and have already been used to gain valuable insights into the chemical, compositional, and structural evolution during the initial stages of metal and metal oxide ALD. In particular, X-ray absorption techniques have provided deep insights into these aspects of the ALD process, as demonstrated by previous studies [48].

7.3 State of the art

Designing an in situ XAS ALD system has several challenges that need to be carefully considered. One crucial aspect is the compatibility of the materials and components used in the system with synchrotron radiation. Materials that outgas or degrade under vacuum or radiation can contaminate the sample or beamline, and potentially damage the equipment. The small size of the sample and limited space in the measurement chamber make it challenging to achieve precise alignment and positioning of the sample relative to the X-ray beam. It is necessary to center and orient the sample correctly to ensure consistent and

reliable measurements. In addition to this, XAS measurements can be affected by various factors such as radiation damage and non-uniform sample heating, which can compromise the quality of the data. These factors need to be carefully controlled and calibrated to ensure accurate and reliable results.

Because of different challenges and limitations in system design, there is always a tradeoff while developing these systems. Although great progress has been made with the design of modular in situ ALD systems depending on the needs of the required process. For instance, a a successful portable and modular in situ XAS system was developed by Klug et al [189], with two separate reactor modules for measuring X-ray scattering, and for X-ray absorption spectroscopy (XAS). In the XAS reactor module the windows on the reactor module were constructed using 5 mil (0.127 mm) thick kapton tape which has a silicone adhesive layer with an adhesive thickness of 38.1 µm. Kapton tape may release volatile organic compounds (VOCs) at high temperatures, which can contaminate the substrate and adversely affect the ALD process. Additionally, some of the chemicals used in ALD may react with the Kapton tape and cause further contamination issues. In addition to this, Kapton tape may also be prone to degradation and may not withstand the high temperatures and reactive environments inside an ALD reactor. This can lead to particles being released into the reactor, which can again negatively affect the quality of the deposited films. The use of pnematically controlled gate valves along with beryllium windows will be a practical and effective approach.

Dendooven et al [190] designed a mobile setup for synchrotron-based in-situ Atomic Layer Deposition (ALD) studies. This system was capable of conducting both thermal and plasma-based processes and included mini gate valves that pneumatically controlled the beryllium windows. The ALD system, along with its components including the turbo pump, was mounted on a Huber tilt stage, a multi-axis positioning system commonly used in beamlines. The reactor's bottom flange was kept flat, and the distance from the sample to the baseplate was restricted to 170 mm, which limited the flexibility of the system for sample alignment. Despite this challenge, the system was designed for mounting stages, and the execution of experiments was problem-free. However, integrating this setup into synchrotron facilities where a goniometer controls incident angle and rotation, as seen in the case of the Stanford Synchrotron Radiation Lightsource (SSRL), could be challenging [127].

In situ ALD systems have been developed to be used at synchrotron facilities for various X-ray techniques, mainly due to the advantages these facilities offer. Synchrotron sources provide a higher photon flux compared to commercial X-ray tubes, resulting in a better signal-to-noise (S/N) ratio. Furthermore, synchrotron sources extend the available range of X-ray radiation beyond the typical 8.04 KeV (Cu Kα emission). Additionally, synchrotron facilities offer much larger instrument space compared to commercial X-ray systems. Although there is limited information available regarding the design and setup of *in situ* ALD X-ray Absorption Spectroscopy (XAS) systems, results obtained by studying different materials have been consistently reported in the literature [191]. While the limited literature is sufficient to understand the design of in-situ XAS systems, practical challenges associated with these complex experiments are difficult to predict and can only be fully understood during the execution of experiments within the limited time offered at synchrotron facilities.

7.4 Design of *in situ* XAS ALD system

The *in situ* XAS ALD system was specifically designed for conducting experiments at the Stanford synchrotron radiation lightsource (SSRL) facility. It's important to note that different facilities may have varying sample mounting procedures, and at SSRL a goniometer was utilized for this purpose.

7.4.1 System design

The reaction chamber was produced by welding together stainless steel AISI316L piping and readily available vacuum parts. Only two CF 40 connections were needed for the XAS study. The additional flanges enabled future use of the chamber for XRR and plasma-enhanced ALD studies.

7.4.2 Sample holder

The placement and alignment of the sample in the reaction chamber with respect to the characterization tool is critical. The perfect alignment of the reaction chamber and the characterization tool along the sample holder is the one which the highest measurement signal is attained. An adjustable sample holder was designed to achieve this, giving flexibility while setting up the system. The sample holder design is based on Kurt. J. Lesker vacuum

feedthrough, with two 8 mm stainless steel rods welded on. The substrate mounting arrangement is fixed to the rods using two grub screws. The rods and the screws give flexibility in adjusting the position of the sample holder in the lengthwise direction of the rods. The sample holder is made from aluminum with a diameter of 35 mm and a thickness of 11 mm. A rectangular slot is milled on the top to position the ceramic heater. Then, with the help of M3 bolts and stainless steel strips, the samples are fixed directly above the ceramic heater.

7.4.3 Optical windows

CF 16 flange beryllium windows were mounted on the X-ray beam inlet flange and the flange of the detector side. During the precursor pulse, the windows were protected with the help of gate valves. Beryllium material has a low mass absorption coefficient, thus resulting in high transmission of x-rays. The windows have an aperture of 13 mm and are designed and rated for vacuum conditions.

7.4.4 Support frame

The support frame helps reducing the direct load on the stage, which is not designed for carrying loads. This would allow the movement of the reactor chamber in XYZ directions with the help of the moving stage present in the beamline. The support frame helped integrating the reactor and the moving stage, allowing more flexibility during the sample alignment. In addition, a more precise adjustment control is provided, which is critical for low incidence setup.

The support frame was designed similarly to the gantry crane with three directional movements (*Figure 62*). Square extruded aluminum profiles of the required length were used for designing the frame. Linear guides were used for the movement in the X and Y direction. The air-bellow was used to move in the Z direction and carry the reactor load. The reactor was connected to a gantry plate through the air bellow. With the help of a pneumatic regulator, a constant output pressure was maintained. Thus, with the help of external pressure via the air below, the load on the stage could be negligible.

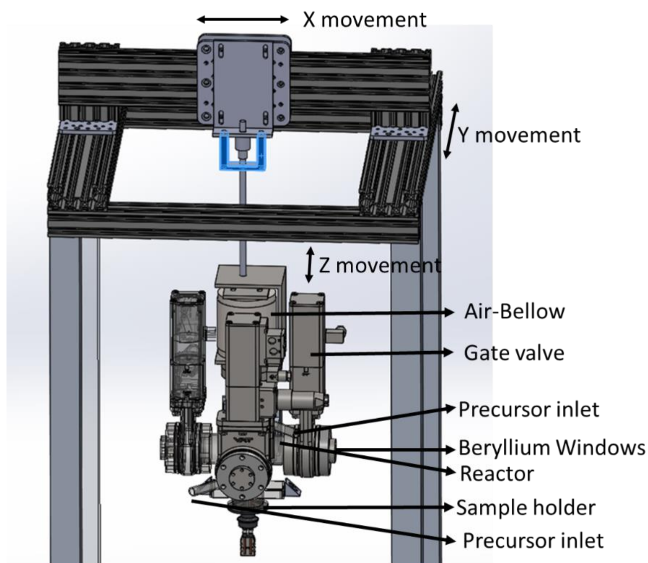

Figure 62: In situ XAS ALD reactor mounted on the support frame.

7.4.5 Beam allignment

The incoming X Rays were centered on the beam inlet flange. Similarly, the center of the detector was aligned with the centerline of the detector flange. The position of the sample holder was such that the sample surface was at the lowest point of the beryllium windows aperture. The sample holder on the rods was positioned such that the sample surface was parallel to the centerline of the beam inlet flange and the detector flange. The precise alignment was performed by moving the stage and positioning it with the help of a fluorescent strip and a camera. The alignment using the fluorescent strip and camera was impossible with beryllium windows; thus, for every sample alignment, the windows had to be switched to quartz windows.

7.4.6 System overview

The reactor, sample holder, and frame design are described in the previous sections. The overall setup and X-Ray beam direction are presented below in *Figure 63*. The other components of the ALD system, precursor, pressure gauge, heating, gate valves, and exhaust assembly, follow the same approach discussed in the FTIR design section.

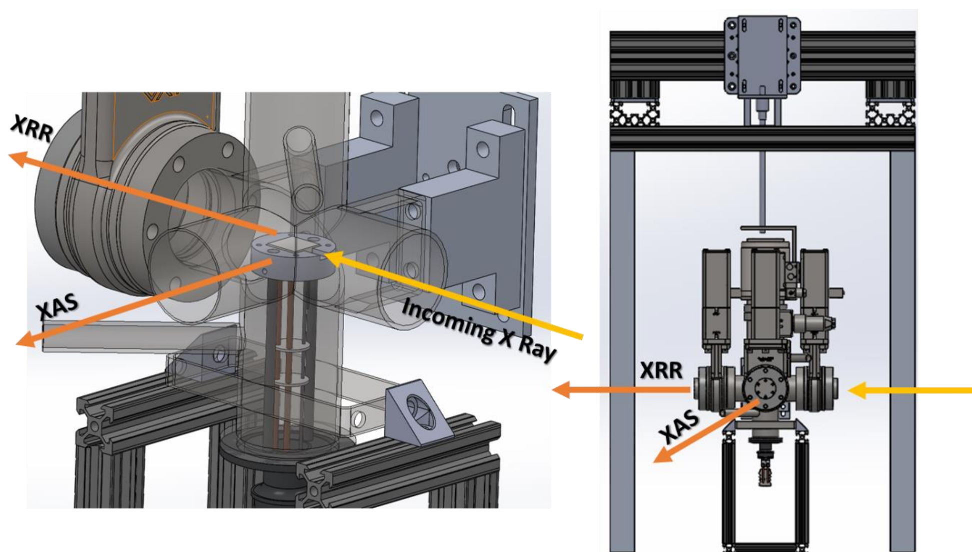

Figure 63: Overview of X-Ray Beam direction and sample position

7.5 Methods

7.5.1 Substrate preparation

In general, ALD Cu with different precursors on an arbitrary substrate has been a major challenge; there has been preferential growth on metallic surfaces such as Ti, Pt, and Ru. Thus, to study the growth process with *in situ* XAS, 100 nm thick Ti, Pt, and Ru substrates were prepared using e-beam evaporation and Magnetron sputtering on a Si wafer.

7.5.2 Cu precursor boosting

Due to the low vapour pressure of the $Cu(acac)_2$ Cu precursor [192], it becomes difficult to transport the precursor molecules from the cylinder to the reactor. The pressure can be increased by boosting the method. This is achieved by supplying the precursor cylinder with the inert gas for a set duration using a divert Valve and mass flow controller (MFC), as shown in *Figure 64*. This arrangement improves precursor vapor delivery into the reactor.

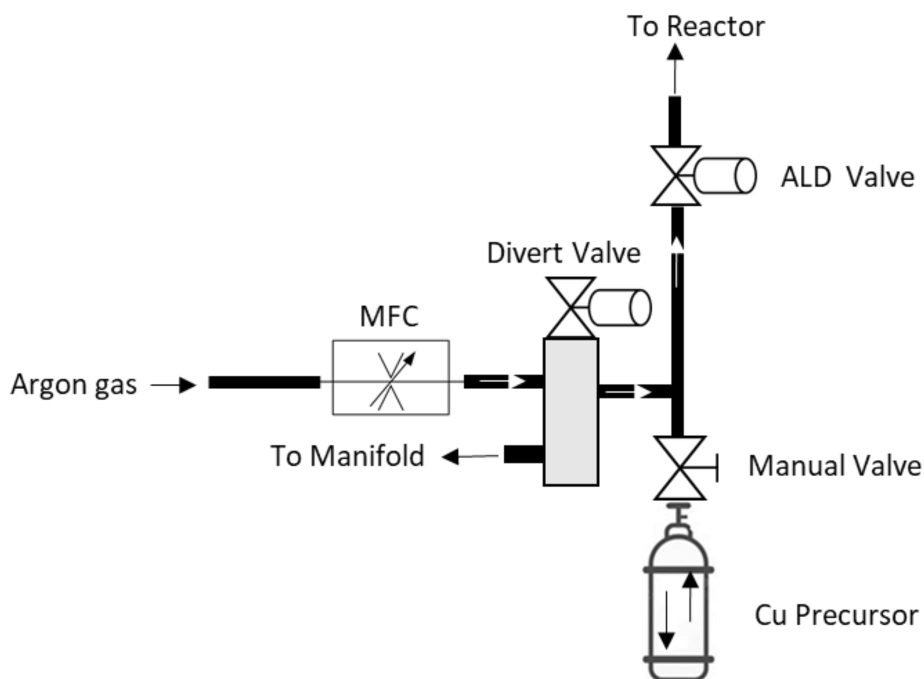

Figure 64: Precursor boosting setup for low vapour pressure precursors.

7.6 Experiment:

$Cu(acac)_2$ was used as the solid precursor for Cu deposition, which was purchased from Gelest. The precursor was sublimated at 145 °C, and H_2 was used as a co-reactant. Due to the low vapor pressure of the precursor, nitrogen (AGA 5.0) was used as a boosting gas to improve the precursor vaporization.

7.6.1 Preliminary *ex situ* experimental study

For the *ex situ* study of ALD Cu growth, a home-built ALD system was used. Nitrogen (AGA 5.0) was used as a boosting gas for the Cu precursor. The base pressure in the reactor was 20 x 10^{-3} torr under no pulse condition. The solid precursor $Cu(acac)_2$ was purchased from Gelest. The $Cu(acac)_2$ precursor was sublimated at 145 °C, while H_2 was used as a co-reactant. High purity Molecular H_2 was produced on demand by using an H_2 generator from Peak scientific.

7.6.2 *In situ* XAS characterization

To perform X-ray absorption studies, a custom-made in situ Atomic-Layer-Deposition (ALD) optical spectroscopy reactor was adapted for 20 x 30 mm samples (described earlier). The reactor consisted of a chamber mounted to two automatic gate valves oriented 90° relative to each other (VAT Vacuumvalves AG). One valve was mounted to the SLAC SSRL beamline, separating the chamber from the incident beam, and a passivated implanted planar silicon (PIPS) detector was fixed to the other valve. A pressure gauge was attached to monitor the chamber pressure, which was maintained at 2 x 10^{-3} torr during the deposition process.

The reactor was connected to a custom-made manifold via a flexible hose, which contained two precursors (H_2 and $Cu(acac)_2$) in 50 cm^3 stainless steel sample cylinders, as well as connections to the N_2 purge gas mass flow controller and the roughing pump. Pneumatic valves (Swagelok) were used for pulsing precursor vapor to the chamber and for separating pumping and purging. All devices could be actuated remotely without opening the hutch of beamline at the National Linear Accelerator Laboratory (Menlo Park, CA, USA).

To increase the vapor pressure of the Cu precursor, a boost setup with N_2 was used, and a ceramic heater plate with a built-in thermocouple (Watlow) was used for heating the substrates and controlling the deposition temperature. To ensure the integrity of the reactor, a rate of rise check was performed before the experiments, and the rate of rise was stable below 20 mtorr/min.

For X-ray absorption studies, an absorption spectrum revealing the chemical evolution of thin Cu films was planned to be taken after every half-cycle of ALD after opening the pneumatic valves. The deposition process involved pumping down the chamber to 10^{-3} torr, pulsing N_2 into the Cu canister to increase the vapor pressure, introducing precursor (H_2 or $Cu(acac)_2$ for each half-cycle, respectively), pumping down, opening gate valves, measuring XAS spectra, and repeating the process for the next half-cycles.

7.7 Results and discussion

7.7.1 Preliminary *ex situ* ALD Cu study

Prior to conducting in situ studies for Cu growth, preliminary growth experiments were conducted to develop the ALD process and confirm growth on various substrates. In the first part of this work, we performed a comparative study of Cu thin film ALD growth. This study investigated the dependence of nucleation and coverage on various parameters such as the type of substrate, number of ALD cycles, growth temperature, H_2 exposure time, and Ar gas flow during Cu precursor boosting. This not only provided insight into the growth mechanism but also helped in determining optimal process parameters and system conditions for the subsequent planned *in situ* XAS study.

7.7.1.1 Background

7.7.1.2 Literature: Nucleation and growth

The first reported ALD Cu process was conducted using cuprous chloride (CuCl), with Zn as a reducing agent [193]; Zn contamination from the co-reactant was detected in the thin film. In addition, the CuCl precursor was found to have low volatility and required a high temperature (>400 °C) for the thermal evaporation and transportation of the precursor. Later, the first metal-organic precursor was used, copper bis(2,2,6,6-tetramethyl-3,5- heptanedionate), $Cu(tmhd)_2$ [194] and subsequently another Cu (2) β-diketonate precursor, copper (II) (bis2,4-pentanedionate) $Cu(acac)_2$ [195] were studied. The β-diketonate precursors were generally found to have low vapour pressure and low reactivity with molecular hydrogen due to the strong Cu-O bond. As a result, a high substrate temperature was required resulting in rough deposition and contamination due to precursor decomposition. Another β-diketonate derivative, copper (II) hexafluoroacetylacetonate hydrate $Cu(hfac)_2{\cdot}x$H2O [196], which was earlier studied for CVD growth, had comparatively higher vapor pressure. However, during the ALD studies, the films were found to have considerable fluorine contamination. In the search for a reactive and higher vapor pressure precursor Cu (I) amidinate precursor, *N,N*'-di-*iso*-propylacetamidinato copper(I) [Cu(*i*Pr-amd)]2 [197] was studied; however, the deposition was found to be non-uniform on different substrates. A variant of amidinate precursor, copper (I) *N*,*N*' di-sec-butylacetamidinate, $Cu(Bu\text{-}amd)_2$ [198], was found to have a lower melting point, and it evaporated from the liquid state, thus giving a stable material flux as

compared to solid precursors which sublimate [199]. However, the growth was substrate dependent and was found to be uniform and conformal, only on metallic cobalt and ruthenium.

A summary of the most common ALD Cu processes is given below in Table 9. In addition, a detailed description of the physical properties of the Cu precursors can be found in reference [198], and a summary of the ALD Cu precursors and process can be found in reference [200].

Table 9: Different ALD Cu precursors and their characteristics.

Precursor	**Co-Reac.**	**Characteristics**	**Ref.**	**Year**
CuCl	Zn	Zn contamination, high process temp.	[193]	1997
$Cu(tmhd)_2$	H_2	Low vapour pressure and low reactivity	[194]	1998
$Cu(acac)_2$	H_2	High growth Temp.	[195]	1999
$Cu(hfac)_2$	H_2	Fluorine contamination	[196]	2000
$[Cu(i\text{Pr-amd})]_2$	H_2	Non-uniform growth, selective deposition, and contamination	[197]	2003
$Cu(Bu\text{-}amd)_2$	H_2	Substrate dependent growth	[198]	2006
$Cu(dmap)_2$	$ZnEt_2$	Not suitable for ultra-thin depositions (<5 nm)	[201]	2009

Specific processes have stringent requirements in terms of substrate temperature in order to grow ALD Cu at low temperatures (<150 °C), bis(dimethylamino-2-propoxy)copper(II), $Cu(dmap)_2$ with diethyl zinc ($ZnEt_2$) as a co-reactant was studied [201], but the process could not produce ultra-thin uniform Cu films below 5 nm.

For the selection of the ALD precursor, it should be thermally stable, reactive, and volatile. Cu β-diketonate precursors [201] are found to be stable and comparatively volatile when compared to other Cu precursors. Among Cu (I) and Cu(II) β-diketonate precursors, Cu(I) β-diketonate precursors tend to undergo disproportionation reaction [201], which is a major limitation for producing self-limiting ALD growth. Recently, renewed interest has been seen in utilizing $Cu(acac)_2$ [202], a Cu(II) β-diketonate precursor with different organic reducers [203]. This is due to broader theoretical [161] and experimental studies [204] on this type of

precursor compared to other precursor types [205]. However, despite the number of reports, understanding the growth process with different process parameters is not yet thoroughly explored.

7.7.1.3 Literature: Selective growth

The selective Cu growth has been evident from the earliest Cu CVD growth studies [206]; later, similar behavior was observed in ALD-grown thin films. ALD Cu growth studied by Jan-Otto Carlsson et al. [194] using Cu(II)-2,2,6,6-tetramethyl-3,5-heptanedionate Cu(tmhd)$_2$ showed selective growth on metallic platinum coated substrates and no growth was observed on glass and oxidized metal surfaces. In the case of Hydroxyl-terminated (OH) and oxidized metal surface, with the reaction of Cu(tmhd)$_2$ precursor, a strong bond is formed between copper and surface oxygen through which electron transfer is hindered, causing the precursor molecule to remain attached to the surface thus terminating further reaction steps. However, in the case of electron-rich metallic surfaces, the transfer of electrons to the adsorbed molecules helps activate the process, thus causing partial removal of the ligands.

7.7.1.4 *Ex situ* experimental study : Results and discussion

We studied the growth behavior of ALD Cu using Cu(acac)$_2$ precursor and Molecular H_2 on three different substrates, Ti, Si, and Ru. The nucleation and growth was found to be limited on n-doped Si, marginally better nucleation was observed on Ru, and among the three substrates, the best growth behavior in terms of nucleation was observed on Ti (*Figure 65*). The selective Cu growth has been evident from the earliest Cu CVD growth studies [206], similar behavior was also observed for ALD grown thin films. ALD Cu growth study [194] using Cu(II)-2,2,6,6-tetramethyl-3,5-heptanedionate Cu(tmhd)$_2$ showed selective growth on metallic platinum coated substrates and no growth was observed on glass and oxidized metal surfaces. It was reported that, in the case of Hydroxyl terminated (OH) and oxidized metal surface, with the reaction of Cu (tmhd)$_2$ precursor a strong bond is formed between Copper and surface Oxygen through which electron transfer is hindered, causing the precursor molecule to remain attached to the surface thus terminating further reaction steps. However, in the case of electron rich metallic surfaces, the transfer of electrons to the adsorbed molecules helps in activation of the ligand exchange process and thus causing partial removal of the ligands.

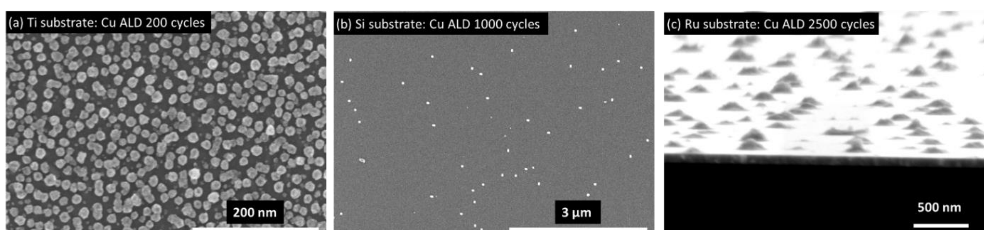

Figure 65: SEM micrographs of ALD Cu nucleation on (a) Ti, (b) Si, and (c) Ru substrates.

The growth process was studied for different number of cycles at the same process conditions (*Figure 66*), at lower number of cycles nucleation is in the form of uniformly distributed small particles, with the increase in the number of cycles formation of bigger islands is observed. With further increase in number of cycles, it results in coalescence of islands.

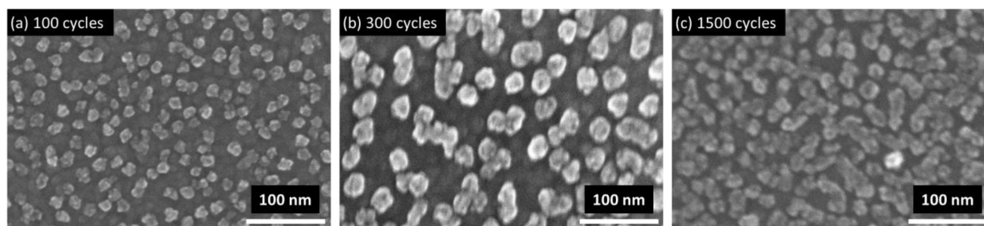

Figure 66: SEM micrographs of ALD Cu on Ti substrate with different number of cycles.

For the uniform and conformal growth of ALD Cu, island formation (*Figure 67*) due to coalescence has been a major challenge [195]. Here, for a fixed 1500 number of cycles, the effect of temperature on ALD Cu growth on Ti substrate's was studied. It is evident form SEM micrographs (*Figure 68*) at lower temperature of 180 °C, the grains are smaller and separated compared to sample at high temperatures. At lower temperature, nucleation looks denser but with a smaller grain size, this could be due to decreased reactivity of the precursor and co-reactant on the surface, thus limiting the growth rate. With the increase in temperature to 210 °C, a clear increase in grain size is observed along with larger separation, which is a typical behavior observed and relates to island coalescence [207]. The coarsening of the particle could be due movement of islands or particles over the substrate undergoing binary collisions resulting in liquid like coalescence of particles, or the other possible mechanism is transport of single atoms between the islands which is also referred as Ostwald Ripening [208]. Interestingly, with further increase in temperature to 245 °C, a connectivity between the islands is observed, this could be due to increased nucleation at this temperature followed

by coalescence phenomenon. The composite behavior, where with increase in temperature results in increase in nucleation and grain size has also been reported before for ALD of TiO_2 [209] .

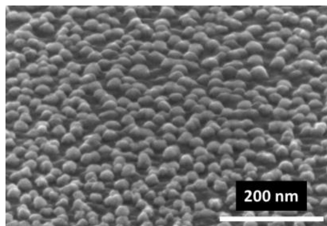

Figure 67: Island growth of ALD Cu on Ti substrate.

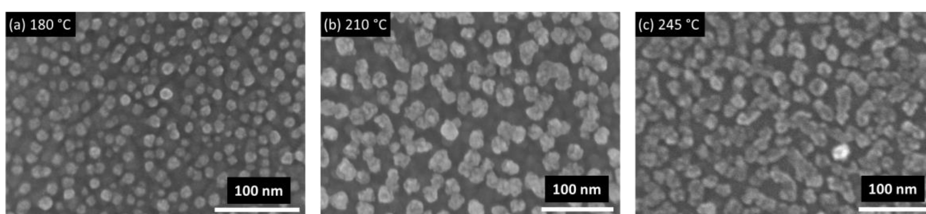

Figure 68: Studying the effect of substrate temperature of ALD Cu on Ti substrate.

The ALD growth behaviour was further investagted at different precursor and co-reactant exposure durations. Molecular H_2 was used as the reducing agent for the ALD of Cu**.** In the study of the effect of H_2 exposure, the ALD Cu surface coverage was found to decrease with increase in H_2 exposure (*Figure 69*). In general, molecular hydrogen is inert at lower temperature, thus it necessitates the use of high temperatures for the activation of hydrogen molecule, thus the substrate temperature was set constant at 245 °C. With the H_2 exposure of 5 seconds a comparatively higher nucleation and surface coverage was observed, with the increase in exposure time to 20 seconds, increase in grain size was seen along with decrease in surface coverage area. However, on further increase in H_2 exposure time smaller Cu grains were seen indicating reduce growth with Cu agglomeration. Molecular Hydrogen when in contact with metal surfaces homolytically dissociates to hydrogen adatoms [200]. The behavior of Hydrogen atom can be understood from the reactive molecular dynamic study (RMD) reported earlier by Thomas Gessner et al [161]. The atomic Hydrogen becomes reactive towards adsorbed $Cu(acac)_2$ precursor molecule, The Cu-O bond is broken between the Cu and the attached ligand. A $H_2(acac)$ molecule is formed, from which H_2O molecule is

released as a product along with ethane and acetone in gas phase. The H_2O molecule is expected re-adsorb itself on the surface. It is also possible the molecular Hydrogen forms Cu-H bonds as a temporary intermediate after the removal of precursor ligands [210]. Reduced grain size and reduced nucleation or inhibited growth could be due to the extended interaction of the reaction products formed after the initial H_2 exposure. The products formed after the H_2 pulse, and which re-adsorbed on the surface could possibly reduce the subsequent interaction of $Cu(acac)_2$ precursor with the surface thus reducing the Cu growth and nucleation.

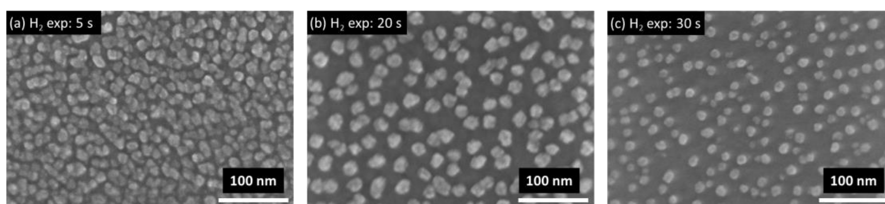

Figure 69: Studying the effect of H_2 exposure of ALD Cu on Ti substrate.

The effect of the Ar flow in to the Cu precursor cylinder for boosting was also evaluated (*Figure 70*), it was found that by increasing the flow rate of the inert gas, the nucleation of the Cu on Ti substrate drastically increased, this could be due increased delivery of the precursor molecules into the reactor.

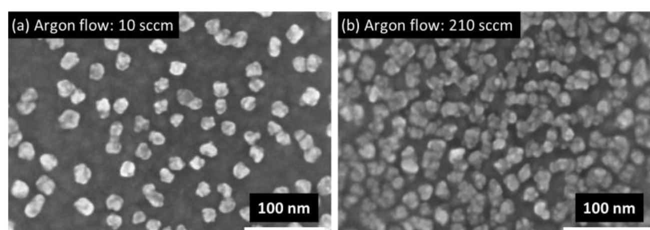

Figure 70: Studying the effect of Ar flow for boosting of the Cu Precursor.

7.7.2 Overview of *in situ* XAS experiments

The general principle of ALD Cu process is known, but the nucleation phase is not yet experimentally studied due to the lack of a characterization technique sensitive enough to probe minute quantities of material, such as those deposited in this process per half-cycle. However, synchrotron based X-ray absorption techniques have this capability.

After the design of the *in situ* system, the main objective was to study the ALD Cu growth. This would help us understand Cu's core level oxidation state, clarifying whether it is in metallic form or oxidized in the first few cycles. In addition, with further analysis, information about the bond distance and Cu coordination number would help determining the strain and interfacial effects.

7.7.2.1 Practical challenges during the experiments

For grazing incidence experiments, the scope of tolerance is minimal. Therefore, any deviation from the required system alignment results in complete measurement failure. Indeed, the difficulty in alignment was the major challenge during our experiments. The difficulty in the alignment was caused due to small aperture of the beryllium window, leaky air bellow, and difficulty in identifying the correct height of the sample holder.

Beryllium windows size

The diameter of the beryllium windows was 13 mm, whereas the internal diameter of the reactor mounting the flange was 37 mm. Thus, there was enough space for mounting larger windows. The reason for not selecting larger windows was high cost compared to smaller ones. This challenge was clearly understood while the experiments were performed. Smaller windows also limited the number of fluorescent photons reaching the detector, resulting in a weak absorption signal.

Leak in air bellow assembly

The air bellow assembly had an unexpected leak causing sagging of the reactor when the pressure of the assembly went below a certain level. In order to maintain the position, a continuous supply of pressurized gas was used. However, this approach was not infallible, as the pressure was not stable. Thus, this contributed to alignment difficulties.

Substrate tilt

The sample holder mounting the ceramic heater, and the substrate was attached to the rods via grub screws. These screws caused misalignment of the substrate during the tightening. As the ideal position of the substrate is to the center line of the windows, any misalignment due to tightening significantly affects the requirement of grazing incidence for the experiments.

Feedthrough selection

A type J thermocouple feedthrough was used to design the sample holder. One of the leads in this type of thermocouple is constant. This alloy is made of Copper and Nickel. It was found that copper inside the reactor, especially in close proximity to the substrate, is not ideal. As this can interfere with copper growth measurements which we were interested in.

7.7.3 Improvements in the system design

Based on the experiments conducted during our beam time at SLAC, several improvements in the system design were proposed and implemented for the next possible beam time. Large Beryllium windows directly mounted on CF40 flange were used for more precise X-Ray beam alignment. Type C thermocouple feedthrough was used, as the thermocouple leads do not contain copper and work with high stability under vacuum and H_2 atmosphere. For simplifying the sample alignment, Yttrium Aluminum Garnet (YAG) crystal was placed closer to the sample position, and its fluorescence characteristics with the incidence of X Rays can be utilized for accurate beam positioning. The fluorescence will be viewed using a camera positioned on the top flange of the reactor.

7.8 Summary

Before conducting in situ studies for Cu growth, preliminary experiments were performed to develop the ALD process and confirm growth on different substrates. In the first part of this work, a comparative study of Cu thin film ALD growth was conducted using $Cu(acac)_2$ and H_2. The growth behavior was compared on Ti, Si, and Ru substrates. It was found that nucleation and growth were limited on n-doped Si, while the best growth behavior in terms of nucleation was observed on Ti. Different numbers of cycles were studied at the same process conditions, and it was observed that with an increase in the number of cycles, coalescence of islands was observed. The impact of growth temperature on the Cu ALD process was evaluated, and it was found that higher temperatures resulted in composite behavior with higher nucleation and coalescence occurring at the same time. The effect of precursor exposure on the growth surface was also studied, and it was observed that the exposure had a clear effect on nucleation, highlighting the need for process optimization.

For the *in situ* X-ray Absorption Spectroscopy (XAS) studies, an *in situ* XAS system was designed and integrated with the X-ray beam at the synchrotron facility. Unfortunately, the experiment could not yield any useful data during the allotted beam time due to beam alignment issues and time constraints. However, the experience gained during the initial experiments proved valuable in identifying opportunities for further system improvements. These improvements were planned for the next beam time, but Covid-related restrictions prevented further experiments from being conducted with the improved system.

This page is intentionally left blank

8. Chapter 8: Conclusions and future work

8.1 Conclusions

The study began by exploring the use of metal oxides, specifically ALD TiO_2, HfO_2, and ZrO_2, to deposit conformal and uniform thin films on AZ31 alloy for corrosion protection. The research then shifted to another application, ALD Cu nucleation and growth behavior was utilized to develop high surface area catalysts by investigating the use of ALD Cu islands on Ti and Ni mesh substrates for the oxygen evolution reaction (OER). In addition, in this work, novel perovskite-based applications were reviewed, which allowed for a deeper understanding of the challenges associated with new materials and precursors. To overcome these challenges and gain better control over the growth process, *in situ* FTIR and XAS systems were designed to enable understanding of the ALD thin films' growth mechanism and structural evaluation. The results of this research demonstrate the potential for ALD in various applications and highlight the importance of *in situ* studies to gain better control over the growth process, ultimately leading to a process-property relationship.

ALD protective coating for corrosion protection

The protective coating applications were explored in three studies. The first study showed that the reduction in corrosion was the primary reason for the reduced susceptibility to stress corrosion cracking (SCC) of Atomic Layer Deposition (ALD) coated AZ31 alloys in simulated body fluid (SBF). In the second study the potential of Mg alloys for biomedical applications was evaluated, the effectiveness of ALD coatings in reducing corrosion of an AZ31 alloy in SBF was studied, and the results showed that the ALD coatings were superior, particularly on 3D aspects, this improved performance was attributed to the higher surface integrity, adhesion strength, and lower line-of-sight restrictions of ALD compared to sputter deposition. The final study evaluated the corrosion behavior and biological response of ALD TiO_2, HfO_2, and ZrO_2 coatings on AZ31 alloy, and all three coatings improved the corrosion behavior and cytotoxicity of the alloy, with HfO_2 coatings exhibiting the highest corrosion resistance and

cell viability. Overall, this thesis provides valuable insights into the use of protective coatings on AZ31 alloys for biomedical applications.

Oxygen evaluation reaction (OER) Cu catalyst

This study explored the potential of ALD Cu deposited on Ti and Ni mesh as cost-effective electrocatalysts for the oxygen evolution reaction (OER). The results showed that Ni mesh substrates had lower overpotential than Ti substrates, with the lowest overpotential recorded for both pristine Ni mesh and Ni mesh with 1500 cycles of ALD Cu. The SEM images revealed that an increase in Cu loading and surface area with the number of deposition cycles could explain the better performance of the Ni 1500 cycles sample. Regarding the Ti mesh substrates, the best performance was observed for the substrate coated with 500 cycles of ALD Cu, with the island density of Cu found to be related to the OER performance. However, the durability test revealed limited adhesion of the best performing sample, indicating the need for further investigation to improve the adhesion and stability of the catalyst surface. Overall, the overpotential measured at 10 mA cm^{-2} for our ALD Cu coated Ni and Ti mesh samples are comparable to state-of-the-art noble metal-free bifunctional catalysts, and the approach used in this work offers less complexity in fabricating islands on highly porous 3D substrates with the use of ALD. This study provides valuable insights into the development of cost-effective electrocatalysts for OER applications.

ALD perovskites growth and application

This review work focused on exploring the potential applications of ALD-deposited perovskites and the challenges associated with their deposition. The advantages of using ALD in depositing perovskites were highlighted. However, challenges such as slow growth rates, difficulty in ultrathin film formation, and carbon contamination due to ligand decomposition were identified. In order to overcome these challenges, an understanding of the growth process and nucleation mechanism is necessary. This work provides valuable insight into the processing, structure, and properties of perovskites in the ultrathin film regime, emphasizing the need for *in situ* studies for better control over growth. Therefore, this review work will contribute to advancing the field of ALD-deposited perovskites and promote further research on the optimization of deposition parameters for different applications.

In situ ALD study

This study presents a novel mechanical design for *in situ* ALD FTIR (and potentially other optical) spectroscopy studies in transmission mode within an existing characterization instrument. The design allows for substrate heating and a coated KBr window substrate, demonstrating its compatibility with most conventional spectroscopy compartments, including the Bruker Vertex 80 FTIR spectrophotometer. The validation of the system's integrity and functionality was successfully demonstrated through *in situ* FTIR absorption measurements of Al_2O_3 using Tri-methyl Aluminum (TMA) and H_2O. Additionally, a comparison of MCT vs DTGS detectors was conducted to show the utility of respective studies in investigating metal complexes during the early stages of ALD nucleation. The study provides critical insights into the successful implementation of *in situ* ALD FTIR studies, which will aid the scientific community in establishing reproducible research results through a proper strategy in in situ system design.

Moreover, the work presents an in situ X-ray absorption spectroscopy (XAS) system designed to deduce structural information from the measured absorption spectra of ALD Cu. Although the study was incomplete due to X-ray beam alignment difficulties and limited beam time, the design improvements to the proposed and implemented system, open up avenues for future research in in situ XAS measurements for the study of ALD film growth. Overall, this study provides valuable knowledge for a wider community working on material growth and its characterization.

8.2 Future Work

ALD applications

For the ALD based catalyst study, based on the results presented in this study, several directions for further research can be pursued to improve the performance of Cu-based OER catalysts. The most urgent is to improve the adhesion of the catalyst to the substrate, which is currently limited in our case and leads to a faster decrease in OER activity compared to state-of-the-art catalysts. This could be achieved by implementing a surface oxide removal

step prior to the deposition of the Cu-based catalyst, using methods such as plasma cleaning [179] or wet chemical etching [180].

Another promising strategy for improving the performance of the catalyst is the use of a graphene conductive layer [181], which has been shown in literature to enhance the electrochemical properties of metal-based catalysts. Additionally, variations in the stoichiometry of the Cu-based catalyst may also be explored to optimize the catalytic activity and stability.

Also, the use of ALD Cu as an electrocatalyst for CO_2 reduction is an intriguing application with significant potential for addressing environmental challenges. In light of the observed advantages of rough Cu surfaces in promoting the formation of multi-carbon products, it would be valuable to investigate the performance of ALD-based Cu catalysts in CO_2 utilization experiments. This would involve conducting electrochemical measurements using various roughness levels of the Cu substrate, as well as exploring the effects of other process parameters.

In the ALD of perovskites work, based on the findings presented in this Ph.D. thesis, there are several future directions for research that would be beneficial to pursue. Those diections include, experimental *in situ* growth studies can be conducted for perovskite-based high-k dielectrics, piezoelectrics, optoelectronics, and solar energy conversion devices to explore the process property relationship for these respective applications. Such studies would enable researchers to better understand the growth mechanisms, as well as optimize the deposition conditions to achieve desired material properties.

***In situ* studies**

The in situ X-ray absorption spectroscopy (XAS) experiments conducted during the beam time at SLAC provided valuable insights into the nucleation and growth of ALD Cu thin films. Based on the results obtained, several improvements in the system design were proposed and implemented to enhance the sensitivity and accuracy of the XAS measurements. However, further investigations are necessary to gain a deeper understanding of the structural evolution of the Cu thin films during the initial few cycles of growth.

In particular, it would be beneficial to conduct additional in situ XAS experiments to monitor the nucleation and growth of the Cu thin films at different stages of the ALD process. This would involve measuring the changes in the local coordination environment and oxidation state of the Cu atoms as a function of cycle number, as well as exploring the effects of different process conditions on the film growth behavior.

This page is intentionally left blank

9. References

1. Cremers, V., Puurunen, R.L., and Dendooven, J. (2019) Conformality in atomic layer deposition: Current status overview of analysis and modelling. *Appl. Phys. Rev.*, **6** (2), 21302.

2. Ritala, M., and Niinisto, J. (2009) Industrial Applications of Atomic Layer Deposition. *ECS Trans.*, **25** (8), 641–652.

3. Mackus, A.J.M., Schneider, J.R., Macisaac, C., Baker, J.G., and Bent, S.F. (2019) Synthesis of Doped, Ternary, and Quaternary Materials by Atomic Layer Deposition: A Review. *Chem. Mater.*, **31** (4), 1142–1183.

4. Molinnus, D., Iken, H., Johnen, A.L., Richstein, B., Hellmich, L., Poghossian, A., Knoch, J., and Schöning, M.J. (2022) Miniaturized pH Sensitive Field Effect Capacitors with Ultrathin Ta2O5 Films Prepared by Atomic Layer Deposition. *Phys. status solidi*, **219** (8), 2100660.

5. George, S.M. (2010) Atomic layer deposition: An overview. *Chem. Rev.*, **110** (1), 111–131.

6. Asundi, A.S., Raiford, J.A., and Bent, S.F. (2019) Opportunities for atomic layer deposition in emerging energy technologies. *ACS Energy Lett.*, **4** (4), 908–925.

7. Ylilammi, M. (1996) Monolayer thickness in atomic layer deposition. *Thin Solid Films*, **279** (1–2), 124–130.

8. Puurunen, R.L. (2003) Growth per cycle in atomic layer deposition: a theoretical model. *Chem. Vap. Depos.*, **9** (5), 249–257.

9. Shahmohammadi, M., Mukherjee, R., Sukotjo, C., Diwekar, U.M., and Takoudis, C.G. (2022) Recent advances in theoretical development of thermal atomic layer deposition: A review. *Nanomaterials*, **12** (5), 831.

10. Puurunen, R.L., and Vandervorst, W. (2004) Island growth as a growth mode in atomic layer deposition: {A} phenomenological model. *J. Appl. Phys.*, **96** (12), 7686–7695.

11. Puurunen, R.L. (2004) Random deposition as a growth mode in atomic layer deposition. *Chem. Vap. Depos.*, **10** (3), 159–170.

12. Richey, N.E., De Paula, C., and Bent, S.F. (2020) Understanding chemical and physical mechanisms in atomic layer deposition. *J. Chem. Phys.*, **152** (4).

13. Clancey, J.W., Cavanagh, A.S., Kukreja, R.S., Kongkanand, A., and George, S.M. (2015) Atomic layer deposition of ultrathin platinum films on tungsten atomic layer deposition adhesion layers: Application to high surface area substrates. *J. Vac. Sci. Technol. A*, **33** (1).

14. Adamsom, A.W., and Gast, A.P. (1997) Physical chemistry of surfaces. *A Wiley-Interscience Publ.*

15. Zhang, J., Li, Y., Cao, K., and Chen, R. (2022) Advances in Atomic Layer Deposition. *Nanomanufacturing Metrol.*, 1–18.

16. Ponraj, J.S., Attolini, G., and Bosi, M. (2013) Review on atomic layer deposition and applications of oxide thin films. *Crit. Rev. solid state Mater. Sci.*, **38** (3), 203–233.

17. Wang, L., Ruan, C., Li, M., Zou, J., Tao, H., Peng, J., and Xu, M. (2017) Enhanced moisture barrier performance for ALD-encapsulated OLEDs by introducing an organic protective layer. *J. Mater. Chem. C*, **5** (16), 4017–4024.

18. Hårkönen, E., Diaz, B., Wiatowska, J., Maurice, V., Seyeux, A., Vehkamäki, M., Sajavaara, T., Fenker, M., Marcus, P., and Ritala, M. (2011) Corrosion protection of steel with oxide nanolaminates grown by atomic layer deposition. *J. Electrochem. Soc.*, **158** (11), C369.

19. Leskela, M., Salmi, E., and Ritala, M. (2017) Atomic layer deposited protective layers. *Mater. Sci. Forum*, **879**, 1086–1092.

20. Gall, D., Cha, J.J., Chen, Z., Han, H.-J., Hinkle, C., Robinson, J.A., Sundararaman, R., and Torsi, R. (2021) Materials for interconnects. *MRS Bull.*, 1–8.

21. Giroire, B., Ahmad, M.A., Aubert, G., Teulé-Gay, L., Michau, D., Watkins, J.J., Aymonier, C., and Poulon-Quintin, A. (2017) A comparative study of copper thin films deposited using magnetron sputtering and supercritical fluid deposition techniques. *Thin Solid Films*, **643**, 53–59.

22. Oviroh, P.O., Akbarzadeh, R., Pan, D., Coetzee, R.A.M., and Jen, T.-C. (2019) New development of atomic layer deposition: processes, methods and applications. *Sci. Technol. Adv. Mater.*, **20** (1), 465–496.

23. Cheng, Y.-L., Lee, C.-Y., and Huang, Y.-L. (2018) Copper metal for semiconductor interconnects. *Noble Precious Met. Nanoscale Eff. Appl.*

24. Waechtler, T., Ding, S.-F., Hofmann, L., Mothes, R., Xie, Q., Oswald, S., Detavernier, C., Schulz, S.E., Qu, X.-P., and Lang, H. (2011) ALD-grown seed layers for electrochemical copper

deposition integrated with different diffusion barrier systems. *Microelectron. Eng.*, **88** (5), 684–689.

25. Knoops, H.C.M., Faraz, T., Arts, K., and Kessels, W.M.M. (2019) Status and prospects of plasma-assisted atomic layer deposition. *J. Vac. Sci. Technol. A Vacuum, Surfaces, Film.*, **37** (3), 30902.

26. Jezewski, C., Lanford, W.A., Wiegand, C.J., Singh, J.P., Wang, P.-I., Senkevich, J.J., and Lu, T.-M. (2005) Inductively coupled hydrogen plasma-assisted Cu ALD on metallic and dielectric surfaces. *J. Electrochem. Soc.*, **152** (2), C60.

27. Profijt, H.B., Potts, S.E., Van de Sanden, M.C.M., and Kessels, W.M.M. (2011) Plasma-assisted atomic layer deposition: basics, opportunities, and challenges. *J. Vac. Sci. Technol. A Vacuum, Surfaces, Film.*, **29** (5), 50801.

28. Gawande, M.B., Goswami, A., Felpin, F.-X., Asefa, T., Huang, X., Silva, R., Zou, X., Zboril, R., and Varma, R.S. (2016) Cu and Cu-based nanoparticles: synthesis and applications in catalysis. *Chem. Rev.*, **116** (6), 3722–3811.

29. Rydosz, A. (2018) The use of copper oxide thin films in gas-sensing applications. *Coatings*, **8** (12), 425.

30. Fabbri, E., and Schmidt, T.J. (2018) Oxygen evolution reaction: the enigma in water electrolysis. *Acs Catal.*, **8** (10), 9765–9774.

31. Jamesh, M.-I., and Sun, X. (2018) Recent progress on earth abundant electrocatalysts for oxygen evolution reaction (OER) in alkaline medium to achieve efficient water splitting: A review. *J. Power Sources*, **400**, 31–68.

32. Zhou, Z., Li, X., Li, Q., Zhao, Y., and Pang, H. (2019) Copper-based materials as highly active electrocatalysts for the oxygen evolution reaction. *Mater. today Chem.*, **11**, 169–196.

33. Liu, X., Jia, H., Sun, Z., Chen, H., Xu, P., and Du, P. (2014) Nanostructured copper oxide electrodeposited from copper (II) complexes as an active catalyst for electrocatalytic oxygen evolution reaction. *Electrochem. commun.*, **46**, 1–4.

34. Bin Afif, A., Dadlani, A.L., Burgmann, S., Kollensperger, P., and Torgersen, J. (2020) Atomic layer deposition of perovskites—Part 1: Fundamentals of nucleation and growth. *Mater. Des. Process. Commun.*, **2** (1), e114.

35. ITRS (2013) INTERNATIONAL TECHNOLOGY ROADMAP FOR SEMICONDUCTORS 2013 EDITION

EMERGING RESEARCH MATERIALS.

36. Choudhury, B.K., Rao, K. V, and Choudhury, R.N.P. (1989) Dielectric properties of SrTiO 3 single crystals subjected to high electric fields and later irradiated with X-rays or -rays. *J. Mater. Sci.*, **24** (10), 3469–3474.

37. Dutta, P.K., Asiaie, R., Akbar, S.A., and Zhu, W. (1994) Hydrothermal synthesis and dielectric properties of tetragonal BaTiO3. *Chem. Mater.*, **6** (9), 1542–1548.

38. Kittl, J.A., Opsomer, K., Popovici, M., Menou, N., Kaczer, B., Wang, X.P., Adelmann, C., Pawlak, M.A., Tomida, K., and Rothschild, A. (2009) High-k dielectrics for future generation memory devices. *Microelectron. Eng.*, **86** (7–9), 1789–1795.

39. Bin Afif, A., Dadlani, A.L., Burgmann, S., Kollensperger, P., and Torgersen, J. (2020) Atomic layer deposition of perovskites part 2: Designing next generation electronic applications. *Mater. Des. Process. Commun.*, **2** (1), e115.

40. Li, F., Wang, L., Jin, L., Lin, D., Li, J., Li, Z., Xu, Z., and Zhang, S. (2015) Piezoelectric activity in Perovskite ferroelectric crystals. *IEEE Trans. Ultrason. Ferroelectr. Freq. Control*, **62** (1), 18–32.

41. Zheng, T., Wu, J., Xiao, D., and Zhu, J. (2018) Recent development in lead-free perovskite piezoelectric bulk materials. *Prog. Mater. Sci.*

42. De Wolf, S., Holovsky, J., Moon, S.-J., Lo per, P., Niesen, B., Ledinsky, M., Haug, F.-J., Yum, J.-H., and Ballif, C. (2014) Organometallic halide perovskites: sharp optical absorption edge and its relation to photovoltaic performance. *J. Phys. Chem. Lett.*, **5** (6), 1035–1039.

43. Sutherland, B.R., Hoogland, S., Adachi, M.M., Kanjanaboos, P., Wong, C.T.O., McDowell, J.J., Xu, J., Voznyy, O., Ning, Z., and Houtepen, A.J. (2015) Perovskite thin films via atomic layer deposition. *Adv. Mater.*, **27** (1), 53–58.

44. Tan, Z.-K., Moghaddam, R.S., Lai, M.L., Docampo, P., Higler, R., Deschler, F., Price, M., Sadhanala, A., Pazos, L.M., and Credgington, D. (2014) Bright light-emitting diodes based on organometal halide perovskite. *Nat. Nanotechnol.*, **9** (9), 687.

45. Onn, T.M., Monai, M., Dai, S., Fonda, E., Montini, T., Pan, X., Graham, G.W., Fornasiero, P., and Gorte, R.J. (2018) Smart Pd catalyst with improved thermal stability supported on high-surface-area LaFeO3 prepared by atomic layer deposition. *J. Am. Chem. Soc.*, **140** (14), 4841–4848.

46. Hatanpää, T., Ritala, M., and Leskelä, M. (2013) Precursors as enablers of ALD technology:

Contributions from University of Helsinki. *Coord. Chem. Rev.*, **257** (23–24), 3297–3322.

47. Ramos, K.B., Saly, M.J., and Chabal, Y.J. (2013) Precursor design and reaction mechanisms for the atomic layer deposition of metal films. *Coord. Chem. Rev.*, **257** (23–24), 3271–3281.

48. Devloo-Casier, K., Ludwig, K.F., Detavernier, C., and Dendooven, J. (2014) In situ synchrotron based x-ray techniques as monitoring tools for atomic layer deposition. *J. Vac. Sci. Technol. A*, **32** (1), 10801.

49. Shim, J.H., Choi, H.J., Kim, Y., Torgersen, J., An, J., Lee, M.H., and Prinz, F.B. (2017) Process property relationship in high-k ALD SrTiO 3 and BaTiO 3: a review. *J. Mater. Chem. C*, **5** (32), 8000–8013.

50. Knapas, K., and Ritala, M. (2013) In situ studies on reaction mechanisms in atomic layer deposition. *Crit. Rev. solid state Mater. Sci.*, **38** (3), 167–202.

51. Dendooven, J., and Detavernier, C. (2017) Basics of atomic layer deposition: growth characteristics and conformality. *At. layer Depos. energy Convers. Appl.*, 1–40.

52. Bin Afif, A., Dadlani, A.L., Flaten, A., Lid, M.J., Ofstad, J., Erbe, A., Köllensperger, P., and Torgersen, J. (2022) A toolbox for easy entry low wavenumber in situ atomic layer deposition transmission FTIR spectroscopy studies . *Rev. Sci. Instrum.*, **93** (8), 085107.

53. Puurunen, R.L. (2014) A short history of atomic layer deposition: Tuomo Suntola's atomic layer epitaxy. *Chem. Vap. Depos.*, **20** (10-11–12), 332–344.

54. Suntola, T. (1989) Atomic layer epitaxy. *Mater. Sci. Reports*, **4** (5), 261–312.

55. Aleskovskii, V.B., and Koltsov, S.I. (1965) Some characteristics of molecular layering reactions. *Abstr. Sci. Tech. Conf. Leningr. Technol. Inst. by Lensovet*, 67.

56. Stafford, N.A., Katamreddy, R., Guerin, L., Feist, B., Dussarrat, C., Pallem, V., Weiland, C., and Opila, R. (2009) Atomic layer deposition of rare-earth oxide thin films for high-k dielectric applications. *ECS Trans.*, **19** (2), 525.

57. Gordon, R.G. (2013) ALD precursors and reaction mechanisms. *At. Layer Depos. Semicond.*, 15–46.

58. Mallick, B.C., Hsieh, C.-T., Yin, K.-M., Gandomi, Y.A., and Huang, K.-T. (2019) On atomic layer deposition: Current progress and future challenges. *ECS J. Solid State Sci. Technol.*, **8** (4), N55.

59. Dendooven, J., Deduytsche, D., Musschoot, J., Vanmeirhaeghe, R.L., and Detavernier, C.

(2010) Conformality of Al2O3 and AlN deposited by plasma-enhanced atomic layer deposition. *J. Electrochem. Soc.*, **157** (4), G111–G116.

60. Dasgupta, N.P., Lee, H.-B.-R., Bent, S.F., and Weiss, P.S. (2016) Recent advances in atomic layer deposition. *Chem. Mater.*, **28** (7), 1943–1947.

61. Sønsteby, H.H., Fjellvåg, H., and Nilsen, O. (2017) Functional Perovskites by Atomic Layer Deposition-An Overview. *Adv. Mater. Interfaces*, **4** (8), 1600903.

62. Wen, L.G., Roussel, P., Pedreira, O.V., Briggs, B., Groven, B., Dutta, S., Popovici, M.I., Heylen, N., Ciofi, I., and Vanstreels, K. (2016) Atomic layer deposition of ruthenium with TiN interface for sub-10 nm advanced interconnects beyond copper. *ACS Appl. Mater. Interfaces*, **8** (39), 26119–26125.

63. Miikkulainen, V., Leskelä, M., Ritala, M., and Puurunen, R.L. (2013) Crystallinity of inorganic films grown by atomic layer deposition: Overview and general trends. *J. Appl. Phys.*, **113** (2), 021301.

64. www.Atomiclimits.com ALD materials table.

65. Elliott, S.D., Dey, G., Maimaiti, Y., Ablat, H., Filatova, E.A., and Fomengia, G.N. (2016) Modeling mechanism and growth reactions for new nanofabrication processes by atomic layer deposition. *Adv. Mater.*, **28** (27), 5367–5380.

66. Sneh, O., Clark-Phelps, R.B., Londergan, A.R., Winkler, J., and Seidel, T.E. (2002) Thin film atomic layer deposition equipment for semiconductor processing. *Thin Solid Films*, **402** (1–2), 248–261.

67. Kuse, R., Kundu, M., Yasuda, T., Miyata, N., and Toriumi, A. (2003) Effect of precursor concentration in atomic layer deposition of Al 2 O 3. *J. Appl. Phys.*, **94** (10), 6411–6416.

68. Chiappim, W., Fraga, M.A., Maciel, H.S., and Pessoa, R.S. (2020) An experimental and theoretical study of the impact of the precursor pulse time on the growth per cycle and crystallinity quality of TiO2 thin films grown by ALD and PEALD technique. *Front. Mech. Eng.*, **6**, 551085.

69. Pakkala, A., and Putkonen, M. (2010) Atomic layer deposition, in *Handbook of deposition technologies for films and coatings*, Elsevier, pp. 364–391.

70. Lubitz, M., Medina IV, P.A., Antic, A., Rosin, J.T., and Fahlman, B.D. (2014) Cost-Effective Systems for Atomic Layer Deposition. *J. Chem. Educ.*, **91** (7), 1022–1027.

71. Munoz-Rojas, D., and MacManus-Driscoll, J. (2014) Spatial atmospheric atomic layer deposition: a new laboratory and industrial tool for low-cost photovoltaics. *Mater. Horizons*, **1** (3), 314–320.

72. Choe, J. (2021) Memory technology 2021: Trends & challenges. *2021 Int. Conf. Simul. Semicond. Process. Devices*, 111–115.

73. Baklanov, M.R., Adelmann, C., Zhao, L., and De Gendt, S. (2015) Advanced interconnects: materials, processing, and reliability. *ECS J. Solid State Sci. Technol.*, **4** (1), Y1–Y4.

74. Singh, A.K., Adstedt, K., Brown, B., Singh, P.M., and Graham, S. (2018) Development of ALD coatings for harsh environment applications. *ACS Appl. Mater. Interfaces*, **11** (7), 7498–7509.

75. Hossain, M.A., Khoo, K.T., Cui, X., Poduval, G.K., Zhang, T., Li, X., Li, W.M., and Hoex, B. (2020) Atomic layer deposition enabling higher efficiency solar cells: A review. *Nano Mater. Sci.*, **2** (3), 204–226.

76. Gougam, A.B., Rajab, B., and Afif, A. Bin (2019) Investigation of c-Si surface passivation using thermal ALD deposited HfO2 films. *Mater. Sci. Semicond. Process.*, **95**, 42–47.

77. Gupta, B., Hossain, M.A., Riaz, A., Sharma, A., Zhang, D., Tan, H.H., Jagadish, C., Catchpole, K., Hoex, B., and Karuturi, S. (2022) Recent advances in materials design using atomic layer deposition for energy applications. *Adv. Funct. Mater.*, **32** (3), 2109105.

78. Dull, S.M., Vinogradova, O., Xu, S., Koshy, D.M., Vullum, P.E., Torgersen, J., Kirsch, S., Viswanathan, V., Jaramillo, T.F., and Prinz, F.B. (2022) Alloyed Pt-Zn Oxygen Reduction Catalysts for Proton Exchange Membrane Fuel Cells. *ACS Appl. Energy Mater.*, **5** (7), 8282–8291.

79. Ma, L., Nuwayhid, R.B., Wu, T., Lei, Y., Amine, K., and Lu, J. (2016) Atomic layer deposition for lithium based batteries. *Adv. Mater. Interfaces*, **3** (21), 1600564.

80. Shin, J.W., Oh, S., Lee, S., Go, D., Park, J., Kim, H.J., Yang, B.C., Cho, G.Y., and An, J. (2021) ALD CeO2-Coated Pt anode for thin-film solid oxide fuel cells. *Int. J. Hydrogen Energy*, **46** (38), 20087–20092.

81. Oviroh, P.O., Jen, T.-C., Ren, J., and van Duin, A. (2023) Towards the realisation of high permi-selective MoS2 membrane for water desalination. *npj Clean Water*, **6** (1), 14.

82. Dangwal, S., Liu, R., Bastatas, L.D., Echeverria, E., Huang, C., Mao, Y., McIlroy, D.N., Han, S., and Kim, S.-J. (2019) ZnO microfiltration membranes for desalination by a vacuum flow-

through evaporation method. *Membranes (Basel).*, **9** (12), 156.

83. Popovici, M., Van Elshocht, S., Menou, N., Swerts, J., Pierreux, D., Delabie, A., Brijs, B., Conard, T., Opsomer, K., and Maes, J.W. (2010) Atomic Layer Deposition of Strontium Titanate Films Using Sr (# 2# 1Cp) 2 and Ti (OMe) 4. *J. Electrochem. Soc.*, **157** (1), G1–G6.

84. Rahtu, A., Hänninen, T., and Ritala, M. (2001) In situ characterization of atomic layer deposition of SrTiO3. *J. Phys. IV JP*, **11** (3), Pr3-923.

85. Wang, H., Jiang, X., Fu, K., and Willis, B.G. (2013) Nucleation, Hydroxylation, and Crystallization Effects in ALD SrO. *J. Phys. Chem. C*, **117** (22), 11578–11583.

86. Niemelä, J.-P., Marin, G., and Karppinen, M. (2017) Titanium dioxide thin films by atomic layer deposition: a review. *Semicond. Sci. Technol.*, **32** (9), 93005.

87. Menou, N., Popovici, M., Clima, S., Opsomer, K., Polspoel, W., Kaczer, B., Rampelberg, G., Tomida, K., Pawlak, M. a., Detavernier, C., Pierreux, D., Swerts, J., Maes, J.W., Manger, D., Badylevich, M., Afanasiev, V., Conard, T., Favia, P., Bender, H., Brijs, B., Vandervorst, W., Van Elshocht, S., Pourtois, G., Wouters, D.J., Biesemans, S., and Kittl, J. a. (2009) Composition influence on the physical and electrical properties of Sr[sub x]Ti[sub 1−x]O[sub y]-based metal-insulator-metal capacitors prepared by atomic layer deposition using TiN bottom electrodes. *J. Appl. Phys.*, **106** (9), 094101.

88. Sunami, H. (2010) Dimension increase in metal-oxide-semiconductor memories and transistors, in *Advances in Solid State Circuit Technologies*, IntechOpen.

89. Vehkamäki, M., Hatanpää, T., Ritala, M., Leskelä, M., Väyrynen, S., and Rauhala, E. (2007) Atomic layer deposition of BaTiO3 thin films - Effect of barium hydroxide formation. *Chem. Vap. Depos.*, **13** (5), 239–246.

90. Lee, S.W., Han, J.H., Han, S., Lee, W., Jang, J.H., Seo, M., Kim, S.K., Dussarrat, C., Gatineau, J., Min, Y.-S., and Hwang, C.S. (2011) Atomic {Layer} {Deposition} of {SrTiO}3 {Thin} {Films} with {Highly} {Enhanced} {Growth} {Rate} for {Ultrahigh} {Density} {Capacitors}. *Chem. Mater.*, **23** (8), 2227–2236.

91. McDaniel, M.D., Hu, C., Lu, S., Ngo, T.Q., Posadas, A., Jiang, A., Smith, D.J., Yu, E.T., Demkov, A.A., and Ekerdt, J.G. (2015) Atomic layer deposition of crystalline SrHfO3 directly on Ge (001) for high-k dielectric applications. *J. Appl. Phys.*, **117** (5), 54101.

92. An, J., Usui, T., Logar, M., Park, J., Thian, D., Kim, S., Kim, K., and Prinz, F.B. (2014) Plasma {Processing} for {Crystallization} and {Densification} of {Atomic} {Layer} {Deposition} {BaTiO}3

{Thin} {Films}. *ACS Appl. Mater. Interfaces*, **6** (13), 10656–10660.

93. Acharya, S., Torgersen, J., Kim, Y., Park, J., Schindler, P., Dadlani, A.L., Winterkorn, M., Xu, S., Walch, S.P., and Usui, T. (2016) Self-limiting atomic layer deposition of barium oxide and barium titanate thin films using a novel pyrrole based precursor. *J. Mater. Chem. C*, **4** (10), 1945–1952.

94. Hu, S., Ji, L., Chen, P.-Y., Edmondson, B.I., Chang, H.-L., Posadas, A., Wu, H.W., Yu, E.T., Smith, D.J., and Demkov, A.A. (2018) Crystalline SrZrO3 deposition on Ge (001) by atomic layer deposition for high-k dielectric applications. *J. Appl. Phys.*, **124** (4), 44102.

95. Sinha, N., Guo, Z., Felmetsger, V. V, and Piazza, G. (2010) 100 NM Thick Aluminum Nitrade Based Piezoelectric Nano Switches Exhibiting 1 MV Threshold Voltage via Body-Biasing.

96. Zhou, H., Chen, Q., Li, G., Luo, S., Song, T., Duan, H.-S., Hong, Z., You, J., Liu, Y., and Yang, Y. (2014) Interface engineering of highly efficient perovskite solar cells. *Science (80-.).*, **345** (6196), 542–546.

97. Zhang, Q., Ha, S.T., Liu, X., Sum, T.C., and Xiong, Q. (2014) Room-temperature near-infrared high-Q perovskite whispering-gallery planar nanolasers. *Nano Lett.*, **14** (10), 5995–6001.

98. Kubicek, M., Bork, A.H., and Rupp, J.L.M. (2017) Perovskite oxides : a review on a versatile material class for solar-to-fuel conversion processes. *J. Mater. Chem. A*, **5** (24), 11983–12000.

99. Bork, A.H., Kubicek, M., Struzik, M., and Rupp, J.L.M. (2015) Perovskite La 0.6 Sr 0.4 Cr 1- x Co x O 3- solid solutions for solar-thermochemical fuel production: strategies to lower the operation temperature. *J. Mater. Chem. A*, **3** (30), 15546–15557.

100. Furler, P., Scheffe, J., Marxer, D., Gorbar, M., Bonk, A., Vogt, U., and Steinfeld, A. (2014) Thermochemical CO 2 splitting via redox cycling of ceria reticulated foam structures with dual-scale porosities. *Phys. Chem. Chem. Phys.*, **16** (22), 10503–10511.

101. Deml, A.M., Stevanovi, V., Muhich, C.L., Musgrave, C.B., and O'Hayre, R. (2014) Oxide enthalpy of formation and band gap energy as accurate descriptors of oxygen vacancy formation energetics. *Energy Environ. Sci.*, **7** (6), 1996–2004.

102. Takacs, M., Hoes, M., Caduff, M., Cooper, T., Scheffe, J.R., and Steinfeld, A. (2016) Oxygen nonstoichiometry, defect equilibria, and thermodynamic characterization of LaMnO3 perovskites with Ca/Sr A-site and Al B-site doping. *Acta Mater.*, **103**, 700–710.

103. Scheffe, J.R., and Steinfeld, A. (2014) Oxygen exchange materials for solar thermochemical

splitting of H_2O and CO_2: a review. *Mater. Today*, **17** (7), 341–348.

104. McDaniel, M.D., Ngo, T.Q., Hu, S., Posadas, A., Demkov, A.A., and Ekerdt, J.G. (2015) Atomic layer deposition of perovskite oxides and their epitaxial integration with Si, Ge, and other semiconductors. *Appl. Phys. Rev.*, **2** (4), 41301.

105. Kil, D.S., Lee, J.M., and Roh, J.S. (2002) Low Temperature ALD Growth of $SrTiO_3$ Thin Films from Sr Diketonates and Ti Alkoxide Precursors Using Oxygen Remote Plasma as an Oxidation Source. *Chem. Vap. Depos.*, **8** (5), 195–197.

106. Putkonen, M., and Niinist, L. (2005) Organometallic precursors for atomic layer deposition, in *Precursor Chemistry of Advanced Materials*, Springer, pp. 125–145.

107. Holme, T.P., and Prinz, F.B. (2007) Atomic layer deposition and chemical vapor deposition precursor selection method application to strontium and barium precursors. *J. Phys. Chem. A*, **111** (33), 8147–8151.

108. Park, P.K., Roh, J.-S., Choi, B.H., and Kang, S.-W. (2006) Interfacial layer properties of HfO_2 films formed by plasma-enhanced atomic layer deposition on silicon. *Electrochem. solid-state Lett.*, **9** (5), F34–F37.

109. Park, H.B., Cho, M., Park, J., Lee, S.W., Hwang, C.S., Kim, J.-P., Lee, J.-H., Lee, N.-I., Kang, H.-K., and Lee, J.-C. (2003) Comparison of HfO_2 films grown by atomic layer deposition using $HfCl_4$ and H_2O or O_3 as the oxidant. *J. Appl. Phys.*, **94** (5), 3641–3647.

110. Choi, S.W., Jang, C.M., Kim, D.Y., Ha, J.S., Park, H.S., Koh, W.Y., and Lee, C.S. (2003) Plasma enhanced atomic layer deposition of Al_2O_3 and TiN. *J. Korean Phys. Soc.*, **42** (Suppl.), 975–979.

111. Bankras, R., Holleman, J., Schmitz, J., Sturm, M., Zinine, A., Wormeester, H., and Poelsema, B. (2006) In Situ Reflective High Energy Electron Diffraction Analysis During the Initial Stage of a Trimethylaluminum/Water ALD Process. *Chem. Vap. Depos.*, **12** (5), 275–279.

112. Temperton, R.H., Gibson, A., and O'Shea, J.N. (2019) In situ XPS analysis of the atomic layer deposition of aluminium oxide on titanium dioxide. *Phys. Chem. Chem. Phys.*, **21** (3), 1393–1398.

113. Werbrouck, A., Mattelaer, F., Dendooven, J., and Detavernier, C. (2019) Fingerprinting of ALD reaction products with time-resolved in situ mass spectrometry. *19th Int. Conf. At. Layer Depos. (ALD 2019)*.

114. Niinistö, J., Rahtu, A., Putkonen, M., Ritala, M., Leskelä, M., and Niinistö, L. (2005) In situ quadrupole mass spectrometry study of atomic-layer deposition of ZrO2 using Cp2Zr (CH3) 2 and water. *Langmuir*, **21** (16), 7321–7325.

115. Langereis, E., Heil, S.B.S., Knoops, H.C.M., Keuning, W., Van de Sanden, M.C.M., and Kessels, W.M.M. (2009) In situ spectroscopic ellipsometry as a versatile tool for studying atomic layer deposition. *J. Phys. D. Appl. Phys.*, **42** (7), 73001.

116. O'Brien, N.J., Rouf, P., Samii, R., Ro nnby, K., Buttera, S.C., Hsu, C.-W., Ivanov, I.G., Kessler, V., Ojama e, L., and Pedersen, H. (2020) In situ activation of an indium (III) triazenide precursor for epitaxial growth of indium nitride by atomic layer deposition. *Chem. Mater.*, **32** (11), 4481–4489.

117. Acharya, J., Wilt, J., Liu, B., and Wu, J. (2018) Probing the dielectric properties of ultrathin Al/Al2O3/Al trilayers fabricated using in situ sputtering and atomic layer deposition. *ACS Appl. Mater. Interfaces*, **10** (3), 3112–3120.

118. Geidel, M., Junige, M., Albert, M., and Bartha, J.W. (2013) In-situ analysis on the initial growth of ultra-thin ruthenium films with atomic layer deposition. *Microelectron. Eng.*, **107**, 151–155.

119. Roger Bosch, E.K. (2018) In situ Studies of ALD Processes & Reaction Mechanismstle. *https://www.atomiclimits.com/2018/07/28/in-situ-studies-of-ald-processes-reaction-mechanisms/*.

120. Fujiwara, H. (2007) *Spectroscopic ellipsometry: principles and applications*, John Wiley & Sons.

121. Goldstein, D.N., McCormick, J.A., and George, S.M. (2008) Al2O3 atomic layer deposition with trimethylaluminum and ozone studied by in situ transmission FTIR spectroscopy and quadrupole mass spectrometry. *J. Phys. Chem. C*, **112** (49), 19530–19539.

122. Yanguas-Gil, A., Libera, J.A., and Elam, J.W. (2013) Modulation of the growth per cycle in atomic layer deposition using reversible surface functionalization. *Chem. Mater.*, **25** (24), 4849–4860.

123. Kwon, J., Dai, M., Halls, M.D., Langereis, E., Chabal, Y.J., and Gordon, R.G. (2009) In situ infrared characterization during atomic layer deposition of lanthanum oxide. *J. Phys. Chem. C*, **113** (2), 654–660.

124. Riha, S.C., Libera, J.A., Elam, J.W., and Martinson, A.B.F. (2012) Design and implementation of an integral wall-mounted quartz crystal microbalance for atomic layer deposition. *Rev. Sci. Instrum.*, **83** (9), 94101.

125. Braeken, E.M.J., Knoops, H.C.M., Potts, S.E., and Kessels, W.M.M. (2013) Development and understanding of a plasma-assisted atomic layer deposition process for silicon nitride.

126. Mackus, A.J.M., Heil, S.B.S., Langereis, E., Knoops, H.C.M., Van de Sanden, M.C.M., and Kessels, W.M.M. (2010) Optical emission spectroscopy as a tool for studying, optimizing, and monitoring plasma-assisted atomic layer deposition processes. *J. Vac. Sci. Technol. A Vacuum, Surfaces, Film.*, **28** (1), 77–87.

127. Geyer, S.M., Methaapanon, R., Johnson, R.W., Kim, W.-H., Van Campen, D.G., Metha, A., and Bent, S.F. (2014) An atomic layer deposition chamber for in situ x-ray diffraction and scattering analysis. *Rev. Sci. Instrum.*, **85** (5), 55116.

128. Calvin, S. (2013) *XAFS for Everyone*, CRC press.

129. Hwang, Y., Heo, K., Chang, C.H., Joo, M.K., and Ree, M. (2006) Synchrotron X-ray reflectivity study of high dielectric constant alumina thin films prepared by atomic layer deposition. *Thin Solid Films*, **510** (1–2), 159–163.

130. Lujala, V., Skarp, J., Tammenmaa, M., and Suntola, T. (1994) Atomic layer epitaxy growth of doped zinc oxide thin films from organometals. *Appl. Surf. Sci.*, **82**, 34–40.

131. Tallarida, M., and Schmeisser, D. (2012) In situ ALD experiments with synchrotron radiation photoelectron spectroscopy. *Semicond. Sci. Technol.*, **27** (7), 74010.

132. Hotalen, J., Murphy, M., Earley, W., Vockenhuber, M., Ekinci, Y., Freedman, D.A., and Brainard, R.L. (2017) Advanced development techniques for metal-based EUV resists. *Extrem. Ultrav. Lithogr. VIII*, **10143**, 17–28.

133. Peron, M., Afif, A. Bin, Dadlani, A.L., Berto, F., and Torgersen, J. (2020) Improving stress corrosion cracking behavior of AZ31 alloy with conformal thin titania and zirconia coatings for biomedical applications. *J. Mech. Behav. Biomed. Mater.*, **111**, 104005.

134. Peron, M., Afif, A. Bin, Dadlani, A., Berto, F., and Torgersen, J. (2020) Comparing physiologically relevant corrosion performances of Mg AZ31 alloy protected by ALD and sputter coated TiO2. *Surf. Coatings Technol.*, **395**, 125922.

135. Peron, M., Cogo, S., Bjelland, M., Afif, A. Bin, Dadlani, A., Greggio, E., Berto, F., and Torgersen, J. (2021) On the evaluation of ALD TiO2, ZrO2 and HfO2 coatings on corrosion and cytotoxicity performances. *J. Magnes. Alloy.*, **9** (5), 1806–1819.

136. Adhikari, S., Selvaraj, S., and Kim, D.H. (2018) Progress in powder coating technology using

atomic layer deposition. *Adv. Mater. Interfaces*, **5** (16), 1800581.

137. Montemor, M.F. (2014) Functional and smart coatings for corrosion protection: A review of recent advances. *Surf. Coatings Technol.*, **258**, 17–37.

138. Wan, Z., Zhang, T.F., Ding, J.C., Kim, C.-M., Park, S.-W., Yang, Y., Kim, K.-H., and Kwon, S.-H. (2017) Enhanced corrosion resistance of PVD-CrN coatings by ALD sealing layers. *Nanoscale Res. Lett.*, **12**, 1–8.

139. He, W. (2015) ALD: atomic layer deposition-precise and conformal coating for better performance. *Handb. Manuf. Eng. Technol.*, 2959–2996.

140. Yu, K., Cai, Z., Wang, X., Shi, T., and Li, W. (2010) Constitutive analysis of AZ31 magnesium alloy plate. *J. Cent. South Univ. Technol.*, **17**, 7–12.

141. Dziubi ska, A., Gontarz, A., Dziubi ski, M. aw, and Barszcz, M. (2016) The forming of magnesium alloy forgings for aircraft and automotive applications. *Adv. Sci. Technol. Res. J.*, **10** (31).

142. Xie, Q., Ma, A., Jiang, J., Liu, H., Cheng, Z., and Gu, Y. (2021) Tailoring the corrosion behavior and mechanism of AZ31 magnesium alloys by different Ca contents for marine application. *Corros. Sci.*, **192**, 109842.

143. liwa, R.E. (2022) Metal Forming of Magnesium Alloys for Various Applications. *Magnes. Alloy. Struct. Prop.*

144. Staiger, M.P., Pietak, A.M., Huadmai, J., and Dias, G. (2006) Magnesium and its alloys as orthopedic biomaterials: a review. *Biomaterials*, **27** (9), 1728–1734.

145. Peron, M., Berto, F., and Torgersen, J. (2020) *Magnesium and Its Alloys as Implant Materials: Corrosion, Mechanical and Biological Performances*, CRC Press.

146. Raman, R.K.S., Jafari, S., and Harandi, S.E. (2015) Corrosion fatigue fracture of magnesium alloys in bioimplant applications: A review. *Eng. Fract. Mech.*, **137**, 97–108.

147. Perumal, G., Ramasamy, B., and Doble, M. (2018) Nanostructure coated AZ31 magnesium cylindrical mesh cage for potential long bone segmental defect repair applications. *Colloids Surfaces B Biointerfaces*, **172**, 690–698.

148. Xu, R., Zhou, Z., Li, J., Zhang, X., Zhu, Y., Xiao, H., Xu, L., Ding, Y., Li, A., and Fang, G. (2022) Reaction mechanism of atomic layer deposition of zirconium oxide using zirconium precursors bearing amino ligands and water. *Front. Chem.*, **10**, 1035902.

149. Xie, Q., Jiang, Y.-L., Detavernier, C., Deduytsche, D., Van Meirhaeghe, R.L., Ru, G.-P., Li, B.-Z., and Qu, X.-P. (2007) Atomic layer deposition of TiO2 from tetrakis-dimethyl-amido titanium or Ti isopropoxide precursors and H2O. *J. Appl. Phys.*, **102** (8).

150. Badovinac, I.J., Peter, R., Omerzu, A., Salamon, K., Šari, I., Samaržija, A., Perčić, M., Piltaver, I.K., Ambrožić, G., and Petravić, M. (2020) Grain size effect on photocatalytic activity of TiO2 thin films grown by atomic layer deposition. *Thin Solid Films*, **709**, 138215.

151. Shan, C.X., Hou, X., and Choy, K.-L. (2008) Corrosion resistance of TiO2 films grown on stainless steel by atomic layer deposition. *Surf. Coatings Technol.*, **202** (11), 2399–2402.

152. Hausmann, D.M., Kim, E., Becker, J., and Gordon, R.G. (2002) Atomic {Layer} {Deposition} of {Hafnium} and {Zirconium} {Oxides} {Using} {Metal} {Amide} {Precursors}. *Chem. Mater.*, **14** (10), 4350–4358.

153. Hernández-Arriaga, H., López-Luna, E., Martinez Guerra, E., Turrubiartes, M.M., Rodriguez, A.G., and Vidal, M.A. (2017) Growth of HfO2/TiO2 nanolaminates by atomic layer deposition and HfO2-TiO2 by atomic partial layer deposition. *J. Appl. Phys.*, **121** (6).

154. González-Martin, M.L., Labajos-Broncano, L., Jańczuk, B., and Bruque, J.M. (1999) Wettability and surface free energy of zirconia ceramics and their constituents. *J. Mater. Sci.*, **34**, 5923–5926.

155. Li, W., and Li, D.Y. (2006) Influence of surface morphology on corrosion and electronic behavior. *Acta Mater.*, **54** (2), 445–452.

156. Tee, S.Y., Win, K.Y., Teo, W.S., Koh, L.D., Liu, S., Teng, C.P., and Han, M.Y. (2017) Recent progress in energy driven water splitting. *Adv. Sci.*, **4** (5), 1600337.

157. Luo, Y., Zhang, Z., Chhowalla, M., and Liu, B. (2022) Recent advances in design of electrocatalysts for high current density water splitting. *Adv. Mater.*, **34** (16), 2108133.

158. Mirica, L.M., Ottenwaelder, X., and Stack, T.D.P. (2004) Structure and spectroscopy of copper-dioxygen complexes. *Chem. Rev.*, **104** (2), 1013–1046.

159. Tomer, S., Panigrahi, J., Srivastava, R., and Rauthan, C.M.S. (2019) Importance of precursor delivery mechanism for Tetra-kis-ethylmethylaminohafnium/water atomic layer deposition process. *Thin Solid Films*, **692**, 137629.

160. Tian, L., Ponton, S., Benz, M., Crisci, A., Reboud, R., Giusti, G., Volpi, F., Rapenne, L., Vallee, C., and Pons, M. (2018) Aluminum nitride thin films deposited by hydrogen plasma enhanced

and thermal atomic layer deposition. *Surf. Coatings Technol.*, **347**, 181–190.

161. Hu, X., Schuster, J., Schulz, S.E., and Gessner, T. (2015) Surface chemistry of copper metal and copper oxide atomic layer deposition from copper (ii) acetylacetonate: a combined first-principles and reactive molecular dynamics study. *Phys. Chem. Chem. Phys.*, **17** (40), 26892–26902.

162. Chen, D.A., Bartelt, M.C., Hwang, R.Q., and McCarty, K.F. (2000) Self-limiting growth of copper islands on TiO2 (110)-(1 x 1). *Surf. Sci.*, **450** (1–2), 78–97.

163. Dai, M., Kwon, J., Chabal, Y.J., Halls, M.D., and Gordon, R.G. (2009) FTIR study of copper agglomeration during atomic layer deposition of copper. *MRS Proc.*

164. Wu, J., Han, B., Zhou, C., Lei, X., Gaffney, T.R., Norman, J.A.T., Li, Z., Gordon, R., and Cheng, H. (2007) Density function theory study of copper agglomeration on the WN (001) surface. *J. Phys. Chem. C*, **111** (26), 9403–9406.

165. Long, X., Xiao, S., Wang, Z., Zheng, X., and Yang, S. (2015) Co intake mediated formation of ultrathin nanosheets of transition metal LDH-an advanced electrocatalyst for oxygen evolution reaction. *Chem. Commun.*, **51** (6), 1120–1123.

166. Tao, Z., Jiang, L., Jia, X., Xiao, H., Liang, Y., Yang, B., Guo, P., Zhang, L., and Yang, H. (2021) In situ growth of Co3O4 nanoneedles on titanium mesh for electrocatalytic oxygen evolution. *J. Mater. Sci. Mater. Electron.*, **32** (18), 23275–23284.

167. Zeng, F., Mebrahtu, C., Liao, L., Beine, A.K., and Palkovits, R. (2022) Stability and deactivation of OER electrocatalysts: A review. *J. Energy Chem.*

168. Lambers, E.S., Dykstal, C.N., Seo, J.M., Rowe, J.E., and Holloway, P.H. (1996) Room-temerature oxidation of Ni (110) at low and atmospheric oxygen pressures. *Oxid. Met.*, **45**, 301–321.

169. Proch, S., Yoshino, S., Takahashi, N., Seki, J., Kosaka, S., Kodama, K., and Morimoto, Y. (2018) The native oxide on titanium metal as a conductive model substrate for oxygen reduction reaction studies. *Electrocatalysis*, **9**, 608–622.

170. Quílez Bermejo, J., García Dalí, S., Daouli, A., Zitolo, A., Canevesi, R.L.S., Emo, M., Izquierdo, M.T., Badawi, M., Celzard, A., and Fierro, V. (2023) Advanced Design of Metal Nanoclusters and Single Atoms Embedded in C1N1 Derived Carbon Materials for ORR, HER, and OER. *Adv. Funct. Mater.*, 2300405.

171. Fabbri, E., Habereder, A., Waltar, K., Kötz, R., and Schmidt, T.J. (2014) Developments and perspectives of oxide-based catalysts for the oxygen evolution reaction. *Catal. Sci. Technol.*, **4** (11), 3800–3821.

172. Han, G.-Q., Liu, Y.-R., Hu, W.-H., Dong, B., Li, X., Shang, X., Chai, Y.-M., Liu, Y.-Q., and Liu, C.-G. (2015) Three dimensional nickel oxides/nickel structure by in situ electro-oxidation of nickel foam as robust electrocatalyst for oxygen evolution reaction. *Appl. Surf. Sci.*, **359**, 172–176.

173. Gao, W., Hood, Z.D., and Chi, M. (2017) Interfaces in heterogeneous catalysts: advancing mechanistic understanding through atomic-scale measurements. *Acc. Chem. Res.*, **50** (4), 787–795.

174. Liu, T., Liang, Y., Liu, Q., Sun, X., He, Y., and Asiri, A.M. (2015) Electrodeposition of cobalt-sulfide nanosheets film as an efficient electrocatalyst for oxygen evolution reaction. *Electrochem. commun.*, **60**, 92–96.

175. Kibria, A.K.M.F., and Tarafdar, S.A. (2002) Electrochemical studies of a nickel copper electrode for the oxygen evolution reaction (OER). *Int. J. Hydrogen Energy*, **27** (9), 879–884.

176. Yu, L., Zhou, H., Sun, J., Qin, F., Yu, F., Bao, J., Yu, Y., Chen, S., and Ren, Z. (2017) Cu nanowires shelled with NiFe layered double hydroxide nanosheets as bifunctional electrocatalysts for overall water splitting. *Energy Environ. Sci.*, **10** (8), 1820–1827.

177. McCrory, C.C.L., Jung, S., Peters, J.C., and Jaramillo, T.F. (2013) Benchmarking heterogeneous electrocatalysts for the oxygen evolution reaction. *J. Am. Chem. Soc.*, **135** (45), 16977–16987.

178. Kannimuthu, K., Sangeetha, K., Sankar, S.S., Karmakar, A., Madhu, R., and Kundu, S. (2021) Investigation on nanostructured Cu-based electrocatalysts for improvising water splitting: a review. *Inorg. Chem. Front.*, **8** (1), 234–272.

179. Wang, Z., Zhang, Y., Neyts, E.C., Cao, X., Zhang, X., Jang, B.W.-L., and Liu, C. (2018) Catalyst preparation with plasmas: how does it work? *ACS Catal.*, **8** (3), 2093–2110.

180. Yao, Q., Huang, B., Xu, Y., Li, L., Shao, Q., and Huang, X. (2021) A chemical etching strategy to improve and stabilize RuO2-based nanoassemblies for acidic oxygen evolution. *Nano Energy*, **84**, 105909.

181. Cui, H., Guo, Y., and Zhou, Z. (2021) Three dimensional graphene based macrostructures for electrocatalysis. *Small*, **17** (22), 2005255.

182. Ott, A.W., Klaus, J.W., Johnson, J.M., and George, S.M. (1997) Al3O3 thin film growth on

Si(100) using binary reaction sequence chemistry. *Thin Solid Films*, **292** (1–2), 135–144.

183. Rai, V.R., Vandalon, V., and Agarwal, S. (2012) Influence of surface temperature on the mechanism of atomic layer deposition of aluminum oxide using an oxygen plasma and ozone. *Langmuir*, **28** (1), 350–357.

184. Van Daele, M., Detavernier, C., and Dendooven, J. (2018) Surface species during ALD of platinum observed with in situ reflection IR spectroscopy. *Phys. Chem. Chem. Phys.*, **20** (39), 25343–25356.

185. Dai, M., Kwon, J., Langereis, E., Wielunski, L.S., Chabal, Y., Li, Z., and Gordon, R. (2007) In-situ FTIR study of atomic layer deposition (ALD) of copper metal films. *ECS Trans.*, **11** (7), 91.

186. Rai, V.R., and Agarwal, S. (2009) Surface reaction mechanisms during plasma-assisted atomic layer deposition of titanium dioxide. *J. Phys. Chem. C*, **113** (30), 12962–12965.

187. Kenneth D. Kempfert, Eric Y. Jiang, Sherwin Oas, J.C. (2001) Detectors for Fourier Transform Spectroscopy. *Thermo Nicolet Appl. Note*.

188. Teo, B.K. (2012) *EXAFS: basic principles and data analysis*, Springer Science & Business Media.

189. Klug, J.A., Weimer, M.S., Emery, J.D., Yanguas-Gil, A., Seifert, S., Schlepütz, C.M., Martinson, A.B.F., Elam, J.W., Hock, A.S., and Proslier, T. (2015) A modular reactor design for in situ synchrotron x-ray investigation of atomic layer deposition processes. *Rev. Sci. Instrum.*, **86** (11), 113901.

190. Dendooven, J., Solano, E., Minjauw, M.M., Van de Kerckhove, K., Coati, A., Fonda, E., Portale, G., Garreau, Y., and Detavernier, C. (2016) Mobile setup for synchrotron based in situ characterization during thermal and plasma-enhanced atomic layer deposition. *Rev. Sci. Instrum.*, **87** (11), 113905.

191. Chen, J.-R., Zhang, W., Nahm, R.K., DiFeo, M.A., and Engstrom, J.R. (2017) Design and characterization of a microreactor for spatially confined atomic layer deposition and in situ UHV surface analysis. *J. Vac. Sci. Technol. A Vacuum, Surfaces, Film.*, **35** (6), 61604.

192. Tonneau, D., Pierrisnard, R., Dallaporta, H., and Marine, W. (1995) Growth kinetics of copper films from photoassisted CVD of copperacetylacetonate. *Le J. Phys. IV*, **5** (C5), C5-629.

193. Juppo, M., Ritala, M., and Leskela, M. (1997) Deposition of copper films by an alternate supply of CuCl and Zn. *J. Vac. Sci. Technol. A Vacuum, Surfaces, Film.*, **15** (4), 2330–2333.

194. Martensson, P., and Carlsson, J.-O. (1998) Atomic layer epitaxy of copper-Growth and

selectivity in the Cu (II)-2, 2, 6, 6-tetramethyl-3, 5-heptanedionate/H-2 process. *J. Electrochem. Soc.*, **145** (8), 2926–2931.

195. Utriainen, M., Kröger-Laukkanen, M., Johansson, L.-S., and Niinistö, L. (2000) Studies of metallic thin film growth in an atomic layer epitaxy reactor using M (acac) 2 (M= Ni, Cu, Pt) precursors. *Appl. Surf. Sci.*, **157** (3), 151–158.

196. Solanki, R., and Pathangey, B. (2000) Atomic layer deposition of copper seed layers. *Electrochem. Solid-State Lett.*, **3** (10), 479.

197. Lim, B.S., Rahtu, A., and Gordon, R.G. (2003) Atomic layer deposition of transition metals. *Nat. Mater.*, **2** (11), 749–754.

198. Li, Z., Rahtu, A., and Gordon, R.G. (2006) Atomic layer deposition of ultrathin copper metal films from a liquid copper (I) amidinate precursor. *J. Electrochem. Soc.*, **153** (11), C787.

199. Hatanpää, T. (2019) Precursor Chemistry for Atomic Layer Deposition-Thesis.

200. Gordon, P.G., Kurek, A., and Barry, S.T. (2014) Trends in copper precursor development for CVD and ALD applications. *ECS J. Solid State Sci. Technol.*, **4** (1), N3188.

201. Lee, B.H., Hwang, J.K., Nam, J.W., Lee, S.U., Kim, J.T., Koo, S.M., Baunemann, A., Fischer, R.A., and Sung, M.M. (2009) Low temperature atomic layer deposition of copper metal thin films: Self limiting surface reaction of copper dimethylamino 2 propoxide with diethylzinc. *Angew. Chemie*, **121** (25), 4606–4609.

202. Tripathi, T.S., and Karppinen, M. (2017) Efficient process for direct atomic layer deposition of metallic Cu thin films based on an organic reductant. *Chem. Mater.*, **29** (3), 1230–1235.

203. Tripathi, T.S., Wilken, M., Hoppe, C., de los Arcos, T., Grundmeier, G., Devi, A., and Karppinen, M. (2021) Atomic Layer Deposition of Copper Metal Films from Cu (acac) 2 and Hydroquinone Reductant. *Adv. Eng. Mater.*, **23** (10), 2100446.

204. Ma, Q., and Zaera, F. (2013) Chemistry of Cu (acac) 2 on Ni (110) and Cu (110) surfaces: Implications for atomic layer deposition processes. *J. Vac. Sci. Technol. A Vacuum, Surfaces, Film.*, **31** (1), 01A112.

205. Hagen, D.J., Pemble, M.E., and Karppinen, M. (2019) Atomic layer deposition of metals: Precursors and film growth. *Appl. Phys. Rev.*, **6** (4), 41309.

206. Webb, J.B., Northcott, D., and Emesh, I. (1995) Growth, selectivity and adhesion of CVD-deposited copper from Cu+ 1 (hexafluoroacetylacetonate trimethylvinylsilane) and

dichlorodimethylsilane. *Thin Solid Films*, **270** (1–2), 483–488.

207. Hagen, D.J., Povey, I.M., Rushworth, S., Wrench, J.S., Keeney, L., Schmidt, M., Petkov, N., Barry, S.T., Coyle, J.P., and Pemble, M.E. (2014) Atomic layer deposition of Cu with a carbene-stabilized Cu (I) silylamide. *J. Mater. Chem. C*, **2** (43), 9205–9214.

208. Granqvist, C.G., and Buhrman, R.A. (1976) Size distributions for supported metal catalysts: Coalescence growth versus ostwald ripening. *J. Catal.*, **42** (3), 477–479.

209. Cheng, H.-E., and Chen, C.-C. (2008) Morphological and photoelectrochemical properties of ALD TiO2 films. *J. Electrochem. Soc.*, **155** (9), D604.

210. Dai, M., Kwon, J., Halls, M.D., Gordon, R.G., and Chabal, Y.J. (2010) Surface and interface processes during atomic layer deposition of copper on silicon oxide. *Langmuir*, **26** (6), 3911–3917.

This page is intentionally left blank

10. Full-text papers included in thesis

Paper 1

Received: 18 September 2019 | Revised: 10 October 2019 | Accepted: 12 October 2019
DOI: 10.1002/mdp2.114

REPORT

WILEY

Atomic layer deposition of perovskites—Part 1: Fundamentals of nucleation and growth

Abdulla Bin Afif[1] | Anup L. Dadlani[1] | Stephanie Burgmann[1] | Peter Köllensperger[2] | Jan Torgersen[1]

[1]Department of Mechanical and Industrial Engineering, NTNU, Trondheim, Norway
[2]Department of Physics, NTNU, Trondheim, Norway

Correspondence
Jan Torgersen, Department of Mechanical and Industrial Engineering, NTNU, Trondheim, Norway.
Email: jan.torgersen@ntnu.no

Funding information
Norges Forskningsråd, Grant/Award Numbers: 245963/F50, 274459; The Norwegian Center for International Cooperation in Education, Grant/Award Number: PNA-2017/10077; Norwegian Micro- and Nano-Fabrication Facility, NorFab, Grant/Award Number: 245963/F50; The Research Council of Norway, Grant/Award Number: 274459

Abstract
A broad spectrum of accessible functionalities and material properties based on slight changes in crystal structure and composition makes perovskites a unique class of materials. Understanding and leveraging of its properties have resulted in its use in a myriad of applications. Today, performance and efficiency demands require these materials in miniaturized devices; hence, a precise control of perovskite synthesis in terms of thickness, crystallinity, and stoichiometry is indispensable. Atomic layer deposition (ALD) makes these requirements potentially conceivable due to the technology's unique self-limiting deposition process. Yet, not all properties of perovskites have been leveraged in the thin film regime due to limited understanding of their synthesis. In part one of a two-part review, we discuss the ALD growth of perovskite-based thin films. After explaining the specific growth characteristics of ALD perovskites, effects of process parameters, and thin film treatments on properties, we discuss an important functional perovskite strontium titanate (STO). In part two, we discuss ALD-deposited perovskites for next generation electronic applications.

KEYWORDS
atomic layer deposition, high-k, interfacial growth, nucleation and growth, perovskites, ultrathin films, piezo-electric

1 | INTRODUCTION

Perovskites with general formula ABO_3 have attracted attention due to their wide range of unique properties. They may possess ferroelectric, antiferroelectric, dielectric, piezoelectric, pyroelectric, superconductive and magneto-resistive behavior.[1] These properties have been leveraged for high-temperature superconductors, high-efficiency solar cells,[2] high-k dielectrics[3] for capacitors and transistors, piezoelectric power generators,[4] and as a thermo-chemical material[5] in the emerging field of solar to energy conversion. With spontaneous and reversible polarization, certain perovskites are ferroelectric in nature.[6] This behavior is seen in perovskite structures with medium-sized cations, such as Ti^{4+} in Barium Titanate ($BaTiO_3$, BTO), a well-known ferroelectric material.[7] The origin of ferroelectric behavior is linked to the position of the medium-sized cation inside the oxygen octahedron. The position of Ti^{4+} cation inside the octahedron changes with the application of an electric field, which gives rise to polarization (Figure 1). The direction of the movement of the ion can be reversed with the change in the direction of the electric field resulting in reversible polarization, making this type of materials ferroelectric in nature. The ferroelectric properties of perovskites are tunable by the replacement of cations in the compound or by controlled introduction of impurities.

This is an open access article under the terms of the Creative Commons Attribution License, which permits use, distribution and reproduction in any medium, provided the original work is properly cited.
© 2019 The Authors. Material Design & Processing Communications published by John Wiley & Sons Ltd

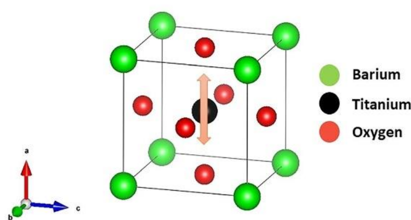

FIGURE 1 Ferroelectric properties in BTO perovskite

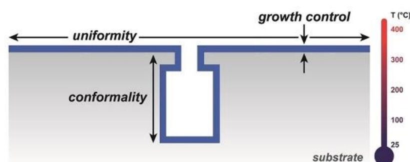

FIGURE 2 Schematic representation of coverage aspect of atomic layer deposition on 3D structures. Reprinted with permission from Elsevier[9]

In case of piezoelectric materials, the functionality is due to development of surface charges by the formation of internal dipoles with the application of external pressure. This effect is seen in noncentrosymmetric structures like perovskites. The off-center position of the Ti^{4+} in oxygen octahedral gives rise to inherent electric polarity. With the application of stress on the material, the Ti^{4+} further translates resulting in surface charge accumulation.[8] This behavior also works in the reverse direction, resulting in deformation of material with the application of an external potential. Some piezoelectric materials attain spontaneous polarization with changes in temperature and are termed as pyroelectrics. Another interesting property of copper-based perovskites, such as lanthanum cuprate (La_2CuO_4), is superconductivity. The nonstoichiometry (oxygen vacancies) in the material results in superconductive behavior. In the next section, we discuss the burgeoning role of atomic layer deposition (ALD) in the fabrication of perovskite thin films, where we learn about ALD's ability to precisely control composition, thickness, and conformality.

2 | THE ALD OF PEROVSKITES

2.1 | Why ALD for perovskites

ALD finds a unique position in research and industry, as it plays an important role in the field of microelectronics and nanoelectronics. ALD has the ability to deposit materials at the nanoscale with high uniformity, conformality (Figure 2), and with an excellent control of stoichiometry. It has also opened the path towards the fabrication of sub 5-nm commercial devices,[10] which is not conceivable by other methods. With a broad range of materials available, it is possible to deposit doped, ternary, quaternary, and higher multicomponent materials[11] within a single process. These competencies provide a perfect toolbox for the creation of perovskite-based devices that be precisely tuned with desired properties.

ALD works on the principle of self-limiting sequential interaction of precursor and coreactant, which allows one to deposit thin films, atomic layer by atomic layer.[12] Multicomponent materials are deposited by the combination of binary cycles, which are defined as a super cycle.[11] Thus, detailed knowledge of the growth mechanism and precursor interaction is required for controlled growth and tunable functionalities. The functionality can be controlled by different parameters such as composition of the films, concentration of point defects,[13] lattice strain[14] or crystal structure, allowing us to explore new applicational possibilities in terms of novel and high-performing electronic devices.[15] Thus, the study of perovskites using ALD is a unique combination, providing us with a possibility to tweak many parameters eventually leading to interesting and unique properties in the thin film regime. Whereas this may bring a paradigm shift in material technology, the understanding of the process and structure developing during growth is yet limited. In the next section, we will briefly discuss the general growth process of perovskites using ALD technique.

2.2 | The growth mechanism of ABO_3 perovskites using ALD

Perovskites are mostly ternary oxide materials with cubic structure. For the ALD of perovskites, a sequential reaction takes place consisting of formation of binary oxides AO and BO_2 (Figure 3). The growth rate of oxide AO on BO_2 or vice versa is different, due to differences in the bonding

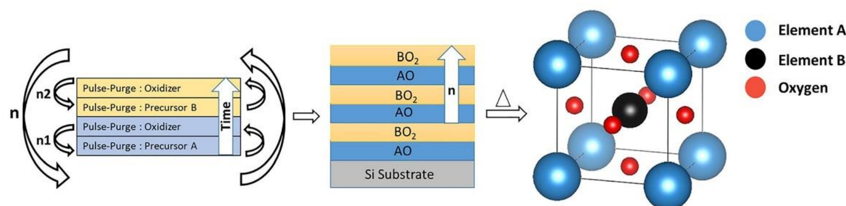

FIGURE 3 Atomic layer deposition growth of ABO_3 compounds

site density and rate of chemisorption provided by the surfaces. A perovskite structure is generally formed by intermixing of binary layers. The diffusion length of the atomic species should be high compared with the binary layer thickness. In ALD, the thickness of each binary layer should be less than 2 Å, which allows for the mobility of atoms resulting in compositional uniformity, whereas restriction to intermixing results in phase segregation.[11] For processes with binary layer thicknesses >2 Å, a higher deposition temperature or a post deposition anneal is required to increase the atomic species diffusion.[11] Thus, for the development of perovskites with a specific composition, an understanding of the interaction of materials with different surfaces is required. On the basis of thin film growth of strontium titanate (STO), we will look at the different steps involved in ALD deposition of perovskite.

2.3 | Growth process (STO)

STO has been studied with several precursor combinations; however, to showcase the general principle of STO deposition, we will focus on Cp (cyclo-pentadienyl) based precursors, due to the compound's high chemical reactivity and low carbon contamination.[16] For the deposition of STO thin films, there are four distinct surface reactions taking place within a super-ordinated cycle, the so-called super cycle. The individual depositions do not necessarily differ from the conventional ALD deposition route. First, the surface is hydroxylated (—OH) by H_2O pulses followed by a purge of the reactor. Next, the Sr precursor reacts with the —OH terminated surface, protonating one of the ligands with H. The ligand leaves the reaction chamber in the vapor phase carried by an inert process gas, the so-called carrier gas.[17,18] In the second step, the remaining C_p ligands are protonated and removed as H_2O is pulsed for a determined duration forming —OH terminated surfaces of Sr again. The preparation for the next binary layer can start. A similar reaction mechanism takes place for the deposition of titanium dioxide (TiO_2) binary layers[19]; the difference in the combined ternary process, however, lies in the energetics of growth between the ternary compounds strontium oxide (SrO) and TiO_2 exhibiting different behavior than the binary compounds alone.

Let us look at a concrete example of such a deposition: the growth process of STO thin films using Sr $(^tBu_3Cp)_2$ (Strontium–bis (tris-butyl cyclopentadienyl)) and Ti (OMe) (Titanium (IV) methoxide) as organometallic precursors and H_2O as oxidant.[16] The reported growth rate of TiO_2 on OH-terminated Si surface is 0.039 nm per cycle with a Ti precursor pulse duration of 2 s and water pulse duration of 1.1 s. The growth rate of SrO on —OH terminated Si surface is 0.059 nm per cycle with a Sr precursor pulse of 3 and 1.1 s for H_2O. Both growth conditions are saturated growth levels, that is, self-limiting growth regimes determined based on the binary's growth saturation curves. When the binary reactions are combined, the growth rate is altered due to the interaction of the precursor molecules with the new species at the interface. For obtaining stoichiometric STO, a pulse ratio of 4:3 or 3:2 is required (a:b, a: number of SrO sub cycles in a super cycle and b: number of TiO_2 subcycles in a super cycle, respectively), signifying the large differences in growth rates. The saturated growth curves of the binaries alone renders a pulse ratio of 2:3 (0.059/0.039) SrO:TiO_2 cycles. Thus, TiO_2 grows better on SrO than on itself. We therefore have to elaborate how their interfaces affect their respective growth.

2.4 | Differential growth at the interface

We have seen that the growth rate of ternary compounds is not a direct combination of the growth rate of binaries. In most cases, the growth rate is higher than anticipated, due to higher surface reactivity between precursor ligands and interfacial functional groups.[20] To have an understanding of how the growth is affected by the different interfaces, we are focusing on the nucleation/wetting aspect, that is, how respective binaries grow on different substrates. This is especially important for ternaries; once a binary is deposited, it becomes the substrate for the other binary. To elaborate on such effects, we review results on the most widely studied perovskite material synthesized by ALD: STO (Table 1).

TABLE 1 Effect of interface condition on the ALD growth

Material	Binary A/B	Reactant/Co Reactant A	Reactant B/Co Reactant B	Temperature, °C	Year	References	Growth Remark
STO	SrO/TiO_2	Sr $(^tBu_3Cp)_2/H_20$	Ti $(OMe)_4/H_2O$	250°C	2009	Popovici et al.[16]	Higher titanium incorporation due to increased strontium pulse ratio
STO	SrO/TiO_2	Sr $(^iPr_3Cp)_2/H_20$	Ti $(O^iPr)_2(tmhd)_2/O_3$	370°C	2011	Lee et al.[3]	Higher SrO growth on TiO_2 surface
STO	SrO/TiO_2	Sr $(^iPr_3Cp)_2/H_20$	Ti$[OCH(CH_3)_2]_4/D_2O$	325°C	2001	Rahtu, Hänninen, & Ritala[18]	Higher SrO growth on TiO_2 surface

A typical ALD growth process of STO consists of subcycles of deposited titania (TiO_2) followed by SrO cycles. The growth of SrO on SrO and SrO on TiO_2 surface is different. The process of STO deposition by the Hwang group from Konkuk University, Korea (Sr $(^iPr_3Cp)_2$ and Ti $(O\text{-}^iPr)_2(tmhd)_2$ precursors) yields higher SrO incorporation than TiO_2.[3] Rahtu et al. used the same Sr precursor together with Ti $(OCH(CH_3)_2)_4$. SrO grows faster on TiO_2 than on itself due to higher adsorption of Sr precursor for a thermodynamically favorable STO formation.[18] The enhanced growth of SrO in the first few cycles is also observed on hydroxylated SiO_2 surface, which has higher reactivity and higher OH density than SrO.[17]

In another study on the growth of STO films (Sr $(^tBu_3Cp)_2$, Ti $(OMe)_4$ and H_2O), the effect of the pulse ratio of Sr over Ti precursor was investigated.[16] With increasing pulse ratio of Sr, the growth rate per cycle of the composite film increases. Conducting Rutherford back scattering (RBS) revealed a slightly decreasing Sr incorporation while Ti incorporation was increasing. This behavior was not due to the SrO inhibition, but rather due to an increase of Ti incorporation with higher Sr pulse ratio resulting in increased surface reactivity. The growth process of ternary compounds is complex due to multiple interdependencies. Substrate/interface effects do not affect the ALD growth process alone. Several other process-affecting parameters will be discussed in the next section.

2.5 | Precursor chemistry, process parameters and their effects

ALD process parameters include in-cycle (during the deposition) conditions and post deposition treatments, both of which have considerable effect on the stoichiometry[21] and crystal structure.[22] This gives us control of property optimization according to the application requirement.

The first step towards perovskite thin film development is the selection of a suitable precursor followed by the determination of process parameters such as temperature and oxidation source. Sr- and Ba-based perovskites are commonly deposited with diketonates-[23] and cyclopentadienyl (Cp)-based precursors.[17,24] The bonding energy between the ligand and the metal atom in different precursors has a direct effect on the growth process.[25] There is usually a tradeoff; the organics should be easily removable from the metal center resulting in high reactivity. Dimerization of the organic substances and cleavage of the chains at different locations from the metal-organic bond must be avoided, putting limitations on the reactivity and compounds utilizable. The Cp-based precursors are found to be the ideal candidates. In the case of SrO, Cp-based ligands have a comparatively weaker bond with the Sr when compared with β-diketonate ligands. With a weaker bond present between the metal and the ligand, the probability of its bond breaking and reacting with the hydroxyl groups on the substrate increases. The energy required for breaking the bond between the metal and the first ligand in Sr (iPr_3Cp) precursor is 2.58 eV, whereas in the case of diketonate-based precursors, a higher energy at 4.94 eV is required. If the bond energy within the ligands is lower than the metal and ligand bond, this could result in carbon contamination due to thermal decomposition of the ligand constituents. Thus, Cp-based precursors are found to be more stable with lower carbon contamination.[25]

In the case of barium oxide (BaO), the situation is similar when comparing bonding enthalpy between the Cp-type and diketonate-based ligands (Cp-Ba 2.38 eV; diketonate-Ba 4.80 eV).[25] For BTO deposition with Ba $(iPr_3Cp)_2$ precursor and titanium tetraisopropoxide (TTIP), the optimized cycle ratio for close to stoichiometric BTO was found to be 1:3 (Ba:Ti).[26] However, low bonding enthalpy is not always a guarantee for film quality. At higher temperatures, Cp-type precursors suffer from thermal decomposition and runaway growth.[27] The lowest temperature deposition of BTO with H_2O (180-210°C) was a reported temperature range using a novel pyrrole-based precursor with bonding enthalpies between the pyrrole and Ba as high as 4.9 eV.[28]

The selected precursors (organometallics and oxidants) determine the process parameters to employ. The types of coreactants being used, such as H_2O, O_2 plasma, or ozone,[8] affect the growth rates and reactor temperatures utilizable.[29] The use of a plasma source has certain advantages—a lower growth temperature can be achieved, allowing us to deposit on thermally fragile substrates or perform processes with thermal limitations. Space defined double patterning method for the fabrication of logic devices requires lower working temperatures, due to the use of temperature sensitive photo resist, thus making the use of plasma imperative.[30] With O_2 plasma, HfO_2 dielectric films with higher interface

quality and density along with lower impurity levels are formed.[31] The low-temperature deposition can also prevent the formation of unwanted oxide layers at the interface.[32] Further, a higher growth rate is possible due to an increase in density of reactive surface sites, thus enhancing the growth per cycle (GPC).[33] There are, however, limitations of PEALD restricting it to certain applications and processes. It yields limited conformality on high aspect ratio structures, due to surface collisions preventing radicals from reaching deep in trenches.[34] In addition, plasma-induced damage can cause defects on the substrate surface due to high-energy ion bombardment. This can also result in undesirable oxidation and nitration at the surface with the use of O_2, or N_2 or NH_3-based plasmas.[35] Yet, in many cases, the advantages of plasma processing for STO and BTO perovskites prevails its drawbacks as not only growth but also crystal structure can be affected. Crystallinity is imperative for obtaining structural properties of perovskites as many of the materials functionalities are hidden in its crystallinity.

For high-k applications, the crystallinity of the thin film affects the dielectric constant; films with lower crystallinity have lower dielectric constant due to a distortion of the B cation within its octahedron, which affects the polarizability.[36] There are different strategies to achieve crystallinity such as seed layering, thermal annealing, plasma treatment, and the use of special precursors.[37] Seed layering is a successful strategy, which crystallizes films comparatively easily when compared with directly deposited layers. A thin layer of 5 nm or less is deposited and annealed at a high temperature for few minutes until crystallized. This is followed by growth of perovskite layers of required thickness, which requires lower annealing time as compared with normal deposition without a seed layer. Thermal annealing is usually a post deposition process, where thermal excitation results in migration of atoms to energy stable positions resulting in improved crystallinity of the perovskite thin film. The use of plasma treatment is advantageous when compared with the two stated techniques, as it achieves crystallinity at a much lower temperature. High-temperature annealing results in microcracks due to film shrinkage in deposited film; similarly, utilization of higher temperature during the deposition process for crystallization results in layer deterioration due to precursor decomposition or desorption.

In an ALD process, there are several reactions taking place creating the possibility of carbon and hydroxide contamination in the layer due to incomplete removal of the precursor ligands. The contamination leads to a decrease in thin film performance, and thus, process parameters should be optimized for optimum ligand interaction during the cyclic process.[38]

A summary of deposition process variations and post deposition treatments is illustrated in Figure 4. These factors need to be optimized for obtaining the perovskite with desired properties.

2.6 | Growth and energetics

STO has been studied with different precursor combinations. The two most common strontium precursors are based on β diketonate and Cp chemistries. With the use of Sr $(TMHD)_2$, Ti $(O^iPr)^4$, and water as coreactant, at a reactor temperature of 390°C, the GPC was found to be 0.015 nm per cycle, which is low for industrial scale production. A low GPC was a result of low chemical reactivity of the strontium precursor with water. Another concern with this precursor combination is carbon contamination, which results in $SrCO_3$ phase formation.[39]

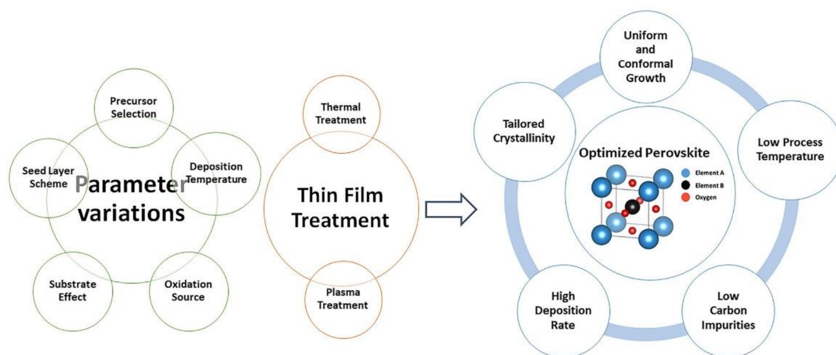

FIGURE 4 Effect of different process parameters on perovskites properties

One can also deposit STO thin films using Cp-based precursors, which are more volatile, thermally stable, and have a higher vapor pressure than the β diketonate-based precursors.[25] With the use of Sr ($^{i}Pr_3Cp$), a 700% increase in growth rate is obtained.[3] The high growth rate is due to the low chemical bond energy between the ligand and the metal center as discussed in the previous section.

The preferred Barium (Ba) precursor for the ALD deposition of BTO is Ba ($Cp^{i}Pr_3)_2$ (Bis (triisopropylcyclopentadienyl)barium). Cp-based precursors are ideal for barium oxide because of the higher rate of reaction, high volatility, and thermal stability compared with other precursor types such as Ba $(acac)_2$, Ba $(hfac)_2$, and Ba $(tmhd)_2$.[25]

3 | CONCLUSION

In the first part of the two-part review, we have examined the growth mechanism of ALD-deposited perovskites, along with interfacial effects, and the effect of different process parameters. With the possibility of depositing a range of materials from an extensive list of accessible elements, ALD provides a way forward for the synthesis of various perovskites. Combining high conformality, uniformity, and control over the growth and stoichiometry of these films makes ALD advantageous to employ compared with other deposition processes. Modern day devices, with novel designs and high efficiencies, require materials with controlled stoichiometries along with complex device designs. The combination of the functionality of perovskites and the deposition advantages of ALD has led to new endeavors in diverse applications. However, the deposition of ALD perovskite still faces challenges. A comprehensive understanding of the growth process and nucleation mechanism is required for wider implementation. Slow growth rates, island formation in the ultrathin regime, and carbon contamination due to ligand decomposition still need to be overcome. Different characterization techniques, especially *in situ* methods, will help us to better understand the growth process, and therefore address and tune parameters.

ACKNOWLEDGEMENT

The Research Council of Norway (Norges Forskningsråd) is acknowledged for the support under the project 274459, Trånslate and for support to the Norwegian Micro- and Nano-Fabrication Facility, NorFab, project 245963/F50. The Norwegian Center for International Cooperation in Education is acknowledged for the funds under project PNA-2017/10077.

ORCID

Anup L. Dadlani https://orcid.org/0000-0002-9311-0713

Jan Torgersen https://orcid.org/0000-0003-1675-8759

REFERENCES

1. Lin EL, Edmondson BI, Hu S, Ekerdt JG. Epitaxial growth of perovskite strontium titanate on germanium via atomic layer deposition. J Vis Exp. 2016;(113):e54268. https://doi.org/10.3791/54268
2. Zhou H, Chen Q, Li G, et al. Interface engineering of highly efficient perovskite solar cells. Science. 2014;345:542-546.
3. Lee SW, Han JH, Han S, et al. Atomic layer deposition of SrTiO3 thin films with highly enhanced growth rate for ultrahigh density capacitors. Chem Mater. 2011;23:2227-2236. https://doi.org/10.1021/cm2002572
4. Defay E., Le Rhun G., Perruchot F., Rey P., Suhm A., Aid M., Liu L.J., Pacheco S., Miller M., Piezoelectric PZT thin films in the 100 nm range: a solution for actuators embedded in low voltage devices, in: 2009 IEEE 22nd International Conference on Micro Electro Mechanical Systems, IEEE, 2009: pp. 619–622.
5. Kubicek M, Bork AH, Rupp JLM. Perovskite oxides—a review on a versatile material class for solar-to-fuel conversion processes. J Mater Chem A. 2017;5:11983-12000. https://doi.org/10.1039/C7TA00987A
6. Withers RL, Thompson JG, Rae AD. The crystal chemistry underlying ferroelectricity in Bi4Ti3O12, Bi3TiNbO9, and Bi2WO6. J Solid State Chem. 1991;94:404-417.
7. Kim DJ, Jo JY, Kim YS, et al. Polarization relaxation induced by a depolarization field in ultrathin ferroelectric BaTiO 3 capacitors. Phys Rev Lett. 2005;95:237602.
8. Wu J, Xiao D, Zhu J. Potassium–sodium niobate lead-free piezoelectric materials: past, present, and future of phase boundaries. Chem Rev. 2015;115:2559-2595. https://doi.org/10.1021/cr5006809
9. Knoops H.C.M., Potts S.E., Bol A.A., Kessels W.M.M., 27—atomic layer deposition, in: Kuech T.F. (Ed.), *Handbook of Crystal Growth (Second Edition)*, North-Holland, Boston, 2015: pp. 1101–1134. https://doi.org/10.1016/B978-0-444-63304-0.00027-5.
10. Ritala M, Niinistö J. Industrial applications of atomic layer deposition. ECS Trans. 2009;25:641-652. https://doi.org/10.1149/1.3207651
11. Mackus AJM, Schneider JR, MacIsaac C, Baker JG, Bent SF. Synthesis of doped, ternary, and quaternary materials by atomic layer deposition: a review. Chem Mater. 2019;31:1142-1183. https://doi.org/10.1021/acs.chemmater.8b02878
12. George SM. Atomic layer deposition: an overview. Chem Rev. 2009;110:111-131. https://doi.org/10.1021/cr900056b
13. Kalinin SV, Spaldin NA. Functional ion defects in transition metal oxides. Science. 2013;341:858-859. https://doi.org/10.1126/science.1243098
14. Chakhalian J, Millis AJ, Rondinelli J. Whither the oxide interface. Nat Mater. 2012;11:92-94. https://doi.org/10.1038/nmat3225
15. Sønsteby HH, Fjellvåg H, Nilsen O. Functional perovskites by atomic layer deposition—an overview. Adv Mater Interfaces. 2017;4:1600903. https://doi.org/10.1002/admi.201600903

16. Popovici M, Van Elshocht S, Menou N, et al. Atomic layer deposition of strontium titanate films using Sr (# 2# 1Cp) 2 and Ti (OMe) 4. J Electrochem Soc. 2010;157:G1-G6.
17. Wang H, Jiang X, Fu K, Willis BG. Nucleation, hydroxylation, and crystallization effects in ALD SrO. J Phys Chem C. 2013;117:11578-11583.
18. Rahtu A, Hänninen T, Ritala M. In situ characterization of atomic layer deposition of $SrTiO_3$. Le J de Phys IV. 2001;11:r3–923-Pr3–930. https://doi.org/10.1051/jp4:20013115
19. Niemelä J-P, Marin G, Karppinen M. Titanium dioxide thin films by atomic layer deposition: a review. Semicond Sci Technol. 2017;32:093005. https://doi.org/10.1088/1361-6641/aa78ce
20. McDaniel MD, Ngo TQ, Hu S, Posadas A, Demkov AA, Ekerdt JG. Atomic layer deposition of perovskite oxides and their epitaxial integration with Si, Ge, and other semiconductors. Appl Phys Rev. 2015;2:41301.
21. Liang Y, Bonnell D. Effect of variations in stoichiometry on the surface structure of SrTiO3 (001). J Am Ceram Soc. 1995;78:2633-2640.
22. Harjuoja J, Kosola A, Putkonen M, Niinistö L. Atomic layer deposition and post-deposition annealing of PbTiO3 thin films. Thin Solid Films. 2006;496:346-352. https://doi.org/10.1016/j.tsf.2005.09.026
23. Kil D-S, Lee J-M, Roh J-S. Low-temperature ALD growth of SrTiO3 thin films from Sr β-diketonates and Ti alkoxide precursors using oxygen remote plasma as an oxidation source. Chem Vap Deposition. 2002;8:195-197. https://doi.org/10.1002/1521-3862(20020903)8:5<195::AID-CVDE195>3.0.CO;2-9
24. Putkonen M., Niinistö L., Organometallic precursors for atomic layer deposition, in: Fischer R.A. (Ed.), *Precursor Chemistry of Advanced Materials*, Springer, Berlin, Heidelberg, 2005: pp. 125–145. https://doi.org/10.1007/b136145.
25. Holme TP, Prinz FB. Atomic layer deposition and chemical vapor deposition precursor selection method application to strontium and barium precursors. J Phys Chem A. 2007;111:8147-8151.
26. Schindler P, Kim Y, Thian D, An J, Prinz FB. Plasma-enhanced atomic layer deposition of BaTiO3. Scr Mater. 2016;111:106-109. https://doi.org/10.1016/j.scriptamat.2015.08.026
27. Lee W, Han JH, Jeon W, et al. Atomic layer deposition of SrTiO3 films with cyclopentadienyl-based precursors for metal–insulator–metal capacitors. Chem Mater. 2013;25:953-961. https://doi.org/10.1021/cm304125e
28. Acharya S, Torgersen J, Kim Y, et al. Self-limiting atomic layer deposition of barium oxide and barium titanate thin films using a novel pyrrole based precursor. J Mater Chem C. 2016;4:1945-1952.
29. Profijt HB, Potts SE, Van de Sanden MCM, Kessels WMM. Plasma-assisted atomic layer deposition: basics, opportunities, and challenges. J Vac Sci Technol A. 2011;29:50801.
30. Beynet J., Wong P., Miller A., Locorotondo S., Vangoidsenhoven D., Yoon T.-H., Demand M., Park H.-S., Vandeweyer T., Sprey H., Low temperature plasma-enhanced ALD enables cost-effective spacer defined double patterning (SDDP), in: Lithography Asia 2009, International Society for Optics and Photonics, 2009: p. 75201 J.
31. Park PK, Roh J-S, Choi BH, Kang S-W. Interfacial layer properties of HfO2 films formed by plasma-enhanced atomic layer deposition on silicon. Electrochem Solid St. 2006;9:F34-F37.
32. Park HB, Cho M, Park J, et al. Comparison of HfO 2 films grown by atomic layer deposition using HfCl 4 and H 2 O or O 3 as the oxidant. J Appl Phys. 2003;94:3641-3647.
33. Choi SW, Jang CM, Kim DY, et al. Plasma enhanced atomic layer deposition of Al 2 O 3 and TiN. J Korean Phys Soc. 2003;42:975-979.
34. Dendooven J, Deduytsche D, Musschoot J, Vanmeirhaeghe RL, Detavernier C. Conformality of Al2O3 and AlN deposited by plasma-enhanced atomic layer deposition. J Electrochem Soc. 2010;157:G111-G116.
35. Kim BH, Jeon WS, Jung SH, Ahn BT. Interstitial oxygen incorporation into silicon substrate during plasma enhanced atomic layer deposition of Al2O3. Electrochem Solid St. 2005;8:G294-G296.
36. Lee SW, Kwon OS, Han JH, Hwang CS. Enhanced electrical properties of Sr Ti O 3 thin films grown by atomic layer deposition at high temperature for dynamic random access memory applications. Appl Phys Lett. 2008;92:222903.
37. Shim JH, Choi HJ, Kim Y, et al. Process–property relationship in high-k ALD SrTiO 3 and BaTiO 3: a review. J Mater Chem C. 2017;5:8000-8013. https://doi.org/10.1039/Ce6TC05158H
38. Vehkamäki M, Hatanpää T, Ritala M, Leskelä M, Väyrynen S, Rauhala E. Atomic layer deposition of BaTiO3 thin films—effect of barium hydroxide formation. Chem Vapor Deposition. 2007;13:239-246. https://doi.org/10.1002/cvde.200606538
39. Kosola A, Putkonen M, Johansson L-S, Niinistö L. Effect of annealing in processing of strontium titanate thin films by ALD. Appl Surf Sci. 2003;211:102-112. https://doi.org/10.1016/S0169-4332(03)00175-2

How to cite this article: Bin Afif A, Dadlani AL, Burgmann S, Köllensperger P, Torgersen J. Atomic layer deposition of perovskites—Part 1: Fundamentals of nucleation and growth. *Mat Design Process Comm*. 2019;1–7. https://doi.org/10.1002/mdp2.114

Paper 2

Received: 18 September 2019 | Revised: 10 October 2019 | Accepted: 12 October 2019

DOI: 10.1002/mdp2.115

REPORT

WILEY

Atomic layer deposition of perovskites part 2: Designing next generation electronic applications

Abdulla Bin Afif[1] | Anup L. Dadlani[1] | Stephanie Burgmann[1] | Peter Köllensperger[2] | Jan Torgersen[1]

[1]Department of Mechanical and Industrial Engineering, NTNU Trondheim, Trondheim, Norway

[2]Department of Physics, NTNU Trondheim, Trondheim, Norway

Correspondence
Jan Torgersen, Department of Mechanical and Industrial Engineering, NTNU Trondheim, Trondheim, Norway.
Email: jan.torgersen@ntnu.no

Funding information
Norges Forskningsråd, Grant/Award Numbers: 245963/F50, 274459; Norwegian Center for International Cooperation in Education, Grant/Award Number: PNA-2017/ 10077; Norwegian Micro- and Nano-Fabrication Facility, NorFab, Grant/Award Number: 245963/F50; Research Council of Norway, Grant/Award Number: 274459

Abstract

From part one, we learned that perovskites are interesting materials with tunable properties. Here, four current applications are elaborated on; high-κ dielectrics, piezoelectrics, optoelectronics, and solar to energy conversion devices. To start with, we discuss perovskite based dynamic random-access memory (DRAM) capacitors, where ALD strontium titanate (STO) of thickness 10 nm can achieve dielectric constants (k) of up to 146. Next, we discuss ALD perovskite piezoelectric-based device design of nanoelectromechanical systems (NEMS) and microelectromechanical systems (MEMS). There is a renewed interest in barium-based ternary compounds which have piezoelectric coefficients up to 500 pC/ N. We further explore ALD perovskite-based solar photovoltaics (PVs), where conformal and uniform layers of lead sulfide (PbS) absorbing layers allow deposition on large surfaces, facilitating perovskite architectures with conversion efficiency reaching 20%. Finally, we learn how lanthanum-based perovskites can replace cerium oxide, which is currently utilized for thermochemical processes for solar to energy conversion. Subsequently, we discuss different characterization techniques allowing us to deepen our understanding of process property relationships eventually leading to further performance enhancements.

KEYWORDS

atomic layer deposition, high-κ, interfacial growth, nucleation and growth, perovskites, piezoelectric, ultra-thin films

1 | PEROVSKITE-BASED APPLICATIONS

In the first part of this two-part review, we developed a fundamental understanding of ALD deposition of perovskites, based on growth mechanisms, interfacial interactions, precursor chemistries, and energetics. Now, we review applications where the ALD deposition of perovskites have been leveraged.

Abdulla bin Afif and Anup L. Dadlani equally contributed

This is an open access article under the terms of the Creative Commons Attribution License, which permits use, distribution and reproduction in any medium, provided the original work is properly cited.
© 2019 The Authors Material Design & Processing Communications published byJohn Wiley & Sons, Ltd.

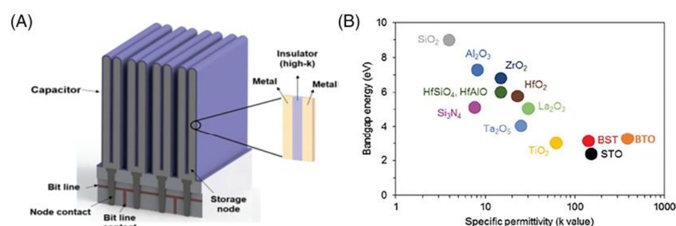

FIGURE 1 (A) Simplified schematic diagrams of a DRAM capacitor, reprint permission obtained from The Royal Society of Chemistry.[47] (B) Bandgap energy and specific permittivity of various dielectric films, available under CC BY-NC-SA 3.0 license from InTech Open.[48] DRAM, dynamic random-access memory

1.1 | High-κ dielectrics for dynamic random-access memory capacitors

ALD has found prominence in the field of micro- and nano-electronics industry due to its ability to deposit conformal and uniform layers, especially for the development of high-κ dielectric materials for dynamic random access memory (DRAM) capacitors (Figure 1A). With downscaling and high capacitance being the requirements of next generation devices, new materials and novel approaches are a prerequisite. The benchmark for the evaluation of dielectric materials for DRAM applications is the equivalent oxide thickness (EOT):

$$EOT = \left(\frac{k_{ox}}{k_{high\text{-}\kappa}}\right) t_{high\text{-}\kappa}, \quad (1)$$

where k_{ox}, $k_{high\text{-}\kappa}$ are the static dielectric constant of SiO_2, and that of the material being studied, respectively, and $t_{high\text{-}\kappa}$ is the thickness of the material. The EOT target is set at 0.3 nm, [1] which can be achieved by the use of high-κ dielectric materials along with ultra-low thickness and high uniformity. Although with ALD, ultra-thin layers can be deposited, they face the challenge of high leakage currents due to the post deposition annealing induced cracks[2] and also with the decrease in thickness, there is an increase in leakage current hampering the performance of the device. Lower thickness can also result in direct electron tunneling, resulting in the flow of electrons through the dielectric or classical forbidden energy states.[3] On the other hand, tunneling has also been observed in thicker films (Fowler-Nordheim Tunneling), where electrons do not tunnel directly to the other side of the barrier, rather, they tunnel from the inversion layer to the SiO_2 conduction band and then to the gate.[4] Thus, an optimized thickness with high dielectric constant is required.

Different materials have been studied as high-κ dielectrics. Figure 1B gives an overview of their bulk dielectric constants; BTO and STO are found to have the highest dielectric constants. With the reduction of thickness into the thin film regime below 50 nm, the dielectric constant decreases due to interfacial dead layer effects, [5] where the dielectric polarization is frozen at the metal dielectric interface.[6] So far, STO and BTO thin films are found to be ideal candidates for future DRAM applications because of the their high dielectric constants (above 120).[7–9] Table 1 gives an overview of the dielectric properties of perovskite thin films and the factors affecting their properties.

TABLE 1 Dielectric constant of perovskite based thin films synthesized by ALD

Material	Thickness, nm	κ (dielectric const.)	EOT	Remarks	Year	Reference
$SrTiO_3$	10	146	0.57	Change in K with composition Ti/ (Ti + Sr) = 32%- 61%	2011	50
$SrZrO_3$	11.5	31	0.8	Epitaxial growth on pretreated Ge substrate	2018	51
$SrHfO_3$	4.6	17	1	Growth on Ge substrate with post- dep. annealing	2014	52
$BaTiO_3$	20	35	2.2	Low temperature deposition (180°C) with the use of Pyrrole- based precursor.	2015	53
$BaTiO_3$	32	73	1.8	Increase in permittivity is observed with post deposition annealing at 600°C	2007	54
$BaTiO_3$	5	122	0.38	Post deposition plasma treatment improves the EOT	2014	55

1.2 | Piezoelectric

Micromechanical systems (MEMS) have found use of thin films based on piezoelectric materials which work on the principle of conversion of applied strain energy to electric signal and vice versa. A renewed interest is seen in recent years towards new piezoelectric materials to replace lead zirconate titanate (PZT), which is facing restrictions due to its hazardous nature.[10] Despite this, PZT has remained the preferred material for micro actuators, microphones, and energy harvesting devices, due to its exceptional piezoelectric properties. With new technologies and applications being explored for the paths toward nanoelectromechanical systems (NEMS), ALD can play a vital role for the deposition of ultra-thin films for NEMS and MEMS technologies. Studies have been conducted on the implementation of thin films using different deposition methods for piezoelectric applications; 100- nm thick PZT perovskite films have been used as piezoelectric material for low voltage actuators[11] (Figure 2A) using sputtering and sol-gel deposition methods. In another work, similar thickness of sputter deposited aluminum nitride (AlN) was used for logical nano-switching.[12] The use of ALD will be advantageous in terms of uniformity and conformality in the ultra-thin regime. With wider availability of precursors, it is now possible to deposit different perovskites, although in many cases, finding the right chemicals and tuning the parameters are challenging. ALD deposited barium-based perovskites can be used, due to their ideal piezoelectric properties along with a proven ALD deposition process of barium oxide and barium titanate. Figure 2B gives an overview of the development of piezoelectric materials with respect to the piezoelectric coefficient. The piezo electric coefficient d_{33} of barium-based perovskites is comparable with PZT.

1.3 | Optoelectronics

Perovskite-based solar cells are one of the most important and widely studied applications using perovskite-based compounds.[13] Efficiencies of more than 20% have been achieved,[14] making perovskite devices competitive to conventional and commercial Si-based PV technology. Methylammonium lead bromide/ iodide ($CH_3NH_3PbI_3$), a lead organo-halide perovskite, is found to have excellent optoelectronic properties with an optical band gap of 1.55 eV in the near-infrared region and a high absorption per unit length of 10^4 cm^{-1} just above the band gap.[15] The excellent optoelectronic properties have been utilized in other applications, such as light emitting diodes[16] and lasers.[17] The advantages of using ALD for the development of organometallic perovskites compared with solution-based processes are that ALD allows us to work at lower temperatures, gives conformal growth on larger areas, and does not require very low vacuum. The above factors make ALD suitable for industrial implementation. Recently, a novel approach was adopted, termed as a hybrid deposition method (Figure 3), where the first step involved ALD deposition of PbS, followed by sublimation of iodine chips in a sealed environment and then dipped in CH_3NH_3I and IPA.[15] By using the above process with ALD deposition of PbS, a 72- nm thin layer had a gain coefficient of 3200 ± 830 cm^{-1}, which is comparable to single crystal semiconductors in optical amplification technology.[18]

This hybrid process can be implemented for the fabrication of light emitting diodes (Figure 4) based on direct band gap semiconductors.[16] Here, ALD provides the feasibility of working at lower temperatures with controlled conformal growth. The thickness of the perovskite layer in this structure is 15 nm, which is a thickness perfectly suitable for ALD.

Coming to the ALD component of the hybrid deposition, the PbS thin film is deposited at a reactor temperature of 150°C using Pb $(tmhd)_2$ [Lead bis(2, 2,6,6- tetramethyl-3,5- heptanedionate)], and H_2S precursors (Figure 3). Whereas PbS was used as an intermediate layer for subsequent sublimation and conversion into PbI_2 for further processing, ALD PbS layers are also directly used for optoelectronic applications. For example, PbS has been deposited using ALD for quantum confinement structures[19]; it is a well-studied and implemented process, which can be extended to hybrid thin films for novel applications.

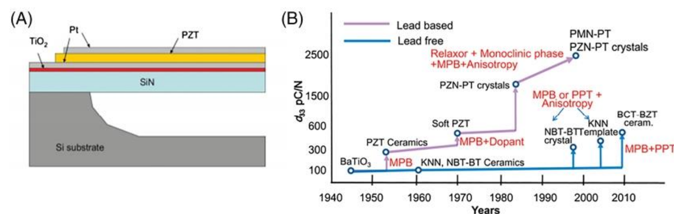

FIGURE 2 (A) A 100- nm thick PZT film in a low voltage actuator, reprinted with permission from IEEE.[11] (B) The development of perovskite ferroelectrics with respect to the piezoelectric coefficient d_{33}. The factors responsible for property enhancement are listed in red, reprinted with permission from IEEE. [49] PZT, lead zirconate titanate

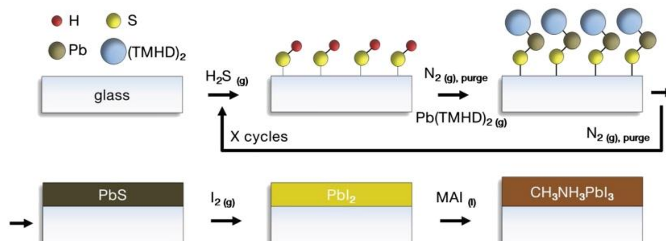

FIGURE 3 Atomic layer deposition of $CH_3NH_3PbI_3$, ALD PbS is deposited from alternating cycles of H_2S and Pb (tmhd)$_2$ vapor on a glass substrate followed by a sublimation process with iodine chips and finally dipped in the solution of CH_3NH_3I in IPA, reprinted with permission from *Advanced Materials*[15]

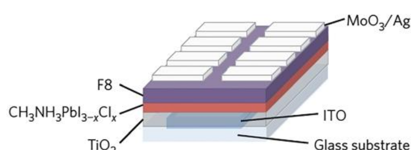

FIGURE 4 Device architecture of the $CH_3NH_3PbI_3$–xClx PeLED, reprinted with permission from Springer Nature[16]

1.4 | Solar to energy conversion (thermo-chemical process)

New devices and technologies are being explored and developed for renewable energy applications with higher efficiency. With one of the most important criteria being environmental sustainability, a technology with great potential is "solar to fuel." It works on the principle of thermochemical reaction cycles, in which H_2O and CO_2 are converted into H_2 and CO gas with the help of perovskite materials. As seen in the Figure 5A, concentrated light provides heat for the endothermic reaction at the perovskite surface, followed by an exothermic reaction with H_2O and CO_2, resulting in the formation of H_2 and CO.

Currently, ceria is the preferred material for this application due to its high efficiency and high thermal and chemical stability, but the higher working temperature is a concern, due to excess thermal load to the system. An alternate family of materials, which is being pitched as a replacement, are perovskites. They have an energetically stable electronic system, which can accommodate a range of elements, [20] and also allow fine-tuning of stoichiometry and electro-chemical properties. With perovskites, a wide range of stoichiometries can be achieved, fitting the process requirement for the exchange reactions occurring at the surface. One of the process requirements is that the material remains in the same phase during the reduction and oxidation conditions, where failure would hamper the durability and performance of the system.[20]

Most of the perovskites being studied for this application are complex quaternary oxides based on La, Sr, Mn, Cr, Fe, Co, and Al.[20] With the development of new ALD precursors and wider availability of different materials, it is now possible to grow complex compounds with good control on the composition and stoichiometry. Lanthanum-based perovskites deposited using ALD have been studied extensively for different applications.[21] Recently, ALD deposited Pd doped $LaFeO_3$ was studied as a smart catalyst which undergoes efficient redox cycling.[22] ALD was

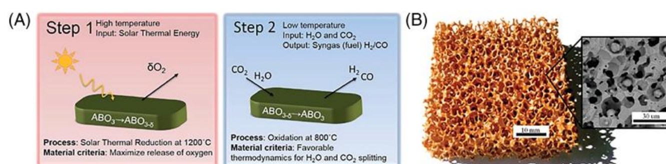

FIGURE 5 (A) Schematic of the two-step thermochemical solar-to-fuel conversion process, reprinted with permission from the Royal Society of Chemistry.[21] (B) Ceria sample with dual-scale porosity, reprinted with permission from the Royal Society of Chemistry[23]

instrumental because of its ability to deposit highly conformal layers on high surface area supports, such as porous structures (Figure 5B), thus opening new avenues for research and development in the field of thermo-chemical splitting of CO_2.[23] There are still challenges with perovskites with regards to chemical stability and low enthalpies, which needs to be addressed.[24] Lower enthalpies are favorable for the reduction reaction and also result in lower hydrogen yield or fuel formation during the oxidation steps.[25,26]

2 | CHARACTERIZATION OF PEROVSKITE THIN FILMS: INSIGHTS ON PEROVSKITE GROWTH

The development of diverse engineered perovskite materials prepared by ALD requires careful identification of their properties and verification of process reproducibility. Characterization techniques for perovskite materials are similar to the approaches used for any other thin film deposited by CVD or PVD. In the case of ALD, the quantities deposited as well as the crystal structure and composition tunability allow freedom in the application specific design; however, the characterization becomes more challenging than with the former thin film deposition techniques.[27] In Table 2, characterization techniques are listed along with the information that can be obtained. Note that we do not intend to review all the methods listed in detail but rather want to give an overview and demonstrate some capabilities through select illustrative examples. Here, we have divided these techniques into three main groups: general optical techniques based on IR or visible light, TEM-based characterization, and X-ray–based techniques.

One of the more common characterizations of ALD films performed is with an ellipsometer. This optical technique is used to readily obtain film thickness and growth rate per cycle (GPC), two important parameters in ALD.[28] FTIR[29] and Raman[30] use IR radiation to give information on chemical functionalities present and bonding environments. Morphological and texture properties can be revealed by AFM, SEM, and TEM. Hara et al.[27] utilized AFM, SEM, and TEM along with other techniques to determine the rationale behind O_2 ppb sensing detectivity of STO. TEM is a versatile tool that can be further combined with other techniques to get crystal structure by electron diffraction (ED)[31] and chemical composition and states through electron energy loss spectroscopy (EELS).[32] EELS is a powerful technique that can be used to get local electronic and geometric structure information within specific positions in the sample.[33]

Expanding into the x-ray regime, a number of scattering and spectroscopic techniques are available to further learn about perovskite thin films. Starting with the scattering techniques, XRR can provide electron density, thickness, and roughness.[34] XRD can provide phase and size of crystalline grains.[35] On the spectroscopic side, XRF can be used to determine composition and impurities.[36] Knowledge on the oxygen vacancies, the reducibility, and the binding/ oxidation state of metals and oxides in the perovskite compound resulting from the crystal structure can be achieved by XPS, making the technique crucial for thin film analysis.[37] In recent years, X-ray absorption spectroscopy (XAS) has been used to obtain critical information in ultra-thin film structures, which was not possible with other techniques.[38] While synchrotrons (where XAS is performed) are not easily accessible as tabletop X-ray sources, the advantages of using such a technique to characterize materials cannot be overstated. This is especially true when one seeks to elucidate mechanistic information of ALD perovskite films and to understand how certain parameters affect its growth and its properties. As the use of synchrotrons has been on the rise to characterize ALD thin films, there still lacks any meaningful number of papers on ALD perovskites.[22,39] XAS is a sensitive, element specific technique that can be used to get local electronic and geometric structure information of materials, similar to EELS, however with several key advantages.[40] XAS at a synchrotron can probe a much wider range of elemental edges and has much higher S/ N due to orders of magnitude higher flux, pushing the limit of elemental detection much lower. Specifically, XAS can be divided into three main regions—pre-edge, X-ray absorption near edge spectroscopy (XANES) region, and extended x-ray absorption fine structure (EXAFS). Each region provides valuable information about the material. The pre-edge regions can be used to estimate ligand-field, spin-state, and centro-symmetry. The XANES region can be used to get some local geometric structure, metal-ligand overlap via shakedown transitions, ligand arrangement, oxidation state, and density of states. The EXAFS region can be used to obtain bond distances, coordination numbers, and Debeye-Waller factors.[41] Given the information that it contains, one can surmise that XAS is a powerful technique and will likely become ubiquitous in the characterization of ALD ternary and quaternary perovskite films. Additionally, combining XAS data with quantum simulations and even machine learning can create an amalgam that can significantly enhance our understanding of ALD reactions and the perovskite thin films that are deposited by this technique.

3 | OUTLOOK

Although ALD has numerous advantages, there are limitations to be addressed. For example, in order to deposit certain materials, narrow ranges in process parameters must be abided by. In addition, the nucleation and growth mechanisms for most of the ALD deposited perovskites are not yet clearly understood. In the ultra-thin film regime, meticulous process optimization is required for uniform growth. Another cause of concern is carbon contamination, which often tends be a detriment in performance. A better understanding of the ALD process and solutions for the above concerns will help us to attain maximal performances in modern devices that utilize perovskites.

TABLE 2 Characterization tools and acquirable information

		Thickness	Reflective index	Density	Topography	Morphology	Chemical state	Electrical state
AFM		x			x	x		
c- AFM								
PFM						x		
SEM		x			x	x		
Raman		x						
ToF- ERDA								
RBS								
IR/ FT- IR		x					x	
Ellipsometry		x	x					
TEM/ STEM	HRTEM	x				x		
	EDS/ EDX							
	HAADF							
	EELS	x					x	x
X- ray- based	XRR	x		x	x			x
	HRXRD	x						
	XPS	x					x	x
	XRD							
	XRF	x					x	x
	GIXRD							
	XAS	x					x	x

TABLE 2 Characterization tools and acquirable information

	Interfacial structure	Conductivity	Absorbance	Oxidation state	
AFM	x				
c- AFM	x		x		
PFM		x			
SEM	x	x			
Raman					
ToF- ERDA					
RBS					
IR/ FT- IR		x		x	
Ellipsometry	x				
TEM/ STEM	x	x			
		x			x
X- ray- based					
					x
				x	x
		x		x	x

Another important aspect is to study the effect of the lattice mismatch with the underlying substrate of the perovskite thin film on its properties. It has been reported that the lattice mismatch at the interface results in strain. Compressive strain has a negative effect on the dielectric constant.[42]

Piezoelectric properties of ALD deposited BT-based perovskites[43] (BCZT—barium calcium zirconium titanium) have not been studied so far. It would be interesting to explore the effect of different dopants, considering the number of possibilities in terms of different materials combined with variations in processing conditions. Here lies an opportunity for identification of the limitations and possibilities of improved performance by process and material optimization.[44] Interest has grown in BT-based materials due to their outstanding piezoelectric properties and provides a lead-free alternate to the commonly used PZT.[45]

Currently, for the fabrication of the spectral radiation absorbing layer in perovskite-based solar cell, a solution-based process[46] is employed. New devices and technologies require the layers to be highly conformal, uniform, and, in some cases, ultra-thin. Thus, it becomes important to use the ALD technique, due to its versatile nature and proven record in industrial implementation. To our knowledge, there have been no reported processes for direct deposition of lead organo-halide perovskites, an area worth exploring.

4 | CONCLUSION

In our study, we have found that there are numerous applications where ALD deposited perovskites are beneficial, due to the advantages the technique has to offer. Currently, ALD is extensively used in the micro and nano fabrication industries for device manufacturing. Considerable research is being carried out on the ALD deposition of perovskites for DRAM applications, where STO and BTO thin films are found to be ideal candidates due to their high dielectric constants over 146, giving an EOT below 0.5 nm. The EOT value is very close to the target of 0.3 nm set by ITRS road map. Another field that has caught the attention of researchers in the last decade is perovskite-based piezo-electrics for NEMS- and MEMS-based applications. BT-based perovskites with high piezoelectric coefficient d_{33} = 500 pC/ N, comparable with PZT can be a promising Pb-free alternative piezoelectric materials. One more application, which has been in the mainstream in terms of industrial implementation, is perovskite-based solar cells. Solar cells with efficiencies of more than 20% have been developed using $CH_3NH_3PbI_3$, thus making them very competitive with silicon-based solar PV technologies. A novel hybrid ALD process combining ALD PbS with further processing can also be implemented for the fabrication of light emitting diodes. For these applications, ALD provides the feasibility of working at lower temperatures with controlled conformal growth. Also in solar to energy conversion, lanthanum-based perovskite compounds are used for thermo-chemical processes where oxidation and reduction reactions are leveraged for the production of H_2 and CO. ALD deposition of these perovskites would help us to conduct conformal deposition on high surface area structures, thus ultimately helping us to improve the fuel yield. Perovskite redox materials will allow for lower temperatures (1200°C) compared with commonplace cerium oxide, which generally require higher temperature (1500°C) resulting in unpractical thermal load to the system. These applications show a great deal of possibilities in terms of performance enhancements and novelty. In this two-part review, we attempted to provide an understanding of the growth of ALD perovskites and gave an application-centered overview of the characteristics of perovskite processing in the ultrathin films regime while providing insight into process, structure, and properties. This will be useful for researchers and developers aiming to implement or better their processes and devices infusing the fascinating properties of this class of materials.

ACKNOWLEDGEMENTS

The Research Council of Norway and Norges Forskningsrad are acknowledged for the support under the project number 274459, Trånslate and for support to the Norwegian Micro- and Nano-Fabrication Facility, NorFab, project number 245963/F50. The Norwegian Center for International Cooperation in Education is acknowledged for the funds under project number PNA-2017/ 10077.

ORCID

Anup L. Dadlani https://orcid.org/0000-0002-9311-0713
Jan Torgersen https://orcid.org/0000-0003-1675-8759

REFERENCES

1. Wilson L., International technology roadmap for semiconductors(ITRS). Semiconductor Industry Association,2013. https://www.semiconductors.org/resources/2013-international-technology-roadmap-for-semiconductors-itrs/.
2. Menou N, Popovici M, Clima S, et al. Composition influence on the physical and electrical properties of SrxTi(1 − x)Oy-based metal–insulator–metal capacitors prepared by atomic layer deposition using TiN bottom electrodes. J Appl Phys. 2009;106:094101. https://doi.org/10.1063/1.3246835
3. Tsu R, Esaki L. Tunneling in a finite superlattice. Appl Phys Lett. 1973;22:562-564.
4. Gehring A. Tunneling models for semiconductor device simulation. Handbook of Theoretical and Computational Nanotechnology. 2006;10:469-543.

5. Oh J, Moon T, Kim T-G, et al. The dependence of dielectric properties on the thickness of (Ba, Sr) TiO_3 thin films. Current Applied Physics. 2007;7: 168-171.
6. Majdoub MS, Maranganti R, Sharma P. Understanding the origins of the intrinsic dead layer effect in nanocapacitors. Physical Review B. 2009;79: 115412.
7. Choudhury BK, Rao KV, Choudhury RNP. J Mater Sci. 1989;24:3469-3474.
8. Dutta PK, Asiaie R, Akbar SA, Zhu W. Hydrothermal synthesis and dielectric properties of tetragonal $BaTiO_3$. Chem Mater. 1994;6:1542-1548.
9. Kittl JA, Opsomer K, Popovici M, et al. High-κ dielectrics for future generation memory devices. Microelectronic Engineering. 2009;86:1789-1795.
10. Zheng T, Wu J, Xiao D, Zhu J. Recent development in lead-free perovskite piezoelectric bulk materials. Progress in Materials Science. 2018;98:552-624. https://doi.org/10.1016/j.pmatsci.2018.06.002
11. Defay E, Le Rhun G, Perruchot F, et al. Piezoelectric PZT thin films in the 100 nm range: a solution for actuators embedded in low voltage devices. 2009 IEEE 22nd International Conference on Micro Electro Mechanical Systems, IEEE. 2009;619-622.
12. Sinha N, Guo Z, Felmetsger V, Piazza G. 100 nm thick aluminum nitrade based piezoelectric nano switches exhibiting 1 MV threshold voltage via body-biasing. Proc. Solid-State Sensors, Actuators & Microsyst. Workshop, Hilton Head, SC, USA,Jun 2010.2010https://repository.upenn.edu/meam_papers/256
13. De Wolf S, Holovsky J, Moon S-J, et al. Organometallic halide perovskites: sharp optical absorption edge and its relation to photovoltaic performance. The Journal of Physical Chemistry Letters. 2014;5:1035-1039.
14. Zhou H, Chen Q, Li G, et al. Interface engineering of highly efficient perovskite solar cells. Science. 2014;345:542-546.
15. Sutherland BR, Hoogland S, Adachi MM, et al. Perovskite thin films via atomic layer deposition. Adv Mater. 2015;27:53-58.
16. Tan Z-K, Moghaddam RS, Lai ML, et al. Bright light-emitting diodes based on organometal halide perovskite. Nat Nanotechnol. 2014;9:687.
17. Zhang Q, Ha ST, Liu X, Sum TC, Xiong Q. Room-temperature near-infrared high-Q perovskite whispering-gallery planar nanolasers. Nano Lett. 2014;14:5995-6001.
18. Delfyett, P.J. *Ultrafast single- and multiwavelength modelocked semiconductorlasers: Physics and applications," in Ultrafast Lasers: Technology and Applications, 1st ed.* New York, NY, USA: CRC Press, 2002.
19. Dasgupta NP, Lee W, Prinz FB. Atomic layer deposition of lead sulfide thin films for quantum confinement. Chem Mater. 2009;21:3973-3978.
20. Kubicek M, Bork AH, Rupp JLM. Perovskite oxides—a review on a versatile material class for solar-to-fuel conversion processes. J Mater Chem A. 2017;5:11983-12000. https://doi.org/10.1039/C7TA00987A
21. Bork AH, Kubicek M, Struzik M, Rupp JLM. Perovskite La 0.6 Sr 0.4 Cr 1 − x Co x O 3 − δ solid solutions for solar-thermochemical fuel production: strategies to lower the operation temperature. J Mater Chem A. 2015;3:15546-15557. https://doi.org/10.1039/C5TA02519B
22. Onn TM, Monai M, Dai S, et al. Smart Pd catalyst with improved thermal stability supported on high-surface-area $LaFeO_3$ prepared by atomic layer deposition. J Am Chem Soc. 2018;140:4841-4848.
23. Furler P, Scheffe J, Marxer D, et al. Thermochemical CO_2 splitting via redox cycling of ceria reticulated foam structures with dual-scale porosities. Phys Chem Chem Phys. 2014;16:10503-10511.
24. Deml AM, Stevanovi V, Muhich CL, Musgrave CB, O'Hayre R. Oxide enthalpy of formation and band gap energy as accurate descriptors of oxygen vacancy formation energetics. Energ Environ Sci. 2014;7:1996-2004.
25. Scheffe JR, Steinfeld A. Oxygen exchange materials for solar thermochemical splitting of H_2O and CO_2: a review. Mater Today. 2014;17:341-348.
26. Takacs M, Hoes M, Caduff M, Cooper T, Scheffe JR, Steinfeld A. Oxygen nonstoichiometry, defect equilibria, and thermodynamic characterization of $LaMnO_3$ perovskites with Ca/ Sr A-site and Al B-site doping. Acta Mater. 2016;103:700-710.
27. Hara T, Ishiguro T. Oxygen sensitivity of $SrTiO_3$ thin film prepared using atomic layer deposition. Sens Actuators B. 2009;136:489-493.
28. Langereis E, Heil SBS, Knoops HCM, Keuning W, Van de Sanden MCM, Kessels WMM. In situ spectroscopic ellipsometry as a versatile tool for studying atomic layer deposition. J Phys D Appl Phys. 2009;42:73001.
29. Klaus JW, Ferro SJ, George SM. Atomic layer deposition of tungsten nitride films using sequential surface reactions. J Electrochem Soc. 2000;147: 1175-1181.
30. Di Giacomo F, Zardetto V, D'Epifanio A, et al. Flexible perovskite photovoltaic modules and solar cells based on atomic layer deposited compact layers and UV-irradiated TiO_2 scaffolds on plastic substrates. Advanced Energy Materials. 2015;5:1401808.
31. Lee SW, Liu Y, Heo J, Gordon RG. Creation and control of two-dimensional electron gas using Al-based amorphous oxides/ $SrTiO_3$ heterostructures grown by atomic layer deposition. Nano Lett. 2012;12:4775-4783.
32. Gallegos-Orozco V, Martínez-Sánchez R, Espinosa-Magaña F. In situ characterization of the ferroelectric transition in Ba TiO_3 by EELS and comparison with ab initio methods. Physical Review B. 2008;77:45128.
33. Kurata H, Isojima S, Kawai M, Shimakawa Y, Isoda S. Local analysis of the edge dislocation core in $BaTiO_3$ thin film by STEM-EELS. J Microsc. 2009; 236:128-131.
34. Lee H, Park YJ, Baik S, Kim H. Initial stage growth during plasma-enhanced atomic layer deposition of cobalt. Chemical Vapor Deposition. 2012;18: 41-45.
35. Methaapanon R, Geyer SM, Brennan S, Bent SF. Size dependent effects in nucleation of ru and ru oxide thin films by atomic layer deposition measured by synchrotron radiation x-ray diffraction. Chem Mater. 2013;25:3458-3463.
36. Levrau E, Devloo-Casier K, Dendooven J, et al. Atomic layer deposition of TiO_2 on surface modified nanoporous low-k films. Langmuir. 2013;29: 12284-12289.
37. Zhu J, Li H, Zhong L, et al. Perovskite oxides: preparation, characterizations, and applications in heterogeneous catalysis. Acs Catalysis. 2014;4:2917-2940.
38. Devloo-Casier K, Ludwig KF, Detavernier C, Dendooven J. In situ synchrotron based x-ray techniques as monitoring tools for atomic layer deposition. Journal of Vacuum Science & Technology A. 2014;32:10801.
39. Torgersen J, Acharya S, Dadlani AL, et al. Relating electronic and geometric structure of atomic layer deposited $BaTiO_3$ to its electrical properties. The Journal of Physical Chemistry Letters. 2016. 8:1428-1433. https://doi.org/10.1021/acs.jpclett.6b00393
40. de Groot F, Kotani A. *Core level spectroscopy of solids*. Boca Raton: CRC Press; 2008.
41. Calvin S, Furst KE. *XAFS for everyone*. Boca Raton: CRC Press; 2013.

42. Shaw TM, Suo Z, Huang M, Liniger E, Laibowitz RB, Baniecki JD. The effect of stress on the dielectric properties of barium strontium titanate thin films. Appl Phys Lett. 1999;75:2129-2131.
43. Acosta M, Novak N, Rojas V, et al. $BaTiO_3$-based piezoelectrics: fundamentals, current status, and perspectives. Appl Phys Rev. 2017;4:041305. https://doi.org/10.1063/1.4990046
44. Mackus AJM, Schneider JR, MacIsaac C, Baker JG, Bent SF. Synthesis of doped, ternary, and quaternary materials by atomic layer deposition: a review. Chem Mater. 2019;31:1142-1183. https://doi.org/10.1021/acs.chemmater.8b02878
45. Liu W, Ren X. Large piezoelectric effect in Pb-free ceramics. Phys Rev Lett. 2009;103:257602. https://doi.org/10.1103/PhysRevLett.103.257602
46. Burschka J, Pellet N, Moon S-J, et al. Sequential deposition as a route to high-performance perovskite-sensitized solar cells. Nature. 2013;499:316-319. https://doi.org/10.1038/nature12340
47. Shim JH, Choi HJ, Kim Y, et al. Process–property relationship in high-κ ALD $SrTiO_3$ and $BaTiO_3$: a review. Journal of Materials Chemistry C. 2017;5:8000-8013. https://doi.org/10.1039/C6TC05158H
48. Sunami H., Dimension Increase in metal-oxide-semiconductor memories and transistors, in: P. K (Ed.), *Advances in Solid State Circuit Technologies*, InTech, 2010. https://doi.org/10.5772/8638.
49. Li F, Wang L, Jin L, et al. Piezoelectric activity in Perovskite ferroelectric crystals, IEEE Transactions on Ultrasonics, Ferroelectrics, and Frequency. Control. 2015;62:18-32.
50. Lee SW, Han JH, Han S, et al. Atomic layer deposition of $SrTiO_3$ thin films with highly enhanced growth rate for ultrahigh density capacitors. Chem Mater. 2011;23:2227-2236. https://doi.org/10.1021/cm2002572
51. Hu S, Ji L, Chen P-Y, et al. Crystalline $SrZrO_3$ deposition on Ge (001) by atomic layer deposition for high-κ dielectric applications. J Appl Phys. 2018;124:44102.
52. McDaniel MD, Hu C, Lu S, et al. Atomic layer deposition of crystalline $SrHfO_3$ directly on Ge (001) for high-κ dielectric applications. J Appl Phys. 2015;117:54101.
53. Acharya S, Torgersen J, Kim Y, et al. Self-limiting atomic layer deposition of barium oxide and barium titanate thin films using a novel pyrrole based precursor. Journal of Materials Chemistry C. 2016;4:1945-1952.
54. Vehkamäki M, Hatanpää T, Ritala M, Leskelä M, Väyrynen S, Rauhala E. Atomic layer deposition of $BaTiO_3$ thin films—effect of barium hydroxide formation. Chemical Vapor Deposition. 2007;13:239-246. https://doi.org/10.1002/cvde.200606538
55. An J, Usui T, Logar M, et al. Plasma processing for crystallization and densification of atomic layer deposition $BaTiO_3$ thin films. ACS Appl Mater Interfaces. 2014;6:10656-10660. https://doi.org/10.1021/am502298z

How to cite this article: Bin Afif A, Dadlani AL, Burgmann S, Köllensperger P, Torgersen J. Atomic layer deposition of perovskites part 2: Designing next generation electronic applications. *Mat Design Process Comm.* 2019;1–10. https://doi.org/10.1002/mdp2.115

Paper 3

journal of the mechanical behavior of biomedical materials 111 (2020) 104005

Contents lists available at ScienceDirect

Journal of the Mechanical Behavior of Biomedical Materials

journal homepage: http://www.elsevier.com/locate/jmbbm

Improving stress corrosion cracking behavior of AZ31 alloy with conformal thin titania and zirconia coatings for biomedical applications

M. Peron *, A. Bin Afif, A.L. Dadlani, F. Berto, J. Torgersen

Department of Industrial and Mechanical Engineering, Norwegian University of Science and Technology, Richard Birkelands vei 2b, 7034, Trondheim, Norway

ARTICLE INFO

Keywords:
Stress corrosion cracking (SCC)
Biomedical applications
Magnesium alloys
Thin films
Atomic layer deposition (ALD)

ABSTRACT

Magnesium and its alloys have been widely studied as materials for temporary implant devices. However, corrosion-assisted cracking phenomena such as stress corrosion cracking (SCC) continue to prevent their mainstream use. For the first time, we explore the SCC susceptibility of Atomic Layer Deposition (ALD) coated AZ31 alloys in Simulated Body Fluid (SBF). Conformal 100 nm coatings of titania and zirconia were deposited on standard dogbone specimens and subjected to slow strain rate tests at 3.5 10^{-6} s^{-1} and a temperature of 37 °C. Remarkably, the SCC susceptibility index I_{UTS} was reduced by 6% and 40% and the I_{ε} was reduced by more than 70% and 76% with a titania and zirconia coating, respectively. Potentiodynamic polarization, hydrogen evolution and fracture behavior of the samples revealed the drastic corrosion reduction to be the main reason for the susceptibility reduction. We discuss the observed SCC behavior of our samples in light of the coatings' electrochemical activities, wettabilities, surface integrities and mechanical properties. This straightforward conformal surface treatment can be useful as a workaround for one of the major bottlenecks of biomedical Mg based implants and hence provides a possible pathway for making them more commonplace in the field.

1. Introduction

The number of orthopedic surgeries is continuously increasing (Ginebra et al., 2006; http://share.iofbonehealt). However, common implant materials are affected by two main issues, i.e. 1) the stress-shielding phenomenon as a consequence of the materials' elastic modulus difference to human bone (Bauer and Schils, 1999; Dujovne et al., 1993; Engh and Bobyn, 1988; Kerner et al., 1999; Sumner and Galante, 1992; Turner et al., 1997; Van Rietbergen et al., 1993; Wolff, 1986) and 2) the risk of long-term complications such as inflammations and secondary surgeries (Pound, 2014a, 2014b; Jacobs et al., 1998, 2003; Beech et al., 2006). The mechanical compatibility to bone renders Magnesium (Mg) and its alloys excellent implant material alternatives (Singh Raman et al., 2015; Peron et al., 2017; Staiger et al., 2006; Hänzi et al., 2009), especially in light of their high biocompatibility. Mg is in fact highly abundant in the human body (Staiger et al., 2006), is essential for the metabolism in many biological mechanisms, is a cofactor for many enzymes (Hänzi et al., 2009), and Mg^{2+} ions resulting from the degradation process are reported to aid the healing process and the growth of tissue (Peron et al., 2020a). However, their application as load bearing implant material is still not clinically accepted (Peron et al., 2020b; Wang et al., 2020). High corrosion rates reduce their compatible properties prematurely, before a respective device can accomplish its defined mission (Song, 2007). Furthermore, alkalization and accumulation of hydrogen pockets next to the implant can cause the necrosis of tissues. It is a necessity to reduce the corrosion rate of load bearing Mg implants to a level where hydrogen evolution and alkalization can be balanced by metabolic mechanisms. However, this challenge cannot be tackled by tailoring the chemical compatibility only. The implant must also possess adequate resistance to cracking under the simultaneous action of the corrosive environment and mechanical load. In this way, corrosion-assisted cracking phenomena, such as stress corrosion cracking (SCC), are already a challenge for non-degradable implant materials in clinical applications (Teoh, 2000; Akahori et al., 2000; Jafari et al., 2015; Antunes and de Oliveira, 2012) and are expected to be of even bigger concern if the implant material is intended to degrade (Jafari et al., 2017, 2018; Kannan and Raman, 2008). It is thus important to develop Mg-based implants that confer a combination of strength and corrosion resistance in physiologically relevant environments such as Simulated Body Fluid (SBF).

Whereas corrosion mitigation of Mg materials is a common research topic (Qi et al., 2014; Zhen et al., 2014; Hou et al., 2012), the literature

* Corresponding author.
E-mail address: mirco.peron@ntnu.no (M. Peron).

https://doi.org/10.1016/j.jmbbm.2020.104005
Received 11 April 2020; Received in revised form 19 July 2020; Accepted 21 July 2020
Available online 27 July 2020
1751-6161/© 2020 The Authors. Published by Elsevier Ltd. This is an open access article under the CC BY license (http://creativecommons.org/licenses/by/4.0/).

on their resistance to SCC is yet scarce (Peron et al., 2020c). For example, Mohajernia et al. (2018) reported that hydroxyapatite coatings containing multi-walled carbon nanotubes reduce the corrosion current density of AZ31 alloys in SBF at 37 °C by three orders of magnitude. The elongation to failure (ε_f) of AZ31 increased by ~70% under slow strain rate tests (SSRT). Chen et al. (2018) coated Mg–4Zn-0.6Zr-0.4Sr with a composite coating consisting of a poly (lactic-co-glycolic acid) on a micro-arc oxidated (MAO) layer on the substrate. They reported an increase in the ε_f in modified SBF by ~120% as compared to the bare alloy. The application of coatings seems promising for SCC susceptibility reduction. However, the reported coating technologies have limitations in line of sight (Smith, 2007), conformality, process inherent density (Lei, 2015) and biocompatibility (Sonia and Sharma, 2014) as well as limited controllability of the thickness (Li, 2013).

Atomic Layer Deposition (ALD) does not have these limitations. It yields thin films with high conformality, uniformity and a thickness controllable on the atomic level (Cremers et al., 2019). Recently, it has been explored for corrosion protection (Graniel et al., 2018; Chalker, 2016), where, for example, a 100 nm thick TiO_2 and ZrO_2 layer reduced the corrosion current density of a commercial AZ31 Mg alloy by two orders of magnitude (Marin et al., 2012) and three orders of magnitude (Liu et al., 2018), respectively. Interestingly, the corrosion protection of ALD coated AZ31 samples was found to be much higher than that of sputter coated AZ31 counterparts, especially when considering complex 3D substrates (Peron et al., 2020d).

To the best of our knowledge, the effect of ALD coatings on the SCC susceptibility is yet underexplored. Promising preliminary results were published by the authors (Peron et al., 2019a, 2019b), yet no thorough investigation has been performed. Here, we explore the SCC susceptibility of AZ31 alloy coated with a 100 nm thick ALD ZrO_2 and TiO_2 layers, where ZrO_2 and TiO_2 were chosen as coating materials due to their known biocompatibility (Kasuga et al., 2002; Wang et al., 2002; Uchida et al., 1999; Harianawala, Kheur, Kheur, Sethi, Bal, Burhanpurwala, Sayed; Rimondini, Cerroni, Carrassi, Torricelli). SSRTs at strain rate 3.5 10^{-6} s^{-1} were carried out while immersing the samples in SBF at physiological temperature (37 °C) for the whole duration of the tests. The corrosion behavior was investigated through potentiodynamic polarization curves and hydrogen evolution experiments. The mechanisms of SCC susceptibility reduction were further discussed through fracture surfaces after SSRTs.

2. Materials and methods

2.1. Materials and environment

AZ31 Mg alloy was supplied in the form of commercially available bars. The microstructure of the material in the as-received condition is shown in Fig. 1 and consists of a quite homogeneous α matrix. The initial grain size was measured by the linear intercept method resulting in sizes of 13.2 ± 8 μm.

The test medium was a simulated body fluid (SBF) prepared according to Ref. (Kokubo and Takadama, 2006).

2.2. Atomic Layer Deposition

The deposition of the ALD coatings was performed in a commercial ALD reactor (Savannah S200, Veeco Instruments Inc., Massachusetts, USA) through successive cyclic reactions. 926 successive cycles of ZrO_2 utilizing Tetrakis (dimethylamino) zirconium (TDMAZ) and deionized water (H_2O) as reactants were carried out at 160 °C to obtain a total thickness of 100 nm. Each cycle was composed of two parts. The first part consisted of a 250-ms TDMAZ precursor pulse and a 10-s Hi-purity N_2 purge (semiconductor grade) with a flow rate of 20 sccm to remove residual reactants and by-products from the chamber to separate the chemical vapor deposition reactions. The second part comprised a 150-ms H_2O precursor pulse and a 15-ms High-purity N_2 purge. In the

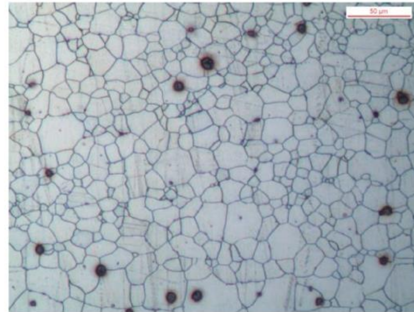

Fig. 1. Microstructure of the AZ31 alloy in the as-received condition.

process of deposition, the TDMAZ precursor and delivery lines were heated to 75 °C and 160 °C, respectively, while the H_2O precursor was kept at room temperature. During the deposition process, the ZrO_2 layer deposition rate was of approximately 1.08 Å/cycle. Concerning TiO_2, the metal organic precursor used was Tetrakis (dimethylamido) titanium (IV) (TDMA-Ti) heated to 75 °C. Each cycle was composed of two parts. The first part consisted of a 0.1 s TDMA-Ti precursor pulse and a 5 s High-purity N_2 purge with a flow rate of 20 sccm. The second part comprised a 0.015 s H_2O precursor pulse and a 5 s High-purity N_2 purge. The deposition rate was found to be 0.5 Å/cycle.

2.3. Coating characterization

The film thickness was determined using spectroscopic ellipsometry (J.A. Woollam M2000U, Lincoln, United States) at a fixed angle of incidence of 65°. The measurements were conducted on thin films deposited on p-doped <100> 500 μm thick, 2 inch Si wafer. A Si wafer per each coating material was put inside the ALD reactor during the deposition on the Mg substrates. The ellipsometer data were fitted using a B-spline model with Si substrate, a native oxide layer and the ALD layer of the required material.

X-ray photoelectron spectroscopy (XPS) measurements were conducted to assess the chemical composition of the TiO_2, and ZrO_2 coating. Kratos Analytical XPS Microprobe (Kratos Analytical Ltd, Manchester, UK) which uses Al (Kα) radiation of 1486 eV in a vacuum environment of $5*10^{-9}$ Torr was used. CasaXPS software was used to analyze the XPS data.

In addition, the surface integrity (amount and length of cracks) of TiO_2, and ZrO_2 coated discs (geometrical details are reported in Section 2.4.) was analyzed using FEI Quanta 450 Scanning electron Microscope (Thermo Fisher Scientific Inc., USA) with an acceleration voltage of 10 kV at a working distance of about 10 mm. Three samples for each respective condition were assessed for reproducibility.

2.4. Potentiodynamic polarization curves

Discs with a diameter of 29 mm and a thickness of 2 mm were manufactured using a lathe from the commercially available bars. The samples were then grounded with 2000 grit silicon carbide papers and cleaned with acetone and ethanol for 5 min in an ultrasonic bath. Fifteen samples were then coated as described in Section 2.2. Potentiodynamic polarization curves of bare and coated samples were carried out in simulated body fluid (SBF) with a pH of 7.4 on a Gamry Reference 600+ potentiostat. As common practice in literature (Cai et al., 2019), the electrochemical tests used a three-electrode equipment with the bare or

coated samples as a working electrode, a Hg/Hg_2SO_4 electrode as a reference electrode, and a platinum plate as counter electrode, respectively. The area of the samples exposed to SBF was 1 cm^2 (excluding roughness induced area deviations). The potentiodynamic polarization tests were conducted at a stable open-circuit potential after a stabilization period of 30 min. The scan rate of the potentiodynamic polarization test was 0.5 mV/s.

2.5. Hydrogen evolution tests

Hydrogen evolution experiments were carried out according to ref (Song et al., 2013). Cubic samples of 5 mm side lengths were obtained from the as-received material, were grounded with 2000 grit silicon carbide paper and cleaned with acetone and ethanol for 5 min in ultrasonic bath. Five samples were then coated as described in Section 2.2. The immersion tests were carried out in SBF at 37 °C for 7 days individually to monitor the hydrogen evolution. Hydrogen bubbles were collected in a burette from each sample.

2.6. Slow strain rate tests (SSRT)

Cylindrical dog-bone-shaped samples, with dimensions reported in Fig. 2, were tested according to a standard (ASTM International, ASTM-E466-96). The samples were machined from the received bars using a lathe.

The samples were then ground with 2000 grit silicon carbide papers and cleaned with acetone and ethanol for 5 min in ultrasonic bath. Fifteen samples were then coated as described in Section 2.2.

The SSRTs were carried out both on bare, TiO_2 and ZrO_2 coated samples, respectively at a strain rate of $3.5{\cdot}10^{-6}$ s^{-1} in SBF solution held at physiologically relevant temperatures (37 ± 1 °C). The strain rate was chosen to render the Mg alloy susceptible to SCC (Bobby Kannan et al., 2008). A schematic representation of the experimental set-up is shown in Fig. 3. The sample was immersed for the whole duration of the test and the SBF was constantly changed with a pumping system. The SBF container was immersed in a water bath, where temperature was controlled. While carrying out the SSRTs, the area of the specimen exposed to SBF was restricted to its gauge length by using Teflon tapes wrapped around the rest of the specimen maintaining a constant area of exposure to the corrosive solution as well as avoiding the possibility of galvanic effects with other components of the testing set-up.

In order to quantify the AZ31 SCC sensitivity, the susceptibility indices I_{UTS} and I_ε were calculated according to Eq. (1) and Eq. (2) (Choudhary et al., 2014):

$$I_{UTS} = \frac{UTS_{air} - UTS_{SBF}}{UTS_{air}} \quad (1)$$

$$I_\varepsilon = \frac{\varepsilon_{air} - \varepsilon_{SBF}}{\varepsilon_{air}} \quad (2)$$

where UTS is the Ultimate Tensile Strength and ε the elongation at

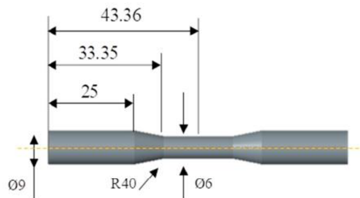

Fig. 2. Geometry and dimensions of the samples for SSRTs.

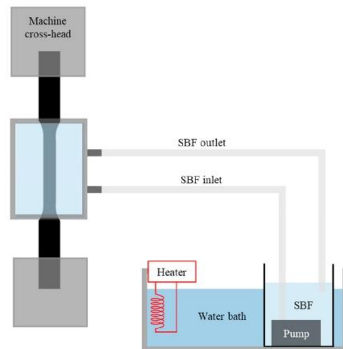

Fig. 3. Schematic representation of the SSRT set-up.

failure both evaluated during tests conducted in SBF and air. When the value of the susceptibility index approaches zero, the material is considered to be highly resistant to SCC, namely the greater the index the greater the susceptibility to SCC.

2.7. Fractography

The specimen fracture surfaces after SSRTs were cleaned by immersion for 1 min in a solution prepared using 50 g chromium trioxide (CrO_3), 2.5 g silver nitrate ($AgNO_3$) and 5 g barium nitrate ($Ba(NO_3)_2$) in 250 ml distilled water, as suggested by (Thirumalaikumarasamy et al., 2014). The specimens were then washed with distilled water and finally ultrasonically cleaned in acetone for 10 min. The fracture surfaces were observed by means of a FEI™ QUANTA 450 SEM (Thermo Fisher Scientific Inc., USA).

3. Results

3.1. Coating characterization

3.1.1. Ellipsometer and XPS analyses

Spectroscopic ellipsometry at a fixed angle of incidence of 65° was conducted to determine the thickness of the deposited coatings. The measurements were carried out on Si wafers coated in the same deposition process of the Mg substrates, and the results reported the TiO_2 and ZrO_2 coatings to be 100.98 and 100.97 nm thick, respectively.

XPS was instead conducted to determine the chemical composition of the ALD deposited TiO_2 and ZrO_2. The measurements were carried out on thin films deposited on p-doped <100> 500 μm thick, 2 inch Si wafers, in order to have minimum effect of the underlying substrate. To start with, etching was conducted on the surface to remove the effect of environmental contamination and surface oxidation. Surface was etched for 180 s with an energy of 2 KeV. On TiO_2 substrates, regional scans for Ti 2p, O 1s and C 1s were carried out at high resolution. Negligible amounts of C were observed in the regional scan indicating an ideal deposition without any process contamination. Fig. 4 (a) and (b) are regional scan of Ti 2p and O 1s, respectively. For Ti, peaks corresponding to the core level binding energies, 459 eV and 464 eV of Ti $2p_{3/2}$ and Ti $2p_{1/2}$ are observed, which is due to Ti^{4+} oxidation state in TiO_2 (Nezar et al., 2017). The shoulder at lower energy around 456 eV is due to the presence of Ti^{3+} caused by the argon etching step (Kim et al., 1999). The O peak at 531 eV is related to O atoms in TiO_2 phase (Yu et al., 2000), while the small shoulder at higher energy is due to O in OH groups

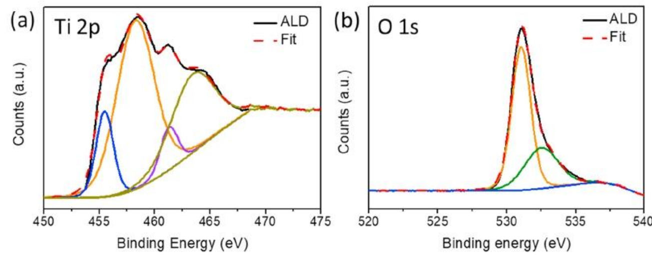

Fig. 4. XPS spectra for ALD deposited TiO_2 (a) Ti 2p (b) O 1s.

present in the form impurities. Stoichiometric TiO_2 thin films should have Ti and O in 1:2 ratio i.e. 66.7% oxygen and 33.3% titanium, but in our case, we have found the composition to be around 60% for oxygen and 40% titanium, thus indicating an oxygen deficient deposition.

Regional scans of Zr 3d, O 1s and C 1s were also carried out for ZrO_2 coated samples at high resolution. No peak was observed in the high-resolution scan for elemental carbon indicating a carbon free ALD deposition. The high-resolution spectra (Fig. 5a) of Zr 3d shows two peaks at binding energy 182 eV and 184 eV, which correspond to Zr $3d_{5/2}$ and Zr $3d_{3/2}$, respectively. The scan conducted for O 1s (Fig. 5b) showed a peak at 530 eV which belongs to ZrO_2 and the shoulder on the higher energy side is due to the oxidation of metal in air forming ZrO. The quantification calculation using CASA XPS software showed a composition as 40% Zr and 60% O. This indicates an oxygen deficient ZrO_2 thin film.

3.1.2. Surface integrity

The presence of cracks on TiO_2 and ZrO_2 coated samples have been assessed by means of SEM analyses and the representative images have been reported in Fig. 6. In addition, the average length and numerosity are reported in Table 1.

It can be noted that the number of cracks (crack density in Table 1) and the length of the cracks increased moving from ZrO_2 to TiO_2 coated samples.

3.2. Potentiodynamic polarization curves

The potentiodynamic polarization curves of the TiO_2 and ZrO_2 coated and bare samples are shown in Fig. 7 and the results of the corrosion potentials (E_{corr}) and of the corrosion current densities (i_{corr}) are shown in Table 2. Compared to the uncoated alloy, the corrosion current densities of the coated samples display declining trends (Fig. 7 and Table 2). In particular, the ZrO_2 coating is shown to provide a higher reduction of the corrosion current density compared to the TiO_2 coating. Since a lower corrosion current density corresponds to a smaller corrosion rate, this suggests that the application of coatings protects Mg alloys from corrosion, which is consistent with previous reports (Liu et al., 2011, 2018; Yang et al., 2017). In particular, the increased protectiveness after the application of coatings is reported to be linked to their barrier properties (Huang et al., 2019).

3.3. Hydrogen evolution tests

The hydrogen evolution curves of bare and coated samples are reported in Fig. 8, and the results further suggest that the application of coatings can prevent the degradation of AZ31 alloy. In particular, the 100 nm thick ZrO_2 coating provides a better protection than the TiO_2 coating. The hydrogen evolved from the bare sample is in fact reduced by 93% with a ZrO_2 coating and by 52% with a TiO_2 coating, respectively.

3.4. Slow strain rate tests (SSRT)

The engineering stress-strain curves for the bare, TiO_2 coated and ZrO_2 coated AZ31 samples tested in air and in SBF are reported in Fig. 9 a, b and c respectively. In addition, Table 3 compares the UTS and elongation at failure values obtained from the curves in Fig. 9.

The surface characteristics did not influence the AZ31 mechanical properties when tested in air. Both the bare and the coated samples are characterized by an excellent and comparable combination of strength and ductility. On the other hand, the coated samples were characterized by a considerably higher elongation to failure than the bare counterparts

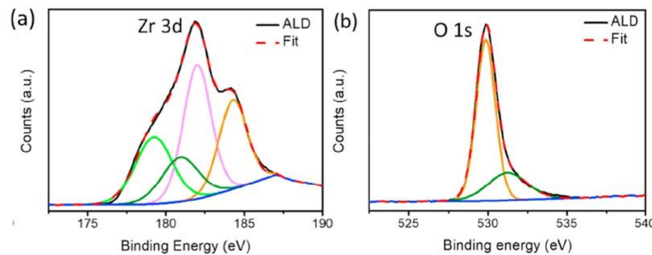

Fig. 5. XPS spectra for ALD deposited ZrO_2 (a) Zr 3d (b) O 1s.

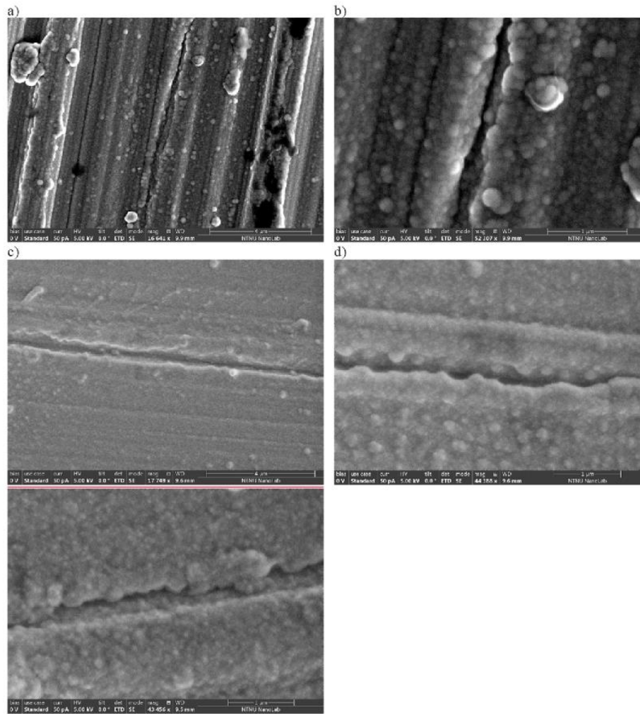

Fig. 6. SEM images of representative cracks formed on TiO_2 coated (a and b) and ZrO_2 coated discs (c and d).

Table1
Average crack length and density (meant as number of cracks per square centimetre) of the cracks detected for the different conditions.

	TiO_2	ZrO_2
Crack length (μm)	4.54 ± 3.05	3.14 ± 2.41
Density (n° cracks/cm^2)	0.87 ± 0.37	0.61 ± 0.28

when tested in SBF, indicating a lower tendency to suffer from embrittlement in SBF. In particular, the elongation to failure of the bare samples tested in SBF was increased by 126% with the application of the TiO_2 coating and by 223% with the ZrO_2 coating.

To quantify the SCC susceptibility of the bare and coated samples, the I_{UTS} and I_{ε} indices were evaluated and are reported in Fig. 10.

The application of 100 nm thick ZrO_2 coating is shown to be more effective in reducing the SCC susceptibility than the TiO_2 counterpart. In fact, the I_{ε} is reduced from 75.1 to 43.2 and to 18.3 applying the TiO_2 and ZrO_2 coating, respectively, while the I_{UTS} is reduced from 8.97 to 8.42 and 2.68 applying the TiO_2 and ZrO_2 coating, respectively. It is interesting to note that the impact on UTS is very low when applying the TiO_2 coating, whereas the impact on elongation is significant.

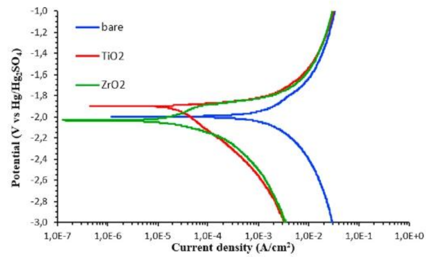

Fig. 7. Potentiodynamic polarization curves of bare (blue), TiO_2 coated (red) and ZrO_2 coated (green) AZ31 alloy in SBF.

Table 2
The results of corrosion potentials (E_{corr}) and corrosion current densities (i_{corr}) for bare and coated AZ31 samples in SBF.

	Bare	TiO_2 coating	ZrO_2 coating
E_{corr} (V)	−2.00 ± 0.02	−1.90 ± 0.01	−2.02 ± 0.01
i_{corr} (A/cm²)	3.0 10^{-3} ± 0.4	2.5 10^{-5} ± 0.6	1.2 10^{-6} ± 0.3

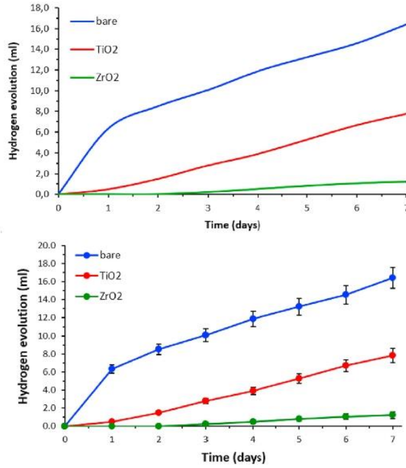

Fig. 8. Hydrogen evolved from the immersion of bare (blue), TiO_2 coated (red) and ZrO_2 coated (green) AZ31 alloy in SBF.

3.5. Fractography

Fracture surfaces of the bare samples tested in air and in SBF are reported in Fig. 11a and 11b and Fig. 11c and 11d, respectively. The overall view of the fracture surface confirms the ductile nature of the failure in the case of testing in air. Here, the fracture surface is characterized by a significant number of dimples (Fig. 11a and 11b), while the sample tested in SBF shows mixed mode fracture features, namely ductile and brittle fracture characteristics. In addition, the surface

Table 3
Mechanical properties of bare and coated samples from Fig. 9.

Surface	In Air		In SBF	
	UTS (MPa)	Elongation at failure (%)	UTS (MPa)	Elongation at failure (%)
Bare	256.3 ± 8.7	24.5 ± 0.7	233.3 ± 1.9	6.1 ± 0.3
TiO_2 Coated	252.7 ± 5.2	24.3 ± 0.6	231.4 ± 5.1	13.8 ± 0.4
ZrO_2 Coated	253.6 ± 5.6	24.1 ± 0.5	246.8 ± 1.0	19.7 ± 0.2

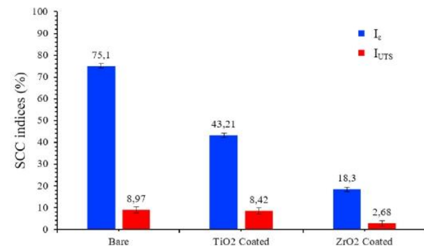

Fig. 10. SCC indices for the bare and coated AZ31 samples.

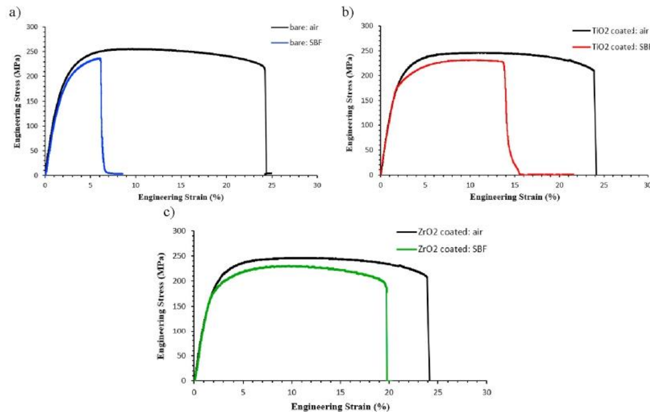

Fig. 9. Engineering stress-strain curves of bare (a) and coated (b) AZ31 samples tested in air and SBF at 37 °C and strain rate of $3.5 \cdot 10^{-6}$ s^{-1}

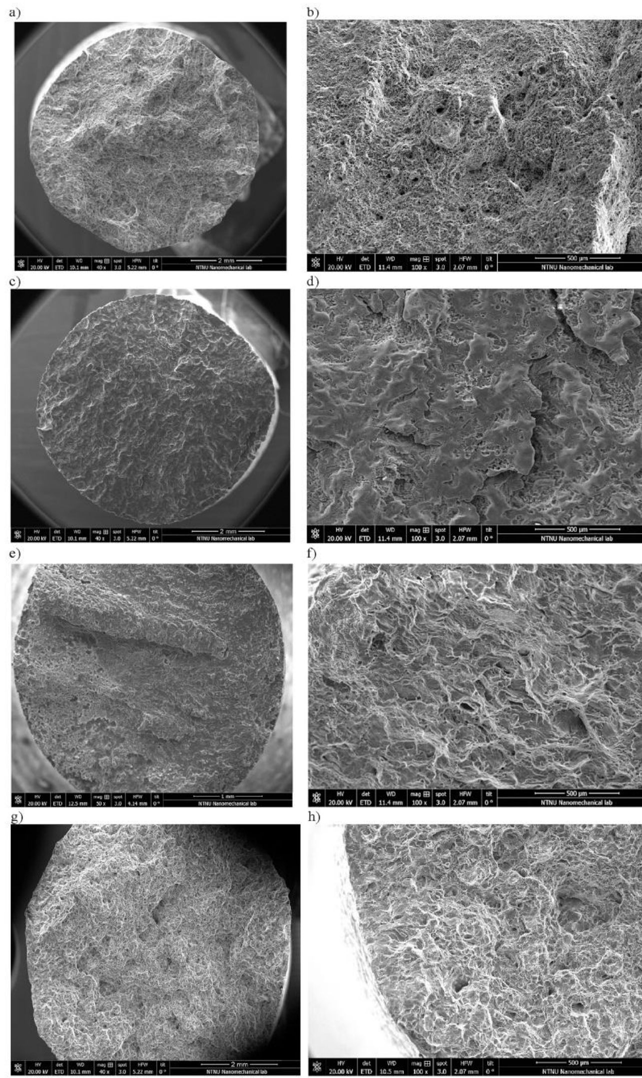

Fig. 11. Fracture surfaces of bare samples tested in air (a and b) and in SBF (c and d), of TiO_2 coated samples tested in SBF (e and f) and of ZrO_2 coated samples tested in SBF (g and h).

fracture appearance is completely different: in the case of SBF condition, both transgranular and intergranular cracks are evident, with a predominance of the former, which are absent in the case of air testing (compare Fig. 11d with Fig. 11b). The application of the coatings did not alter the AZ31 response mechanisms to SCC, being the fracture characterized by both a ductile and brittle zone, with the latter characterized by the presence of both intergranular and transgranular cracks. However, the application of the TiO_2 coating leads to the change of the fracture appearance in the brittle zone due to the reduced embrittlement of the material as a consequence of the reduced corrosion: in fact, while in the bare samples, the transgranular fracture was predominant, the TiO_2 coated samples show intergranular cracking as the main mechanism (Fig. 11f). Finally, the application of the ZrO_2 coating leads to a failure that is predominantly ductile (Fig. 11g). This is particularly apparent in the center of the sample, with the mixed mode fracture features close to the sample edges appearing to have experienced transgranular and intergranular cracking (Fig. 11h).

The reduced corrosion of the coated samples tested in SBF with respect to the bare sample is also confirmed by the tilted views of the gauge section (compare Fig. 12b and c with Fig. 12a), where deep secondary cracks and some pits can be observed in the bare samples, while no deep secondary cracks and no pits are present in the coated sample. In addition, necking can also be observed in the ZrO_2 coated samples confirming the increased ductility (Fig. 12c).

4. Discussions

An adequate resistance to cracking under the simultaneous action of a physiologically relevant corrosive environment and mechanical load is a fundamental requirement for an implant material. For Mg and its alloys, SCC is particularly relevant representing one of the main limitations for their acceptance as implant material (Winzer et al., 2007). Specifically, the high electrochemical activity of Mg must be reduced without changing its bulk properties, its surface characteristics and ability to degrade, even under mechanical stress. Here, a mechanically stable, ultrathin conformal and dense coating of a material with high electrochemical barrier is required. 100 nm ALD TiO_2 and ZrO_2 coated AZ31 alloys showed already significant reduction in i_{corr} by two (Marin et al., 2012) and three (Liu et al., 2018) orders of magnitude, respectively. However, is such an approach viable to reduce the SCC susceptibility, namely an increase in elongation to failure and UTS when tested in a physiologically relevant corrosive environment? Is the reduction in susceptibility related to the electrochemical barrier of the coating only?

Our 100 nm ALD TiO_2 and ZrO_2 coated AZ31 samples were subjected to SSRT at a strain rate of $3.5 \cdot 10^{-6}$ s^{-1} in SBF at 37 °C. Both coatings improve the SCC resistance (Figs. 9 and 10), their performances, however, vastly differ. While TiO_2 reduced the I_{UTS} and the I_ε by 6% and 40%, respectively, ZrO_2 reduced the I_{UTS} and the I_ε by 70% and 76%, respectively. The general SCC behavior of Mg alloys can be attributed to the combination of two mechanisms; (1) the anodic dissolution and (2) the cleavage-like fracture due to hydrogen embrittlement (HE) (Winzer et al., 2005). The rupture of the protective native $Mg(OH)_2$ film through anodic dissolution or mechanical loads allows evolved hydrogen from the corrosion process to enter into the matrix, thereby embrittling the material ultimately leading to premature fracture (Jafari et al., 2015). Altering the corrosion rate hence affects the SCC susceptibility directly. In particular, the lower the corrosion rate, the lower the SCC susceptibility due to a reduced effect of the anodic dissolution and of the HE. Therefore, the reduced SCC susceptibility of the coated samples can be explained directly with the corrosion performances of the coatings (Figs. 7 and 8). The i_{corr} of the bare samples is reduced by two and three orders of magnitude with the TiO_2 and ZrO_2 coatings, consistent with previous reports (Marin et al., 2012; Liu et al., 2018; Yang et al., 2017).

The highest impact in corrosion reduction can however be seen by the evolved hydrogen: from the bare samples it is reduced by 52% and 93% for TiO_2 and ZrO_2 coatings, respectively. Regarding the drastic decrease in I_ε, the lower embrittlement of the material can be directly linked to the reduced amount of evolved hydrogen. This is shown by the mechanical tests (Fig. 9), the fractographies of the samples tested in SBF (Fig. 11) and by the tilted view of the gauge section (Fig. 12). The TiO_2 coated samples are characterized by a brittle fracture zone, where the intergranular fracture, characteristic of the anodic dissolution, is predominant (Fig. 11b). This is different from the bare samples, where the transgranular fracture related to the HE phenomenon is predominant (Fig. 11a). We can thus conclude that a lower amount of hydrogen entering the material with the application of the coating decreases its SCC susceptibility. Further improvements are achieved by applying ZrO_2

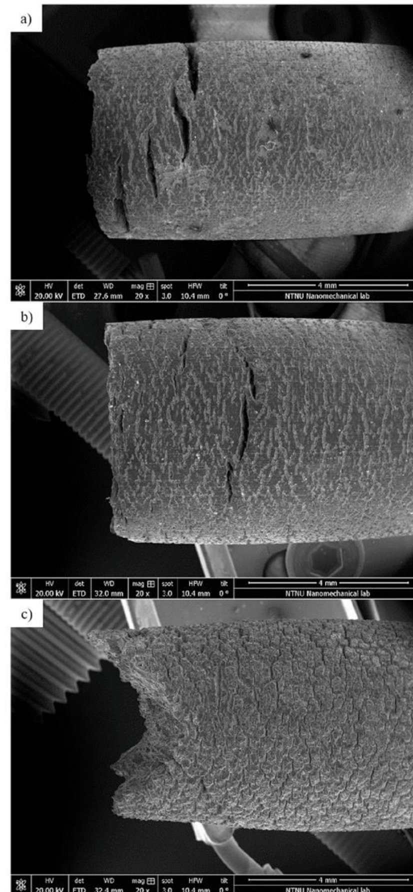

Fig. 12. SEM fractographies of the gauge section of bare (a), of TiO_2 coated (b) and of ZrO_2 coated (c) AZ31 samples after SSRTs in SBF.

coatings. Here, the fracture behavior changes from predominantly cleavage facets towards a mixed brittle-ductile behavior where cleavage facets and dimple-like morphologies are present (Fig. 11c). The increased ductility is confirmed by the tilted views of the gauge section of ZrO_2 coated samples (Fig. 12c), where necking can be observed. Figs. 12b and 12c shows that pitting was significantly reduced with respect to the bare sample (Fig. 12a). This hints towards the conformality of the coating protecting all cavities on the surface of the sample. As pitting is known as the main precursor for SCC crack initiation (Stampella et al., 1984; Raja and Padekar, 2013), this reduced tendency represents another important reason for the reduced SCC susceptibility.

Electrochemical stability can explain the different corrosion performances of the TiO_2 and ZrO_2 coatings. ZrO_2 is electrochemically more stable than TiO_2 due to its higher cohesive energy (Turchanin and Agraval, 2008). A higher cohesive energy makes a material more electrochemically stable and lowers its corrosion (Li and Li, 2006). In addition, TiO_2 is also reported to be more hydrophilic than ZrO_2, thus leading to a higher corrosion rate in aqueous solutions (Akaltun et al., 2016). Miyauchi et al. reported in fact TiO_2 to have a water contact angle of around 55° (Miyauchi et al., 2002), while Gonzalez-Martin et al. reported ZrO_2 to have a water contact angle of around 70° (González-Martín et al., 1999).

Furthermore, the integrity of the coating is another important aspect. Defects such as pores and cracks provide a path for the fluid to access the substrate. More and longer cracks are observed on the TiO_2 coated sample (Fig. 6 and Table 1) compared to the ZrO_2 coated counterpart, which may further explain the drastic difference in corrosion behavior. A comparison to the corrosion rate of bulk TiO_2 and ZrO_2 helps to explain the influence of the observed defects. According to Faraday's law (Pardo et al., 2010), bulk TiO_2 and ZrO_2 corrodes at a rate equal to $0.37 \cdot 10^{-6}$ and $0.87 \cdot 10^{-7}$ mm/year, respectively (Lorenzetti et al., 2014; Sowa et al., 2017), when exposed to simulated body fluid at 37 °C. However, we experience much higher corrosion rates; $2.11 \cdot 10^{-4}$ and $1.14 \cdot 10^{-5}$ mm/year, respectively, rates that are 570 and 130 times higher, confirming the lower defectiveness in ZrO_2 coated samples. Defects usually form as cracks as a consequence of the induced residual stresses on the coating due to the difference in the thermal expansion coefficient between the coating and the substrate (Il Pyun et al., 1993; ((Christoph Leyens and ManfredPetersJohn Wiley and Sons, 2003))). The coefficient of thermal expansion of Mg is $27 \cdot 10^{-6}$ °C^{-1} (Yang et al., 2011), that of ZrO_2 is $11 \cdot 10^{-6}$ °C^{-1} and that of TiO_2 is $7 \cdot 10^{-6}$ °C^{-1} (Hayashi et al., 2005; Hummer et al., 2007). Hence, the lower number of defects in ZrO_2 with respect to TiO_2 coatings may be attributed to its closer match in the coefficient of thermal expansion to the substrate.

Finally, the difference in the coating's mechanical properties can further influence the SCC susceptibility. ZrO_2 has a higher UTS and higher elongation to failure compared to TiO_2, eventually resisting higher strains without rupture (Cristache et al., 2011; Titanium Dioxide - online). We hypothesize that the longer the coating layer resists to the applied stresses, the longer the barrier effect of the coating will last, which directly affects the SCC behaviour.Whereas the drastic reduction of the SCC susceptibility indices I_ε and I_{UTS} show the potential to render ALD coated AZ31 materials interesting for biomedical applications, our results also show the importance of choosing a proper coating material. A wide range of factors, including the cohesive energy, the wettability and the thermal expansion mismatch of the coating with respect to the substrate must be considered. Further, we indicate the fundamental role of the mechanical characteristics of the protective layer for tailoring the SCC behaviour. A high elongation to failure may guarantee the coating's integrity when strained.

5. Conclusion

In this study, the effect of a 100 nm thick TiO_2 and ZrO_2 coatings on the SCC susceptibility of the AZ31 Mg alloy was assessed. Slow strain rate tests (SSRTs) at a strain rate of $3.5 \cdot 10^{-6}$ s^{-1} were carried out in Simulated Body Fluid (SBF) at 37 °C on bare and coated samples, respectively. In addition, potentiodynamic polarization tests, hydrogen evolution tests and fracture surfaces analyses were carried out.

The main findings can be summarized as follows:

- Both coatings reduce the SCC susceptibility of AZ31 alloy. TiO_2 reduced the I_{UTS} and the I_ε of 6% and 40%, respectively, while ZrO_2 of 70% and 76%, respectively. The fracture surface analyses showed a transition from a mixed mode fracture where the brittle zone was predominantly transgranular in the bare samples, to a predominance of intergranular failures in the TiO_2 coated samples and to a predominantly ductile failure for ZrO_2 coated samples.
- The different SCC susceptibility was attributed to the improved corrosion of the coated samples. The difference in the corrosion behavior between TiO_2 and ZrO_2 coated samples was related to the four main aspects, i.e. the different cohesive energies, wettabilities, defect densities and sizes as well as mechanical properties. With a comparably higher cohesive energy, ZrO_2 coatings are less prone to corrosion and are also characterized by a lower wettability. Moreover, a lower mismatch between the coefficient of thermal expansion of ZrO_2 and Mg with respect to that between TiO_2 and Mg reduced the number of defects providing a more stable barrier to the fluid. Finally, ZrO_2 has a higher UTS and higher ε_f compared to TiO_2, which increases its stability when mechanically stressed, hindering the fluid's access to the base material, even under strained conditions.

This work shows that all factors - cohesive energy, wettability, thermal expansion and elongation at break of the coating are important parameters to be considered when designing an effective corrosion barrier for biomedical Mg alloys that are subject to mechanical loads.

CRediT authorship contribution statement

M. Peron: Conceptualization, Data curation, Investigation, Methodology, Validation, Visualization, Writing - original draft, Writing - review & editing. **A. Bin Afif:** Data curation, Investigation, Validation. **A.L. Dadlani:** Data curation, Investigation, Validation. **F. Berto:** Supervision. **J. Torgersen:** Supervision, Writing - original draft, Writing - review & editing.

Declaration of competing interest

The authors declare that they have no known competing interests or personal relationships that could have appeared to influence the work reported in this pap

Acknowledgement

Abdulla Bin Afif was supported by NTNU's Enabling technologies: Nanotechnology. The Research Council of Norway is acknowledged for the support to the Norwegian Micro- and Nano-Fabrication Facility, NorFab, project number 245963/F50. Anup Lal Dadlani was funded by the Norwegian Research Council under project number 274459 Translate.

References

Akahori, T., Niinomi, M., Fukunaga, K.-I., Inagaki, I., 2000. Effects of microstructure on the short fatigue crack initiation and propagation characteristics of biomedical α/β titanium alloys. Metall. Mater. Trans. 31, 1949–1958. https://doi.org/10.1007/s11661-000-0222-z.

Akaltun, Y., Aslan, M., Yetim, T., Çayir, T., Çelik, A., 2016. The effect of wettability on corrosion resistance of oxide films produced by SILAR method on magnesium, aluminum and copper substrates. Surf. Coating. Technol. 292, 121–131. https://doi.org/10.1016/j.surfcoat.2016.03.011.

Antunes, R.A., de Oliveira, M.C.L., 2012. Corrosion fatigue of biomedical metallic alloys: mechanisms and mitigation. Acta Biomater. 8, 937–962. https://doi.org/10.1016/j.actbio.2011.09.012.

ASTM International, ASTM-E466-96. Standard practice for slow strain rate testing to evaluate the susceptibility of metallic materials to environmentally assisted cracking. n.d. https://doi.org/10.1520/G0129-00R13.

Bauer, T.W., Schils, J., 1999. The pathology of total joint arthroplasty.II. Mechanisms of implant failure. Skeletal Radiol. 28, 483–497. http://www.ncbi.nlm.nih.gov/pubmed/10525792. (Accessed 31 March 2017).

Beech, I.B., Sunner, J.A., Arciola, C.R., Cristiani, P., 2006. Microbially-influenced corrosion: damage to prostheses, delight for bacteria. Int. J. Artif. Organs 29, 443–452. http://www.ncbi.nlm.nih.gov/pubmed/16705614. (Accessed 20 June 2017).

Bobby Kannan, M., Dietzel, W., Blawert, C., Atrens, A., Lyon, P., 2008. Stress corrosion cracking of rare-earth containing magnesium alloys ZE41, QE22 and Elektron 21 (EV31A) compared with AZ80. Mater. Sci. Eng. 480, 529–539. https://doi.org/10.1016/J.MSEA.2007.07.070.

Cai, D.G., Bao, M.M., Wang, X.Y., Yang, L., Qin, G.W., Wang, R.X., Chen, D.F., Zhang, E. L., 2019. Biocorrosion properties of Ti–3Cu alloy in F ion-containing solution and acidic solution and biocompatibility. Rare Met. 38, 503–511. https://doi.org/10.1007/s12598-019-01202-9.

Chalker, P.R., 2016. Photochemical atomic layer deposition and etching. Surf. Coating. Technol. 291, 258–263. https://doi.org/10.1016/j.surfcoat.2016.02.046.

Chen, L., Sheng, Y., Zhou, H., Li, Z., Wang, X., Li, W., 2018. Influence of a MAO + PLGA coating on biocorrosion and stress corrosion cracking behavior of a magnesium alloy in a physiological environment. Corrosion Sci. 148, 134–143. https://doi.org/10.1016/J.CORSCI.2018.12.005.

Choudhary, L., Singh Raman, R.K., Hofstetter, J., Uggowitzer, P.J., 2014. In-vitro characterization of stress corrosion cracking of aluminium-free magnesium alloys for temporary bio-implant applications. Mater. Sci. Eng. C 42, 629–636. https://doi.org/10.1016/J.MSEC.2014.06.018.

(Christoph) Leyens, C., (Manfred) Peters, M., John Wiley & Sons, 2003. Wiley InterScience (Online Service), Titanium and Titanium Alloys : Fundamentals and Applications. Wiley-VCH.

Cremers, V., Puurunen, R.L., Dendooven, J., 2019. Conformality in atomic layer deposition: current status overview of analysis and modelling. Appl. Phys. Rev. 6, 021302 https://doi.org/10.1063/1.5060967.

Cristache, C.M., Burlibasa, M., Cristache, G., Drafta, S., Popovici, I.A., Iliescu, A.A., Zisi, S., Burlibasa, L., 2011. Zirconia and its biomedical applications. Metal. Int XVI, 18–23. https://www.researchgate.net/publication/286038141_Zirconia_and_its_biomedical_applications. (Accessed 20 January 2020).

Dujovne, A.R., Bobyn, J.D., Krygier, J.J., Miller, J.E., Brooks, C.E., 1993. Mechanical compatibility of noncemented hip prostheses with the human femur. J. Arthroplasty 8, 7–22. https://doi.org/10.1016/S0883-5403(06)80102-6.

Engh, C.A., Bobyn, J.D., 1988. The influence of stem size and extent of porous coating on femoral bone resorption after primary cementless hip arthroplasty. Clin. Orthop. Relat. Res. 7–28. http://www.ncbi.nlm.nih.gov/pubmed/3370887. (Accessed 31 March 2017).

Ginebra, M.P., Traykova, T., Planell, J.A., 2006. Calcium phosphate cements as bone drug delivery systems: a review. J. Contr. Release 113, 102–110. https://doi.org/10.1016/j.jconrel.2006.04.007.

González-Martín, M.L., Labajos-Broncano, L., Jańczuk, B., Bruque, J.M., 1999. Wettability and surface free energy of zirconia ceramics and their constituents. J. Mater. Sci. 34, 5923–5926. https://doi.org/10.1023/A:1004767914895.

Graniel, O., Weber, M., Balme, S., Miele, P., Bechelany, M., 2018. Atomic layer deposition for biosensing applications. Biosens. Bioelectron. 122, 147–159. https://doi.org/10.1016/J.BIOS.2018.09.038.

Hänzi, A.C., Sologubenko, A.S., Uggowitzer, P.J., 2009. Design strategy for new biodegradable Mg–Y–Zn alloys for medical applications. Int. J. Mater. Res. 100, 1127–1136. https://doi.org/10.3139/146.110157.

H. Harianawala, M. Kheur, S. Kheur, T. Sethi, A. Bal, M. Burhanpurwala, F. Sayed, Biocompatibility of Zirconia, n.d.

Hayashi, H., Saitou, T., Maruyama, N., Inaba, H., Kawamura, K., Mori, M., 2005. Thermal expansion coefficient of yttria stabilized zirconia for various yttria contents. Solid State Ionics 176, 613–619. https://doi.org/10.1016/j.ssi.2004.08.021.

Hou, S.S., Zhang, R.R., Guan, S.K., Ren, C.X., Gao, J.H., Lu, Q.B., Cui, X.Z., 2012. In vitro corrosion behavior of Ti-O film deposited on fluoride-treated Mg–Zn–Y–Nd alloy. Appl. Surf. Sci. 258, 3571–3577. https://doi.org/10.1016/J.APSUSC.2011.11.116.

http://share.iofbonehealth.org/EU-6-Material/Reports/IOF%20Report_EU.pdf, (n.d). http://share.iofbonehealth.org/EU-6-Material/Reports/IOF Report_EU.pdf (accessed November 20, 2019).

Huang, L., Su, K., Zheng, Y.F., Yeung, K.W.K., Liu, X.M., 2019. Construction of TiO2/silane nanofilm on AZ31 magnesium alloy for controlled degradability and enhanced biocompatibility. Rare Met. 38, 588–600. https://doi.org/10.1007/s12598-018-1187-7.

Hummer, D.R., Heaney, P.J., Post, J.E., 2007. Thermal expansion of anatase and rutile between 300 and 575 K using synchrotron powder X-ray diffraction. Powder Diffr. 22, 352–357. https://doi.org/10.1154/1.2790965.

Il Pyun, S., Yoon, Y.G., Lugscheider, E., Mathesius, R., 1993. Relationship between interfacial reaction and adhesion at PVD TiO2 film-metal (Ti or Al) interfaces. Surf. Coating. Technol. 61, 233–237. https://doi.org/10.1016/0257-8972(93)90231-C.

Jacobs, J.J., Gilbert, J.L., Urban, R.M., 1998. Corrosion of metal orthopaedic implants. J. Bone Joint Surg. Am. 80, 268–282. http://www.ncbi.nlm.nih.gov/pubmed/9486734. (Accessed 31 March 2017).

Jacobs, J.J., Hallab, N.J., Skipor, A.K., Urban, R.M., 2003. Metal degradation products: a cause for concern in metal-metal bearings? Clin. Orthop. Relat. Res. 139–147. https://doi.org/10.1097/01.blo.0000096810.78689.62.

Jafari, S., Harandi, S.E., Singh Raman, R.K., 2015. A review of stress-corrosion cracking and corrosion fatigue of magnesium alloys for biodegradable implant applications. Jom 67, 1143–1153. https://doi.org/10.1007/s11837-015-1366-z.

Jafari, S., Raman, R.K.S., Davies, C.H.J., Hofstetter, J., Uggowitzer, P.J., Löffler, J.F., 2017. Stress corrosion cracking and corrosion fatigue characterisation of MgZn1Ca0.3 (ZX10) in a simulated physiological environment. J. Mech. Behav. Biomed. Mater. 65, 634–643. https://doi.org/10.1016/J.JMBBM.2016.09.033.

Jafari, S., Raman, R.K.S., Davies, C.H.J., 2018. Stress corrosion cracking of an extruded magnesium alloy (ZK21) in a simulated body fluid. Eng. Fract. Mech. 201, 47–55. https://doi.org/10.1016/J.ENGFRACMECH.2018.09.002.

Kannan, M.B., Raman, R.K.S., 2008. In vitro degradation and mechanical integrity of calcium-containing magnesium alloys in modified-simulated body fluid. Biomaterials 29, 2306–2314. https://doi.org/10.1016/J.BIOMATERIALS.2008.02.003.

Kasuga, T., Kondo, H., Nogami, M., 2002. Apatite formation on TiO2 in simulated body fluid. J. Cryst. Growth 235, 235–240. https://doi.org/10.1016/S0022-0248(01)01782-1.

Kerner, J., Huiskes, R., van Lenthe, G.H., Weinans, H., van Rietbergen, B., Engh, C.A., Amis, A.A., 1999. Correlation between pre-operative periprosthetic bone density and post-operative bone loss in THA can be explained by strain-adaptive remodelling. J. Biomech. 32, 695–703. https://doi.org/10.1016/S0021-9290(99)00041-X.

Kim, J.H., Lee, S., Im, H.S., 1999. Effect of target density and its morphology on TiO2 thin films grown on Si(100) by PLD. Appl. Surf. Sci. 151, 6–16. https://doi.org/10.1016/S0169-4332(99)00269-X.

Kokubo, T., Takadama, H., 2006. How useful is SBF in predicting in vivo bone bioactivity? Biomaterials 27, 2907–2915. https://doi.org/10.1016/J.BIOMATERIALS.2006.01.017.

Lei, T., 2015. Anodic electrodeposition of MgO coatings to improve corrosion resistance in vivo. In: Surf. Modif. Magnes. Its Alloy. Biomed. Appl. Elsevier Inc., pp. 135–150. https://doi.org/10.1016/B978-1-78242-078-1.00006-2

Li, Q., 2013. Sol-gel coatings to improve the corrosion resistance of magnesium (Mg) alloys. In: Corros. Prev. Magnes. Alloy. Woodhead Publ. Ser. Met. Surf. Eng., Elsevier Ltd, pp. 469–485. https://doi.org/10.1533/9780857098962.3.469. A Vol.

Li, W., Li, D.Y., 2006. Influence of surface morphology on corrosion and electronic behavior. Acta Mater. 54, 445–452. https://doi.org/10.1016/j.actamat.2005.09.017.

Liu, F., Shan, D., Song, Y., Han, E.-H., Ke, W., 2011. Corrosion behavior of the composite ceramic coating containing zirconium oxides on AM30 magnesium alloy by plasma electrolytic oxidation. Corrosion Sci. 53, 3845–3852. https://doi.org/10.1016/J.CORSCI.2011.07.037.

Liu, X., Yang, Q., Li, Z., Yuan, W., Zheng, Y., Cui, Z., Yang, X., Yeung, K.W.K., Wu, S., 2018. A combined coating strategy based on atomic layer deposition for enhancement of corrosion resistance of AZ31 magnesium alloy. Appl. Surf. Sci. 434, 1101–1111. https://doi.org/10.1016/J.APSUSC.2017.11.032.

Lorenzetti, M., Pellicer, E., Sort, J., Baró, M.D., Kovač, J., Novak, S., Kobe, S., 2014. Improvement to the corrosion resistance of Ti-based implants using hydrothermally synthesized nanostructured anatase coatings. Materials (Basel) 7, 180–194. https://doi.org/10.3390/ma7010180.

Marin, E., Lanzutti, A., Guzman, L., Fedrizzi, L., 2012. Chemical and electrochemical characterization of TiO2/Al2O3 atomic layer depositions on AZ-31 magnesium alloy. J. Coating Technol. Res. 9, 347–355. https://doi.org/10.1007/s11998-011-9372-8.

Miyauchi, M., Kieda, N., Hishita, S., Mitsuhashi, T., Nakajima, A., Watanabe, T., Hashimoto, K., 2002. Reversible wettability control of TiO2 surface by light irradiation. Surf. Sci. 511, 401–407. https://doi.org/10.1016/S0039-6028(02)01551-0.

Mohajernia, S., Pour-Ali, S., Hejazi, S., Saremi, M., Kiani-Rashid, A.-R., 2018. Hydroxyapatite coating containing multi-walled carbon nanotubes on AZ31 magnesium: mechanical-electrochemical degradation in a physiological environment. Ceram. Int. 44, 8297–8305. https://doi.org/10.1016/J.CERAMINT.2018.02.015.

Nezar, S., Saoula, N., Sali, S., Faiz, M., Mekki, M., Laoufi, N.A., Tabet, N., 2017. Properties of TiO 2 thin films deposited by rf reactive magnetron sputtering on biased substrates. Appl. Surf. Sci. 395, 172–179. https://doi.org/10.1016/j.apsusc.2016.08.125.

Pardo, A., Feliu, S., Merino, M.C., Arrabal, R., Matykina, E., 2010. Electrochemical estimation of the corrosion rate of magnesium/aluminium alloys. Int. J. Corros. 2010 https://doi.org/10.1155/2010/953850.

Peron, M., Torgersen, J., Berto, F., 2017. Mg and its alloys for biomedical applications: exploring corrosion and its interplay with mechanical failure. Metals (Basel) 7, 252. https://doi.org/10.3390/met7070252.

Peron, M., Torgersen, J., Berto, F., 2019a. Effect of Zirconia ALD coating on stress corrosion cracking of AZ31 alloy in simulated body fluid. In: Procedia Struct. Integr. Elsevier B.V., pp. 538–548. https://doi.org/10.1016/j.prostr.2019.08.198

Peron, M., Berto, F., Torgersen, J., 2019b. Stress corrosion cracking behavior of zirconia ALD-coated AZ31 alloy in simulated body fluid. Mater. Des. Process. Commun. 126. https://doi.org/10.1002/mdp2.126 mdp.2.

Peron, M., Bertolini, R., Ghiotti, A., Torgersen, J., Bruschi, S., Berto, F., 2020a. Enhancement of stress corrosion cracking of AZ31 magnesium alloy in simulated body fluid thanks to cryogenic machining. J. Mech. Behav. Biomed. Mater. 101, 103429. https://doi.org/10.1016/J.JMBBM.2019.103429.

Peron, M., Berto, F., Torgersen, J., 2020b. Magnesium and its Alloys as Implant Materials : Corrosion, Mechanical and Biological Performances. CRC Press LLC.

Peron, M., Skaret, P.C., Fabrizi, A., Varone, A., Montanari, R., Roven, H.J., Ferro, P., Berto, F., Torgersen, J., 2020c. The effect of Equal Channel Angular Pressing on the stress corrosion cracking susceptibility of AZ31 alloy in simulated body fluid. J. Mech. Behav. Biomed. Mater. 103724. https://doi.org/10.1016/j.jmbbm.2020.103724.

Peron, M., Bin Afif, A., Dadlani, A., Berto, F., Torgersen, J., 2020d. Comparing physiologically relevant corrosion performances of Mg AZ31 alloy protected by ALD and sputter coated TiO2. Surf. Coating. Technol. 125922. https://doi.org/10.1016/j.surfcoat.2020.125922.

Pound, B.G., 2014a. Corrosion behavior of metallic materials in biomedical applications. I . Ti and its alloys 32, 1–20. https://doi.org/10.1515/corrrev-2014-0007.

Pound, B.G., 2014b. Corrosion behavior of metallic materials in biomedical applications. II . Stainless steels and Co-Cr alloys 32, 21–41. https://doi.org/10.1515/corrrev-2014-0008.

Qi, Z.-R., Zhang, Q., Tan, L.-L., Lin, X., Yin, Y., Wang, X.-L., Yang, K., Wang, Y., 2014. Comparison of degradation behavior and the associated bone response of ZK60 and PLLA in vivo. J. Biomed. Mater. Res. 102, 1255–1263. https://doi.org/10.1002/jbm.a.34795.

Raja, V.S., Padekar, B.S., 2013. Role of chlorides on pitting and hydrogen embrittlement of Mg–Mn wrought alloy. Corrosion Sci. 75, 176–183. https://doi.org/10.1016/J.CORSCI.2013.05.030.

L. Rimondini, L. Cerroni, A. Carrassi, P. Torricelli, Bacterial colonization of zirconia ceramic surfaces: an in vitro and in vivo study., Int. J. Oral Maxillofac. Implants 17 (n.d.)793–8. http://www.ncbi.nlm.nih.gov/pubmed/12507238 (accessed January 23, 2020).

Singh Raman, R.K., Jafari, S., Harandi, S.E., 2015. Corrosion fatigue fracture of magnesium alloys in bioimplant applications: a review. Eng. Fract. Mech. 137, 97–108. https://doi.org/10.1016/j.engfracmech.2014.08.009.

Smith, M.F., 2007. Comparing cold spray with thermal spray coating technologies. In: Cold Spray Mater. Depos. Process Fundam. Appl. Elsevier Ltd., pp. 43–61. https://doi.org/10.1533/9781845693787.1.43

Song, G., 2007. Control of biodegradation of biocompatable magnesium alloys. Corrosion Sci. 49, 1696–1701. https://doi.org/10.1016/J.CORSCI.2007.01.001.

Song, G., Atrens, A., StJohn, D., 2013. An hydrogen evolution method for the estimation of the corrosion rate of magnesium alloys. In: Magnes. Technol. 2001. John Wiley & Sons, Inc., Hoboken, NJ, USA, pp. 254–262. https://doi.org/10.1002/9781118805497.ch44.

Sonia, T.A., Sharma, C.P., 2014. Polymers in oral insulin delivery. In: Oral Deliv. Insul. Elsevier, pp. 257–310. https://doi.org/10.1533/9781908818683.257.

Sowa, M., Łastówka, D., Kukharenko, A.I., Korotin, D.M., Kurmaev, E.Z., Cholakh, S.O., Simka, W., 2017. Characterisation of anodic oxide films on zirconium formed in sulphuric acid: XPS and corrosion resistance investigations. J. Solid State Electrochem. 21, 203–210. https://doi.org/10.1007/s10008-016-3369-2.

Staiger, M.P., Pietak, A.M., Huadmai, J., Dias, G., 2006. Magnesium and its alloys as orthopedic biomaterials: a review. Biomaterials 27, 1728–1734. https://doi.org/10.1016/j.biomaterials.2005.10.003.

Stampella, R.S., Procter, R.P.M., Ashworth, V., 1984. Environmentally-induced cracking of magnesium. Corrosion Sci. 24, 325–341. https://doi.org/10.1016/0010-938X(84)90017-9.

Sumner, D.R., Galante, J.O., 1992. Determinants of stress shielding: design versus materials versus interface. Clin. Orthop. Relat. Res. 202–212. http://www.ncbi.nlm.nih.gov/pubmed/1729005. (Accessed 31 March 2017).

Teoh, S., 2000. Fatigue of biomaterials: a review. Int. J. Fatig. 22, 825–837. https://doi.org/10.1016/S0142-1123(00)00052-9.

Thirumalaikumarasamy, D., Shanmugam, K., Balasubramanian, V., 2014. Comparison of the corrosion behaviour of AZ31B magnesium alloy under immersion test and potentiodynamic polarization test in NaCl solution. J. Magnes. Alloy. 2, 36–49. https://doi.org/10.1016/J.JMA.2014.01.004.

Titanium Dioxide - online catalogue source - supplier of research materials in small quantities - Goodfellow. n.d. http://www.goodfellow.com/E/Titanium-Dioxide.html. (Accessed 20 January 2020).

Turchanin, M.A., Agraval, P.G., 2008. Cohesive energy, properties, and formation energy of transition metal alloys. Powder Metall. Met. Ceram. 47, 26–39. https://doi.org/10.1007/s11106-008-0006-3.

Turner, T.M., Sumner, D.R., Urban, R.M., Igloria, R., Galante, J.O., 1997. Maintenance of proximal cortical bone with use of a less stiff femoral component in hemiarthroplasty of the hip without cement. An investigation in a canine model at six months and two years. J. Bone Joint Surg. Am. 79, 1381–1390. http://www.ncbi.nlm.nih.gov/pubmed/9314401. (Accessed 31 March 2017).

Uchida, M., Kim, H.-M., Kokubo, T., Nakamura, T., 1999. APATITE-FORMING ability OF titania gels with different structures. In: Bioceramics. WORLD SCIENTIFIC, pp. 149–152. https://doi.org/10.1142/9789814291064_0036.

Van Rietbergen, B., Huiskes, R., Weinans, H., Sumner, D.R., Turner, T.M., Galante, J.O., 1993. The mechanism of bone remodeling and resorption around press-fitted THA stems. J. Biomech. 26, 369–382. https://doi.org/10.1016/0021-9290(93)90001-U.

Wang, X.X., Hayakawa, S., Tsuru, K., Osaka, A., 2002. Bioactive titania gel layers formed by chemical treatment of Ti substrate with a H2O2/HCl solution. Biomaterials 23, 1353–1357. https://doi.org/10.1016/S0142-9612(01)00254-X.

Wang, J., Xu, J., Hopkins, C., Chow, D.H., Qin, L., 2020. Biodegradable magnesium-based implants in orthopedics—a general review and perspectives. Adv. Sci. 1902443. https://doi.org/10.1002/advs.201902443.

Winzer, N., Atrens, A., Song, G., Ghali, E., Dietzel, W., Kainer, K.U., Hort, N., Blawert, C., 2005. A critical review of the Stress Corrosion Cracking (SCC) of magnesium alloys. Adv. Eng. Mater. 7, 659–693. https://doi.org/10.1002/adem.200500071.

Winzer, N., Atrens, A., Dietzel, W., Song, G., Kainer, K.U., 2007. Stress corrosion cracking in magnesium alloys: characterization and prevention. JOM 59, 49–53. https://doi.org/10.1007/s11837-007-0104-6.

Wolff, J., 1986. The Law of Bone Remodelling. Springer Berlin Heidelberg, Berlin, Heidelberg. https://doi.org/10.1007/978-3-642-71031-5.

Yang, H., Huang, L., Zh, M., 2011. Hot forming characteristics of magnesium alloy AZ31 and three-dimensional FE modeling and simulation of the hot splitting spinning process. In: Magnes. Alloy. - Des. Process. Prop. InTech. https://doi.org/10.5772/13778.

Yang, Q., Yuan, W., Liu, X., Zheng, Y., Cui, Z., Yang, X., Pan, H., Wu, S., 2017. Atomic layer deposited ZrO2 nanofilm on Mg-Sr alloy for enhanced corrosion resistance and biocompatibility. Acta Biomater. 58, 515–526. https://doi.org/10.1016/J.ACTBIO.2017.06.015.

Yu, J., Zhao, X., Du, J., Chen, W., 2000. Preparation, microstructure and photocatalytic activity of the porous TiO2 anatase coating by sol-gel processing. J. Sol. Gel Sci. Technol. 17, 163–171. https://doi.org/10.1023/A:1008703719929.

Zhen, Z., Xi, T., Zheng, Y., Li, L., Li, L., 2014. Vitro study on Mg–Sn–Mn alloy as biodegradable metals. J. Mater. Sci. Technol. 30, 675–685. https://doi.org/10.1016/J.JMST.2014.04.005.

Paper 4

Surface & Coatings Technology 395 (2020) 125922

Contents lists available at ScienceDirect

Surface & Coatings Technology

journal homepage: www.elsevier.com/locate/surfcoat

Comparing physiologically relevant corrosion performances of Mg AZ31 alloy protected by ALD and sputter coated TiO_2

Mirco Peron*, Abdulla Bin Afif, Anup Dadlani, Filippo Berto, Jan Torgersen

Department of Mechanical and Industrial Engineering, Norwegian University of Science and Technology, Richard Birkelands vei 2b, 7034 Trondheim, Norway

ARTICLE INFO

Keywords:
Magnesium alloys
Temporary metallic implants
Corrosion resistance
Biocompatible coatings
Atomic Layer Deposition (ALD)
Sputter

ABSTRACT

The utilization of Mg alloys for biomedical applications is so far underexplored due to the accelerated corrosion hampering patient recovery post implantation. Here, we explore the effectiveness of corrosion reduction of an AZ31 alloy in Simulated Body Fluid when coated with a 40 nm sputtered TiO_2 layer and compare it to a similar coating made by Atomic Layer Deposition (ALD). Potentiodynamic polarization and hydrogen evolution experiments were performed on coated samples having different surface roughness and 3D topologies. Interestingly, ALD layers reduce corrosion current density by 94% on Ra = 118.6 ± 5.1 nm and 93% on Ra = 4794.3 ± 49.4 nm, whereas sputtered only by 84% on Ra = 118.6 ± 5.1 nm and 60% on Ra = 4794.3 ± 49.4 nm. Particularly on 3D aspects, the ALD coatings are superior, where a scaffold of 85% porosity with 1 mm pore sizes released 68% lower hydrogen compared to the sputtered counterparts. We relate these observations to the higher surface integrity, adhesion strength and lower line-of-sight restrictions of ALD compared to sputter deposition. The results can be interesting for researchers and practitioners aiming to make Mg alloys more commonplace as temporary metallic implant materials.

1. Introduction

The ageing of our society paired with increasing obesity raises the demand for orthopedic interventions requiring the implantation of medical devices [1]. Among these procedures, the number of orthopedic implantations is growing the fastest [2]. The materials currently used in orthopedic surgery are usually permanent metallic materials, such as stainless steel, titanium, and cobalt-chromium alloys [3] due to their high strength and good corrosion resistance [3–5]. However, two key issues arise with such materials. Firstly, the vast difference in elastic modulus compared to human bone results in the occurrence of stress-shielding phenomenon [6–12]. Secondly, to avoid possible long-term complications such as local inflammations [13–17], the implant shall ideally vanish when the healing process is completed. However common metallic implants are permanent and thus remain in the body. When complications arise, additional surgeries are required to remove the implant causing an increase in costs to the health care system, as well as emotional stress to the patient.

Biodegradable metallic materials may resolve these issues. Here, Mg and its alloys are promising candidates [18–21] due to their low density and an elastic modulus compatible with natural bone that minimize the risk of stress shielding [19]. In addition, Mg is abundant in the human body [22], essential for metabolism, is a cofactor for many enzymes [23] and supports the growth of tissues via the release of Mg^{2+} ions during its degradation. Despite their highly attractive properties, Mg and its alloys have not yet been used as implant materials because of their high corrosion rates in physiological environments, which may result in a loss of mechanical integrity and in hydrogen evolution beyond what bone tissue is able to accommodate. Yet, Mg's high corrosion rates in physiological environments yield a loss of mechanical integrity before healing is complete and triggers hydrogen evolution beyond what bone tissue can accommodate. Designed porosity and surface roughness sought to enhance osseointegration and cell adhesion on today's implants [24–26] further enhances corrosion and makes this material impractical for biomedical applications.

In the last several years, two main possibilities of reducing Mg's corrosion rate have been studied: 1) severe plastic deformation (SPD) and 2) coatings. Dealing with 1), either (a) the entire bulk or (b) the surface only can be subjected to SPD. Regarding (a), the corrosion current density can be reduced by almost two orders of magnitude [27–30] but it requires bulk property changes that might hamper the match to physiological conditions. Regarding (b), the authors reported a one order of magnitude current density reduction after cryogenic machining [31]. However, they also observed a rapid increase of corrosion upon removal of the surface layer.

A potential Mg implant may need surface texture and porosity to

* Corresponding author.
E-mail address: mirco.peron@ntnu.no (M. Peron).

https://doi.org/10.1016/j.surfcoat.2020.125922
Received 17 March 2020; Received in revised form 20 April 2020; Accepted 13 May 2020
Available online 15 May 2020
0257-8972/ © 2020 The Authors. Published by Elsevier B.V. This is an open access article under the CC BY license (http://creativecommons.org/licenses/BY/4.0/).

enhance ingrowth of cells and tissue at the patient specific site of interest [32,33]. In such a scenario, cryogenic machining, despite its benefits in initial corrosion resistance, might not be applicable as (1) intricate features are difficult to be made and (2) the resulting surfaces are smooth without texture. Hence an alternative, surface confined approach might be required that allows the control of surface texture. Coatings have thus emerged as an effective way to preserve designed macroscopic porosity and surface roughness tailored for osseointegration and to match mechanical characteristics [34,35]. Particularly sputtering has been studied due to the possibility to carry out the deposition at low temperatures, making the coating relatively insensitive to thermal expansion mismatches between the substrate and the coating, that are reported to affect the protectiveness of the coating due to the formation of cracks [36,37]. Jin et al. reported that the application of a 600 nm thick TaN layer on WE43 alloy reduced the corrosion current density in Simulated Body Fluid (SBF) by two orders of magnitude [38]. Ref. [39] reports a similar improvement when coating a WE43 alloy with 30 nm of TiN. However, the effectiveness of sputtering can be limited as it is subject to the line-of-sight. When considering implants, their complex shapes such as notches, pores and undercuts cannot be entirely coated due to this limitation, rendering corrosion most severe at places that are not accessible to the coating process.

Atomic Layer Deposition (ALD), in contrast, is not limited by the line-of-sight. Conformal, dense and pinhole-free films can be deposited on complex 3D substrates due to the self-limiting surface gas phase reactions; a technique newly explored for corrosion protection [40,41]. For example, Liu et al. reported a three orders of magnitude decrease in the corrosion current density of a 10 nm ZrO_2 coated AZ31 Mg alloy [40], while Yang et al. reported a two orders of magnitude corrosion current density reduction with a 40 nm ZrO_2 layer on a MgSr alloy [42].

Taking these results one step further, we explore the corrosion reduction of ALD layers on realistic AZ31 alloy implant surfaces and compare the results with those obtained by sputter technique. Specimens of different surface roughness (smooth and rough) and 3D topologies (flat and cube with pass-through holes) were coated with a 40 nm layer of TiO_2 by sputtering and ALD, respectively. The choice of the coating material felt on TiO_2 due to the high interest encountered in the biomedical field as a consequence of its high biocompatibility (it can induce in vitro bone-like apatite formation and stimulate osteoconductivity in vivo [43–45], along with the ability to bond directly and reliably to living bone in a short period after implantation [46]). The corrosion properties of the samples in SBF were evaluated by means of potentiodynamic polarization curves tests and hydrogen evolution experiments and were compared to bare samples for reference.

In addition, the chemical composition of the layer obtained by the two techniques was assessed by X-ray photoelectron spectroscopy (XPS) before and after 24 h of corrosion in SBF. The surface integrity of smooth and rough samples was assessed by a Scanning Electron Microscope (SEM).

2. Materials and methods

2.1. Sample preparation

AZ31 magnesium alloy was supplied in the form of commercially available bars (Dynamic Metals Ltd., Bedfordshire, UK). The microstructure was analyzed using a Leica DMRETM Optical Microscope (Leica microsystems, Wetzlar, Germany) after polishing the surface and etching it using a solution of alcohol (95 ml), picric acid (5 g), and acetic acid (10 ml). The microstructure is shown in Fig. 1 and consists of a homogeneous α matrix. The initial grain size was measured by linear intercept method which gave 14.8 ± 8 μm.

To simulate different biologically relevant conditions, flat discs (for potentiodynamic polarization curves) and plates (for hydrogen evolution experiments) with two different roughnesses and small cubes (for hydrogen evolution experiments) with pass-through holes to resemble the induced porosity in real implants have been machined. Discs with a diameter of 29 mm and a thickness of 2 mm (Fig. 2a) and 2 mm thick plates (60 mm long and 25 mm wide, Fig. 2b) were manufactured from the bars. The discs and the plates were then ground either using 40 grit silicon carbide papers to obtain a rough surface and up to 4000 grit silicon carbide papers to obtain a smooth surface. In the following, we will refer to the former group as "rough", while to the latter as "smooth". Both the typologies of samples were cleaned with acetone and ethanol for 5 min in an ultrasonic bath and then coated with a 40 nm TiO_2 layer using sputtering and ALD, respectively.

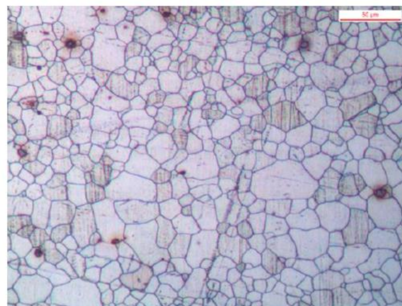

Fig. 1. Microstructure of the AZ31 alloy in the as-received condition.

The induced porosity of real implants has instead been resembled by manufacturing cubic samples of side 10 mm with six rows and six columns of equally spaced pass-through holes (φ = 1 mm) on each side (Fig. 2c) obtained by means of a CNC milling machine. After machining, the 3D samples were cleaned with acetone and ethanol for 5 min in an ultrasonic bath and then coated with a 40 nm TiO_2 layer using sputtering and ALD, respectively.

2.2. Sputtering

Thin film of TiO_2 is deposited using an AJA ATC-2200 V magnetron sputtering tool (AJA International Inc., MA, USA). The source used is 99.99% pure 2″ TiO_2 target. The sputtering chamber is pumped down to base pressure below 2e-7 Torr. Deposition is carried out with RF power of 63 W, at a pressure of 3mtorr with an Argon gas flow rate of 63 sccm. Initial depositions are conducted to determine the deposition rate, which is found to be 0.21 nm/min.

2.3. ALD

The ALD growth of TiO_2 thin film was conducted on a Savannah S200 system (Ultratech/Cambridge NanoTech, MA, USA), operating on thermal mode at reactor temperature of 160 °C. The metal organic precursor used was Tetrakis (dimethyl amido) titanium (IV) or TDMA-Ti, supplied by Sigma-Aldrich (Merck Life Sciences AS, Norway), heated at 75 °C and with deionized water as an oxidizer. Nitrogen was flown as a carrier gas at a constant flow rate of 20 sccm. The oxidant and precursor were pulsed in the following sequence, Water pulse 0.015 s, purge 5 s, TDMA-Ti precursor pulse 0.1 s and purge 5 s. SiO_2 witness wafers were also coated to determine the growth rate using a spectroscopic ellipsometry (Woollam M2000, J.A. Woollam, NE, USA). The growth rate was found to be 0.5 Å/cycle.

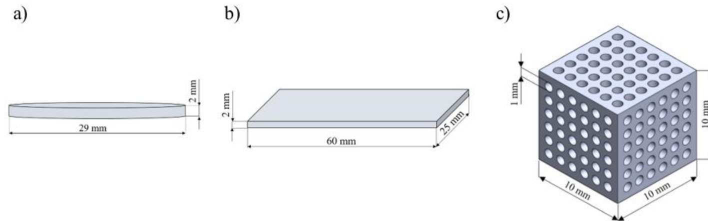

Fig. 2. Representation of the discs (a), plates (b) and 3D structures (c) used in the hydrogen evolution experiments.

2.4. Surface characterization

The roughness values of bare smooth and rough discs were measured using a Dektak 150 Profilometer (Veeco, AZ, USA). A linear scan was conducted in a hills and value mode. For calculating the Roughness average (R_a), an assessment length of 300 µm was defined, where an arithmetic average deviation from the mean line is calculated. Measurements were carried out on multiple points in the sample and an average value was calculated.

In addition, the surface integrity (amount and length of cracks) of sputtered and ALD smooth and rough coated discs was analyzed using FEI Quanta 450 Scanning electron Microscope (Thermo Fisher Scientific Inc., USA) with an acceleration voltage of 10 kV at a working distance of about 10 mm. Three samples for each condition, respectively, were assessed for reproducibility.

Finally, X-ray photoelectron spectroscopy (XPS) measurements were conducted to evaluate the chemical composition of the sputter and ALD coated samples. In addition, the chemical composition of the smooth samples coated by ALD and sputter, respectively, after 24 h of immersion in SBF was also assessed. Kratos Analytical XPS Microprobe (Kratos Analytical Ltd., Manchester, UK) which uses Al (Kα) radiation of 1486 eV in a vacuum environment of $5 * 10^{-9}$ Torr was used. CasaXPS software was used to analyze the XPS data.

2.5. Potentiodynamic polarization curves

Discs with a diameter of 29 mm and a thickness of 2 mm were manufactured as reported in Section 2.1. Potentiodynamic polarization tests were carried out on a Gamry Interface1000 potentiostat (Gamry Instruments, PA, USA) in order to compare the effectiveness of sputtered and ALD coatings in improving the corrosion resistance with different surface roughness. Bare samples were also tested as reference. The electrochemical tests used three-electrode equipment with the bare or coated samples as a working electrode, a Hg/Hg_2SO_4 electrode as a reference electrode, and a platinum plate electrode as a counter electrode. The samples were immersed in SBF solution (composition reported in Table 1). The temperature was set to 37 ± 1 °C to reproduce human body conditions. The potentiodynamic polarization curves were obtained applying a potential from ± 1 V with respect to the open circuit potential (OCP), obtained after a stabilization period of 30 min. The scan rate of the potentiodynamic polarization test was 0.5 mV/s. The area of the samples exposed to SBF was 1 cm^2 disregarding the surface roughness and the corrosion potential and corrosion current density was determined using the Tafel extrapolation method, according to the ASTM G5-14 standard [47]. The tests were repeated three times for each surface roughness.

2.6. Hydrogen evolution experiments

During the immersion tests, the chemical reaction between Mg and electrolyte occurs as shown in the following equation [19]:

$$Mg + 2H_2O \rightarrow Mg(OH)_2 + H_2 \quad (1)$$

Table 1
Reagents and their quantities for preparation of 1000 ml of the SBF solution according to [48].

Reagents	Amount
NaCl	8.035 g
$NaHCO_3$	0.355 g
KCl	0.225 g
$K_2HPO_4 \cdot 3H_2O$	0.231 g
$MgCl_2 \cdot 6H_2O$	0.311 g
1.0_M-HCl	39 ml
$CaCl_2$	0.292 g
Na_2SO_4	0.072 g
Tris	6.118 g

From the above equation it can be easily understood that the dissolution of one magnesium atom generates one hydrogen gas molecule. In other words, the evolution of one mole of hydrogen gas corresponds to the dissolution of one mole of magnesium. Therefore, measuring the volume of hydrogen evolved allows to assess the corrosion rate of Mg and its alloys [49]. Hence, hydrogen evolution tests were used to compare the protection of sputter- and ALD- coated samples considering two different surface conditions each. To do so, the commercially available bars were manufactured into 2 mm thick plates (60 mm long and 25 mm wide) as described in Section 2.1. The samples were then immersed individually in 500 ml SBF at 37 °C for 72 h and the hydrogen bubbles were collected into a burette from each sample (Fig. 3), as suggested in Ref. [49]. The SBF was replaced with a fresh one every 24 h to limit the pH variations [50] that could have otherwise altered the corrosion behavior [51]. Bare "rough" and "smooth" samples were also tested as references, respectively.

In addition, hydrogen evolution tests were carried out on the cubic samples described in Section 2.1. These samples were used to compare the performances of sputter and ALD in the case of 3D structures that resemble the induced porosity in real implants. Bare samples were also tested as reference.

2.7. Degradation behaviour

Bare and coated cylindrical and cubic samples, prepared as described in Sections 2.5 and 2.1, respectively, were soaked for one day in SBF at 37 °C to carry out macro- and micro-morphological characterizations before and after corrosion. All samples were ultrasonically cleaned for 5 min in acetone and ethanol, dried in the air, and then observed by means of Canon EOS 4000D (Canon, Tokyo, Japan) and FEI Quanta 450 Scanning Electron Microscope (Thermo Fisher Scientific Inc., USA) for macro- and micro-morphological characterizations, respectively. In addition, 3D samples after corrosion have been sliced to

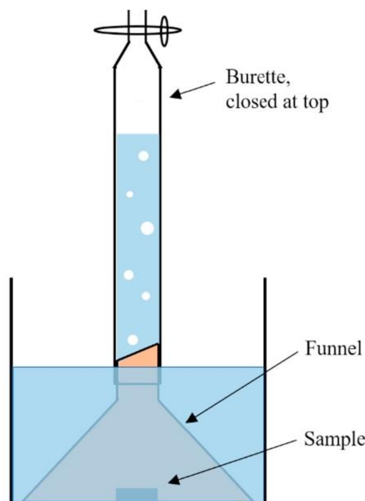

Fig. 3. Schematic illustration of the set-up for measurement of the volume of hydrogen evolved.

show the corroded aspect of the undercuts for bare, sputter coated and ALD coated samples.

3. Results

3.1. Surface characterization

3.1.1. Surface integrity

The presence of cracks on ALD and sputter smooth and rough discs has been assessed by means of SEM analyses and the representative images have been reported in Fig. 4. In addition, the average length and numerosity are reported in Table 2.

It can be noted that the number of cracks (crack density in Table 2) and the length of the cracks increased moving from smooth to rough samples. In addition, under the same conditions, sputter coated samples are shown to be characterized by more and longer cracks.

3.1.2. Roughness evaluation

The average surface roughness of the smooth bare samples was 118.6 ± 5.1 nm, while that of the rough bare samples was 4794.3 ± 49.4 nm.

3.1.3. XPS

3.1.3.1. Composition of the coating. XPS was conducted to determine the chemical composition of the ALD and sputter deposited TiO_2. The measurements were carried out on thin films deposited on Si wafer. To start with, etching was conducted on the surface to remove the effect of environmental contamination and surface oxidation. Surface was etched for 180 s with an ion beam energy of 2 KeV. Regional scans for the elements, titanium, O and C were carried out at high resolution. Negligible amounts of C were observed in the regional scan, thus indicating an ideal deposition without any process contamination. Fig. 5a and c are regional scans of titanium deposited using ALD and Sputter deposition techniques, respectively. The peaks are found to be very similar in both the deposition techniques. Peaks corresponding to the core level binding energies, 459 eV and 464 eV of Ti $2p_{3/2}$ and Ti $2p_{1/2}$ are observed, which is due to Ti^{4+} oxidation state in TiO_2 [52]. The shoulder at lower energy around 456 eV is due to the presence of Ti^{3+} caused by the argon etching step [53]. Fig. 5b and d are regional scans of the oxygen peak in ALD coated and sputter coated samples, respectively. The peak at 531 eV is due to oxygen atoms in TiO_2 phase [54], while the small shoulder at higher energy is due to O in –OH groups present in the form of impurities. Stoichiometric TiO_2 thin films should have Ti and oxygen in 1:2 ratio i.e. 66.7% O and 33.3% Ti, but in our case, we have found the composition to be around 60% for O and 40% Ti indicating an O deficient deposition in both cases (Table 3).

3.1.3.2. XPS after corrosion. The chemical composition of sputter and ALD coated smooth discs after 24 h of corrosion in SBF (Fig. 6) was evaluated using XPS and reported in Table 4. In this case, the main focus was on the number of chemical elements, and thus the binding energies were not assessed. Etching was conducted on the surface to remove the effect of environmental contamination and surface oxidation. The surface was etched for 180 s with an ion beam energy of 2 KeV. Regional scans for Mg, Ti and O were carried out at high resolution. In addition, Ca and P have also been assessed since Mg and its alloys are reported to form Mg (Ca) phosphates [55].

3.2. Potentiodynamic polarization tests

The potentiodynamic polarization curves of the AZ31 cylindrical rough and smooth samples plotted on a semi-logarithmic scale are shown in Figs. 7 and 8, respectively. Bare, sputter coated and ALD coated curves are reported in black, blue and red lines, respectively. The related kinetic and thermodynamic corrosion electrochemical characteristics are reported in Tables 5 and 6.

Considering both rough and smooth samples, the presence of TiO_2 coatings led to an improvement in corrosion resistance, namely an ennoblement of corrosion potential E_{corr} and a reduction of corrosion current density i_{corr} of more than one order of magnitude. It is worth noting that the corrosion current density is directly related to the corrosion rate by the Faraday's law, which expresses the material loss of the implant during its permanence into the human body. This implies that the application of coatings leads to a reduced corrosion rate. ALD coatings are shown to be more effective in the protection from corrosion, especially when a high surface roughness is considered.

3.3. Hydrogen evolution tests

The hydrogen evolution of rough and smooth plates is reported in Figs. 9 and 10, respectively. Bare, sputter coated and ALD coated hydrogen evolution are reported in black, blue and red lines, respectively.

The results of the hydrogen evolution tests are in line with the potentiodynamic polarization curves, i.e. the application of the coating decelerates the corrosion process, irrespective of the considered surface roughness. In addition, the difference in the efficiency of the sputter and ALD coatings is more visible in the rough samples, again in agreement with the potentiodynamic polarization curves.

The better performances of ALD compared to sputtering in reducing corrosion is further confirmed by the hydrogen evolution tests carried out on 3D structures reported in Fig. 11.

3.4. Degradation behavior

3.4.1. Cylindrical samples

Figs. 12 and 13 display the macro-morphologies of sputter and ALD coated cylindrical samples before and after one day of corrosion in SBF for smooth and rough samples, respectively. The bare AZ31 smooth and rough samples were taken as control.

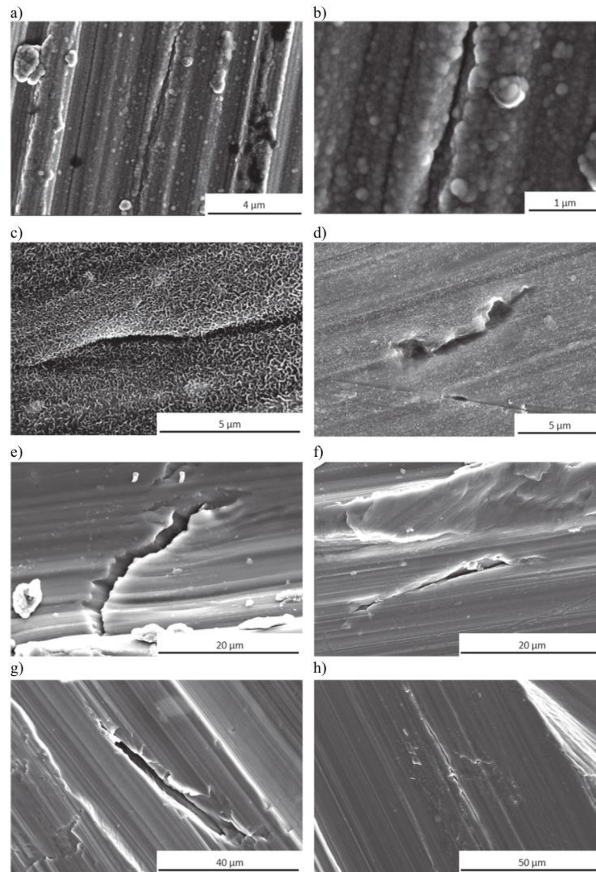

Fig. 4. SEM images of representative cracks formed on smooth ALD (a and b), smooth sputter (c and d), rough ALD (e and f) and rough sputter (g and h) discs. Since the size of cracks are different for each condition, the scale bars differ from picture to picture.

Table 2
Average crack length and density (meant as number of cracks per square centimetre) of the cracks detected for the different conditions.

	Smooth ALD	Smooth sputter	Rough ALD	Rough sputter
Crack length (µm)	4.54 ± 3.05	8.04 ± 2.48	23.59 ± 3.96	58.12 ± 7.25
Density (n° cracks/cm^2)	0.87 ± 0.37	1.71 ± 0.68	3.18 ± 0.62	5.3 ± 0.78

From the macro-morphologies it can be clearly seen that the degree of corrosion damage decreased with the application of coatings for both smooth and rough samples. In particular, the protectiveness of the ALD coating is shown to be higher since most of the TiO_2 coating is still present both in the smooth and rough samples, whereas several spots exposing the Mg substrate are visible on the sputter coated samples, particularly regarding the rough specimen. The higher protectiveness of the ALD coating are further confirmed by the micro-morphologies after corrosion of smooth and rough cylindrical samples, gathered in Figs. 14 and 15, respectively.

Table 3
Chemical composition of ALD and Sputter deposited TiO_2.

Deposition mode	O 1s	Ti 2p
ALD	60%	40%
Sputtering	61%	39%

Table 4
Chemical composition of ALD and sputter smooth discs before and after 24 h of immersion in SBF.

Element	Concentration (%) before corrosion		Concentration (%) after corrosion	
	ALD	Sputter	ALD	Sputter
Mg	9	11	9	8
Ti	21	22	3	11
O	69	66	73	69
Ca	1	1	6	7
P	0	0	9	5

In the micro-morphologies of ALD coated samples, wider un-corroded areas are visible compared to sputter coated and especially bare samples. This is even more evident when smooth samples are considered. For all the samples, the corroded areas have numerous cracks dividing the surface into a network structure, where the delamination

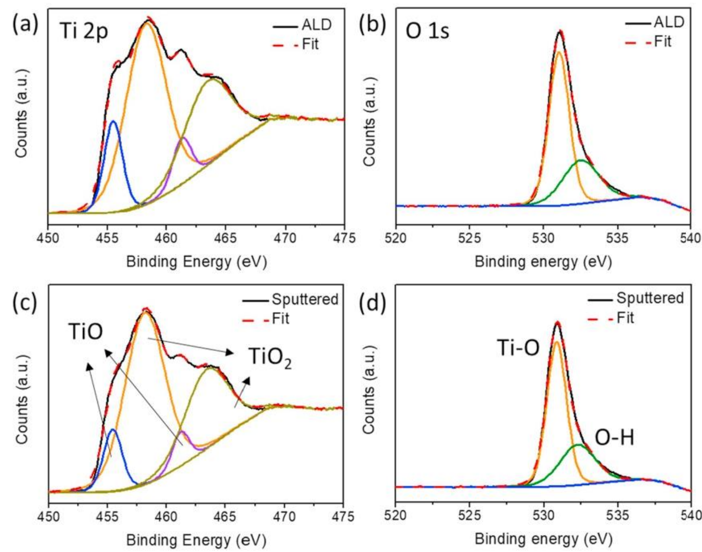

Fig. 5. XPS spectra for ALD deposited TiO_2 (a) Ti 2p (b) O 1s and Sputter deposited TiO_2 (c) Ti 2p (d) O 1s.

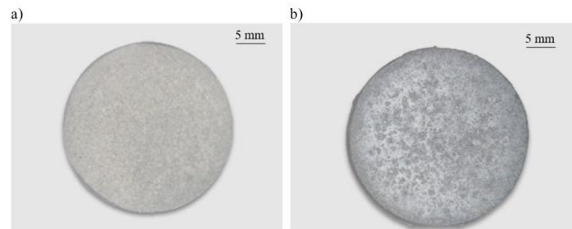

Fig. 6. Images of ALD (a) and sputter (b) coated smooth samples after 24 h of immersion in SBF.

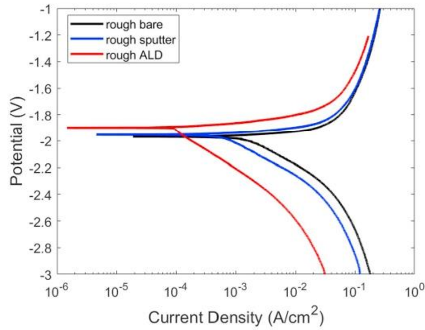

Fig. 7. Potentiodynamic polarization curves of rough samples.

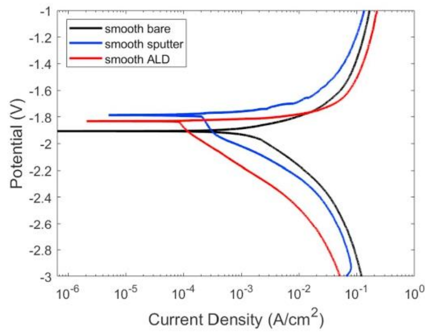

Fig. 8. Potentiodynamic polarization curves of smooth samples.

Table 5
Electrochemical corrosion data extrapolated from Fig. 7.

	Ecorr (V)	icorr (μA/cm^2)
Bare	−1.97 ± 0.025	1500 ± 40
Sputter coated	−1.95 ± 0.035	600 ± 10
ALD coated	−1.90 ± 0.015	102 ± 4

Table 6
Electrochemical corrosion data extrapolated from Fig. 8.

	Ecorr (V)	icorr (μA/cm^2)
Bare	−1.91 ± 0.02	1400 ± 25
Sputter coated	−1.79 ± 0.033	220 ± 15
ALD coated	−1.83 ± 0.016	84 ± 6

and the flaking off of the protective film can be observed.

3.4.2. 3D samples

The macro-morphologies of 3D bare, sputter coated and ALD coated samples before and after one day of corrosion in SBF are reported in Fig. 16.

The bare samples are highly corroded, rendering it difficult to

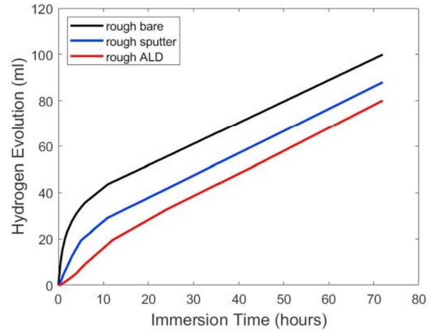

Fig. 9. Hydrogen evolution of rough samples.

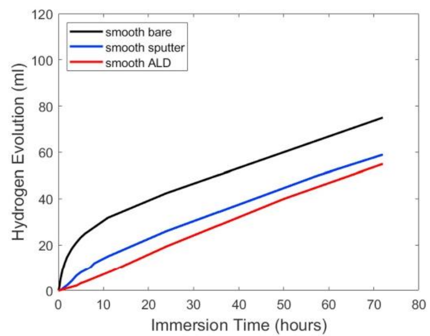

Fig. 10. Hydrogen evolution of smooth samples.

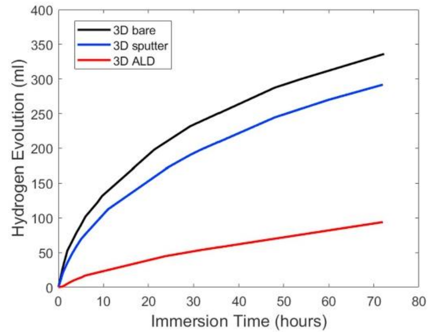

Fig. 11. Hydrogen evolution of the 3D structures reported in Fig. 2.

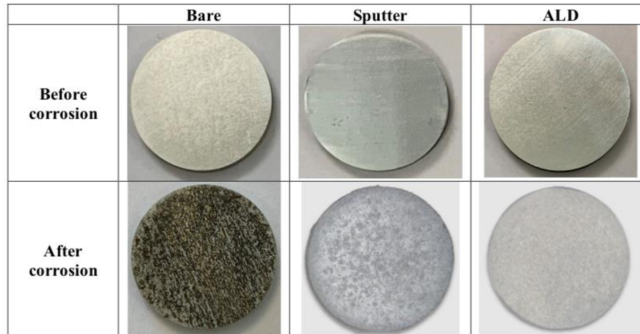

Fig. 12. Macro-morphologies of smooth bare, sputter and ALD TiO_2 coated samples before and after corrosion.

recognize the original shape. A reduction in corrosion is obtained by the application of coatings, particularly in the case of ALD coated samples. This is confirmed by the micro-morphologies of the corroded samples (Fig. 17). In fact, while for bare samples the structure is fully covered by corrosion products (Fig. 17a) and the original structure can be barely detected in some locations (in particular within the holes that are obstructed by the corrosion products (Fig. 17b)), the sputter coated samples are characterized by a lower amount of corrosion products (Fig. 17c) and the original structure can still be recognized retaining visible un-corroded areas (Fig. 17d). An even lower corrosion is detected in the ALD coated samples (Fig. 17e and f).

However, the improvement in corrosion resistance of sputter coated samples with respect to bare samples is not obvious when looking at the micro-morphology of the corroded sample's sliced cross-section (Fig. 18). The micro-morphologies of the corroded sputter 3D samples (Fig. 18b) are comparable to those of the bare counterparts (Fig. 18a). In ALD samples (Fig. 18c), in contrast, the corrosion seems consistently lower, which we attribute to the nature of the coating process providing effective barriers also within a given 3D aspect, independent from its topological and surface complexity.

4. Discussions

Macroscopic porosity and surface roughness are known to assist the surface attachment and growth of various cell types on implant surfaces [56,57]. A realistic biodegradable implant surface must possess these characteristics and must maintain its integrity during its designed lifetime. In an attempt to mimic such a scenario, we compared the corrosion reduction induced by TiO_2 sputtered and ALD layers on AZ31 implant surfaces with different surface roughness and induced macroscopic porosities through potentiodynamic polarization curves and hydrogen evolution tests.

Although both sputter and ALD TiO_2 40 nm coatings improve the corrosion resistance, their performances differ. Deviations increase with surface and topological complexity (roughness and porosity). Whereas the corrosion current density (i_{corr}) of ALD coated smooth samples differs by a factor of three compared to sputter coated counterparts, the i_{corr} is six times lower on ALD coated rough samples. These results are corroborated by hydrogen evolution experiments. After 72 h of exposure to SBF, the amount of evolved hydrogen from smooth samples coated with ALD is 6.8% lower than on sputter coated samples, while the difference is as high as 10% on rough samples.

The lower corrosion reduction of sputtered coatings on rough

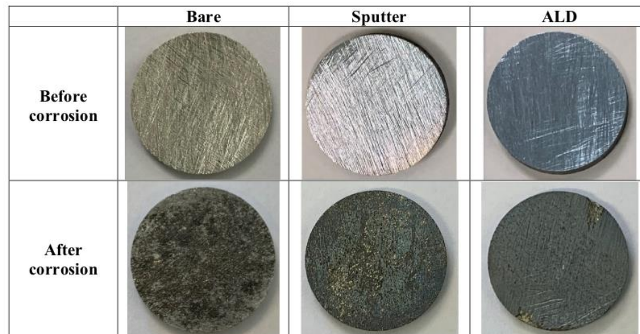

Fig. 13. Macro-morphologies of rough bare, sputter and ALD TiO_2 coated samples before and after corrosion.

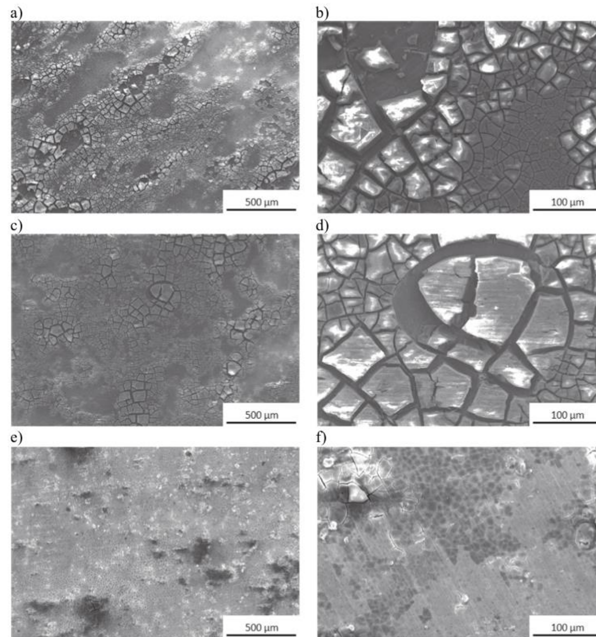

Fig. 14. Micro-morphologies of bare (a and b), sputter (c and d) and ALD (e and f) coated cylindrical smooth samples after corrosion.

surfaces is in agreement with the results of Munemasa and Kumakiri [58]. They reported that the corrosion protection of sputter coated carbon steel decreases with the increase in substrate roughness. They related this effect to an increased amount of uncovered surface area in the case of rougher substrates. Sputter is subject to line-of-sight limitations hindering complete surface coverage of areas shadowed by surface features. This becomes particularly problematic on 3D aspects in cell scaffolds that naturally provide 3D features as topological cues for cells to anchor and proliferate [59,60]. Our simple 3D porous structures possess several macroscopic undercuts and shadowed areas, which are likely superior for cell attachment as compared to flat surfaces. Here, the hydrogen evolution experiments show that the ALD coatings perform significantly better; the respective specimens are characterized by a 68% reduced hydrogen evolution compared to sputter coated counterparts. Interestingly, the SEM micrograph of the undercuts and shadowed areas of the sliced 3D structures reveals the sputter coated samples (Fig. 18b) to possess a similar morphology to bare samples (Fig. 18a). This indicates that these areas have not or only barely been covered in the first place. ALD coatings, instead, are conformal, and thus cover the inner areas of the structure (Fig. 18c). We hypothesize that this is the main contribution to the significant observed differences in degradation upon the internal structure's exposure to SBF.

The corrosion reduction with ALD compared to sputter coatings cannot be ascribed to the line-of-sight limitation only, but also to defects in the coating. Defects such as cracks and pores provide access for the media to attack the underlying substrate thereby reducing the coatings' effectiveness. If the coatings deposited were perfectly conformal, dense and defect-free, their corrosion rate would ideally match the literature reported values for pure TiO_2 in SBF. However, the corrosion rate of the sputter and ALD coated samples (measured by the Faraday's law [61] after normalization by the surface area) differs significantly from that of pure TiO_2 ($0.37{\cdot}10^{-6}$ mm/year) [62]. Smooth samples (characterized by a Sdr[1] of 0.06) have corrosion rates $1.8{\cdot}10^{-3}$ and $6.8{\cdot}10^{-4}$ mm/year for sputter and ALD coated samples, respectively, while rough samples (characterized by a Sdr of 0.1) have rates of $4.7{\cdot}10^{-3}$ and $8.1{\cdot}10^{-4}$ mm/year, respectively. The higher difference reported between the corrosion rate of sputter coated AZ31 samples and that of pure TiO_2 compared to that for ALD coated samples indicates a higher amount and size of defects in the sputtered TiO_2 coatings. This is corroborated by the surface integrity assessments of Fig. 4 and Table 2. The higher number of cracks shown for rough samples further increases the deviation in corrosion rate from pure and defect-free TiO_2.

Cracks usually form due to induced residual stresses in the coating resulting from thermal expansion coefficient differences between coating and substrate [63,64]. The thermal expansion coefficient of Mg is reported to be $27{\cdot}10^{-6}$ °C^{-1} [64], while that of TiO_2 is $7{\cdot}10^{-6}$ °C^{-1} [65,66]. The higher amount of cracks in the sputter coating may be attributed to the higher process temperature during sputtering (260 °C)

[1] Area roughness parameter, describes the additional area provided by texture with respect to the planar area [72].

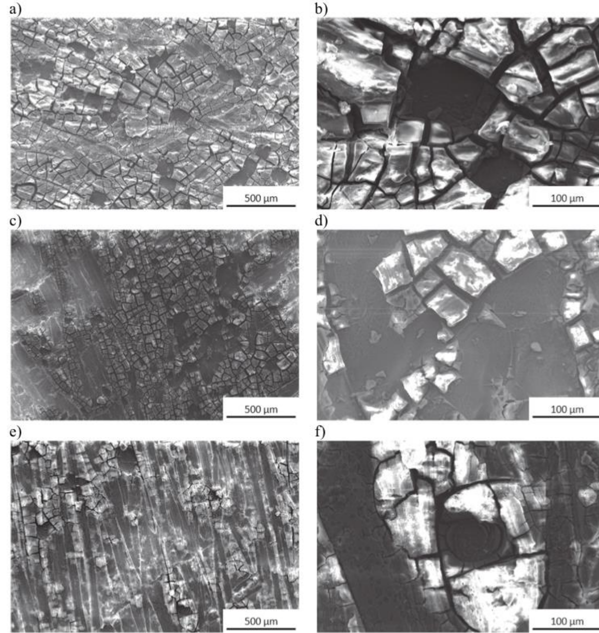

Fig. 15. Micro-morphologies of bare (a and b), sputter (c and d) and ALD (e and f) coated cylindrical rough samples after corrosion.

compared to ALD (160 °C) [67]. It is reported that higher residual stresses are to be expected with higher substrate roughness during the coating process [68,69]. This is reported to lead to a higher number and longer cracks [70], an observation that can be made in our rough samples too (Fig. 4 and Table 2).

The exposure of the Mg substrate on the flat samples can likely not be attributed to the cracks through the coating only. After 24 h of immersion in SBF sputter coated samples are characterized by large areas

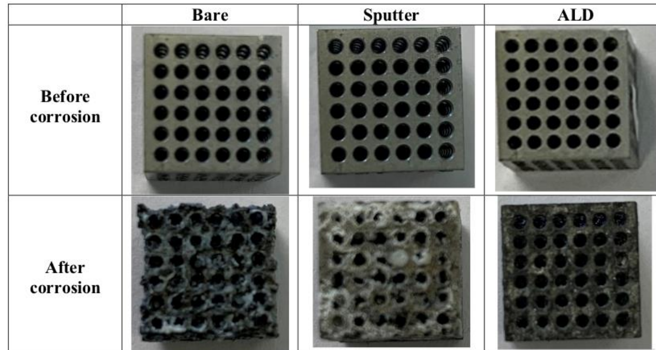

Fig. 16. Macro-morphologies of smooth bare, sputter and ALD TiO_2 coated samples before and after corrosion.

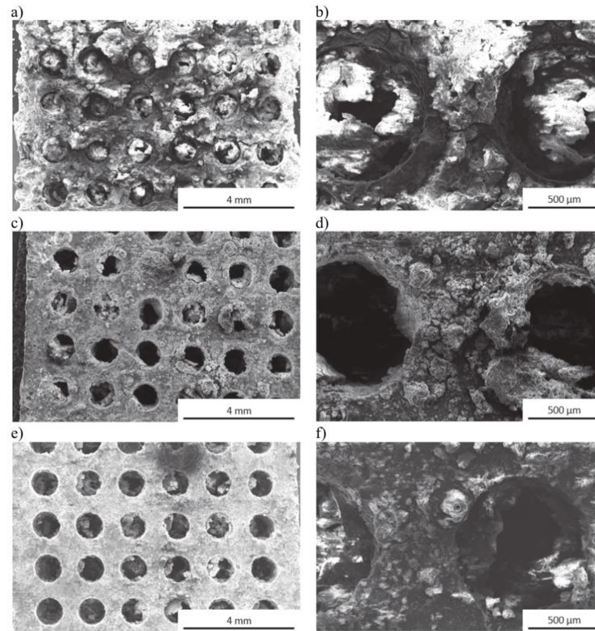

Fig. 17. Micro-morphologies of bare (a and b), sputter (c and d) and ALD (e and f) coated 3D samples after corrosion.

of the substrate obviously exposed to the corrosive environment (darker dots in Fig. 6b), which are not visible in ALD coated samples (Fig. 6a). These areas are of diameter (0.97 mm, StdDev 0.25 mm), which is significantly larger than the reduction of thickness in the bare samples after immersion in SBF for 24 h (thickness 0.12 mm StdDev 0.03 mm). We therefore hypothesize in-plane corrosion between substrate and coating has likely taken place facilitated by interfacial delamination as also reported elsewhere [71]. The ALD samples are instead characterized by a more uniform corrosion mode, indicative of a stronger film adhesion, as suggested also by the XPS measurements after corrosion. These measurements indicate that ALD films have a lower concentration of titanium after corrosion (3%, as compared to 21% before corrosion) and an unchanged amount of Mg. After 24 h of immersion, the Mg substrate coated by ALD has barely been affected with the corrosive media mainly attacking the TiO_2 layer. Contrarily, in the sputter coated samples, the corrosion is less uniform. A higher amount of Ti prevails after corrosion whereas Mg is reduced after immersion indicative of an attack on the underlying substrate.

We conclude that both coatings can be considered viable for the fabrication of biodegradable implants with a prolonged durability inside the human body. However, the choice of the coating technique has to be taken based on the specific scenario. Surface integrity of the coatings and an effective barrier in undercuts and shadowed areas render ALD superior in our study, which may have an impact on the choice of coating techniques for Mg based biomedical implants in the future.

5. Conclusions

In this work, we provided new insights into the corrosion performances of ALD coated AZ31 Mg alloy and compared corrosion protection performances of ALD and sputtered biocompatible TiO_2 coatings. As for a real implant, complex 3D geometry and surface texture are likely important for cell adhesion and ingrowth, we evaluated the corrosion protection performances on substrates with two different surface roughnesses as well as complex 3D architectures (designed porosity). All samples were coated with a 40 nm layer of TiO_2 by either sputter deposition or ALD and their corrosion properties have been evaluated by means of potentiodynamic polarization curves tests and hydrogen evolution experiments. The evaluation of the surface integrity (number and size of cracks) prior to the corrosion and the assessment of the chemical composition before and after corrosion are reported.

The main findings can be summarized as follows:

- The ALD technique provides better corrosion protection both for smooth and rough surfaces. Dealing with the former, the corrosion current density of bare samples has been reduced from 1400 $\mu A/cm^2$ to 220 $\mu A/cm^2$ and 84 $\mu A/cm^2$ using sputtering and ALD, respectively, while for rough samples, the corrosion current density of the bare material was reduced from 1500 $\mu A/cm^2$ to 600 $\mu A/cm^2$ and 102 $\mu A/cm^2$ using sputtering and ALD, respectively.
- A similar trend was obtained in hydrogen evolution tests. The hydrogen evolved from bare smooth samples was reduced by 21% and 27% with sputter and ALD, respectively. Dealing with rough

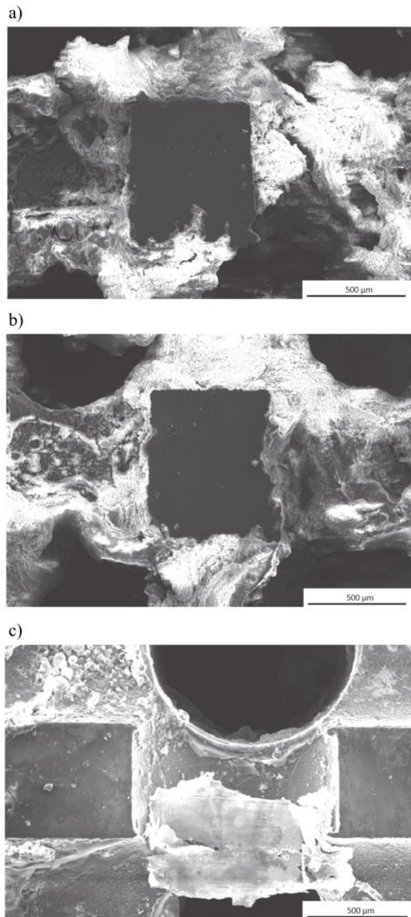

Fig. 18. Micro-morphology of the bare (a), sputter coated (b) and ALD coated (c) corroded sample's sliced cross-section.

samples, the hydrogen evolved from the bare material was reduced by 12% and 20% with sputter and ALD, respectively.

- The line-of-sight limitation of sputtering is particularly evident in the case of 3D porous structures, where the hydrogen evolved from the bare samples is reduced by 13% only with sputtering, while ALD coatings lead to a reduction of 72%.
- In the as-deposited condition, sputter coatings have more and longer cracks. Before corrosion, the composition of the sputter and ALD TiO_2 coating were identical, whereas after 24 h of corrosion, the amount of Ti and Mg differed. XPS results indicate a significantly higher decrease in the Ti concentration for the ALD coated samples after corrosion, whereas the Mg concentration remains unchanged. Instead, the sputter coating experiences a decrease in both Ti and Mg content indicating a corrosion attack on the underlying substrate as well as the remaining of parts of the protective TiO_2 layer on the substrate. We hence hypothesize that the improved corrosion performances of ALD cannot be attributed to the line-of-sight limitation only, but also to the coatings' surface integrity differences by either technology.

It can be concluded that both sputtering and ALD are effective coating techniques to increase the corrosion resistance of AZ31 alloy, but ALD has been shown to provide the lowest corrosion rates regardless of the surface conditions (roughness and topology). Therefore, the ALD technique can be considered viable for the fabrication of next-generation biodegradable implants with a prolonged durability inside the human body.

CRediT authorship contribution statement

Mirco Peron: Conceptualization, Data curation, Investigation, Methodology, Validation, Visualization, Writing - original draft, Writing - review & editing.**Abdulla Bin Afif:**Data curation, Investigation, Validation.**Anup Dadlani:**Data curation, Investigation, Validation.**Filippo Berto:**Supervision.**Jan Torgersen:**Supervision, Writing - original draft, Writing - review & editing.

Declaration of competing interest

The authors declare that they have no known competing financial interests or personal relationships that could have appeared to influence the work reported in this paper.

Acknowledgement

Abdulla Bin Afif was supported by NTNU's Enabling technologies: Nanotechnology. The Research Council of Norway is acknowledged for the support to the Norwegian Micro- and Nano-Fabrication Facility, NorFab, project number 245963/F50. Anup Dadlani was funded by the Norwegian Research Council under project number 274459 Translate.

References

[1] M.P. Ginebra, T. Traykova, J.A. Planell, Calcium phosphate cements as bone drug delivery systems: a review, J. Control. Release 113 (2006) 102–110, https://doi.org/10.1016/j.jconrel.2006.04.007.
[2] http://share.iofbonehealth.org/EU-6-Material/Reports/IOF%20Report_EU.pdf (web archive link, 20 November 2019), (n.d.). http://share.iofbonehealth.org/EU-6-Material/Reports/IOF Report_EU.pdf (accessed November 20, 2019).
[3] T. Hanawa, Overview of metals and applications, Met. Biomed. Devices, Elsevier, 2010, pp. 3–24, , https://doi.org/10.1533/9781845699246.1.3.
[4] T. Albrektsson, P.-I. Brånemark, H.-A. Hansson, J. Lindström, Osseointegrated titanium implants: *requirements for ensuring a long-lasting, direct bone-to-implant anchorage in man*, Acta Orthop. Scand. 52 (1981) 155–170, https://doi.org/10.3109/17453678108991776.
[5] F. Rossi, N.P. Lang, E. De Santis, F. Morelli, G. Favero, D. Botticelli, Bone-healing pattern at the surface of titanium implants: an experimental study in the dog, Clin. Oral Implants Res. 25 (2014) 124–131, https://doi.org/10.1111/clr.12097.
[6] T.W. Bauer, J. Schils, The pathology of total joint arthroplasty. II. Mechanisms of implant failure, Skelet. Radiol. 28 (1999) 483–497 http://www.ncbi.nlm.nih.gov/pubmed/10525792 , Accessed date: 31 March 2017.
[7] A.R. Dujovne, J.D. Bobyn, J.J. Krygier, J.E. Miller, C.E. Brooks, Mechanical compatibility of noncemented hip prostheses with the human femur, J. Arthroplast. 8 (1993) 7–22, https://doi.org/10.1016/S0883-5403(06)80102-6.
[8] C.A. Engh, J.D. Bobyn, The influence of stem size and extent of porous coating on femoral bone resorption after primary cementless hip arthroplasty, Clin. Orthop. Relat. Res. (1988) 7–28 http://www.ncbi.nlm.nih.gov/pubmed/3370887 , Accessed date: 31 March 2017.
[9] J. Kerner, R. Huiskes, G.H. van Lenthe, H. Weinans, B. van Rietbergen, C.A. Engh, A.A. Amis, Correlation between pre-operative periprosthetic bone density and post-operative bone loss in THA can be explained by strain-adaptive remodelling, J.

Biomech. 32 (1999) 695–703, https://doi.org/10.1016/S0021-9290(99)00041-X.
[10] D.R. Sumner, J.O. Galante, Determinants of stress shielding: design versus materials versus interface, Clin. Orthop. Relat. Res. (1992) 202–212 http://www.ncbi.nlm.nih.gov/pubmed/1729005 , Accessed date: 31 March 2017.
[11] T.M. Turner, D.R. Sumner, R.M. Urban, R. Igloria, J.O. Galante, Maintenance of proximal cortical bone with use of a less stiff femoral component in hemi-arthroplasty of the hip without cement. An investigation in a canine model at six months and two years, J. Bone Joint Surg. Am. 79 (1997) 1381–1390 http://www.ncbi.nlm.nih.gov/pubmed/9314401 , Accessed date: 31 March 2017.
[12] B. Van Rietbergen, R. Huiskes, H. Weinans, D.R. Sumner, T.M. Turner, J.O. Galante, The mechanism of bone remodeling and resorption around press-fitted THA stems, J. Biomech. 26 (1993) 369–382, https://doi.org/10.1016/0021-9290(93)90001-U.
[13] B.G. Pound, Corrosion behavior of metallic materials in biomedical applications. I. Ti and its alloys, 32 (2014) 1–20, https://doi.org/10.1515/corrrev-2014-0007.
[14] B.G. Pound, Corrosion behavior of metallic materials in biomedical applications. II. Stainless steels and Co-Cr alloys, 32 (2014) 21–41, https://doi.org/10.1515/corrrev-2014-0008.
[15] J.J. Jacobs, J.L. Gilbert, R.M. Urban, Corrosion of metal orthopaedic implants, J. Bone Joint Surg. Am. 80 (1998) 268–282 http://www.ncbi.nlm.nih.gov/pubmed/9486734 , Accessed date: 31 March 2017.
[16] J.J. Jacobs, N.J. Hallab, A.K. Skipor, R.M. Urban, Metal degradation products: a cause for concern in metal-metal bearings? Clin. Orthop. Relat. Res. (2003) 139–147, https://doi.org/10.1097/01.blo.0000096810.78689.62.
[17] I.B. Beech, J.A. Sunner, C.R. Arciola, P. Cristiani, Microbially-influenced corrosion: damage to prostheses, delight for bacteria, Int. J. Artif. Organs. 29 (2006) 443–452 http://www.ncbi.nlm.nih.gov/pubmed/16705614 , Accessed date: 20 June 2017.
[18] M. Peron, F. Berto, J. Torgersen, Magnesium and its Alloys as Implant Materials: Corrosion, Mechanical and Biological Performances, CRC Press LLC, 2020.
[19] M. Peron, J. Torgersen, F. Berto, Mg and its alloys for biomedical applications: exploring corrosion and its interplay with mechanical failure, Metals (Basel) 7 (2017) 252, https://doi.org/10.3390/met7070252.
[20] N. Li, Y. Zheng, Novel magnesium alloys developed for biomedical application: a review, J. Mater. Sci. Technol. 29 (2013) 489–502, https://doi.org/10.1016/J.JMST.2013.02.005.
[21] R.K. Singh Raman, S. Jafari, S.E. Harandi, Corrosion fatigue fracture of magnesium alloys in bioimplant applications: a review, Eng. Fract. Mech. 137 (2015) 97–108, https://doi.org/10.1016/j.engfracmech.2014.08.009.
[22] M.P. Staiger, A.M. Pietak, J. Huadmai, G. Dias, Magnesium and its alloys as orthopedic biomaterials: a review, Biomaterials 27 (2006) 1728–1734, https://doi.org/10.1016/j.biomaterials.2005.10.003.
[23] A.C. Hänzi, A.S. Sologubenko, P.J. Uggowitzer, Design strategy for new biodegradable Mg–Y–Zn alloys for medical applications, Int. J. Mater. Res. 100 (2009) 1127–1136, https://doi.org/10.3139/146.110157.
[24] M. Fraldi, L. Esposito, G. Perrella, A. Cutolo, S.C. Cowin, L. Esposito, Topological optimization in hip prosthesis design, Biomech. Model. Mechanobiol. 9 (2010) 389–402, https://doi.org/10.1007/s10237-009-0183-0.
[25] L.E. Murr, S.M. Gaytan, E. Martinez, F.R. Medina, R.B. Wicker, Fabricating functional Ti-alloy biomedical implants by additive manufacturing using electron beam melting, J. Biotechnol. Biomater. (2012) 2, https://doi.org/10.4172/2155-952X.1000131.
[26] A.-F. Obaton, J. Fain, M. Djemaï, D. Meinel, F. Léonard, E. Mahé, B. Lécuelle, J.-J. Fouchet, G. Bruno, In vivo XCT bone characterization of lattice structured implants fabricated by additive manufacturing, Heliyon 3 (2017), https://doi.org/10.1016/J.HELIYON.2017.E00374.
[27] M. Peron, P.C. Skaret, A. Fabrizi, A. Varone, R. Montanari, H.J. Roven, P. Ferro, F. Berto, J. Torgersen, The effect of Equal Channel Angular Pressing on the stress corrosion cracking susceptibility of AZ31 alloy in simulated body fluid, J. Mech. Behav. Biomed. Mater. (2020) 103724, , https://doi.org/10.1016/j.jmbbm.2020.103724.
[28] K.R. Gopi, H.S. Nayaka, S. Sahu, Corrosion behavior of ECAP-processed AM90 magnesium alloy, Arab. J. Sci. Eng. 43 (2018) 4871–4878, https://doi.org/10.1007/s13369-018-3203-5.
[29] B. Ratna Sunil, T.S. Sampath Kumar, U. Chakkingal, V. Nandakumar, M. Doble, V. Devi Prasad, M. Raghunath, In vitro and in vivo studies of biodegradable fine grained AZ31 magnesium alloy produced by equal channel angular pressing, Mater. Sci. Eng. C. 59 (2016) 356–367, https://doi.org/10.1016/J.MSEC.2015.10.028.
[30] S. Dobatkin, N. Martynenko, N. Anisimova, M. Kiselevskiy, D. Prosvirnin, V. Terentiev, N. Yurchenko, G. Salishchev, Y. Estrin, Mechanical properties, biodegradation, and biocompatibility of ultrafine grained magnesium alloy WE43, Materials (Basel) 12 (2019), https://doi.org/10.3390/ma12213627.
[31] M. Peron, R. Bertolini, A. Ghiotti, J. Torgersen, S. Bruschi, F. Berto, Enhancement of stress corrosion cracking of AZ31 magnesium alloy in simulated body fluid thanks to cryogenic machining, J. Mech. Behav. Biomed. Mater. 101 (2020) 103429, , https://doi.org/10.1016/J.JMBBM.2019.103429.
[32] R. Smeets, B. Stadlinger, F. Schwarz, B. Beck-Broichsitter, O. Jung, C. Precht, F. Kloss, A. Gröbe, M. Heiland, T. Ebker, T. Ebker, Impact of dental implant surface modifications on osseointegration, Biomed. Res. Int. 2016 (2016) 1–16, https://doi.org/10.1155/2016/6285620.
[33] T. Albrektsson, A. Wennerberg, Oral implant surfaces: part 1–review focusing on topographic and chemical properties of different surfaces and in vivo responses to them., Int. J. Prosthodont. 17 (n.d.) 536–43. http://www.ncbi.nlm.nih.gov/pubmed/15543910 (accessed October 30, 2017).
[34] J. M.Rúa, A.A. Zuleta, J. Ramírez, P. Fernández-Morales, Micro-arc oxidation coating on porous magnesium foam and its potential biomedical applications, Surf. Coatings Technol. 360 (2019) 213–221, https://doi.org/10.1016/j.surfcoat.2018.12.106.
[35] C. Gao, S. Peng, P. Feng, C. Shuai, Bone biomaterials and interactions with stem cells, Bone Res 5 (2017) 1–33, https://doi.org/10.1038/boneres.2017.59.
[36] T.S.N. Sankara Narayanan, I.-S. Park, M.H. Lee, Surface modification of magnesium and its alloys for biomedical applications, Modification and Coating Techniques, Volume 2 2015.
[37] I.S. Abela, Physical vapour deposition on mg alloys for biomedical applications, Surf. Modif. Magnes. Its Alloy. Biomed. Appl, Elsevier Inc, 2015, pp. 81–100, , https://doi.org/10.1016/B978-1-78242-078-1.00004-9.
[38] W. Jin, G. Wang, X. Peng, W. Li, A.M. Qasim, P.K. Chu, Tantalum nitride films for corrosion protection of biomedical Mg-Y-RE alloy, J. Alloys Compd. 764 (2018) 947–958, https://doi.org/10.1016/J.JALLCOM.2018.06.151.
[39] W. Jin, G. Wang, A.M. Qasim, S. Mo, Q. Ruan, H. Zhou, W. Li, P.K. Chu, Corrosion protection and enhanced biocompatibility of biomedical Mg-Y-RE alloy coated with tin dioxide, Surf. Coatings Technol. 357 (2019) 78–82, https://doi.org/10.1016/j.surfcoat.2018.10.005.
[40] X. Liu, Q. Yang, Z. Li, W. Yuan, Y. Zheng, Z. Cui, X. Yang, K.W.K. Yeung, S. Wu, A combined coating strategy based on atomic layer deposition for enhancement of corrosion resistance of AZ31 magnesium alloy, Appl. Surf. Sci. 434 (2018) 1101–1111, https://doi.org/10.1016/J.APSUSC.2017.11.032.
[41] E. Marin, A. Lanzutti, L. Guzman, L. Fedrizzi, Chemical and electrochemical characterization of TiO2/Al2O3 atomic layer depositions on AZ-31 magnesium alloy, J. Coatings Technol. Res. 9 (2012) 347–355, https://doi.org/10.1007/s11998-011-9372-8.
[42] Q. Yang, W. Yuan, X. Liu, Y. Zheng, Z. Cui, X. Yang, H. Pan, S. Wu, Atomic layer deposited ZrO2 nanofilm on Mg-Sr alloy for enhanced corrosion resistance and biocompatibility, Acta Biomater. 58 (2017) 515–526, https://doi.org/10.1016/J.ACTBIO.2017.06.015.
[43] T. Kasuga, H. Kondo, M. Nogami, Apatite formation on TiO2 in simulated body fluid, J. Cryst. Growth 235 (2002) 235–240, https://doi.org/10.1016/S0022-0248(01)01782-1.
[44] X.X. Wang, S. Hayakawa, K. Tsuru, A. Osaka, Bioactive titania gel layers formed by chemical treatment of Ti substrate with a H2O2/HCl solution, Biomaterials 23 (2002) 1353–1357, https://doi.org/10.1016/S0142-9612(01)00254-X.
[45] M. Uchida, H.-M. Kim, T. Kokubo, T. Nakamura, Apatite-forming ability of titania gels with different structures, Bioceramics, WORLD SCIENTIFIC, 1999, pp. 149–152, , https://doi.org/10.1142/9789814291064_0036.
[46] J.-M. Wu, S. Hayakawa, K. Tsuru, A. Osaka, Low-temperature preparation of anatase and rutile layers on titanium substrates and their ability to induce in vitro apatite deposition, J. Am. Ceram. Soc. 87 (2004) 1635–1642, https://doi.org/10.1111/j.1551-2916.2004.01635.x.
[47] ASTM G5 - 14 Standard Reference Test Method for Making Potentiodynamic Anodic Polarization Measurements, (n.d.). https://compass.astm.org/Standards/HISTORICAL/G5-14.htm (accessed December 3, 2019).
[48] T. Kokubo, H. Takadama, How useful is SBF in predicting in vivo bone bioactivity? Biomaterials 27 (2006) 2907–2915, https://doi.org/10.1016/J.BIOMATERIALS.2006.01.017.
[49] G. Song, A. Atrens, D. StJohn, An hydrogen evolution method for the estimation of the corrosion rate of magnesium alloys, Magnes. Technol, John Wiley & Sons, Inc, Hoboken, NJ, USA, 2001, pp. 254–262, , https://doi.org/10.1002/9781118805497.ch44 2013.
[50] Y. Shi, M. Qi, Y. Chen, P. Shi, MAO-DCPD composite coating on Mg alloy for degradable implant applications, Mater. Lett. 65 (2011) 2201–2204, https://doi.org/10.1016/J.MATLET.2011.04.037.
[51] S. Johnston, Z. Shi, A. Atrens, The influence of pH on the corrosion rate of high-purity Mg, AZ91 and ZE41 in bicarbonate buffered Hanks' solution, Corros. Sci. 101 (2015) 182–192, https://doi.org/10.1016/J.CORSCI.2015.09.018.
[52] S. Nezar, N. Saoula, S. Sali, M. Faiz, M. Mekki, N.A. Laoufi, N. Tabet, Properties of TiO 2 thin films deposited by rf reactive magnetron sputtering on biased substrates, Appl. Surf. Sci. 395 (2017) 172–179, https://doi.org/10.1016/j.apsusc.2016.08.125.
[53] J.H. Kim, S. Lee, H.S. Im, Effect of target density and its morphology on TiO2 thin films grown on Si(100) by PLD, Appl. Surf. Sci. 151 (1999) 6–16, https://doi.org/10.1016/S0169-4332(99)00269-X.
[54] J. Yu, X. Zhao, J. Du, W. Chen, Preparation, microstructure and photocatalytic activity of the porous TiO2 anatase coating by sol-gel processing, J. Sol-Gel Sci. Technol. 17 (2000) 163–171, https://doi.org/10.1023/A:1008703719929.
[55] Y. Xin, K. Huo, T. Hu, G. Tang, P.K. Chu, Corrosion products on biomedical magnesium alloy soaked in simulated body fluids, J. Mater. Res. 24 (2009) 2711–2719, https://doi.org/10.1557/jmr.2009.0323.
[56] Q. Zhang, Y. Jiang, Y. Zhang, Z. Ye, W. Tan, M. Lang, Effect of porosity on long-term degradation of poly (ε-caprolactone) scaffolds and their cellular response, Polym. Degrad. Stab. 98 (2013) 209–218, https://doi.org/10.1016/j.polymdegradstab.2012.10.008.
[57] C. Hadjicharalambous, O. Prymak, K. Loza, A. Buyakov, S. Kulkov, M. Chatzinikolaidou, Effect of porosity of alumina and zirconia ceramics toward pre-osteoblast response, Front. Bioeng. Biotechnol. 3 (2015) 175, https://doi.org/10.3389/fbioe.2015.00175.
[58] J. Munemasa, T. Kumakiri, Effect of the surface roughness of substrates on the corrosion properties of films coated by physical vapour deposition, Surf. Coatings Technol. 49 (1991) 496–499, https://doi.org/10.1016/0257-8972(91)90106-7.
[59] V. Karageorgiou, D. Kaplan, Porosity of 3D biomaterial scaffolds and osteogenesis, Biomaterials 26 (2005) 5474–5491, https://doi.org/10.1016/j.biomaterials.2005.02.002.
[60] F.J. O'Brien, B.A. Harley, M.A. Waller, I.V. Yannas, L.J. Gibson, P.J. Prendergast, The effect of pore size on permeability and cell attachment in collagen scaffolds for tissue engineering, Technol. Heal. Care, IOS Press, 2007, pp. 3–17, , https://doi.

org/10.3233/thc-2007-15102.

[61] A. Pardo, S. Feliu, M.C. Merino, R. Arrabal, E. Matykina, Electrochemical estimation of the corrosion rate of magnesium/aluminium alloys, Int. J. Corros. 2010 (2010), https://doi.org/10.1155/2010/953850.

[62] M. Lorenzetti, E. Pellicer, J. Sort, M.D. Baró, J. Kovač, S. Novak, S. Kobe, Improvement to the corrosion resistance of Ti-based implants using hydrothermally synthesized nanostructured anatase coatings, Materials (Basel) 7 (2014) 180–194, https://doi.org/10.3390/ma7010180.

[63] S. Il Pyun, Y.G. Yoon, E. Lugscheider, R. Mathesius, Relationship between interfacial reaction and adhesion at PVD TiO2 film-metal (Ti or Al) interfaces, Surf. Coatings Technol. 61 (1993) 233–237, https://doi.org/10.1016/0257-8972(93)90231-C.

[64] C. (Christoph) Leyens, M. (Manfred) Peters, John Wiley & Sons, Wiley InterScience (Online Service), Titanium and Titanium Alloys: Fundamentals and Applications, Wiley-VCH, 2003.

[65] H. Hayashi, T. Saitou, N. Maruyama, H. Inaba, K. Kawamura, M. Mori, Thermal expansion coefficient of yttria stabilized zirconia for various yttria contents, Solid State Ionics 176 (2005) 613–619, https://doi.org/10.1016/j.ssi.2004.08.021.

[66] D.R. Hummer, P.J. Heaney, J.E. Post, Thermal expansion of anatase and rutile between 300 and 575 K using synchrotron powder X-ray diffraction, Powder Diffract. 22 (2007) 352–357, https://doi.org/10.1154/1.2790965.

[67] Y. Xu, Y. Zhang, T. He, K. Ding, X. Huang, H. Li, J. Shi, Y. Guo, J. Zhang, The effects of thermal and atmospheric pressure radio frequency plasma annealing in the crystallization of TiO2 thin films, Coatings 9 (2019) 357, https://doi.org/10.3390/coatings9060357.

[68] N. Kumar, T.M. Wilkinson, C.E. Packard, M. Kumar, Design of low surface roughness-low residual stress-high optoelectronic merit a-IZO thin films for flexible OLEDs Articles you may be interested in, J. Appl. Phys. 119 (2016) 225303, , https://doi.org/10.1063/1.4953212.

[69] P. Yáñez-Contreras, J.D.O. Barceinas-Sánchez, C.A. Poblano-Salas, J.M. Medina-Flores, A.L. García-García, I. Domínguez-López, Estudio de la evolución del perfil de esfuerzos residuales en recubrimientos barrera térmica depositados sobre acero inoxidable AISI 304, DYNA 83 (2016) 160–166, https://doi.org/10.15446/dyna.v83n197.51150.

[70] H.J. Moon, Development of Thin Film Inorganic Membranes for Oxygen Separation, Forschungszentrum Jülich, 2012.

[71] Robert B. Heimann, H.D. Lehmann, Bioceramic Coatings for Medical Implants: Trends and Techniques, n.d.

[72] ISO - ISO 25178-2:2012 - Geometrical product specifications (GPS) — surface texture: areal — part 2: terms, definitions and surface texture parameters, (n.d.). https://www.iso.org/standard/42785.html (accessed February 7, 2020).

Paper 5

Available online at www.sciencedirect.com

ScienceDirect

Journal of Magnesium and Alloys 9 (2021) 1806–1819

www.elsevier.com/locate/jma

On the evaluation of ALD TiO_2, ZrO_2 and HfO_2 coatings on corrosion and cytotoxicity performances

Mirco Peron[a,*], Susanna Cogo[b], Maria Bjelland[a], Abdulla Bin Afif[a], Anup Dadlani[a], Elisa Greggio[b], Filippo Berto[a], Jan Torgersen[a]

[a] *Department of Industrial and Mechanical Engineering, Norwegian University of Science and Technology, Richard Birkelands vei 2b, 7034 Trondheim, Norway*

[b] *Department of Biology, University of Padova, Via Ugo Bassi 58/b, 35131, Padova, Italy*

Received 20 October 2020; received in revised form 28 February 2021; accepted 13 March 2021
Available online 15 May 2021

Abstract

Magnesium alloys have been widely studied as materials for temporary implants, but their use has been limited by their corrosion rate. Recently, coatings have been proven to provide an effective barrier. Though only little explored in the field, Atomic Layer Deposition (ALD) stands out as a coating technology due to the outstanding film conformality and density achievable. Here, we provide first insights into the corrosion behavior and the induced biological response of 100nm thick ALD TiO_2, HfO_2 and ZrO_2 coatings on AZ31 alloy by means of potentiodynamic polarization curves, electrochemical impedance spectroscopy (EIS), hydrogen evolution and MTS colorimetric assay with L929 cells. All three coatings improve the corrosion behavior and cytotoxicity of the alloy. Particularly, HfO_2 coatings were characterized by the highest corrosion resistance and cell viability, slightly higher than those of ZrO_2 coatings. TiO_2 was characterized by the lowest corrosion improvements and, though generally considered a biocompatible coating, was found to not meet the demands for cellular applications (it was characterized by grade 3 cytotoxicity after 5 days of culture). These results reveal a strong link between biocompatibility and corrosion resistance and entail the need of taking the latter into consideration in the choice of a biocompatible coating to protect degradable Mg-based alloys.

© 2021 Chongqing University. Publishing services provided by Elsevier B.V. on behalf of KeAi Communications Co. Ltd.
This is an open access article under the CC BY-NC-ND license (http://creativecommons.org/licenses/by-nc-nd/4.0/)
Peer review under responsibility of Chongqing University

Keywords: Atomic layer deposition (ALD); Coatings; Corrosion resistance; Cytocompatibility; Magnesium.

1. Introduction

As aging and obesity increase the demand for the implantation of medical devices [1], medical technology advances, with a raising interest in the use of metallic materials for implantable devices to assist with tissue repair or replacement. Implantable devices can be divided into permanent and temporary. For the latter, implants are only required to remain within the human body until the tissue regains load bearing capacity and integrity. To this aim, biodegradable materials are desired and Magnesium (Mg) stands out [2–4] due to its attractive features: (1) an elastic modulus compatible with natural bone minimizing the risk of stress shielding [2] and (2) the ability to degrade in vivo without releasing toxic products [5–7]. Accelerated corrosion of pure Mg hampers its usability in clinical applications as mechanical failure of the implant is prone to occur before the tissue has recovered [8]. In addition, during corrosion, hydrogen gas gets produced at rates beyond what bone tissue is able to accommodate, causing severe host tissue damage [9,10].

In the last years, different strategies have been investigated to reduce the corrosion rate of Mg, such as alloying and mechanical processing inducing severe plastic deformation (SPD) like Equal Channel Angular Pressing (ECAP) and machining [11–14]. However, both these approaches are char-

* Corresponding author.
E-mail address: mirco.peron@ntnu.no (M. Peron).

https://doi.org/10.1016/j.jma.2021.03.010
2213-9567/© 2021 Chongqing University. Publishing services provided by Elsevier B.V. on behalf of KeAi Communications Co. Ltd. This is an open access article under the CC BY-NC-ND license (http://creativecommons.org/licenses/by-nc-nd/4.0/) Peer review under responsibility of Chongqing University

acterized by some main limitations. Alloying may introduce elements causing adverse biological reactions [15], ECAP requires multiple deformation passes before achieving the goal, while machining might not be applicable in the development of Mg implants as it does not allow to make the intricate features and textured surfaces needed to enhance ingrowth of cells and tissue [16–18].

Hence, an alternative, surface confined approach allowing the control of surface texture might be required. In this perspective, coatings have recently gained wide interest among researchers since they allow to preserve the surface texture and the designed macroscopic porosity tailored for osseointegration and to match mechanical characteristics. Several coating techniques, such as anodizing, fluoride conversion coating, sol-gel techniques and physical vapor deposition techniques, have been developed in the last years to increase the corrosion resistance [19]. However, all these techniques are characterized by some drawbacks that limit their use, mainly low control of the thickness and high porosity and cracking [20–22]. In addition, the effectiveness of physical vapor deposition techniques, such as sputtering, may be limited due to the inherent line-of-sight deposition process [23,24].

To overcome this issue, Chemical Vapor Deposition (CVD) is employed. In this class of processes, the substrate surface is exposed to one or more volatile precursors that react and/or decompose to produce the desired surface deposit. Among CVD techniques, Atomic Layer Deposition (ALD) stands out in terms of conformality, film density and possibility for compositional control due to its self-limiting surface-gas phase reactions and it has recently found application in corrosion protection of biomedical implants [25,26]. In this field, researchers have mainly focused on the effect of biocompatible coatings deposited by means of ALD on the corrosion resistance of metallic implant materials [27,28]. In particular, their interest has focused on TiO_2 and ZrO_2. TiO_2 is in fact known to be biocompatible since it can (1) stimulate in vivo osteoconductivity [29–31], (2) induce in vitro bone-like apatite formation and (3) bind directly and reliably to living bone [32]. On the other hand, ZrO_2 is an important biomaterial, widely used in applications such as dental implants, where osteointegration is of minor importance compared to the requirements of corrosion and wear resistance [33] and of a reduced bacterial colonization [34,35]. Dealing with Mg and its alloys, although limited data are available, the application of both ALDed TiO_2 and ZrO_2 has been shown to promisingly improve the corrosion resistance. Marin et al. [26] reported a reduced corrosion current density (i.e., from 10^{-4} A/cm^2 to 10^{-6} A/cm^2) when a commercial AZ31 Mg alloy was coated with a 100 nm thick TiO_2 layer, while a 10 nm thick ZrO_2 layer was found to reduce the corrosion current density of an AZ31 Mg alloy by three order of magnitude [25], agreeing with the results obtained by our group for a 100 nm thick ZrO_2 layer [36–38].

However, in the development of reliable Mg-based implants, and more in general of temporary implants, the corrosion resistance of a material is fundamental also because it can affect the cell response: degradation products evolving during the corrosion process may in fact cause adverse effect on the surrounding (the vicinity of the implant). In the case of Mg and its alloys, H_2 evolves from the corrosion process. This leads to an increase in the pH around the implant, and it is widely known that a high pH has harmful effects on cell viability, migration and proliferation [39]. For example, a pH higher than 8.5 was reported to inhibit the proliferation of human bone marrow-derived mesenchymal stem cells [40]. Nevertheless, to the best of the authors' knowledge, the cytotoxicity of ALD TiO_2 and ZrO_2 coatings has never been evaluated.

In this work, we aim to evaluate the effect of TiO_2 and ZrO_2 ALD coatings on cell viability in the vicinity of the implant by carrying out MTS proliferation assay using the murine subcutaneous connective tissue L929 cell line. Moreover, to provide further insights into the corrosion performances of ALD TiO_2 and ZrO_2 coatings in a physiologically relevant environment, potentiodynamic polarization curves, electrochemical impedance spectroscopy (EIS) and hydrogen evolution tests have been carried out on 100 nm thick TiO_2 and ZrO_2 coated AZ31 samples. In addition to that, a new biocompatible coating has recently emerged as a very effective coating material to increase the corrosion resistance of biocompatible materials [41], i.e. HfO_2. Zhang et al., in fact, reported a 30 nm HfO_2 coating to reduce the corrosion current density of a die-cast AZ91D from 44.29 μA/cm^2 to 0.78 μA/cm^2 [42]. These results agree with those reported in Ref. [43] where 60 nm HfO_2 coating was reported to decrease the corrosion current density of an AZ31 alloy of almost three orders of magnitude. However, much still needs to be uncovered, since very few studies have addressed this aspect. Moreover, to the best of the authors' knowledge, the effects of ALD HfO_2 on cell viability have never been investigated before. Hence, with this work, we also aim to fill these gaps, carrying out potentiodynamic polarization curves, EIS, hydrogen evolution tests and MTS colorimetric assay using L929 cells on 100 nm thick ALD HfO_2 coated AZ31 samples. This could open the avenue for the use of new coating materials for degradable Mg alloys used as implant material.

2. Materials and methods

2.1. Materials and environment

Commercially available bars of AZ31 Mg alloy were purchased from Dynamic Metals LTD (Leighton Buzzard, UK). More than 500 grains have been considered for the grain analysis by using LAS image software, and a representative image of the microstructure is depicted in Fig. 1. As it can be seen, the material is characterized by a homogeneous α matrix, and the average grain size, obtained by means of linear intercept method, was equal to $13.2 \pm 8\,\mu m$.

The environment used for the corrosion experiments was simulated body fluid (SBF) prepared according to Ref. [44], while that used for the cytotoxicity experiments was Dulbecco's Modified Eagle Medium (DMEM – Life Technologies Corp, California, USA) supplemented with 10%v/v fetal

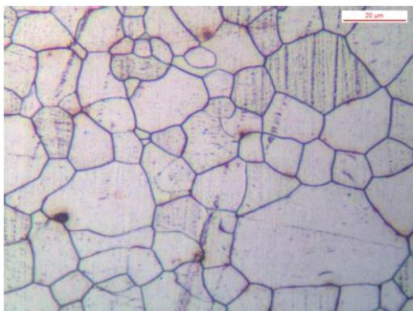

Fig. 1. Micrography of the AZ31 alloy microstructure.

bovine serum (FBS), 100 μg/ml streptomycin and 100 U/ml penicillin.

2.2. Atomic layer deposition

A commercial ALD reactor (Savannah S200, Veeco Instruments Inc., Massachusetts, USA) was used to deposit the ALD coatings. The deposition was carried out through successive cyclic reactions. In particular, 926 successive cyclic reactions between Tetrakis (dimethylamino) zirconium (TDMAZ) and deionized water (H_2O) were used to deposit 100 nm of ZrO_2 (deposition rate of approximately 1.08 Å/cycle), at a temperature of 160 °C. Each cycle was composed of two parts:

(1) 250-ms TDMAZ precursor pulse followed by a 10-s Hi-purity N_2 purge with a flow rate of 20 sccm.
(2) 150-ms H_2O precursor pulse followed by a 15-ms Hi-purity N_2 purge.

The N_2 purge was used to remove residual reactants and by-products from the chamber so as to prevent any additional chemical vapor deposition reactions. During the deposition process, the TDMAZ precursor was heated at 75 °C, while the H_2O precursor and the delivery lines were kept at 25 °C and 160 °C, respectively. Concerning TiO_2, the metal organic precursor used was Tetrakis (dimethylamino) titanium (IV) or TDMA-Ti heated at 75°C. Each cycle was again composed of two parts:

(1) 0.1 s TDMA-Ti precursor pulse followed by a 5 s Hi-purity N_2 purge with a flow rate of 20 sccm.
(2) 0.015 s H_2O precursor pulse followed by a 5 s Hi-purity N_2 purge.

The deposition rate was found to be 0.5 A°/cycle. Finally, the deposition of HfO_2 was carried out through successive cyclic reactions between Tetrakis (dimethylamino) Hafnium (TDMAH) and deionized water (H_2O) at 160 °C. Again, each cycle was composed of two parts:

(1) 200-ms TDMAZ precursor pulse followed by a 10-s Hi-purity N_2 purge (flow rate of 20 sccm).
(2) 150-ms H_2O precursor pulse followed by a 10 s Hi-purity N_2 purge.

During the deposition process, the TDMAZ precursor was heated at 75 °C, while the H_2O precursor and the delivery lines were kept at 25 °C and 160 °C, respectively. The deposition rate was measured at 1.3 Å/cycle. All the chemical precursors have been supplied by Sigma Aldrich (St. Louis, Missouri, USA).

2.3. Coating characterization

X-ray photoluminescence (XPS) measurements were conducted to assess the chemical composition of the TiO_2, ZrO_2 and HfO_2 ALD coatings. To do so, a Kratos Analytical XPS Microprobe (Kratos Analytical Ltd, Manchester, UK) using Al (Kα) radiation of 1486 eV in a vacuum environment of 5×10^{-9} Torr was used. The XPS data were analyzed using CasaXPS software.

2.4. Corrosion experiments

The corrosion performances of coated and uncoated AZ31 alloy have been characterized by means of potentiodynamic polarization curves, electrochemical impedance spectroscopy and hydrogen evolution tests. The environment used for the corrosion experiments was simulated body fluid (SBF) prepared according to Ref. [44].

2.4.1. Potentiodynamic polarization curves

The commercially available bars were machined into discs with a thickness of 2 mm and a diameter of 29 mm. The discs were then grounded with 2000 grit silicon carbide papers. Afterwards, the samples were cleaned with acetone for five minutes in ultrasonic bath and subsequently with ethanol using the same procedure. A Gamry Reference 600+ potentiostat was used to obtain the potentiodynamic polarization curves of bare and coated samples. A three-electrode setup was used, with the bare or coated samples being the working electrode, the Hg/Hg_2SO_4 electrode being the reference electrode, and the platinum plate electrode being the counter electrode. Static simulated body fluid (SBF) with a pH of 7.4 and at a temperature of 37 °C was used as electrolyte. The surface area of the samples exposed to the SBF was 1 cm^2. Before carrying out the potentiodynamic polarization tests, 30 min were waited to achieve a stable open-circuit potential. The potentiodynamic polarization tests were carried out at a scan rate of 0.5 mV/s, and the tests were repeated three times for each condition.

2.4.2. Electrochemical impedance spectroscopy

Electrochemical impedance spectroscopy was carried out using the same three-electrode configuration and the same

potentiostat as described in the previous Section. Additionally, the electrochemical cell was placed inside a Faraday's cage to avoid noise in the results. To fit the results, the software Gamry Echem Analyst (Gamry Instruments, Warminster, PA, USA) was used. The signal amplitude during EIS was 10 mV relative to the open circuit potential (OCP) at a frequency range of 10^{-2} to 10^5 Hz, and the samples were kept in SBF for half an hour before measurements to stabilize and measure OCP. The tests were repeated three times for each condition.

2.4.3. Hydrogen evolution tests

Mg, when in contact with an aqueous environment, leads to the evolution of hydrogen gas according to the following equation [2]:

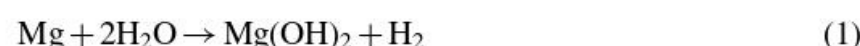

$$Mg + 2H_2O \rightarrow Mg(OH)_2 + H_2 \quad (1)$$

Specifically, the dissolution of one mole of magnesium leads to the release of one mole of hydrogen. It is hence clear that it is possible to measure the corrosion rate of Mg and its alloys by measuring the evolved hydrogen. The use of this method, besides being simple, allows to overcome the limitations of the weight loss method and of the electrochemical techniques [45]. To perform such experiments, the commercially available bars were machined into cubic samples of 5 mm side and they were then prepared as described in Section 2.4. Finally, the samples were immersed in SBF at 37 °C for 7 days and the hydrogen bubbles were collected into a burette according to the procedure reported in Ref. [45]. The tests were repeated three times for each condition.

2.5. Degradation behavior

Micro- and macro-morphological characterizations of bare and coated samples were carried out by means of FEI Quanta 450 Scanning Electron Microscope (Thermo Fisher Scientific Inc., USA) and Canon EOS 4000D (Canon, Tokyo, Japan), respectively. To do so, cylindrical samples were prepared as described in Section 2.4. The samples were characterized before and after corrosion, having been soaked in SBF at 37 °C for one day.

2.6. Cytotoxicity testing

Cytotoxicity was assessed via the MTS cell proliferation assay (Promega) in L929 murine fibroblasts as per manufacturer's recommendations. To compare the cytocompatibility of the different coatings, extracts were prepared by incubating the samples in Dulbecco's Modified Eagle Medium (DMEM – Life Technologies Corp, California, USA), supplemented with 10%v/v fetal bovine serum (FBS), 100 U/ml penicillin and 100 µg/ml streptomycin (complete DMEM) with 1.25 ml/cm^2 extraction ratio for 72 h at 37 °C in a humidified atmosphere with 5% CO_2 [46,47]. The supernatants were collected and centrifuged, and 100% extracts were employed for the cell proliferation assay. Briefly, 3×10^3 cells/well were seeded on 96-well plates and incubated for 24 h to allow attachment. Starting from the following day, 100 µl of the different extracts were added to each well. Complete DMEM was applied as a negative control. The effect of the extracts on cell viability was assessed after 1, 3 and 5 days of treatment. The generation of colored formazan by reduction of the MTS tetrazolium compound was monitored by measuring absorbance at 490 nm on a VICTOR^{TM}X3 plate reader (Perkin Elmer, Massachusetts, USA).

In addition, another set of samples was incubated as just described to assess the pH evolution of the extracts with a pH meter Inolab 730 (WTW, Weilheim, Germany).

3. Results

3.1. Coating characterization

XPS was conducted to determine the chemical composition of the ALD deposited TiO_2, ZrO_2 and HfO_2. In order to have minimum effect of the underlying substrate, the measurements were carried out on thin film deposited on Si wafer. Prior to chemical characterization, the effect of environmental contamination and surface oxidation were removed by etching the surface for three minutes with an energy of 2 KeV. Dealing with titania, high resolution regional scans were carried out for titanium, oxygen and carbon. The negligible amount of carbon detected excluded the presence of any process contamination, thus indicating an ideal deposition. Regional scans of titanium and oxygen are reported in Fig. 2(a) and (b), respectively. Particularly, from the regional scan of titanium, peaks corresponding to the core level binding energies of Ti $2p_{3/2}$ and Ti $2p_{1/2}$ (i.e., 459 eV and 464 eV, respectively) can be observed, indicating the presence of Ti^{4+} oxidation state in TiO_2 [48]. Moreover, the presence of Ti^{3+} due to the argon etching step caused the shoulder at lower energy around 456 eV is due to [49]. Dealing with oxygen, oxygen atoms in TiO_2 phase lead to the peak at 531 eV [50], while the oxygen in hydroxyl groups present in the form of impurities induces the small shoulder at higher energy. From a composition perspective, we found an oxygen deficient deposition since we found 60% of oxygen and 40% of titanium, while the stochiometric composition should be 66.7% oxygen and 33.3% titanium (Ti and oxygen in 1:2 ratio).

With respect to zirconia, regional scans of zirconium, oxygen and carbon were also carried out at high resolution. No peak was observed in the high resolution scan for the element carbon, thus showing a nearly carbon-free ALD deposition. The high resolution spectra (Fig. 3a) of Zr 3d showed two peaks at binding energy 182 eV and 184 eV, which correspond to Zr $3d_{5/2}$ and Zr $3d_{3/2}$, respectively. The scan conducted for O 1 s (Fig. 3b) showed a peak at 530 eV which belongs to ZrO_2 and the shoulder on the higher energy side is due to the oxidation of metal in air forming ZrO. The quantification calculation using CASAXPS software showed a composition as 40% Zr and 60% O, indicating an oxygen deficient zirconia thin film.

Finally, dealing with hafnia, high resolution regional scans for hafnium, oxygen and carbon were carried out. Again, an

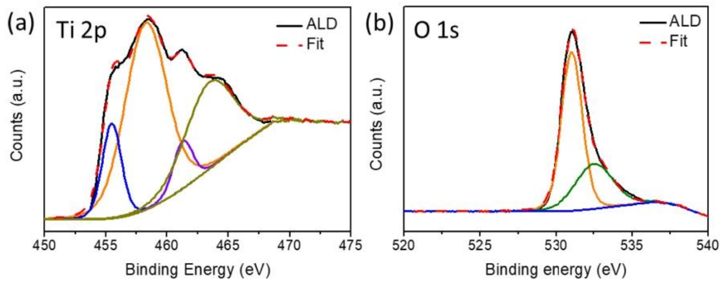

Fig. 2. XPS spectra for ALD deposited TiO_2 (a) Ti 2p (b) O 1s.

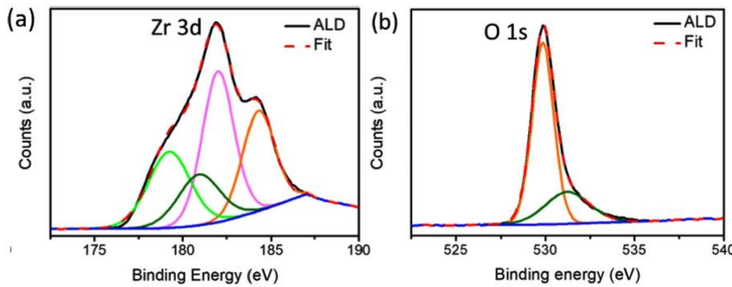

Fig. 3. XPS spectra for ALD deposited ZrO_2 (a) Zr 3d (b) O 1s.

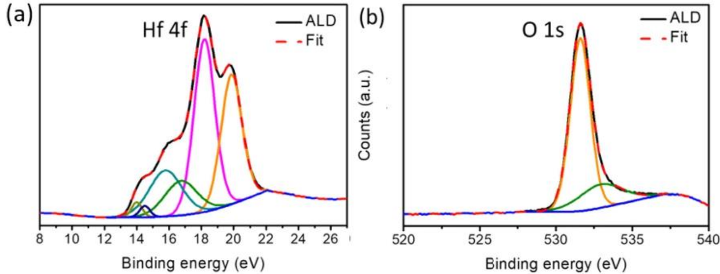

Fig. 4. XPS depth profile spectra of ALD deposited HfO_2 (a) Hf 4f and (b) O 1s.

ideal deposition without any contaminants was highlighted by the negligible amount of carbon detected. Fig. 4b shows the core level spectra of O 1s associated with HfO_2 [51]. The region at higher energy above the peak at 531 eV shows a shoulder due to presence of a small amount of contamination, likely carbon or moisture. In the regional scan of element Hf 4f, peak positions at 18.5 eV and 20.7 eV correspond to Hf $4f_{7/2}$ and Hf $4f_{5/2}$ in HfO_2 [52]. The shoulders at lower energies below 18.5 eV are due to Hf interstitials and oxygen vacancies [53]. Again, we observed an oxygen deficient deposition. In fact, we observed a composition of 63% oxygen and 37% hafnium, while the stoichiometric composition of HfO_2 should have Hf and O in 1:2 ratio i.e. 66.7% oxygen and 33.3% hafnium.

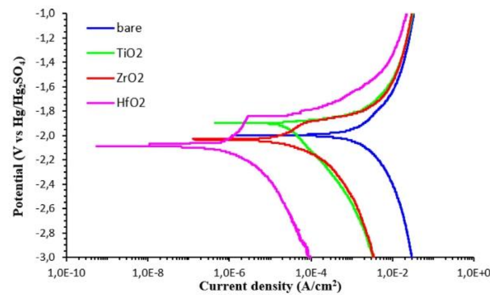

Fig. 5. Potentiodynamic polarization curves of bare (blue), TiO_2 (green), ZrO_2 (red) and HfO_2 (fuchsia) AZ31 alloy in SBF. (For interpretation of the references to colour in this figure legend, the reader is referred to the web version of this article.)

Table 1
Corrosion potentials (E_{corr}) and corrosion current densities (i_{corr}) values for bare and coated AZ31 samples in SBF.

	Bare	TiO_2 coating	ZrO_2 coating	HfO_2 coating
E_{corr} (V)	-2.0 ± 0.02	-1.90 ± 0.01	-2.02 ± 0.01	-2.09 ± 0.02
i_{corr} (A/cm²)	$3.0\ 10^{-3} \pm 0.4$	$24.9\ 10^{-6} \pm 0.6$	$1.2\ 10^{-6} \pm 0.3$	$0.6\ 10^{-6} \pm 0.4$

3.2. Corrosion experiments

3.2.1. Potentiodynamic polarization curves

Fig. 5 reports the potentiodynamic polarization curves of bare and coated samples. Moreover, the average values of the corrosion potentials (E_{corr}) and of the corrosion current densities (i_{corr}) are reported in Table 1. In the light of the well-known relation between the corrosion resistance of a sample and the observed values of the corrosion current density and of the corrosion potential (i.e., the lower the corrosion current density, the lower the corrosion rate, and the higher the corrosion potential, the lower the tendency to corrode), it can be observed that the presence of the coatings increases the corrosion resistance of the material. In particular, the HfO_2 coating is reported to provide the lowest corrosion current density, that is half of that provided by ZrO_2 and 40 times lower than that of TiO_2.

3.2.2. Electrochemical impedance spectroscopy

The Nyquist-plots of bare and TiO_2, ZrO_2, and HfO_2 coated samples are shown in Fig. 6a, b, c and d, respectively. It is worth mentioning that, for sake of clarity, the Figures are characterized by different axis scales. In the Nyquist plots, the bare and the coated samples are characterized by three time constants being the capacitive loop in the high and medium frequency range (related to the charge transfer process between the base and the coatings) and the inductive loop in the low-frequency range (related to the superficial corrosion state of AZ31 alloy in the solution) [54,55]. Being the capacity loop connected to the transfer process between the coating and the substrate, a larger capacitive loop means better corrosion resistance [56]. Due to the larger diameter of the capacitive loops of the coated samples compared to the bare sample, the treated samples show much better performance in corrosion resistance. The capacitive loops and hence the corrosion performance are ranked $HfO_2 > ZrO_2 > TiO_2 >$ bare, confirming the results of the potentiodynamic polarization curves. There is a large difference in impedance among the different samples, as can be seen by inspecting the order of magnitudes on the axes.

The Bode plots of bare and TiO_2, ZrO_2, and HfO_2 are shown in Fig. 7a, b, c and d, respectively. The Bode plots also help to investigate the corrosion resistance, as a higher value of $|Z|_{f\to0}$ means greater corrosion resistance [57,58]. The $|Z|_{f\to0}$ value for the bare, TiO_2, ZrO_2 and HfO_2 coated samples is $1.4 \cdot 10^2\ \Omega \cdot cm^2$, $4.5 \cdot 10^3\ \Omega \cdot cm^2$, $2.1 \cdot 10^6\ \Omega \cdot cm^2$ and $4 \cdot 10^7\ \Omega \cdot cm^2$, respectively, confirming the results found in the Nyquist plots.

3.2.3. Hydrogen evolution tests

Fig. 8 reports the results of the hydrogen evolution tests from bare and coated samples. In agreement with the results of the potentiodynamic polarization tests and of the electrochemical impedance spectroscopy, the hydrogen evolution experiments further suggest that the application of the coatings can prevent the degradation of AZ31 alloy. In particular, after 7 days, the hydrogen evolved from the bare samples is reduced by 52% if 100 nm of ALD TiO_2 is considered. Higher improvements are obtained if ZrO_2 and, above all, HfO_2 are employed: the former leads to a reduction in the hydrogen evolved by 92.5%, while the latter to a reduction by 95%.

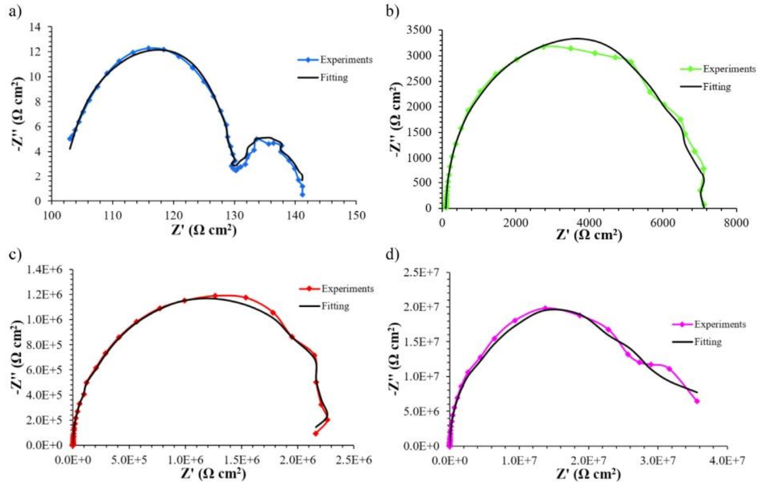

Fig. 6. Nyquist plots of bare (a), TiO_2 (b), ZrO_2 (c) and HfO_2 (d) coated AZ31 alloy in SBF.

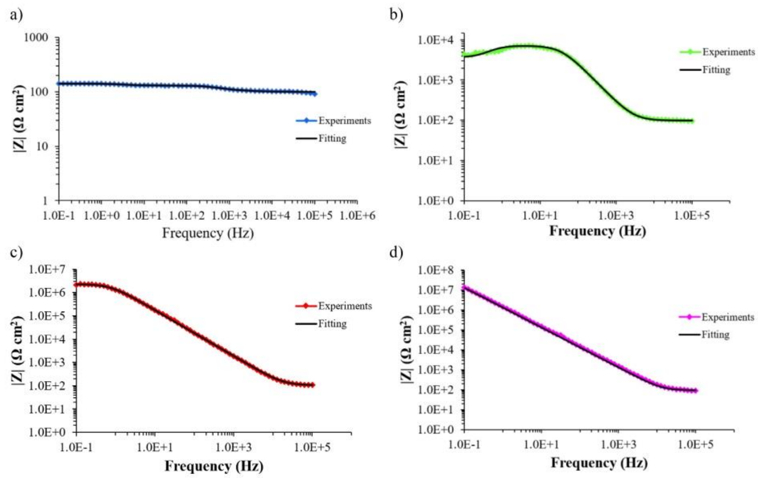

Fig. 7. Bode plots of bare (a), TiO_2 (b), ZrO_2 (c) and HfO_2 (d) coated AZ31 alloy in SBF.

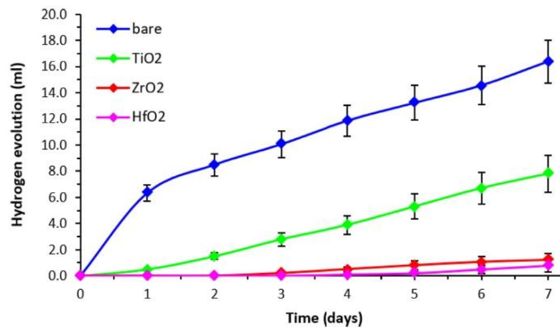

Fig. 8. Hydrogen evolved from the immersion of bare and coated AZ31 alloy in SBF.

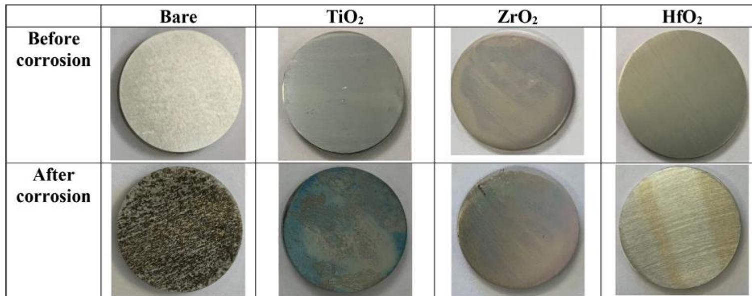

Fig. 9. Macro-morphologies of bare, TiO_2, ZrO_2 and HfO_2 coated samples before and after corrosion.

It is interesting to note the behavior of the bare samples. After a first phase where the hydrogen evolution rate is high, the slope of the curve highly reduces. This is linked to the presence of corrosion products. At first, in fact, the bare alloy is covered by a surface layer of MgO and/or $Mg(OH)_2$ that spontaneously form. This surface layer is however very soluble in water environment, hence the corrosion rate is high. With the continuation of the surface process, the pH increase leads to the precipitation of Ca-phosphate on the surface, which is protective, and determines a reduction of the corrosion rate [59].

3.3. Degradation behavior

Fig. 9 displays the macro-morphologies of coated samples before and after being soaked for one day in SBF. The bare AZ31 sample was employed as control.

It is clearly observable from the figure that the application of coatings reduced the corrosion damage. Particularly, in the case of HfO_2 coated samples, the corrosion damage became negligible. The extensively corroded surface of bare samples, characterized by pits, was reduced by applying a TiO_2 layer, where un-corroded areas were accompanied by corroded areas characterized by a filiform corrosion. Barely any corrosion apart from the small area at the edge of the sample was observable from the macro-morphologies of ZrO_2 coated samples. However, the micro-morphologies revealed some small corroded area in the center of the ZrO_2 coated samples (Figs. 10h and i). In addition, although the macro-morphologies of HfO_2 coated samples did not reveal any corrosion, the micro-morphologies showed the presence of some small areas where the early stage of the corrosion products formation can be seen, together with the onset of filiform corrosion (Figs. 10k and l). TiO_2 coated samples and bare samples are characterized by a large number of cracks dividing the surface into network structure (Figs. 10b and c and Figs. 10e and f for bare and TiO_2 coated samples, respectively). In addition, in the bare samples, the surface film layer began to delaminate and flake off (Figs. 10b and c).

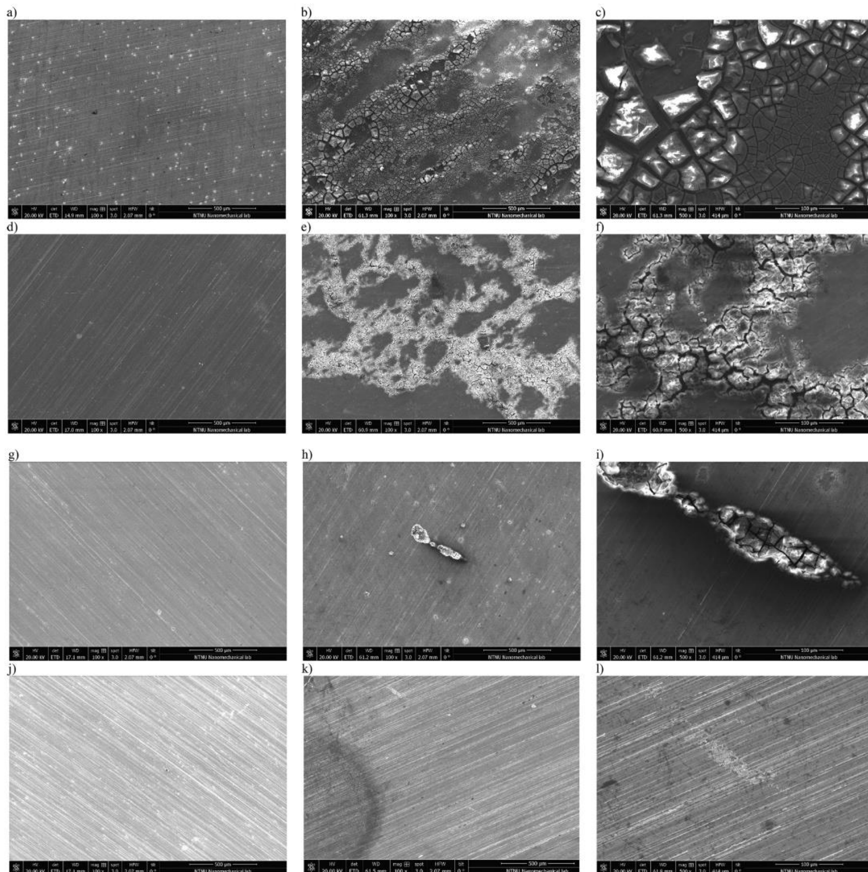

Fig. 10. Micro-morphologies of bare (b and c), TiO_2 (e and f), ZrO_2 (h and i) and HfO_2 (k and l) coated samples after corrosion. Micro-morphologies of samples before corrosion are also reported (a, d, g and j for bare, TiO_2, ZrO_2 and HfO_2 coated samples, respectively).

3.4. Cytotoxicity testing

The MTS assay was performed on L929 murine cell line to determine the cytotoxicity of the different ALD coatings. Fig. 11 shows the viability of L929 cells after exposure to extracts of the AZ31 alloy and coated samples after 1, 3 and 5 days in culture (Fig. 11).

Finally, Fig. 12 reports the pH evolution during the preparation of the extracts.

As it can be observed, the application of the coatings can lower the increase in pH produced by the bare alloy. In particular, the pH is reduced by 15.5% if 100 nm of ALD TiO_2 is considered. Higher improvements are obtained if ZrO_2 and, above all, HfO_2 are employed: the former leads to a reduc-

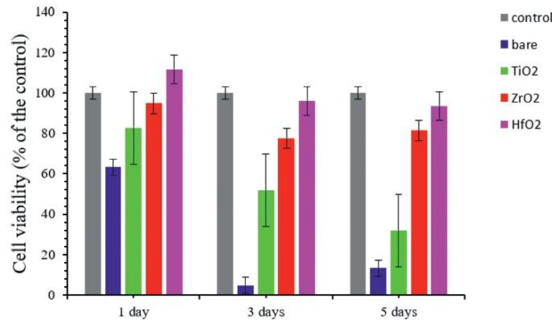

Fig. 11. Cell viability of L-929 cultured in extracts from bare and coated AZ31 substrates after culture for 1, 3 and 5 days. Error bars represent means ± SEM for $n=3$. (For interpretation of the references to colour in this figure legend, the reader is referred to the web version of this article.)

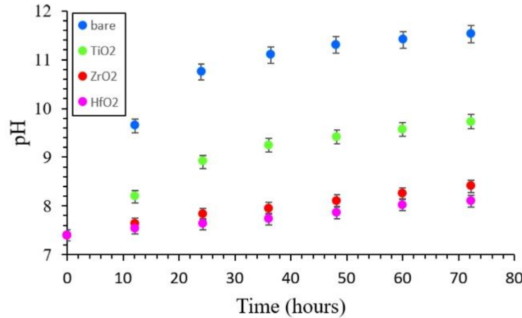

Fig. 12. pH evolution of bare and coated samples in DMEM supplemented with 10% FBS and penicillin/streptomycin.

tion in the hydrogen evolved by 27.1%, while the latter to a reduction by 29.7%.

4. Discussion

In this work, we aimed to evaluate the effects of three biocompatible ALD coatings (TiO_2, ZrO_2 and HfO_2) on the corrosion resistance and cytotoxicity of AZ31 alloy. Particularly, being Mg and its alloys optimal materials for temporary implants, the impact of the corrosion products on cell viability in the immediate surrounding of the implant represents one of the most important aspects to take into consideration. In the light of this, MTS colorimetric assays with L929 cells were used to evaluate the effect of sample extracts on cell viability. As shown in Fig. 11, the application of coatings increases the cell viability of the bare AZ31 alloy. Specifically, HfO_2 coating is found to lead to the highest improvements, while TiO_2 to the lowest. However, according to the evaluation of cytotoxicity listed in Table 2, not all the coatings lead to Grade 1 cytotoxicity, that represents the threshold above which a material is considered to meet the demands for cellular applications [60].

Table 2
The standard evaluation of cytotoxicity (%).

Cell viability	≥100	75–99	50–74	25–49	1–24	<1
Grade	0	1	2	3	4	5

In fact, Grade 1 cytotoxicity was constantly found only for ZrO_2 and HfO_2, with the latter to be the only one showing Grade 0 cytotoxicity at day 1. TiO_2 coatings are instead characterized by Grade 1 cytotoxicity only at 1 day of culture, after that the viability decreases to Grade 2. Considering bare samples, they are always characterized by a too low viability to meet the demands for cellular applications. Detailed results are reported in Table 3.

The different cell viability degrees shown by the coated and uncoated samples can be related to the different pH of

Table 3
Classification of the observed cytotoxicity of uncoated and coated AZ31 alloys. The cell viability corresponding to the coating type is reported in brackets.

Cytotoxicity Grade	0	1	2	3	4	5
Viability at 1 day of culture	HfO_2 (111.6%)	ZrO_2 (94.8%) TiO_2 (82.8%)	Bare (63.4%)			
Viability at 3 day of culture		HfO_2 (96.1%) ZrO_2 (77.6%)	TiO_2 (51.7%)		Bare (4.7%)	
Viability at 5 day of culture		HfO_2 (93.5%) ZrO_2 (81.5%)		TiO_2 (31.9%)	Bare (13.4%)	

the extracts. A pH higher than 9 has in fact been reported to inhibit the proliferation of L929 cells [61]. In the light of this, the pH of the extracts reported in Fig. 12 can, at least partially, explain the different Cytotoxicity Grades. Specifically, ZrO_2 and HfO_2 coatings are the only ones characterized by Grade 1 cytotoxicity, and they indeed always show a pH lower than 9. In particular, HfO_2 coating is the only one showing Grade 0 cytotoxicity as a consequence of the lowest increase in pH. The correlation of the Cytotoxicity Grades with the pH is even more evident in the case of TiO_2 coatings: when the pH of the extracts is lower than 9 (after 1 day of culture), the TiO_2 coatings can meet the demands for cellular applications, whereas, when the pH of the extracts is higher, the proliferation of the L929 cells is inhibited, thus resulting in Grade 2 and 3. Finally, bare samples are characterized by a pH higher than 9 also after 1 day of culture, thus explaining the reported high Cytotoxicity Grades.

To pH behavior can then be linked to the corrosion behavior: the increase in the pH is in fact due to the evolution of OH^- ions from the corrosion process of Mg and its alloys, and the lower the corrosion resistance, the higher the increase of the pH. The corrosion resistance has herein been evaluated in three different ways, i.e. through potentiodynamic polarization curves, EIS spectra and hydrogen evolution experiments. Starting from the potentiodynamic polarization curves, the most important parameter to be considered is the corrosion current density. Specifically, the corrosion current density is directly related to the corrosion rate (i.e., the lower the corrosion current density, the lower the corrosion rate). From Fig. 5 and Table 1, it can be seen that the corrosion current density of the bare sample is decreased by three orders of magnitude. In particular, the HfO_2 coating is reported to provide the lowest corrosion current density, with the corrosion resistance following the trend $HfO_2 > ZrO_2 > TiO_2 >$ bare. More in detail, the corrosion current density of HfO_2 is half of that provided by ZrO_2 and 40 times lower than that of TiO_2. A similar trend can be found considering the hydrogen evolution test and the EIS spectra. Dealing with the former, Fig. 8 shows that HfO_2 coating reduces the hydrogen evolved from the bare sample by 95%. A similar, but lower, reduction (92.5%) is achieved when considering ZrO_2 coating, while a much lower reduction (52%) is provided by TiO_2 coating. Dealing with the EIS spectra (Fig. 6), then, the diameters of the capacitive loops of the Nyquist-plots confirm the corrosion trend again: the higher the diameter of the capacitive loops (and equivalently the value of $|Z|_{f\to 0}$), in fact, the higher the corrosion resistance. Moreover, the EIS spectra are particularly interesting to better understand the corrosion process. The EIS spectra of each material indicate, in fact, its specific electronic transportation process. This can be simulated by an equivalent circuit (EC). In this work the EC used is that suggested in previous works on ALD [25,62] and it is reported in Fig. 13.

Table 4
Fitting results for EIS Spectra.

	Bare	TiO_2	ZrO_2	HfO_2
R_s (Ω cm^2)	100.16	98.42	106.40	95.0
R_1 (Ω cm^2)	9.34	2.63×10^3	1.64×10^{11}	3.30×10^7
C_1 (Ω^{-1} cm^{-2} s^{-n})	5.71×10^{-3}	1.29×10^{-4}	1.05×10^{-5}	1.29×10^{-7}
Q_1 (Ω^{-1} cm^{-2} s^{-n})	7.07×10^{-5}	7.24×10^{-7}	9.71×10^{-8}	1.30×10^{-6}
n	0.748	0.938	0.984	1
R_2 (Ω cm^2)	3.79×10^1	6.88×10^3	2.25×10^6	3.80×10^7
R_L (Ω cm^2)	1.78×10^2	1.05×10^3	3.21×10^{-1}	1.71×10^6
L (H cm^2)	1.84×10^{-1}	2.35×10^{-3}	2.42×10^7	1.25×10^7

R_s, R_1 and R_2 represent the electrical impedance of the electrolyte, the surface modification layer (MgO in the case of bare samples), and the charge transfer resistance respectively. C_1 represents the capacitance of either the coatings or the surface corrosion products of the bare AZ31. R_L and L represent the resistance and inductance of the species absorbed into the coating, respectively [63]. Q_1 acts as a constant phase element (CPE) of the electric double layer on the electrode surface [56]. Yang et al. reported that high values for R_1 and R_2 and low values for Q_1 and C_1 are characteristics of a better corrosion resistance [62], and, from the fitting results (Table 4), it can be seen that all the coated samples exhibit higher corrosion resistance than the bare samples (due to higher values for R_1 and R_2 and lower values for Q_1 and C_1).

Moreover, they also stated that R_1 and R_2 are directly related to the integrity of the coating. Therefore, to understand the different corrosion performances, the coating integrities need to be considered together with their electrochemical properties. Dealing with the former, the presence of defects such as cracks and pores are known to affect the corrosion behavior inducing filiform corrosion (Fig. 10) and to reduce the protectiveness of the coating allowing a path for the fluid to enter the material [64]. Cracks are known to form as a consequence of the induced residual stresses on the coating due to the different thermal expansion coefficient of the coating and of the substrate [65,66]. Mg, in fact, is reported to have a coefficient of thermal expansion of $27{\cdot}10^{-6}$ $°C^{-1}$ [67], while TiO_2, ZrO_2 and HfO_2 of $7{\cdot}10^{-6}$ $°C^{-1}$, $11{\cdot}10^{-6}$ $°C^{-1}$ and

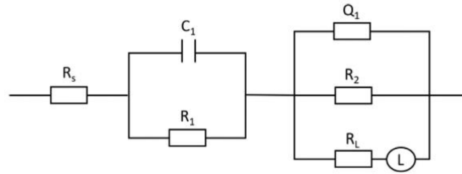

Fig. 13. Equivalent Circuit for EIS spectra.

Table 5
Polarization resistance of bare and coated samples.

	Bare	TiO_2	ZrO_2	HfO_2
Polarization Resistance (Ω cm^2)	42.9	7.0 10^3	2.3 10^6	3.8 10^8

$10{\cdot}10^{-6}$ $°C^{-1}$, respectively [68–70]. The mismatch between the substrate and the coating is lower with ZrO_2 and higher with TiO_2. This would suggest ZrO_2 coating to provide the highest corrosion resistance among the considered materials. However, the results herein reported showed that the highest improvements in terms of corrosion resistance were provided by the HfO_2 coatings. This can be linked to the lower porosity of the HfO_2 compared to ZrO_2 and, even more, to TiO_2. Elsener et al. [71] proposed an electrochemical method to estimate the porosity of thin films based on the following Equation:

$$Porosity = \left(\frac{R_{p,s}}{R_p}\right) \cdot 10^{-\frac{\Delta E_{corr}}{b_a}} \quad (2)$$

Where $R_{p,s}$ and R_p are the polarization resistances of the bare and coated material in Ωcm^2, respectively, ΔE_{corr} is the change of the corrosion potential caused by the presence of the coating layer in mV and b_a is the anodic Tafel slope of the bare substrate in mV/decade. The polarization resistances, corresponding to the diameter of the capacitive loop in the Nyquist plots, are reported in Table 5, the ΔE_{corr} can be measured from the results of the potentiodynamic polarization curves reported in Table 1, and the anodic Tafel slope of the bare substrate was measured equal to 442 mV/decade from the potentiodynamic polarization curves. The corresponding porosity was found to be 0.36%, 0.0016% and 0,00,007% for TiO_2, ZrO_2 and HfO_2, respectively.

Another reason for the better corrosion resistance of HfO_2 is the difference in cohesive energies [72]. In fact, the higher the cohesive energy, the more electrochemically stable is the material and thus, the lower its corrosion. The cohesive energy of HfO_2 is the highest among the three materials herein studied, while TiO_2 is the lowest [73]; the cohesive energy of ZrO_2 is instead slightly lower than that of HfO_2 and this could explain the different corrosion behavior observed. Finally, the lower wettability of HfO_2 compared to ZrO_2 and TiO_2 further explains the herein reported corrosion behavior [74–76] and hence the cell viability results.

It is worth mentioning that, with respect to the biocompatibility of TiO_2, the results herein reported differ from what is known from the literature. In fact, TiO_2 is widely known as one of the most biocompatible materials since it induces fast deposition of apatite from SBF in vitro and stimulates the adhesion and proliferation of cells [77,78]. However, although the biocompatibility of TiO_2 remains undisputed when the cells are in direct contact, biocompatibility issues may arise when TiO_2 is used as coating material for Mg and its alloys, and it is not effective in reducing the corrosion rate of the magnesium substrate leading to an environment that reveals to be toxic for the cells due to the increase in the pH and to the high concentration of Mg^{2+} ions.

Therefore, in the choice of a coating material for degradable Mg alloys used as implant material, it is important to consider its cohesive energy, wettability, porosity and thermal expansion coefficient to provide an effective reduction of the corrosion rate of the Mg substrate that otherwise would affect the biocompatibility of the coating itself, creating a lethal environment for cells and tissues.

5. Conclusions

In this study, the effects of a 100 nm thick TiO_2, ZrO_2 and HfO_2 ALD coating on the corrosion behavior and on the cytotoxicity of the AZ31 Mg alloy were assessed. To this regard, potentiodynamic polarization curves, EIS and hydrogen evolution experiments have been carried out to assess the former, while MTS proliferation assay using L929 cells to assess the latter. Whereas the presence of TiO2 coatings is reported to improve the corrosion performances with respect to the bare AZ31 alloys, ZrO_2 and, above all, HfO_2 ALD coatings provide a significantly higher corrosion resistance. This can be explained considering their lower wettability, their higher electrochemical stability and their higher surface integrity (i.e., less cracks and pores). This improved corrosion resistance has positive effects on the cytotoxicity of AZ31 alloy. Indeed, the reduced corrosion provided by the coatings leads to a lower increase in the pH and in the concentration of Mg^{2+} ions, inducing the cytotoxicity Grade to move from Grade 4 for bare AZ31 alloy to Grade 2 for TiO_2 coating and to Grade 1 for ZrO_2 and HfO_2 coatings. In particular, HfO_2 coating was also found to report a Grade 0 cytotoxicity considering the extracts assessed at 1 day of culture. As a grade 1 toxicity is the minimum requirement

for FDA approval, the choice of the appropriate coating has to include a cytotoxicity benchmark of its corrosion products and cannot be linked to the assessment of cell attachment to the biomaterial surface only.

Declaration of Competing Interest

None.

References

[1] M.P. Ginebra, T. Traykova, J.A. Planell, J. Control. Release. 113 (2006) 102–110, doi:10.1016/j.jconrel.2006.04.007.

[2] M. Peron, J. Torgersen, F. Berto, Metals (Basel) 7 (2017) 252, doi:10.3390/met7070252.

[3] N. Li, Y. Zheng, J. Mater. Sci. Technol. 29 (2013) 489–502, doi:10.1016/J.JMST.2013.02.005.

[4] R.K. Singh Raman, S. Jafari, S.E. Harandi, Eng. Fract. Mech. 137 (2015) 97–108, doi:10.1016/j.engfracmech.2014.08.009.

[5] M.P. Staiger, A.M. Pietak, J. Huadmai, G. Dias, Biomaterials 27 (2006) 1728–1734, doi:10.1016/j.biomaterials.2005.10.003.

[6] A.C. Hänzi, A.S. Sologubenko, P.J. Uggowitzer, Int. J. Mater. Res. 100 (2009) 1127–1136, doi:10.3139/146.110157.

[7] Y. Sasaki, G.A. Sathi, O. Yamamoto, Mater. Sci. Eng. C. 77 (2017) 52–57, doi:10.1016/j.msec.2017.03.236.

[8] M. Peron, F. Berto, J. Torgersen, Magnesium and Its Alloys As Implant Materials: Corrosion, Mechanical and Biological Performances, CRC Press LLC, 2020.

[9] F. Witte, V. Kaese, H. Haferkamp, E. Switzer, A. Meyer-Lindenberg, C.J. Wirth, H. Windhagen, Biomaterials 26 (2005) 3557–3563, doi:10.1016/j.biomaterials.2004.09.049.

[10] B. Zberg, P.J. Uggowitzer, J.F. Löffler, Nat. Mater. 8 (2009) 887–891, doi:10.1038/nmat2542.

[11] M. Bobby Kannan, W. Dietzel, C. Blawert, A. Atrens, P. Lyon, Mater. Sci. Eng. A. 480 (2008) 529–539, doi:10.1016/J.MSEA.2007.07.070.

[12] L. Choudhary, R.K. Singh Raman, J. Hofstetter, P.J. Uggowitzer, Mater. Sci. Eng. C. 42 (2014) 629–636, doi:10.1016/J.MSEC.2014.06.018.

[13] M. Peron, P.C. Skaret, A. Fabrizi, A. Varone, R. Montanari, H.J. Roven, P. Ferro, F. Berto, J. Torgersen, J. Mech. Behav. Biomed. Mater. (2020) 103724, doi:10.1016/j.jmbbm.2020.103724.

[14] M. Peron, R. Bertolini, A. Ghiotti, J. Torgersen, S. Bruschi, F. Berto, J. Mech. Behav. Biomed. Mater. 101 (2020) 103429, doi:10.1016/J.JMBBM.2019.103429.

[15] K.T. Rim, K.H. Koo, J.S. Park, Saf. Health Work. 4 (2013) 12–26, doi:10.5491/SHAW.2013.4.1.12.

[16] R. Smeets, B. Stadlinger, F. Schwarz, B. Beck-Broichsitter, O. Jung, C. Precht, F. Kloss, A. Gröbe, M. Heiland, T. Ebker, T. Ebker, Biomed Res. Int. 2016 (2016) 1–16, doi:10.1155/2016/6285620.

[17] T. Albrektsson, A. Wennerberg, Int. J. Prosthodont. 17 (2017) 536–543 n.d. http://www.ncbi.nlm.nih.gov/pubmed/15543910 . (accessed October 30.

[18] R. Bertolini, S. Bruschi, A. Ghiotti, L. Pezzato, M. Dabalà, Procedia CIRP 65 (2017) 7–12, doi:10.1016/J.PROCIR.2017.03.168.

[19] T.S.N. Sankara Narayanan, I.-.S. Park, M.H. Lee, Volume 2, Modification and coating techniques (2020) n.d.

[20] T. Lei, in: Surf. Modif. Magnes. Its Alloy. Biomed. Appl., Elsevier Inc., 2015, pp. 135–150, doi:10.1016/B978-1-78242-078-1.00006-2.

[21] T.F. da Conceição, N. Scharnagl, in: Surf. Modif. Magnes. Its Alloy. Biomed. Appl., Elsevier Inc., 2015, pp. 3–21, doi:10.1016/B978-1-78242-078-1.00001-3.

[22] Q. Li, in: Prev. Magnes. Alloy. A Vol. Woodhead Publ. Ser. Met. Surf. Eng., Elsevier Ltd, 2013, pp. 469–485, doi:10.1533/9780857098962.3.469.

[23] M. Peron, A. Bin Afif, A. Dadlani, F. Berto, J. Torgersen, Surf. Coatings Technol. (2020) 125922, doi:10.1016/j.surfcoat.2020.125922.

[24] I.S. Abela, in: Surf. Modif. Magnes. Its Alloy. Biomed. Appl., Elsevier Inc., 2015, pp. 81–100, doi:10.1016/B978-1-78242-078-1.00004-9.

[25] X. Liu, Q. Yang, Z. Li, W. Yuan, Y. Zheng, Z. Cui, X. Yang, K.W.K. Yeung, S. Wu, Appl. Surf. Sci. 434 (2018) 1101–1111, doi:10.1016/J.APSUSC.2017.11.032.

[26] E. Marin, A. Lanzutti, L. Guzman, L. Fedrizzi, J. Coatings Technol. Res. 9 (2012) 347–355, doi:10.1007/s11998-011-9372-8.

[27] E. Marin, A. Lanzutti, L. Paussa, L. Guzman, L. Fedrizzi, Mater. Corros. 66 (2015) 907–914, doi:10.1002/maco.201408012.

[28] C.X. Shan, X. Hou, K.L. Choy, Surf. Coatings Technol. 202 (2008) 2399–2402, doi:10.1016/j.surfcoat.2007.08.066.

[29] T. Kasuga, H. Kondo, M. Nogami, J. Cryst. Growth. 235 (2002) 235–240, doi:10.1016/S0022-0248(01)01782-1.

[30] X.X. Wang, S. Hayakawa, K. Tsuru, A. Osaka, Biomaterials 23 (2002) 1353–1357, doi:10.1016/S0142-9612(01)00254-X.

[31] M. Uchida, H.-.M. Kim, T. Kokubo, T. Nakamura, APATITE-FORMING ABILITY OF TITANIA GELS WITH DIFFERENT STRUCTURES, Bioceramics, WORLD SCIENTIFIC (1999) 149–152, doi:10.1142/9789814291064_0036.

[32] J.-.M. Wu, S. Hayakawa, K. Tsuru, A. Osaka, J. Am. Ceram. Soc. 87 (2004) 1635–1642, doi:10.1111/j.1551-2916.2004.01635.x.

[33] R. Osman, M. Swain, Materials (Basel) 8 (2015) 932–958, doi:10.3390/ma8030932.

[34] H. Harianawala, M. Kheur, S. Kheur, T. Sethi, A. Bal, M. Burhanpurwala, F. Sayed, Biocompatibility of Zirconia, n.d.

[35] L. Rimondini, L. Cerroni, A. Carrassi, P. Torricelli, Bacterial colonization of zirconia ceramic surfaces: an in vitro and in vivo study., Int. J. Oral Maxillofac. Implants. 17 (n.d.) 793–8. http://www.ncbi.nlm.nih.gov/pubmed/12507238 (accessed January 23, 2020).

[36] M. Peron, A. Bin Afif, A.L. Dadlani, F. Berto, J. Torgersen, J. Mech. Behav. Biomed. Mater. 111 (2020) 104005, doi:10.1016/j.jmbbm.2020.104005.

[37] M. Peron, F. Berto, J. Torgersen, Mater. Des. Process. Commun. 126 (2019) mdp2, doi:10.1002/mdp2.126.

[38] M. Peron, J. Torgersen, F. Berto, in: Procedia Struct. Integr, Elsevier B.V., 2019, pp. 538–548, doi:10.1016/j.prostr.2019.08.198.

[39] C.R. Kruse, M. Singh, S. Targosinski, I. Sinha, J.A. Sørensen, E. Eriksson, K. Nuutila, Wound Repair Regen 25 (2017) 260–269, doi:10.1111/wrr.12526.

[40] L.-.E. Monfoulet, P. Becquart, D. Marchat, K. Vandamme, M. Bourguignon, E. Pacard, V. Viateau, H. Petite, D. Logeart-Avramoglou, Tissue Eng. Part A. 20 (2014) 1827–1840, doi:10.1089/ten.tea.2013.0500.

[41] M. Li, Z.-.X. Jin, W. Zhang, Y.-.H. Bai, Y.-.Q. Cao, W.-.M. Li, D. Wu, A.-.D. Li, Comparison of chemical stability and corrosion resistance of group IV metal oxide films formed by thermal and plasma-enhanced atomic layer deposition, (n.d.). doi:10.1038/s41598-019-47049-z.

[42] D. Zhang, Z. Qi, B. Wei, Z. Wang, Mater. Lett. 190 (2017) 181–184, doi:10.1016/j.matlet.2017.01.009.

[43] L. Staišiūnas, K. Leinartas, E. Juzeliūnas, D. Bučinskienė, A. Grigucevičienė, P. Kalinauskas, A. Selskis, S. Stanionytė, Surf. Coatings Technol. 397 (2020) 126046, doi:10.1016/j.surfcoat.2020.126046.

[44] T. Kokubo, H. Takadama, Biomaterials 27 (2006) 2907–2915, doi:10.1016/J.BIOMATERIALS.2006.01.017.

[45] G. Song, A. Atrens, D. StJohn, in: Magnes. Technol. 2001, John Wiley & Sons, Inc., Hoboken, NJ, USA, 2013, pp. 254–262, doi:10.1002/9781118805497.ch44.

[46] ISO 10993-12:2012 - Biological evaluation of medical devices – Part 12: sample preparation and reference materials, (n.d.). https://www.iso.org/standard/53468.html (accessed December 26, 2018).

[47] ISO 10993-5:2009 - Biological evaluation of medical devices – Part 5: tests for in vitro cytotoxicity, (n.d.). https://www.iso.org/standard/36406.html (accessed December 26, 2018).

[48] S. Nezar, N. Saoula, S. Sali, M. Faiz, M. Mekki, N.A. Laoufi, N. Tabet, Appl. Surf. Sci. 395 (2017) 172–179, doi:10.1016/j.apsusc.2016.08.125.

[49] J.H. Kim, S. Lee, H.S. Im, Appl. Surf. Sci. 151 (1999) 6–16, doi:10.1016/S0169-4332(99)00269-X.

[50] J. Yu, X. Zhao, J. Du, W. Chen, J. Sol-Gel Sci. Technol. 17 (2000) 163–171, doi:10.1023/A:1008703719929.

[51] A.R. Chourasia, J.L. Hickman, R.L. Miller, G.A. Nixon, M.A. Seabolt, Int. J. Spectrosc. 2009 (2009) 1–6, doi:10.1155/2009/439065.

[52] H. Hernández-Arriaga, E. López-Luna, E. Martínez-Guerra, M.M. Turrubiartes, A.G. Rodríguez, M.A. Vidal, J. Appl. Phys. (2017) 121, doi:10.1063/1.4975676.
[53] C. Morant, L. Galán, J.M. Sanz, Surf. Interface Anal. 16 (1990) 304–308, doi:10.1002/sia.740160163.
[54] T.S. Lim, H.S. Ryu, S.H. Hong, Corros. Sci. 62 (2012) 104–111, doi:10.1016/j.corsci.2012.04.043.
[55] G. Song, A. Atrens, D. St. John, X. Wu, J. Nairn, Corros. Sci. 39 (1997) 1981–2004, doi:10.1016/S0010-938X(97)00090-5.
[56] Q. Yang, W. Yuan, X. Liu, Y. Zheng, Z. Cui, X. Yang, H. Pan, S. Wu, Acta Biomater 58 (2017) 515–526, doi:10.1016/j.actbio.2017.06.015.
[57] Y. Liu, Z. Yu, S. Zhou, L. Wu, Appl. Surf. Sci. 252 (2006) 3818–3827, doi:10.1016/j.apsusc.2005.05.072.
[58] J. Zhao, X. Xie, C. Zhang, Corros. Sci. 114 (2017) 146–155, doi:10.1016/j.corsci.2016.11.007.
[59] M. Esmaily, J.E. Svensson, S. Fajardo, N. Birbilis, G.S. Frankel, S. Virtanen, R. Arrabal, S. Thomas, L.G. Johansson, Prog. Mater. Sci. 89 (2017) 92–193, doi:10.1016/J.PMATSCI.2017.04.011.
[60] H. Yang, K. Xia, T. Wang, J. Niu, Y. Song, Z. Xiong, K. Zheng, S. Wei, W. Lu, J. Alloys Compd. 672 (2016) 366–373, doi:10.1016/J.JALLCOM.2016.02.156.
[61] Z. Zhen, X. Liu, T. Huang, T. Xi, Y. Zheng, Mater. Sci. Eng. C. 46 (2015) 202–206, doi:10.1016/j.msec.2014.08.038.
[62] Q. Yang, W. Yuan, X. Liu, Y. Zheng, Z. Cui, X. Yang, H. Pan, S. Wu, Acta Biomater 58 (2017) 515–526, doi:10.1016/J.ACTBIO.2017.06.015.
[63] X. Li, X. Liu, S. Wu, K.W.K. Yeung, Y. Zheng, P.K. Chu, Acta Biomater 45 (2016) 2–30, doi:10.1016/J.ACTBIO.2016.09.005.
[64] A.S. Hamdy Makhlouf, in: Intell. Coatings Corros. Control, Elsevier Inc., 2015, pp. 537–555, doi:10.1016/B978-0-12-411467-8.00015-5.
[65] S. Il Pyun, Y.G. Yoon, E. Lugscheider, R. Mathesius, Surf. Coatings Technol. 61 (1993) 233–237, doi:10.1016/0257-8972(93)90231-C.
[66] C. (Christoph) Leyens, M. (Manfred) PetersJohn Wiley & Sons., Wiley InterScience (Online service), Titanium and titanium alloys: fundamentals and applications, Wiley-VCH, 2003.
[67] H. Yang, L. Huang, M. Zh, Magnes. Alloy. - Des. Process. Prop., InTech, 2011, doi:10.5772/13778.
[68] H. Hayashi, T. Saitou, N. Maruyama, H. Inaba, K. Kawamura, M. Mori, Solid State Ionics 176 (2005) 613–619, doi:10.1016/j.ssi.2004.08.021.
[69] D.R. Hummer, P.J. Heaney, J.E. Post, Powder Diffr 22 (2007) 352–357, doi:10.1154/1.2790965.
[70] R.P. Haggerty, P. Sarin, Z.D. Apostolov, P.E. Driemeyer, W.M. Kriven, J. Am. Ceram. Soc. 97 (2014) 2213–2222, doi:10.1111/jace.12975.
[71] B. Elsener, A. Rota, H. Böhni, Mater. Sci. Forum. 44–45 (1991) 29–38 https://doi.org/10.4028/www.scientific.net/msf.44-45.29.
[72] W. Li, D.Y. Li, Acta Mater 54 (2006) 445–452, doi:10.1016/j.actamat.2005.09.017.
[73] M.A. Turchanin, P.G. Agraval, Powder Metall. Met. Ceram. 47 (2008) 26–39, doi:10.1007/s11106-008-0006-3.
[74] M.L. González-Martín, L. Labajos-Broncano, B. Jańczuk, J.M. Bruque, J. Mater. Sci. 34 (1999) 5923–5926, doi:10.1023/A:1004767914895.
[75] F. Zhang, B.W. Robinson, H. De Villiers-Lovelock, R.J.K. Wood, S.C. Wang, J. Mater. Chem. A. 3 (2015) 13864–13873, doi:10.1039/c5ta02130h.
[76] A. Wiatrowski, A. Obstarczyk, M. Mazur, D. Kaczmarek, D. Wojcieszak, Characterization of HfO2 optical coatings deposited by MF magnetron sputtering, Coatings. 9 (2019). doi:10.3390/COATINGS9020106.
[77] H. Li, Q. Cui, B. Feng, J. Wang, X. Lu, J. Weng, Appl. Surf. Sci. 284 (2013) 179–183, doi:10.1016/j.apsusc.2013.07.076.
[78] T. Sun, M. Wang, Appl. Surf. Sci. 255 (2008) 396–400, doi:10.1016/j.apsusc.2008.06.123.

Paper 6

Studying high surface area atomic layer deposited Cu islands on Ti and Ni mesh as an electrocatalyst for oxygen evolution reaction

Abdulla Bin Afif [1], Alaa Faid [2], Anup L Dadlani [1], Andreas Flaten [1],
, Peter Köllensperger [3], Svein Sunde [2], Jan Torgersen [4]

[1] Department of Industrial and Mechanical Engineering, Norwegian University of Science and Technology, Trondheim, Norway

[2] Department of Materials Science and Engineering, Norwegian University of Science and Technology, Trondheim, Norway

[3] Department of Physics, Norwegian University of Science and Technology, Trondheim, Norway,

[4] Chair of Materials Science, Department of Materials Engineering, TUM School of Engineering and Design, Technical University of Munich, Munich, Germany

Abstract

In this study, we examined the oxygen evolution reaction (OER) of Cu deposited on Ti and Ni mesh substrates. The results revealed distinct growth behavior with Cu islands forming uniformly on Ti and Cu clusters observed on Ni. We also found a significant difference in the atomic layer deposition (ALD) Cu surface area between the two substrates, with higher surface area values observed on Ni. By conducting linear sweep voltammetry in a 1 M KOH solution, we determined that Cu-coated Ni exhibited lower overpotential compared to Cu coated Ti, with overpotentials as low as 320 mV observed for both pristine and 1500-cycle ALD Cu coated Ni. On Ti, we observed a correlation between Cu island density and OER performance, with the highest island density (58 islands per μm^2) at 500 cycles resulting in an overpotential of 345 mV. However, we also observed Cu particle detachment/dissolution on Ti after a KOH dip test. Stability tests for ALD Cu on Ni mesh showed a reduction in current density within 3 hours, possibly due to Cu detachment from the mesh. Overall, this study provides valuable insights into the relationship between Cu catalyst topography and OER performance on high surface area substrates.

Keywords: Oxygen evolution reaction, Copper catalysts, Atomic layer deposition, Catalyst topography.

1. Introduction

The world is facing an energy crisis, with the instability of conventional fossil fuels and increasing concerns about the impact of greenhouse gas emissions on global warming [1]. To solve this problem, water splitting, the conversion of water into chemical energy [2], has been identified as a potential solution, which is an important reaction for enabling hydrogen based renewable energy technologies [3,4]. The anodic oxygen evolution reaction is a key step in this process, but it is a complex and slow reaction that requires high energy inputs [5], thus effective and efficient catalyst are required for potential large scale industrial implementation [6]. Currently, noble metal-based catalysts, such as RuO_2, IrO_2, and Pt, have high OER performance but are of high costs and limited availability [7].

To address this challenge, researchers are exploring alternative economical electrocatalysts [8]. Copper based catalysts [9] have gained attention in recent years due to their low costs, low toxicity, high strength, and higher resistance to erosion and abrasion compared to other transition metals [10]. They also possess promising electrocatalytic activity with an overpotential in the range of 300 - 400 mV [11] and stability up to 24 hours under typical testing conditions [12,13].

The biggest advantage of specifically copper oxides are related to the simplicity of the compound and earth abundancy compared to others, which is critical for large-scale implementation. Copper oxides

have a well-defined coordination chemistry [14], and a comparably stable chemical form that resists chemical transformation at high potentials [11,15].

To increase activity, copper oxide catalysts are often nanostructured to improve their electrochemically active surface area (ECSA). In a recent work, copper oxide nanostructures were prepared with different morphologies such as nanosheets, nanocubes, nanoflowers, and nanoleaves. Copper oxide nanoflowers exhibited high catalytic activity in 1 M KOH solution, with an overpotential of 270 mV [16]. In comparison, similar performance with an overpotential of 256 mV at 10 $mAcm^{-2}$ was achieved using electrodeposited selenides based on Fe-Cu-Co [17], however this process required precise composition control in catalyst preparation, thus making the process complex.

Also Ni meshes can serve as high surface area substrates that are efficient as catalyst material for OER, with an overpotential requirement of 350 – 450 mV to achieve a current density of j=10 mA cm^{-2} [18]. Different strategies have been studied to further enhance the OER activity to a level comparable to the benchmark IrO_2 and RuO_2 such as nano-porous structures and surface coatings with e.g. Ni/Fe composites [19]. The use of porous and high surface area three-dimensional (3D) conductive membranes based on Ni/Fe (oxy)hydroxide mesoporous nano-rod arrays on Ni foam has allowed reaching high performances with just 154 mV overpotential needed to achieve a current density of 10 mA cm^{-2} [20].

Similarly, Co_3O_4 nanoneedles on titanium meshes have shown good OER activity with a small overpotential of 416 mV at a current density of 20 mA cm^{-2} in 1M KOH, which is comparable with commercial RuO_2 catalyst [21]. The high OER performance was linked to the deposition of Co_3O_4 nanoneedles on Ti mesh with sufficient active sites. Thus, the use of high surface area with active catalyst is found to be the key strategy in achieving efficient OER catalyst, as the electrode activity is related to number of active sites, which is directly proportional to surface area, density of active sites and conductivity of materials [22].

For other catalyst systems, ALD has been a useful tool to study the effect of particle size [23,24], shape [25] and distribution [26] on high surface area structures [27]. Like no other technology, it allows conformal deposition and precise placement and control of matter that leads to precise relations between nanoscale structure and macroscopic properties [28]. It is interesting to utilize this ability for investigating the process property relationship in Cu systems on high surface area metallic substrates, which has not been dealt with so far.

The objective of this study is to assess the OER performance of copper islands deposited on 3D Ni and Ti mesh. We use ALD to achieve conformal deposition of Cu on 3D Ti and Ni mesh, which enables control over particle size, distribution, and shape. A similar approach using high surface area Ti mesh substrate and Pt-Ir electrodeposition has been explored as an electrode for OER, which showed superior anodic kinetics parameters compared to a polished Ir-disc [29]. In our study, we want to understand how and in what way the controlled deposition of Cu particles alters the electrochemical activity of a non-active 3D structured substrate (Ti) as well as an active one (Ni) and how this changes with the amount of deposited material.

2. Experimental

2.1 Synthesis of Catalyst

Cu was deposited on Ti and Ni mesh (Figure *1* (c)) with consistent diameters and high porosity, giving us a high surface area substrate. The mesh was purchased from BEKAERT, Belgium, the porosity of the Ti and Ni mesh was 56% and 66%, respectively.

A custom-built ALD reactor was employed for depositing copper islands, utilizing nitrogen (AGA 5.0) as a carrier gas for the copper precursor. The base pressure of the system was 20 mtorr. The solid precursor copper (II) acetylacetonate ($Cu(acac)_2$) was sourced from Gelest (USA). The sublimation of $Cu(acac)_2$ was carried out at 145°C, with high purity molecular hydrogen produced on demand by using a generator from Peak Scientific (Scotland, UK) serving as the co-reactant.

The solid Cu precursor was evaporated in a heated stainless steel cylinder and introduced to the reaction chamber through the opening of a solenoid valve (Swagelok, Stavanger, Norway). To enhance the state of pressure of the precursor, a boosting process was employed [30], where an inert gas was utilized to collect and mix with the precursor vapor thereby increasing the absolute pressure, which is a combination of vapour pressure of precursor and pressure build up due additional N_2 introduction. A schematic illustration of the ALD system, including its different components and the boosting mechanism utilized is depicted in Figure *1*(a).

The deposition of Cu islands is performed through successive cyclic reactions between $Cu(acac)_2$ and H_2 at 245 °C, the substrate is directly mounted above the ceramic cartridge heater as shown in Figure 1 (b) . Each ALD cycle is composed of two parts. The first part consists of a 5 s copper precursor boost [31] using Ar gas flowing at 200 sccm, which is an effective strategy to deliver low vapour pressure precursors. This is followed by precursor pulse of 3 s under exposure mode with the exhaust valve closed, which allows more time for the precursor to react with the substrate surface [32]. Finally sytem evacuation is carried out for 10 s to complete the first step . The second part consists of a 5 s H_2 pulse under exposure mode followed by a similar system evacuation.

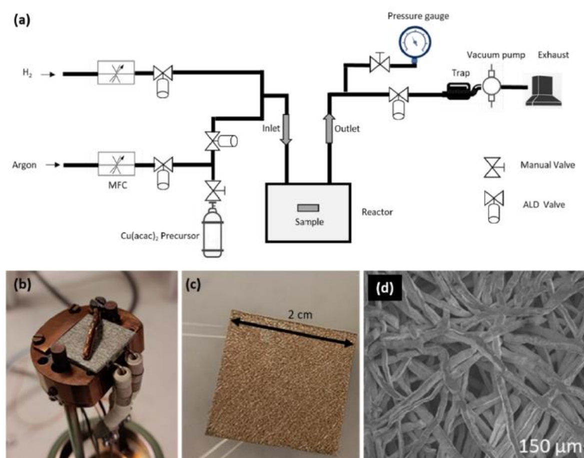

Figure 1: (a) Schematic of the *home built* ALD system *used for depositing Cu on Ti and Ni mesh as OER catalyst, (b) Description of sample mounting showing the provision of uniform sample heating during the ALD process for deposition on high surface area 3D substrate (c) Sample size description with 3D Ti mesh, and (d) SEM image of the Ti mesh illustrating high surface area.*

3. Characterization of catalyst

3.1 SEM

The ALD Cu Catalyst surface was imaged using Scanning Electron Microscopy (SEM) on a Hitachi High-Tech SU9000 electron microscope at an acceleration voltage of 3 kV. Energy dispersive spectroscopy (EDS) was performed using an Oxford Ultim Extreme 120 mm^2 instrument, attached to the SEM.

3.2 XPS

The chemical composition of ALD Cu on Ti and Ni Mesh was evaluated using X-ray photoluminescence spectroscopy (XPS). The measurements were conducted using the Kratos Analytical XPS Microprobe (Kratos Analytical Ltd, Manchester, UK) in a vacuum environment of $5x10^{-9}$ Torr with Al (Kα) radiation of 1486 eV. The XPS data was analyzed using Casa XPS software.

3.3 Electrochemical measurement

The catalysts electrochemical investigation was conducted using an Ivium-n-Stat potentiostat in a three-electrode cell where ALD Cu catalyst, Hg/HgO electrode (Pine Research), and a carbon rod were used as a working reference, and counter electrodes, respectively. The KOH electrolytes (semiconductor grade, Sigma Aldrich) were N_2 saturated. The OER catalyst was activated by cycling for 10 cycles at a scan rate of 100 mV/s between 1.1 V and 1.8 V vs reversible hydrogen electrode (RHE). The linear sweep voltammetry (LSV) polarization curves were carried out in a (1.2 – 1.8 V vs RHE) potential range at a 1 mV/s scan rate. Electrochemical impedance spectroscopy (EIS) was done at an amplitude of 10 mV root mean square (rms) alternating current (AC) perturbation in a 0.1– 10^5 Hz frequency range. The ohmic resistance was compensated at 100 % of the high-frequency resistance

(HFR) collected by EIS at 1.7 V vs RHE. The stability testing was carried out at 1.8 V vs RHE in 1 M KOH for a Ni sample with 500 cycles of copper.

The reference electrode (Hg/HgO) was calibrated in hydrogen-saturated electrolyte using Pt counter and working electrodes. By determining the potential at which the current drops to zero in the polarization curve, the (Hg/HgO) reference electrode is assessed versus RHE. The Hg/HgO electrode is calibrated versus RHE in 1 M KOH:

$$E_{vs\mathrm{RHE}} = E_{\mathrm{vsHg/HgO}} + 0.9 \qquad (1)$$

The over-potential (η) is calculated, considering $E_{O2/H2O}$ = 1.23 V versus RHE, as follows:

$$\eta = E_{vs\mathrm{RHE}} - 1.23 \qquad (2)$$

4. Results and discussion

4.1 Morphology of ALD Cu on Ti and Ni

We try to leverage the distinctive ability of ALD to deposit Cu uniformly and conformally onto OER active Ni and non-active Ti 3D mesh substrates. Additionally, we analyze the interaction of ALD Cu with the two different substrates in terms of phase mixing. By varying the number of ALD Cu cycles, we can evaluate nucleation behavior, particle size, and particle density.

Our results show that when depositing Cu on Ti mesh using ALD, the Cu forms islands, and the size of the islands increase as the number of cycles increases (Figure 2 (a-c)). This type of growth behavior has been previously described as self-limiting island growth [33]. The average diameter of the Cu islands is 10 nm, 24 nm, and 54 nm for 100, 500, and 1500 cycles, respectively. The particle density of the Cu islands on the Ti mesh substrate was 36, 58, and 39 islands per μm^2 for 100, 500, and 1500 cycles, respectively. Assuming a spherical shape (Figure S1, supplementary information andTable s1), the surface area of Cu per μm^2 is 0.01, 0.10, and 0.35 μm^2 for 100, 500, and 1500 cycles, respectively (*Table* 1).

In contrast to Ti mesh, Cu grows on Ni in clusters (Figure 2 (d-f)), where large islands represent collections of closely spaced Cu particles. Notably, the surface coverage of ALD Cu on Ni mesh is higher than on the Ti mesh. The size of the Cu clusters ranges from 30-60 nm for 100 cycles, 200-300 nm for 500 cycles, and 400-600 nm for 1500 cycles. Qualitatively, the Cu surface area on Ni mesh was found to be higher with 1500 ALD Cu cycles due to the presence of larger clusters with a higher number of particles, followed by 500 and 100 ALD Cu cycles samples. For an approximation, assuming the islands are hemispheres and are uniformly distributed ALD Cu hemispheres on Ni surface (Table s2 and s3), the surface area of Cu per μm^2 is evaluated as 1.53, 1.57, and 1.57 μm^2 for 100, 500, and 1500 cycles, respectively (*Table* 1). A recent study [34] discusses the correlation between the OER performance of Cu catalysts and their structural forms, indicating that the presence of Cu nanoclusters enhances the catalyst performance.

Table 1: Surface area of ALD Cu on Ti and Ni mesh substrate

ALD Cu cycles	Total surface area of Cu particles $\mu m^2/\mu m^2$	
	Ti substrate	Ni substrate
100	0.01	1.53
500	0.10	1.57
1500	0.35	1.57

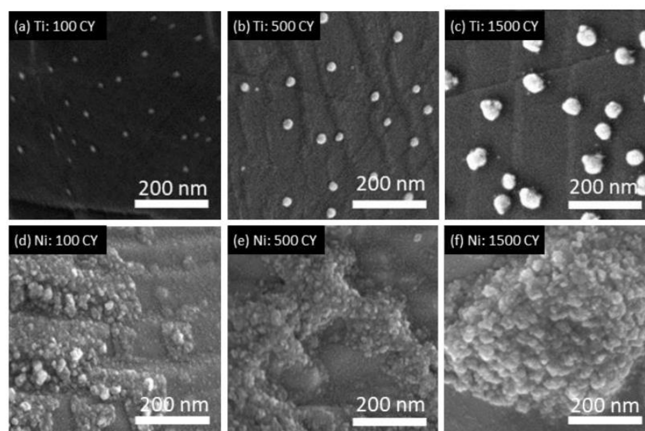

Figure 2: SEM images of the ALD deposited Cu for different numbers of cycles showing separate island Ti (a-c) mesh, as compared to cluster formation on Ni (d-f) mesh.

4.2 XPS

Regional scans for Cu at high resolution and survey scans are carried out as shown in Figure 3. The survey scan for the two materials shows the peaks for Cu 2p, O 1s, and C 1s apart from Ti 2p and Ni 2p due to the substrate. The presence of carbon could be due to impurities from the environment. The presence of CuO and Cu_2O is seen on both Ti and Ni mesh substrates. Studies have shown that a metallic Cu surface undergoes rapid oxidation with exposure to air, approximately 1.21 nm of Cu_2O can be formed in 10 min [35].

The binding energy between 965 - 930 eV shows the presence of Cu2p, the high resolution core level spectra shows peaks at 934 eV and 954 eV, which confirm the presence of Cu^{2+}, the approximate gap of 20 eV between the two peaks is due to spin orbit coupling [16]. However, the Cu2p spectra also indicates the presence of Cu^{1+}, which can be a result of photoreduction of CuO to Cu_2O [36]. Also shake-up satellites are visible in the spectrum, which is a typical indication of the presence of CuO [37]. The Cu $2p_{3/2}$ and Cu $2p_{1/2}$ peaks in literature are located at about 934.1 eV and 954.1 eV, as well as their associated shakeup peaks at 941.2 and 961.2 eV respectively, which corresponds well with our work [9,38].

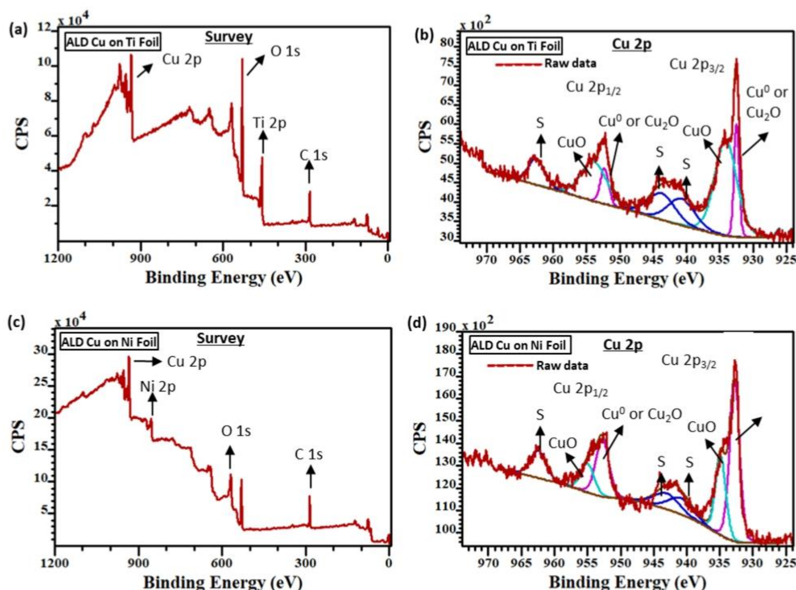

Figure 3: XPS data showing higher presence of ALD Cu in the form of CuO and Cu_2O on (d) Ni Foil compared to (b) Ti foil, (a) XPS survey data ALD Cu on Ti sample, (b) Cu 2p region on ALD Cu on Ti sample, (c) XPS survey data ALD Cu on Ni sample, (d) Cu 2p region on ALD Cu on Ni sample.

4.3 Electrochemical OER characterization

The results of the electrochemical OER performance in terms of onset potential and potential required to reach 10 mA cm^{-2} for Ni and Ti substrates coated with ALD Cu for different number of cycles is presented in Figure 4. Figure 4 (a) shows the linear sweep voltammetry of ALD Cu coated Ti substrates and reveals that the Ti substrate coated with 500 cycles of Cu show the best performance compared to the bare Ti substrate. However, no trend was observed with the number of ALD Cu cycles on the Ti substrate, potentially due to poor adhesion of the ALD-deposited Cu on the Ti substrate. It might be interesting to note here, the native oxide layer on NiO on Ni mesh should be less than 0.8nm [39], whereas a comparatively thicker native oxide layer is expected on the Ti (thickness of native TiO_2 ~10 nm [40]). The presence of oxide layer on the metallic substrate can result in poor adhesion as seen in the case of electrodeposition of Cu on Ru substrate [41]. In addition to this, the thickness of the oxide layer may be detrimental in adhesion strength, thicker oxide layers of TiO_2 were found to have poor adhesion on metallic substrates [42]. The poor adhesion of ALD Cu on Ti mesh as compared to Ni mesh can also be understood from the morphology of the deposition; island type growth is observed on Ti substrate as compared to spread out clusters in the case of Ni mesh (Figure 2). This behavior shows agglomeration on the surface resulting in a difference in wetting angle of the Cu particles, which is directly related to the adhesion strength of the deposited layer. A lower wetting angle indicates higher

adhesion strength [43], whereas higher wetting angle as seen on the ALD Cu growth on Ti mesh indicates poor adhesion strength.

For Ni substrates with ALD Cu, Figure 4 (b) shows the linear sweep voltammetry data. The best performance was observed in the Ni substrate coated with 1500 cycles, with a trend of improved OER performance in terms of lower overpotential with increasing number of ALD Cu deposition cycles. However, it was also noted that the bare Ni mesh performed similarly to the best-performing ALD Cu on Ni mesh sample.

In Figure 4 (c), the potentials at a current density of 10 mA cm^{-2} were evaluated. Overpotential, which is the standard metric used for water splitting studies and calculated as $\eta=E_{vsRHE}-1.23$, is measured at 10 mA cm^{-2}. Results showed that the Ni mesh samples performed better than the Ti substrates, interestingly with the lowest overpotential of 320 mV recorded for both the pristine Ni mesh and Ni mesh with 1500 cycles of ALD Cu. The Ni substrate with 100 and 500 cycles of ALD Cu had an overpotential of 390 and 370 mV respectively.

Upon closer inspection of the Cu 2p XPS spectra (as shown in Figure S2, supplementary information), it was found that after 1500 cycles of ALD Cu, there was a noticeable shift in peak position of approximately 0.5 eV for Ni mesh compared to Ti mesh. This suggests the possibility of an interaction between the Cu and Ni atoms [44]. However, in the case of ALD Cu on Ti mesh substrate, there may be little to no interaction between the two metals, resulting in distinct phases.

The better performance of Ni mesh samples, compared to Ti, can be attributed to the concentration of oxygen species on the surface. This factor is known to have a significant impact on transition metal oxide-based catalysts [45]. The high-resolution O 1s spectra (depicted in Figure S3, supplementary information) can be deconvoluted into different components, namely, O1, O2, O3, and O4, which correspond to varying concentrations of oxygen species. The O1 component, which has the lowest binding energy peak, is related to the typical metal-oxygen bond [46]. The O2 component is associated with defect sites having low oxygen coordination, with oxygen species present in the form of O_2^{2-} or O^-. The presence of hydroxyl groups on the surface leads to the O3 component [47], while O4 is linked to the presence of water or carbonates on the surface [48]. Table s4 lists the relative concentration of these species for our samples, which is calculated based on the peak area. The high performance of catalysts, in the case of transition metal oxide catalysts, is generally attributed to the presence of O_2^{2-} or O^- species (which corresponds to the O2 component in our case) due to their strong electrophilic nature, making them highly active in the oxidation process [49]. These species originate from the defect sites with low oxygen coordination. However, the concentration of the O2 component was found to be quite similar at 12.2 and 10.6% for Ti and Ni mesh samples, respectively, which suggests that the performance improvement cannot be attributed to a higher presence of O_2^{2-} or O^- species. On the other hand, there was a significant difference in the concentration of the O1 component, which is due to the metal-oxygen bond. The concentration of the O1 component was found to be 42.7 and 18.3% for Ti and Ni mesh samples, respectively. A higher O1 content is associated with a higher oxidation degree of the surface, which is known to retard the catalyst activity in the case of ternary metal oxides [49]. Hence, this could be a possible reason for the superior performance of the Ni mesh samples over the Ti mesh samples.

In order to investigate the effect of the number of ALD Cu cycles on the Ni mesh substrates, we studied the ALD Cu nucleation and growth using SEM images (Figure 2). The results showed that the nucleation

of ALD Cu was observed throughout the surface even with lowest deposition cycles. However, with the increase in cycles formation of Cu clusters was observed with an increasing size. The size of the Cu clusters increased, ranging from 30-60 nm for 100 cycles, 200-300 nm for 500 cycles, and 400-600 nm for 1500 cycles. It is possible that the increase in Cu loading and surface area with the number of deposition cycles along with better adhesion when compared on Ti mesh could explain why the 1500 cycles sample exhibited better performance compared with lower numbers of cycles.

Furthermore, our observations also revealed that there was similar performance between the pristine Ni mesh and the Ni mesh with 1500 cycles of ALD Cu. This may be a result of the formation of $Ni(OH)_2$ on the pristine Ni surface. Previous studies have shown that $Ni(OH)_2$ enhances OER activity [50]. When pristine Ni is immersed in an alkaline media, such as 1M KOH, it immediately forms a layer of $Ni(OH)_2$ above the NiO layer. These layers tend to grow with increasing electrochemical cycles, resulting in increased surface roughness and increased electrochemically active sites. The deconvulated O 1s spectra also reveals that relative OH concentration on the surface of Ni mesh substrate with 1500 cycles of ALD Cu to be 55.8% (Figure S3, supplementary information), a higher OH concentration is expected on pristine Ni mesh substrate. Therefore, the formation of $Ni(OH)_2$ on the pristine Ni surface may explain why it exhibited similar OER activity to the Ni mesh with 1500 cycles of ALD Cu.

For the Ti mesh samples, the best performance was achieved by the substrate coated with 500 cycles of ALD Cu, with an overpotential of 345 mV. In comparison, the pristine Ti mesh, 100 cycles Cu, and 1500 cycles Cu sample had overpotentials of 490 mV, 550 mV, and 540 mV respectively.

The enhancement of catalytic performance through the creation of more active sites is a widely researched strategy in the field of heterogeneous catalysis [51]. This can be coupled with the strong metal support interaction (SMSI) [52] dealing with the tuning of electronic, geometric, and bi-functional properties to affect activity, selectivity, and stability of a catalyst. This has been extensively studied on group VIII metals supported by reducible oxides [53]. However, the SMSI concept can also be extended to other metals and supports [54]. In the context of electrocatalysis, carbon has been traditionally used as a support [55], but has shown poor stability under the conditions of the oxygen evolution reaction (OER) [56]. The combination of copper nanoparticles on TiO_2 support has been shown to enhance performance in the electrocatalytic nitrogen reduction reaction (NRR), attributed to SMSI [57].

SEM images (Figure 2 (a-c)) of Ti mesh samples showed that the ALD growth of Cu resulted in island formation. With an increase in the number of Cu deposition cycles (100, 500, and 1500), the size of the islands increased. The Cu Island density was 36, 58, and 39 islands per μm^2 for 100, 500, and 1500 cycles, respectively. The number of islands increased from 100 cycles to 500 cycles, but decreased with 1500 cycles, possibly due to coalescence of smaller islands to form larger ones.

The island density was found to be related to the OER performance; with the sample having 500 ALD Cu cycles and the highest Cu Island density (58 islands per μm^2) performing the best with an overpotential of 345 mV among the different Ti mesh samples. The other two samples with 100 and 1500 cycles performed lower but had approximately similar island density and OER performance. It is noteworthy that the Ti mesh with no Cu deposition performed slightly better than the samples with 100 and 1500 ALD Cu cycles. This indicates that a lower number of Cu islands 36 and 39 per μm^2 (100 and 1500 cycles respectively) lowers the OER performance indicating a possible synergistic effects [46] as seen in other transition metal oxide combinations [21]. Additionally, transition metal oxide-based

catalysts on Ti substrates have exhibited surface deactivation and stability loss due to mixed mechanisms [21]. Firstly, there could be catalyst dissolution and detachment, which results in a rapid change in catalyst performance. Moreover, the gradual formation of a thicker oxide layer can lead to the loss of electrical conductivity, hindering performance in the form of surface passivation. Lastly, a change in surface chemical composition can have an adverse effect on the catalyst's performance [58].

The Tafel plots (Figure S4, supplementary information) display an up-turn at high potentials, that is considered as a typical feature of OER Tafel plots in the literature [59]. The change in Tafel slope at higher potentials can be due to change in the OER mechanism/rate-determining step or due to the surface intermediates saturating or depleting during the reaction.

The stability of the sample (Ni 500 ALD cycles of Cu) was evaluated for 43 hours in 1 M KOH at 1.8 V vs RHE, as shown in Figure 4 (d). The catalyst showed a performance loss within the first 3 hours, indicating a possibility of detachment/dissolution of the catalyst coating (Figure S5, supplementary information). Also, dissolution of copper has also been reported in the case of a 30% nickel-copper alloy during the OER process [60], indicating a possible effect on adhesion behavior on Ni mesh substrates during extended durations.

When we compare the OER performance of our samples with catalyst to similar mesh designs, foils or other 3D structures, the results are found to be comparable to literature values. For example, Ni foams underwent electro-oxidation to yield a NiO_x/Ni type surface, which resulted in an OER overpotential of 390 mV (j = 10 mA cm^{-2}) along with high stability (20000 sec in 1 M KOH) [18]. The high stability was linked to interface effect of NiO_x/Ni, where the interface enhances the intrinsic catalytic activity and stability by optimizing the surface atomic and chemical structures [61]. In another work, a benchmark of different catalyst systems was conducted, and the performance of NiO_x and $NiCuO_x$ in 1M NaOH was measured. Overpotentials of 420 and 410 mV, respectively, were required to reach a current density of j = 10 mA cm^{-2} [62]. For a similar material combination, a study was conducted to evaluate the performance of $NiCuO_x$ nanoparticles on ITO (indium tin oxide) substrate with different atomic ratio of Cu/Ni. It was found that a Cu/Ni ratio of 4:1 was found to be an active catalyst with an onset potential of 320 mV in 1 M Na_2CO_3 electrolyte, the variation in performance with Ni alloying was linked to higher concentration of O_2^{2-} and O^- species on the catalyst surface which are positively linked to catalyst activity [44]. Similarly, in the case of Ti based support, the OER activity of cobalt sulphite nano-sheets electrodeposited on Ti foil required an overpotential of 361 mV to achieve a current density of j = 10 mA cm^{-2} [63], which is similar to performance we achieve with ALD Cu on Ti mesh.

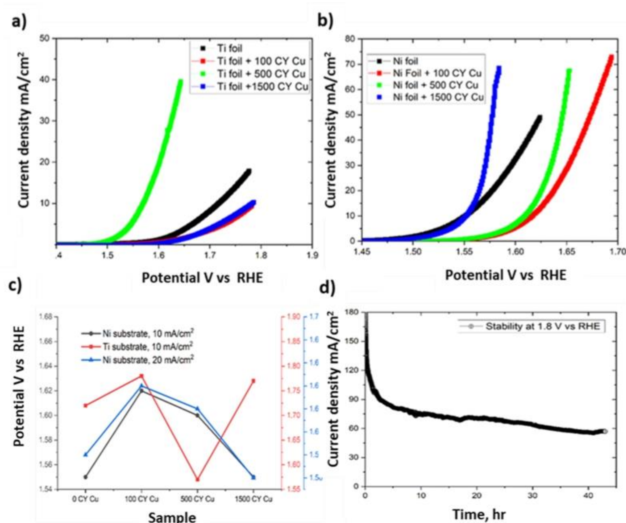

Figure 4: OER performance of different Cu coated and pristine sample Ti and Ni mesh samples in 1 M KOH, (a) and (b) Linear sweep voltammogram of the oxygen evaluation reaction, (c) Potential at constant current densities for different samples, and (d) Stability test for Ni with 500 cycles of Cu.

Postmortem analysis of ALD coated samples after OER stability test was crucial to investigate the reasons behind the reduction in performance during stability test. First, to investigate the mechanical integrity of the coating and substrate, an adhesion test was performed, where the ALD Cu deposited on the Ti mesh was soaked in 1 M KOH solution for a duration similar to the OER process. As seen in Figure 5 (a), the Cu islands on the Ti mesh before the test showed a clear transition after the KOH dip with the removal of Cu in the form of flakes or dendrites (Figure 5 (b)). The Cu coating on the Ti mesh was removed during the OER process leading to a change in surface texture. The electrochemical process resulted in a nanoscale hairy surface on the Ti mesh, as evidenced in Figure 5 (c). Similar surface modifications have been observed in previous studies, such as the laser-assisted etching of Ti sheets [28]. Research on the behavior of sputtered Ti and evaporated Cu in KOH solutions at 80°C has indicated surface modifications due to the softening of Ti and thickening of Cu [64]. In the case of Ni mesh, the ALD Cu remained attached to the Ni mesh after the OER experiment, indicating better adhesion on the Ni mesh, as confirmed by SEM images and EDS experiments (Figure 5 (d-g)). This indicates that the observed loss in performance may not necessarily be linked to coating detachment/dissolution. For a deeper insight into the degradation mechanism of this catalyst system, future work will be needed.

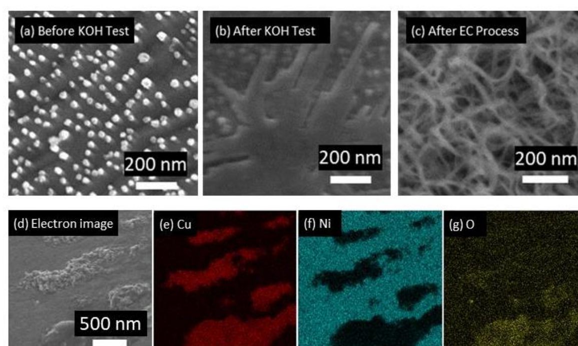

Figure 5: Surface transformation of Ti mesh observed as seen in SEM images of the ALD Cu on Ti mesh (a) before the KOH soak test, (b), after the KOH soak test, (c), after the EC OER process, and (d-g), EDS of ALD Cu on Ni mesh after the OER process.

In comparison with state of art of noble metal-free bifunctional catalysts [65] and other complex catalysts, the overpotentials measured at 10 mA cm^{-2} for our ALD Cu coated Ni and Ti mesh samples are found to be 320 mV and 345 mV, respectively [62]. However, we argue that the preparation route presented here is facile, requiring the pristine substrate to undergo one automated deposition cycle only. No further processing is required, in addition, there is less complexity involved in our case for the fabrication of islands on highly porous 3D substrates with the use of ALD. It must be noted, however, that the OER activity decreases faster than with the published counterparts, which we argue being a matter of poor adhesion. In future studies, the latter could be enhanced by increasing the process complexity through a removal of the surface oxide prior to the deposition, through a plasma cleaning process [66] or a wet chemical etching routine [67]. Further, a graphene conductive layer [68] or a variation in stoichiometry may be strategies to employ.

5. Conclusions

We investigated the potential of ALD Cu deposited on Ti and Ni mesh as cost-effective electrocatalysts for the OER process. Our results showed that the utilization of Ni mesh substrates generally led to lower overpotentials than the utilization of Ti substrates, with the lowest overpotential of 320 mV recorded for both pristine Ni mesh and Ni mesh with 1500 cycles of ALD Cu. The SEM images revealed that the Ni sample with 1500 deposition cycles exhibited better performance, which may be attributed to an increase in both Cu loading and surface area. Additionally, the study found a significant difference in the ALD Cu surface area between Ti and Ni substrates. Specifically, for Ti, the surface area of Cu per μm^2 increased from 0.01 to 0.35 μm^2 as the number of deposition cycles increased from 100 to 1500. For Ni, the surface area of Cu per μm^2 remained nearly constant at 1.53 to 1.57 μm^2 for 100 to 1500 cycles. Moreover, the formation of $Ni(OH)_2$ on the pristine Ni surface may explain why it exhibited similar OER activity to the Ni mesh with 1500 cycles of ALD Cu.

For Ti mesh substrates, the best performance was achieved by the substrate coated with 500 cycles of ALD Cu, with an overpotential of 345 mV. The island density of Cu was found to be related to the OER performance, with the sample having 500 ALD Cu cycles and the highest Cu-island density performing the best. The Ti mesh with no Cu deposition performed slightly better than the samples

with 100 and 1500 ALD Cu cycles, indicating that a low presence of Cu islands and poor surface adhesion can negatively affect the performance.
The durability test also revealed a limited adhesion of the Ni sample (500 Cu cycles), with performance reduction observed within the first three hours. The SEM and EDS analysis of the adhesion test samples further revealed detachment and modifications of the ALD Cu layer.
Furthermore, the overpotentials measured at 10 mA cm^{-2} for our ALD Cu coated Ni and Ti mesh samples are comparable to state-of-the-art noble metal-free bifunctional catalysts, and our approach offers less complexity in fabricating islands on highly porous 3D substrates with the use of ALD.
Overall, this study contributes to the ongoing efforts to develop efficient and stable catalysts for OER, with the potential to advance the development of renewable energy technologies. Further investigation is needed to improve the adhesion and stability of the catalyst surface, which could enhance the performance and durability of the ALD Cu catalysts on high surface area metallic substrates.

Supplementary information

See the supplementary information for ALD Cu surface area calculation and high-resolution O 1s spectra.

Acknowledgments

Abdulla Bin Afif was supported by NTNU's Enabling technologies: Nanotechnology. The Research Council of Norway (Norges Forskningsråd) is acknowledged for its support under project 274459, Trånslate, and the Norwegian micro-and nano-fabrication Facility, NorFab, project 245963/F50. The Norwegian Center for International Cooperation in Education is acknowledged for the funds under project PNA-2017/10077.

Author declarations

Conflict of Interest

The authors have no conflicts to disclose.

Data availability

The data supporting this study's findings are available from the corresponding author upon request.

References

1. Kweku, D.W., Bismark, O., Maxwell, A., Desmond, K.A., Danso, K.B., Oti-Mensah, E.A., Quachie, A.T., and Adormaa, B.B. (2018) Greenhouse effect: greenhouse gases and their impact on global warming. *J. Sci. Res. reports*, **17** (6), 1–9.

2. Tee, S.Y., Win, K.Y., Teo, W.S., Koh, L.D., Liu, S., Teng, C.P., and Han, M.Y. (2017) Recent progress in energy driven water splitting. *Adv. Sci.*, **4** (5), 1600337.

3. Barber, J. (2020) Solar-driven water-splitting provides a solution to the energy problem underpinning climate change. *Biochem. Soc. Trans.*, **48** (6), 2865–2874.

4. Oliveira, A.M., Beswick, R.R., and Yan, Y. (2021) A green hydrogen economy for a renewable energy society. *Curr. Opin. Chem. Eng.*, **33**, 100701.

5. Fabbri, E., and Schmidt, T.J. (2018) Oxygen evolution reaction: the enigma in water electrolysis. *Acs Catal.*, **8** (10), 9765–9774.

6. Luo, Y., Zhang, Z., Chhowalla, M., and Liu, B. (2022) Recent advances in design of

electrocatalysts for high current density water splitting. *Adv. Mater.*, **34** (16), 2108133.

7. Jamesh, M.-I., and Sun, X. (2018) Recent progress on earth abundant electrocatalysts for oxygen evolution reaction (OER) in alkaline medium to achieve efficient water splitting: A review. *J. Power Sources*, **400**, 31–68.

8. Alshehri, S.M., Alhabarah, A.N., Ahmed, J., Naushad, M., and Ahamad, T. (2018) An efficient and cost-effective tri-functional electrocatalyst based on cobalt ferrite embedded nitrogen doped carbon. *J. Colloid Interface Sci.*, **514**, 1–9.

9. Liu, X., Jia, H., Sun, Z., Chen, H., Xu, P., and Du, P. (2014) Nanostructured copper oxide electrodeposited from copper (II) complexes as an active catalyst for electrocatalytic oxygen evolution reaction. *Electrochem. commun.*, **46**, 1–4.

10. Zhou, Z., Li, X., Li, Q., Zhao, Y., and Pang, H. (2019) Copper-based materials as highly active electrocatalysts for the oxygen evolution reaction. *Mater. today Chem.*, **11**, 169–196.

11. Kannimuthu, K., Sangeetha, K., Sankar, S.S., Karmakar, A., Madhu, R., and Kundu, S. (2021) Investigation on nanostructured Cu-based electrocatalysts for improvising water splitting: a review. *Inorg. Chem. Front.*, **8** (1), 234–272.

12. Rajput, A., Kundu, A., and Chakraborty, B. (2021) Recent Progress on Copper Based Electrode Materials for Overall Water Splitting. *ChemElectroChem*, **8** (10), 1698–1722.

13. Liu, X., Cui, S., Qian, M., Sun, Z., and Du, P. (2016) In situ generated highly active copper oxide catalysts for the oxygen evolution reaction at low overpotential in alkaline solutions. *Chem. Commun.*, **52** (32), 5546–5549.

14. Mirica, L.M., Ottenwaelder, X., and Stack, T.D.P. (2004) Structure and spectroscopy of copper-dioxygen complexes. *Chem. Rev.*, **104** (2), 1013–1046.

15. Deng, Y., Handoko, A.D., Du, Y., Xi, S., and Yeo, B.S. (2016) In situ Raman spectroscopy of copper and copper oxide surfaces during electrochemical oxygen evolution reaction: identification of CuIII oxides as catalytically active species. *Acs Catal.*, **6** (4), 2473–2481.

16. Arshad, F., Munir, A., Kashif, Q.Q., ul Haq, T., Iqbal, J., Sher, F., and Hussain, I. (2020) Controlled development of higher-dimensional nanostructured copper oxide thin films as binder free electrocatalysts for oxygen evolution reaction. *Int. J. Hydrogen Energy*, **45** (33), 16583–16590.

17. Cao, X., Johnson, E., and Nath, M. (2019) Expanding multinary selenide based high-efficiency oxygen evolution electrocatalysts through combinatorial electrodeposition: case study with Fe-Cu-Co selenides. *ACS Sustain. Chem. Eng.*, **7** (10), 9588–9600.

18. Han, G.-Q., Liu, Y.-R., Hu, W.-H., Dong, B., Li, X., Shang, X., Chai, Y.-M., Liu, Y.-Q., and Liu, C.-G. (2015) Three dimensional nickel oxides/nickel structure by in situ electro-oxidation of nickel foam as robust electrocatalyst for oxygen evolution reaction. *Appl. Surf. Sci.*, **359**, 172–176.

19. Lu, X., and Zhao, C. (2015) Electrodeposition of hierarchically structured three-dimensional nickel/iron electrodes for efficient oxygen evolution at high current densities. *Nat. Commun.*, **6** (1), 1–7.

20. Zhou, H., Yu, F., Zhu, Q., Sun, J., Qin, F., Yu, L., Bao, J., Yu, Y., Chen, S., and Ren, Z. (2018) Water splitting by electrolysis at high current densities under 1.6 volts. *Energy Environ. Sci.*, **11** (10), 2858–2864.

21. Tao, Z., Jiang, L., Jia, X., Xiao, H., Liang, Y., Yang, B., Guo, P., Zhang, L., and Yang, H. (2021) In situ growth of Co3O4 nanoneedles on titanium mesh for electrocatalytic oxygen evolution. *J.*

Mater. Sci. Mater. Electron., **32** (18), 23275–23284.

22. Zhao, J., Wu, W., Jia, X., Zhao, Z., and Hu, X. (2020) A coaxial three-layer (Ni, Fe) O x H y/Ni/Cu mesh electrode: excellent oxygen evolution reaction activity for water electrolysis. *Catal. Sci. Technol.*, **10** (6), 1803–1808.

23. O'Neill, B.J., Jackson, D.H.K., Lee, J., Canlas, C., Stair, P.C., Marshall, C.L., Elam, J.W., Kuech, T.F., Dumesic, J.A., and Huber, G.W. (2015) Catalyst design with atomic layer deposition. *Acs Catal.*, **5** (3), 1804–1825.

24. Sarnello, E., Lu, Z., Seifert, S., Winans, R.E., and Li, T. (2021) Design and characterization of ALD-based overcoats for supported metal nanoparticle catalysts. *ACS Catal.*, **11** (5), 2605–2619.

25. Canlas, C.P., Lu, J., Ray, N.A., Grosso-Giordano, N.A., Lee, S., Elam, J.W., Winans, R.E., Van Duyne, R.P., Stair, P.C., and Notestein, J.M. (2012) Shape-selective sieving layers on an oxide catalyst surface. *Nat. Chem.*, **4** (12), 1030–1036.

26. Dai, P., Xie, J., Mayer, M.T., Yang, X., Zhan, J., and Wang, D. (2013) Solar hydrogen generation by silicon nanowires modified with platinum nanoparticle catalysts by atomic layer deposition. *Angew. Chemie*, **125** (42), 11325–11329.

27. Lu, J., Elam, J.W., and Stair, P.C. (2016) Atomic layer deposition-Sequential self-limiting surface reactions for advanced catalyst "bottom-up" synthesis. *Surf. Sci. Rep.*, **71** (2), 410–472.

28. Bin Afif, A., Dadlani, A.L., Burgmann, S., Kollensperger, P., and Torgersen, J. (2020) Atomic layer deposition of perovskites—Part 1: Fundamentals of nucleation and growth. *Mater. Des. Process. Commun.*, **2** (1), e114.

29. Cieluch, M., Podleschny, P.Y., Kazamer, N., Wirkert, F.J., Rost, U.W., and Brodmann, M. (2022) Development of a Bifunctional Ti-Based Gas Diffusion Electrode for ORR and OER by One-and Two-Step Pt-Ir Electrodeposition. *Nanomaterials*, **12** (7), 1233.

30. Liu, G., Bertuch, A., Deguns, E.W., Dalberth, M.J., Sundaram, G.M., and Becker, S. Method and Apparatus for precursor delivery.

31. Tomer, S., Panigrahi, J., Srivastava, R., and Rauthan, C.M.S. (2019) Importance of precursor delivery mechanism for Tetra-kis-ethylmethylaminohafnium/water atomic layer deposition process. *Thin Solid Films*, **692**, 137629.

32. Tian, L., Ponton, S., Benz, M., Crisci, A., Reboud, R., Giusti, G., Volpi, F., Rapenne, L., Vallee, C., and Pons, M. (2018) Aluminum nitride thin films deposited by hydrogen plasma enhanced and thermal atomic layer deposition. *Surf. Coatings Technol.*, **347**, 181–190.

33. Chen, D.A., Bartelt, M.C., Hwang, R.Q., and McCarty, K.F. (2000) Self-limiting growth of copper islands on TiO2 (110)-(1 x 1). *Surf. Sci.*, **450** (1–2), 78–97.

34. Quílez Bermejo, J., García Dalí, S., Daouli, A., Zitolo, A., Canevesi, R.L.S., Emo, M., Izquierdo, M.T., Badawi, M., Celzard, A., and Fierro, V. (2023) Advanced Design of Metal Nanoclusters and Single Atoms Embedded in C1N1 Derived Carbon Materials for ORR, HER, and OER. *Adv. Funct. Mater.*, 2300405.

35. Zuo, Z.-J., Li, J., Han, P.-D., and Huang, W. (2014) XPS and DFT studies on the autoxidation process of Cu sheet at room temperature. *J. Phys. Chem. C*, **118** (35), 20332–20345.

36. Priamushko, T., Budiyanto, E., Eshraghi, N., Weidenthaler, C., Kahr, J., Jahn, M., Tüysüz, H., and Kleitz, F. (2022) Incorporation of Cu/Ni in Ordered Mesoporous Co Based Spinels to

Facilitate Oxygen Evolution and Reduction Reactions in Alkaline Media and Aprotic Li- O2 Batteries. *ChemSusChem*, **15** (5), e202102404.

37. Yu, J., Hai, Y., and Jaroniec, M. (2011) Photocatalytic hydrogen production over CuO-modified titania. *J. Colloid Interface Sci.*, **357** (1), 223–228.

38. Cui, S., Liu, X., Sun, Z., and Du, P. (2016) Noble metal-free copper hydroxide as an active and robust electrocatalyst for water oxidation at weakly basic pH. *ACS Sustain. Chem. Eng.*, **4** (5), 2593–2600.

39. Lambers, E.S., Dykstal, C.N., Seo, J.M., Rowe, J.E., and Holloway, P.H. (1996) Room-temerature oxidation of Ni (110) at low and atmospheric oxygen pressures. *Oxid. Met.*, **45**, 301–321.

40. Proch, S., Yoshino, S., Takahashi, N., Seki, J., Kosaka, S., Kodama, K., and Morimoto, Y. (2018) The native oxide on titanium metal as a conductive model substrate for oxygen reduction reaction studies. *Electrocatalysis*, **9**, 608–622.

41. Moffat, T.P., Walker, M., Chen, P.J., Bonevich, J.E., Egelhoff, W.F., Richter, L., Witt, C., Aaltonen, T., Ritala, M., and Leskelä, M. (2005) Electrodeposition of Cu on Ru barrier layers for damascene processing. *J. Electrochem. Soc.*, **153** (1), C37.

42. Coddet, C., Craze, A.M., and Beranger, G. (1987) Measurements of the adhesion of thermal oxide films: application to the oxidation of titanium. *J. Mater. Sci.*, **22**, 2969–2974.

43. Shima, K., Shimizu, H., Momose, T., and Shimogaki, Y. (2014) Study on the adhesion strength of CVD-Cu films with ALD-Co (W) underlayers made using amidinato precursors. *ECS J. Solid State Sci. Technol.*, **4** (2), P20.

44. Wang, L., Ge, X., Li, Y., Liu, J., Huang, L., Feng, L., and Wang, Y. (2017) Nickel enhanced the catalytic activities of amorphous copper for the oxygen evolution reaction. *J. Mater. Chem. A*, **5** (9), 4331–4334.

45. Long, X., Ma, Z., Yu, H., Gao, X., Pan, X., Chen, X., Yang, S., and Yi, Z. (2016) Porous FeNi oxide nanosheets as advanced electrochemical catalysts for sustained water oxidation. *J. Mater. Chem. A*, **4** (39), 14939–14943.

46. Long, X., Xiao, S., Wang, Z., Zheng, X., and Yang, S. (2015) Co intake mediated formation of ultrathin nanosheets of transition metal LDH-an advanced electrocatalyst for oxygen evolution reaction. *Chem. Commun.*, **51** (6), 1120–1123.

47. Jiménez, V.M., Fernández, A., Espinós, J.P., and González-Elipe, A.R. (1995) The state of the oxygen at the surface of polycrystalline cobalt oxide. *J. Electron Spectros. Relat. Phenomena*, **71** (1), 61–71.

48. Liang, F., Yu, Y., Zhou, W., Xu, X., and Zhu, Z. (2015) Highly defective CeO 2 as a promoter for efficient and stable water oxidation. *J. Mater. Chem. A*, **3** (2), 634–640.

49. Fan, J., Chen, Z., Shi, H., and Zhao, G. (2016) In situ grown, self-supported iron-cobalt-nickel alloy amorphous oxide nanosheets with low overpotential toward water oxidation. *Chem. Commun.*, **52** (23), 4290–4293.

50. Fabbri, E., Habereder, A., Waltar, K., Kötz, R., and Schmidt, T.J. (2014) Developments and perspectives of oxide-based catalysts for the oxygen evolution reaction. *Catal. Sci. Technol.*, **4** (11), 3800–3821.

51. Bele, M., Stojanovski, K., Jovanovi, P., Moriau, L., Koderman Podborsek, G., Moskon, J., Umek, P., Sluban, M., Drazic, G., and Hodnik, N. (2019) Towards Stable and Conductive Titanium

Oxynitride High Surface Area Support for Iridium Nanoparticles as Oxygen Evolution Reaction Electrocatalyst. *ChemCatChem*, **11** (20), 5038–5044.

52. Lou, Y., Xu, J., Zhang, Y., Pan, C., Dong, Y., and Zhu, Y. (2020) Metal-support interaction for heterogeneous catalysis: from nanoparticles to single atoms. *Mater. Today Nano*, **12**, 100093.

53. Pan, C.-J., Tsai, M.-C., Su, W.-N., Rick, J., Akalework, N.G., Agegnehu, A.K., Cheng, S.-Y., and Hwang, B.-J. (2017) Tuning/exploiting strong metal-support interaction (SMSI) in heterogeneous catalysis. *J. Taiwan Inst. Chem. Eng.*, **74**, 154–186.

54. del Arco, M., and Rives, V. (1986) Metal-support and metal oxide-support interactions in Cu/TiO2. *React. Kinet. Catal. Lett.*, **31** (1), 239–244.

55. Yu, X., Hua, T., Liu, X., Yan, Z., Xu, P., and Du, P. (2014) Nickel-based thin film on multiwalled carbon nanotubes as an efficient bifunctional electrocatalyst for water splitting. *ACS Appl. Mater. Interfaces*, **6** (17), 15395–15402.

56. Yi, Y., Weinberg, G., Prenzel, M., Greiner, M., Heumann, S., Becker, S., and Schlogl, R. (2017) Electrochemical corrosion of a glassy carbon electrode. *Catal. Today*, **295**, 32–40.

57. Utomo, W.P., Wu, H., and Ng, Y.H. (2022) Modulating the Active Sites of Oxygen Deficient TiO2 by Copper Loading for Enhanced Electrocatalytic Nitrogen Reduction to Ammonia. *Small*, 2200996.

58. Zeng, F., Mebrahtu, C., Liao, L., Beine, A.K., and Palkovits, R. (2022) Stability and deactivation of OER electrocatalysts: A review. *J. Energy Chem.*

59. Poureshghi, F., Seland, F., Jensen, J.O., and Sunde, S. (2022) Activity of carbon-encapsulated Ni12- xFexP5 catalysts for the oxygen evolution reaction: Combination of high activity and stability. *Appl. Catal. A Gen.*, **643**, 118786.

60. Kibria, A.K.M.F., and Tarafdar, S.A. (2002) Electrochemical studies of a nickel copper electrode for the oxygen evolution reaction (OER). *Int. J. Hydrogen Energy*, **27** (9), 879–884.

61. Gao, W., Hood, Z.D., and Chi, M. (2017) Interfaces in heterogeneous catalysts: advancing mechanistic understanding through atomic-scale measurements. *Acc. Chem. Res.*, **50** (4), 787–795.

62. McCrory, C.C.L., Jung, S., Peters, J.C., and Jaramillo, T.F. (2013) Benchmarking heterogeneous electrocatalysts for the oxygen evolution reaction. *J. Am. Chem. Soc.*, **135** (45), 16977–16987.

63. Liu, T., Liang, Y., Liu, Q., Sun, X., He, Y., and Asiri, A.M. (2015) Electrodeposition of cobalt-sulfide nanosheets film as an efficient electrocatalyst for oxygen evolution reaction. *Electrochem. commun.*, **60**, 92–96.

64. Williams, K.R., Gupta, K., and Wasilik, M. (2003) Etch rates for micromachining processing-Part II. *J. microelectromechanical Syst.*, **12** (6), 761–778.

65. Yu, L., Zhou, H., Sun, J., Qin, F., Yu, F., Bao, J., Yu, Y., Chen, S., and Ren, Z. (2017) Cu nanowires shelled with NiFe layered double hydroxide nanosheets as bifunctional electrocatalysts for overall water splitting. *Energy Environ. Sci.*, **10** (8), 1820–1827.

66. Wang, Z., Zhang, Y., Neyts, E.C., Cao, X., Zhang, X., Jang, B.W.-L., and Liu, C. (2018) Catalyst preparation with plasmas: how does it work? *ACS Catal.*, **8** (3), 2093–2110.

67. Yao, Q., Huang, B., Xu, Y., Li, L., Shao, Q., and Huang, X. (2021) A chemical etching strategy to improve and stabilize RuO2-based nanoassemblies for acidic oxygen evolution. *Nano Energy*, **84**, 105909.

68. Cui, H., Guo, Y., and Zhou, Z. (2021) Three dimensional graphene based macrostructures for electrocatalysis. *Small*, **17** (22), 2005255.

Studying high surface area Atomic layer deposited Cu islands on Ti and Ni Mesh as an Electrocatalyst for Oxygen Evolution Reaction (OER)

Abdulla Bin Afif [1], Alaa Faid [2], Anup L Dadlani [1], Andreas Flaten [1],
, Peter Köllensperger [3], Svein Sunde [2], Jan Torgersen [4]
[1] Department of Industrial and Mechanical Engineering, Norwegian University of Science and Technology, Trondheim, Norway
[2] Department of Materials Science and Engineering, Norwegian University of Science and Technology, Trondheim, Norway
[3] Department of Physics, Norwegian University of Science and Technology, Trondheim, Norway,
[4] Institute of Materials Science and Mechanics of Materials, TUM, Germany

Supplementary information

Estimation of surface ALD Cu surface coverage on Ti substrate

Table S1 describes the ALD deposited Cu particle surface area for different number of ALD Cu cycles on Ti mesh. The effect of the Cu surface area on OER performance is discussed in the manuscript. The size and number of particles were approximated using imageJ software.

Table S1: Cu particle surface area for different ALD Cu cycles on Ti mesh

	Diameter (nm)	Diameter (um)	radius (um)	Surface Area of speherical particle um2	density of particle (particles/um2)	Total surface area of Cu particles/ µm²
100 cycle	10	0.01	0.005	0.000314	36	0.011304
500cycle	24	0.024	0.012	0.00180864	58	0.10490112
1500 cycle	54	0.054	0.027	0.00915624	39	0.35709336

Estimation of surface ALD Cu surface coverage on Ni substrate

Assuming (Figure S1),

- The islands are hemispheres
- There is complete surface coverage of ALD Cu hemispheres on Ni surface

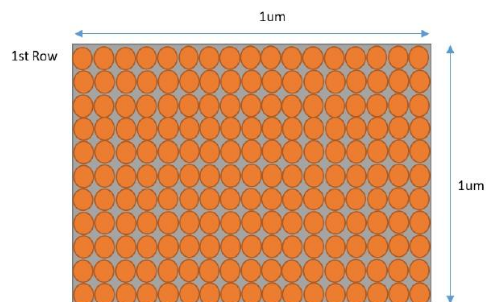

Figure S1: Schematic representation of the top view of ALD Cu on Ni for surface area approximation

The islands density is calculated as,

Table S2: Number of particles approximation based on complete surface coverage on Ni mesh

ALD Cu	Diameter (um)	No of particle in a row	Total number of particles
100 cycle	0.045	22	484
500 cycle	0.25	4	16
1500 cycle	0.5	2	4

Table S3: Cu particle surface area for different ALD Cu cycles on Ni mesh

	Diameter (nm)	Diameter (um)	radius (um)	Surface Area of hemisphere particle um^2	density of particle (particles/um^2)	Total surface area of Cu particles/um^2
100	45	0.045	0.0225	0.00317925	484	1.53
500	250	0.25	0.125	0.098125	16	1.57
1500	500	0.5	0.25	0.3925	4	1.57

a. XPS

Cu 2p XPS spectra is shown in Figure S2.

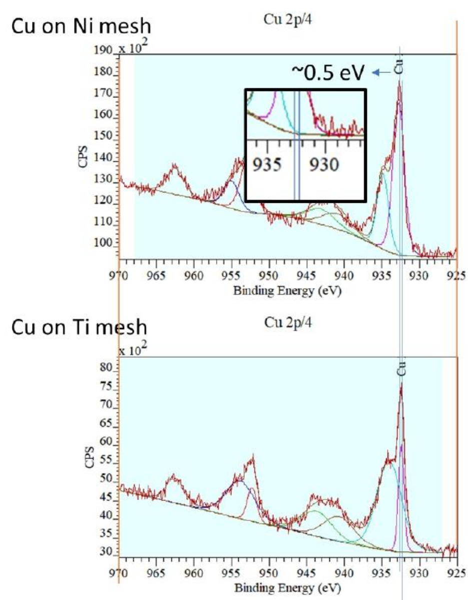

Figure S2: XPS data showing a peak position shift to higher energy by ~0.5eV in the case of ALD Cu on Ni substrate, which could be due chemical bonding or phase mixing in the case of Cu on Ni substrate.

Table S4 lists the relative concentration of these species for our samples, which is calculated based on the peak area in Figure S3.

Table S4: Percentage concentration of oxygen components

Name	Species	% conc. in Ti	% conc. in Ni	Peak pos. on Ti	Peak pos. on Ni
O1	O^{2-}	42.7	18.3	529.93	529.60
O2	O_2^{2-} or O^-	12.2	10.6	530.46	530.11
O3	OH	11	55.8	531.34	531.41
O4	H_2O or carbonate	34	15.2	531.65	532.53

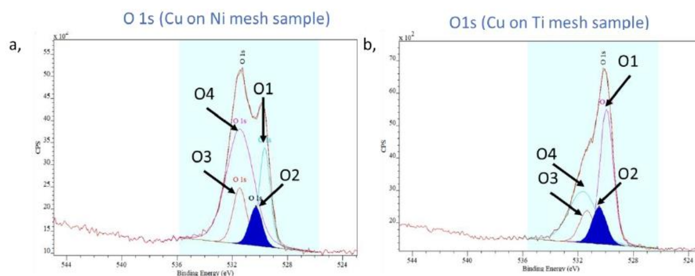

Figure S3: High-resolution regional spectra for O 1s with deconvulated components for (a) Ni and (b) Ti mesh sample with ALD Cu.

b. Electrochemical OER characterization

The Tafel plots (Figure S4)

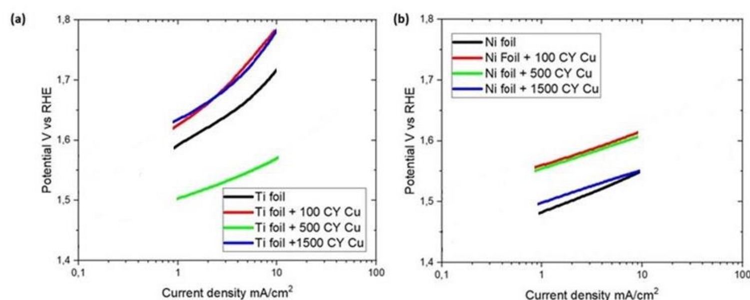

Figure S4: The Tafel plots for Ti (a) and Ni (b) substrates with different cycles of ALD Cu.

c. Stability test

Figure S5 shows surface of ALD Cu Ni mesh sample on which the stability of the ALD Cu on Ni was evaluated for 43 hours in 1 M KOH at 1.8 V vs RHE.

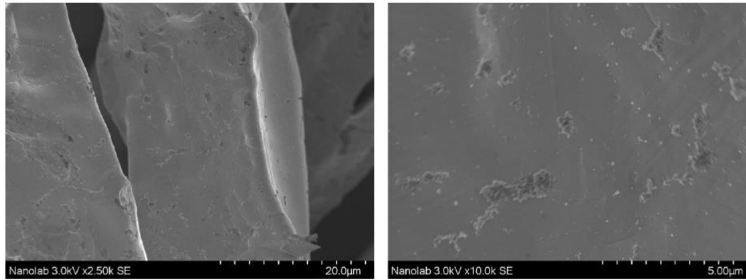

Figure S5: SEM Images of stability test sample of ALD CU on Ni mesh with different magnifications

Paper 7

Review of Scientific Instruments ARTICLE scitation.org/journal/rsi

A toolbox for easy entry low wavenumber *in situ* atomic layer deposition transmission FTIR spectroscopy studies

Cite as: Rev. Sci. Instrum. 93, 085107 (2022); doi: 10.1063/5.0102518
Submitted: 10 June 2022 • Accepted: 5 August 2022 •
Published Online: 30 August 2022

Abdulla Bin Afif,[1,a)] Anup L. Dadlani,[1] Andreas Flaten,[1] Markus Joakim Lid,[1] Johannes Ofstad,[2] Andreas Erbe,[2] Peter Köllensperger,[3] and Jan Torgersen[1]

AFFILIATIONS

[1] Department of Industrial and Mechanical Engineering, Norwegian University of Science and Technology, Trondheim, Norway
[2] Department of Materials Science and Engineering, Norwegian University of Science and Technology, Trondheim, Norway
[3] Department of Physics, Norwegian University of Science and Technology, Trondheim, Norway

[a)] Author to whom correspondence should be addressed: abdulla.binafif@ntnu.no

ABSTRACT

A detailed description of a flexible and portable atomic layer deposition (ALD) system is presented for conducting *in situ* Fourier transform infrared (FTIR) absorption spectroscopy studies during the evolution and growth of ALD films. The system is directly integrated with a commercial FTIR spectrometer (Bruker Vertex 80V) to avoid the necessity of an external optical path to the instrument, thereby mitigating complexity and optical losses. In this work, we use potassium bromide (KBr) with a 5 nm layer of sputtered Si as a substrate due to higher infrared transmittance when compared to a single-side polished Si wafer. The FTIR absorption study is conducted at normal incidence in transmission mode using a deuterated L-alanine doped triglycine sulfate (DTGS) detector owing to its potential applicability for reliable measurements at wavenumbers below ~700 cm^{-1}. We demonstrate this by measuring *ex situ* the transverse optical phonon of bulk Al_2O_3 centered at 680 cm^{-1}. The integrity and functionality of the system to track the nucleation stage are validated by conducting *in situ* FTIR absorption measurements of Al_2O_3 using tri-methyl aluminum (TMA) and H_2O. The measured IR absorption spectra for the Al_2O_3 growth after each cycle of TMA and H_2O show the formation and removal of CH_3 (2800–3000 cm^{-1}) groups on the substrate surface and CH_4 (3016 and 1306 cm^{-1}) molecules in the reactor, thus confirming the successful tracking of ligand exchange. Thus, this instrument, together with the choice of KBr as substrate, can enable straightforward ALD nucleation studies using a DTGS detector having sufficient signal without additional optical setup and modifications to off-the-shelf FTIR systems that allow low wavenumber experiments.

Published under an exclusive license by AIP Publishing. https://doi.org/10.1063/5.0102518

NOMENCLATURE

Abbreviation explanation

ALD	atomic layer deposition
CF	ConFlat
DTGS	deuterated L-alanine doped triglycine sulfate
FTIR	Fourier transform infrared
GPC	growth per cycle
IR	infrared
KF	quick flange
MFC	mass flow controller
S/N	signal to noise
TMA	trimethyl aluminum

I. INTRODUCTION

The atomic layer deposition (ALD) system's ability to deposit ultrathin films with uniformity and conformality on 3D surfaces gives it a unique position in the field of micro and nanofabrication. Due to ALD's distinct capabilities, it plays an increasingly important role in modern semiconductors[1] and energy applications.[2] The deposition process works on the principle of self-limiting sequential

interaction of the precursor and co-reactant.[3] Among the available thin film deposition techniques, ALD stands out in terms of thickness control and conformality on 3D surfaces. The resulting films are dense and of high quality.[4]

In the electronic industry, ALD's capabilities are already being utilized to fabricate sub 5 nm commercial devices.[5] Other industries aiming to minimize the use of precious materials find ALD an increasingly viable fabrication technique. In the 5–10 nm thickness range, ALD films are typically in the nucleation phase, where islands form and later coalesce to form a continuous film.[6] It is known that a surface with high nucleation site density and efficient ligand exchange reactions are prerequisites for achieving ultrathin films.[7] Yet, the effects prohibiting this condition are manifold, including but not limited to steric hindrance[8] and wetting limitations.[9–11] For achieving the deposition of uniform ultrathin films, it is crucial to understand and select the deposition chemistry and to determine the optimized process parameters. This ability is obtained through *in situ* techniques, allowing surface monitoring during the deposition process[12] while the sample is kept as close as possible in deposition conditions. Alterations to the surface caused by the exposure to air are minimized as the sample is kept under vacuum at all times as compared to *ex situ* techniques.[13]

One of the chemical analytical techniques that enabled *in situ* ALD studies is infrared (IR) spectroscopy. It combines a high signal-to-noise (S/N) ratio, low data-acquisition time, inexpensive equipment, wide availability, and flexibility in sample preparation. Home-built ALD reactors dedicated to *in situ* ALD-Fourier transform infrared (FTIR) studies have added to the scientific knowledge[14] but also revealed specific challenges affecting both the ALD process and the characterization capability.[15] One of the deterrents is connected to the commonplace cold-wall reactor design, causing precursor condensation in specific locations and chemical residues that are difficult to remove, even with excessive system purge.[16] While such a design is suitable for specific processes involving reactive precursors and chemistries at low temperatures, it might not suffice for facilitating processes with less reactive precursors and narrower ALD windows. In addition, slow precursor desorption over time may result in a virtual leak that hampers the quality of the surface under study.

Another aspect where current reactor designs may have deficiencies is the reactor size. A small reaction chamber ensures straightforward and fast system evacuation, reducing the chance of chemical crosstalk. However, most reported *in situ* FTIR-ALD systems have multiple optical ports, resulting in large reactor volumes.[17] The level of complexity is further enhanced as chambers are routinely placed outside the system's characterization compartment. This necessitates coupling out the IR beam from the instrument for its utilization in an additional inert gas purged optics compartment outside the instrument. This compartment comprises multiple mirrors and an additional detector.[17–19] Apart from the additional costs such as design entails, significant optical losses and difficulties in maintaining a low contamination level within the characterization environment can be expected. Instead, an ALD system working directly within an FTIR spectrometer compartment would not need those additional components, would avoid stagnant volumes, and would prevent the mixing of reactive gasses, thus improving the quality of the *in situ* experiments conducted.

In this work, we have designed and built a compact and flexible *in situ* transmission FTIR spectroscopy ALD system, allowing us to detect surface organometallic species from the first reactant half-cycle and map out ligand exchange reactions in the subsequent half-cycles. Our ALD reactor allows direct operation within a Bruker Vertex 80V FTIR spectrometer. In theory, it can be flanged to any characterization apparatus with a straight optical beam path, if the sample compartment is large enough to contain the reactor. Apart from the versatility of this design, it avoids intensity losses along the beam path due to the complexity of the optical setup.[14,20] We propose the use of a double-sided polished potassium bromide (KBr) window coated with a thin sputtered silicon oxide film for ALD nucleation studies, reducing absorption losses while maintaining the surface chemistry under study. A novel sample heater design for transmission studies allows uniform heating across the sample surface, reducing cold spots, precursor condensation, and subsequent desorption. We focus on the rigorous separation of reaction and characterization steps to ensure an ALD process that is close to *ex situ* conditions. We utilize KBr windows as optical access ports for the IR beam together with gate valves. An Argon shield mechanism is proposed for protecting the windows from chemical alterations during the absorption measurements. Gate valves seal the reaction chamber entirely during the deposition process.

The remainder of this paper is structured as follows: first, we describe the reactor, manifold, sample holder, vacuum accessories, and the control system designed for running the ALD process. Then, we discuss the integration of the ALD reactor with the FTIR system and the selection of the IR detector and substrate. Next, we present growth-per-cycle (GPC) studies performed within the *in situ* ALD-FTIR tool, which constitutes a standard test in ALD, but one in that *in situ* spectroscopy systems are not routinely subjected to Refs. 14, 21, and 22, to the best of our knowledge. Finally, we test the *in situ* capability of the ALD reactor by tracking the ligand exchange reaction for the growth of Al_2O_3.

II. SYSTEM DESIGN

A. Reaction chamber

The ALD reactor resembles a T shape, as shown in Fig. 1(a), with three flanges CF-40 (ConFlat) type welded directly on the center T-piece, the center flange (R-3) is used for mounting the sample holder, and the other two flanges, R-1 and R-2, are used for optical diagnostic. The reactor body is made of SS 304. Precursor gasses are introduced into the reactor through an inlet port, positioned on the front side of the reactor, in the form of a welded tube with a Swagelok Vacuum Coupling Radiation (VCR) fitting. The outlet or the exhaust is positioned at the top. The reactor is designed to be compact with a small reactor volume, aiding in efficient precursor delivery and purging of the reactor. The reactor walls are heated with electrical heating tapes.

A CF (ConFlat) to KF (Quick Flange) adapter is placed between the reactor body and the sample holder. The optical diagnostic flanges (R-1 and R-2) are assembled with the gate valve, optical flange, and a polypropylene cap for the IR beam to pass through. The final vacuum component on the beam bath is an optical flange (DN40) (Thorlabs) with KBr windows Ø1″ (Merck), which provides a clear aperture of Ø0.7125″. A temperature-resistant polypropylene cap is mounted between the optical flange and the FTIR

Published under an exclusive license by AIP Publishing

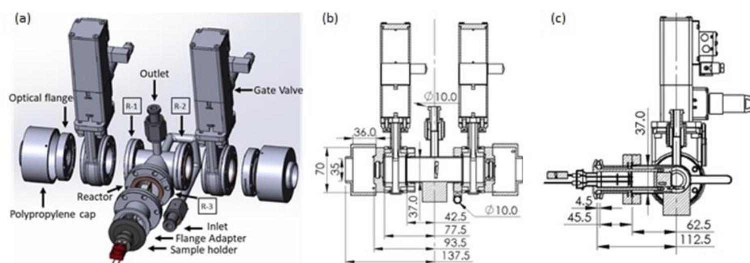

FIG. 1. (a) 3D representation of the *in situ* ALD reactor, (b) front-view cross-sectional diagram of the ALD reactor (dimensions in mm), and (c) side-view cross-sectional diagram of the ALD reactor.

system, which is continuously purged during the FTIR measurement to avoid the atmospheric effect. The cross-sectional diagrams, Figs. 1(b) and 1(c), describe the design and the position of different reactor components and sample holders.

B. Manifold

The manifold of the ALD system is designed (Fig. 2) using stainless steel VCR components from Swagelok. The compact design of the manifold facilitates portability and offers the possibility of modifications based on process needs. Pneumatic controlled diaphragm valves (6LVV-ALD3TFR4-P-C, Swagelok) with normally closed actuation are used for pulsing the precursors and are, in the following, referred to as ALD valves. A mass flow controller (MFC) from Alicat scientific controls the introduction of the carrier gas into the system. The manifold, inlet, and outlet are all heated using electrical heating tapes (Omega Engineering).

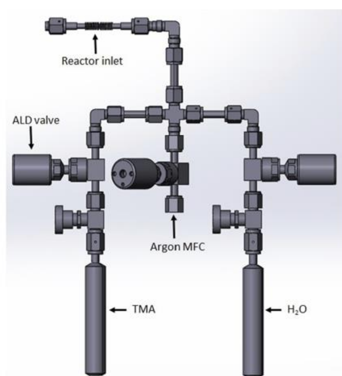

FIG. 2. 3D representation of the manifold design with the ALD valves and precursor cylinders.

C. Sample holder

The sample holder assembly (Fig. 3) is built around a type J KF 40 thermocouple feedthrough TFT1JY2C308B (Kurt J. Lesker). It consists of a ceramic holder, a ceramic heater, and Stainless steel (SS) sample holder. In our preliminary experiments, we found that a type J thermocouple works better under vacuum and at high temperatures when compared to type K and type N thermocouples; the latter two are sensitive to vacuum and reducing conditions. In addition, when under high temperature and vacuum for extended periods of time, the vaporization of chrome is possible in type K and type N thermocouples, resulting in inaccurate measurements.[23]

The sample holder is heated using a $20 \times 20 \times 2.5$ mm^3 advanced ceramic heater (Ultramic 600, Watlow) with a power rating of 200 W. The ceramic heater is mounted on a specially designed ceramic holder, giving it a stable and rigid surface. The SS sample holder is placed above the heater, and it is designed to provide homogeneous sample heating, with a hole drilled in the center to allow the infrared light beam to pass through. Finally, the sample under study is mounted with the help of SEM clips (Ted Pella) on the sample holder.

D. Sample heating

We used the Solidworks simulation package to assess the heat distribution on the sample. The in-built thermocouple inside the ceramic heater is of type k. To avoid the measurement error discussed in Sec. II C, a type J thermocouple is positioned on top of the stainless steel sample holder. The sample holder surface in contact with the thermocouple is defined as the heat source, which is set at 220°C. The thermal resistance between the KBr substrate and the SS 316 sample holder has assumed at 0.006° K/W.[24]

Published under an exclusive license by AIP Publishing

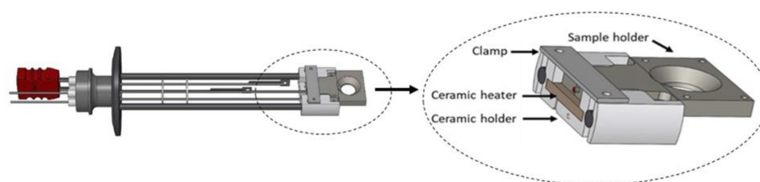

FIG. 3. 3D representation of sample holder assembly.

The thermal simulations show that the variation in thermal contact resistance from 0.006 to 60° K/W does not result in non-uniform temperature distribution on the sample, indicating that the thermal contact resistance does not affect the temperature distribution in steady-state conditions. Here, we considered that the heat loss from the KBr substrate and the sample holder is due to the radiation from the reactor walls. To account for this, the thermal emissivity is set to 0.65 for the SS holder and 0.85 for the polished transparent KBr substrate.[25] The design of the sample holder is illustrated by a drawing in Fig. 4(a). From the simulated results [Fig. 4(b)], it is found that the heat distribution on the KBr substrate is uniform, with only 3°C temperature variation on the sample holder. This was confirmed by physical measurements conducted using a thermocouple in contact with the sample holder's surface.

E. Vacuum system

An RV5 rotary vane vacuum pump (Edwards) was installed and attained an ultimate pressure of 6 mTorr. A molecular sieve trap with zeolite particles (Kurt J. Lesker) was mounted to the exhaust line to remove the hydrocarbons, water vapor, and other gases from the outlet gas stream. The vacuum measurements were conducted using a Pirani gauge (PT R26951, Pfeiffer vacuum). For the protection of the pressure gauge during the reactant pulse, an ALD valve was mounted between the reactor and the pressure gauge.

A "rate of rise" test was conducted to determine the reactor's integrity. When the system attained the base pressure, the exhaust valve was closed, and the rate of rise was measured at 3 min.. The rate of rise corresponds to the increase in the pressure and should be less than 20 mTorr/min. For our system, the rate of rise was less than 10 mTorr/min.

We introduced the Hi-pace 300P turbopump (Pfeiffer vacuum) to further improve the system evacuation without long purge steps.

F. Software and electronics

In this section, we describe the control of the ALD valves in the system. The control system is based on Arduino Mega 2560 Rev.3, combined with a MOSFET shield (Baked Distributions). In addition, a PC running a custom-developed Python (version 3) based software ensures communication and control of the Arduino.

The Arduino is connected to and powered by a PC, offering a simple integration of 12 N-channel MOSFETs (NXP PSMN3R4 -30PL) to the Arduino's logic ports. The individual MOSFETs are

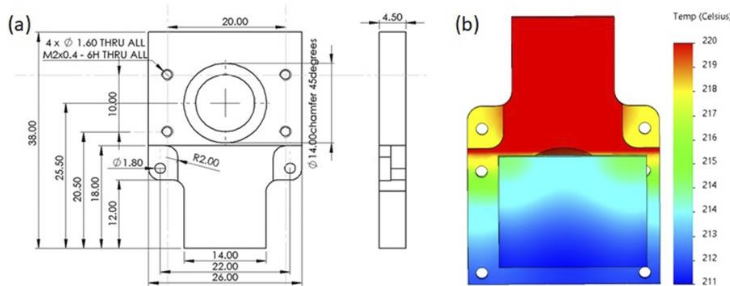

FIG. 4. (a) Drawing of the sample holder (dimensions in mm). (b) Thermal simulation of the heat distribution on the sample.

Published under an exclusive license by AIP Publishing

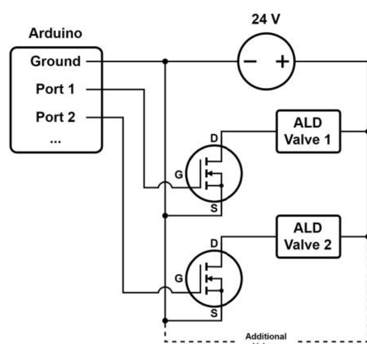

FIG. 5. Schematic of electrical circuit diagram of the ALD control system.

connected to a power supply (Mean Well EDR-120-24 5A 120 W) and 24 V solenoid valves. The solenoid valves (MAC 34 series) actuate the pneumatic ALD valves. The electrical circuit diagram is presented in Fig. 5. Systematic valve control is achieved using the self-developed PC software, enabling users to load, edit, and execute ALD recipes. The software's user interface is designed using Dash by Plotly and Dash DAQ.

III. METHODS

A. FTIR Spectroscopy

FTIR spectroscopy was performed with the Bruker Vertex 80V spectrometer. The spectroscopy data were obtained from 400 to 4000 cm^{-1} at a resolution of 4 cm^{-1} with an average of 200 scans for all the measured spectra. The schematic in Fig. 6(a) describes the positioning of different components and the integration of the ALD and FTIR systems. The ALD system was placed inside the sample compartment volume of the spectrometer. The reactor was designed with limited space availability, while provisions were made for the reactor outlet and inlet to reduce interference with the spectrometer. The IR from the spectrometer was aligned to pass through the center of the sample holder, and the sample was placed normal to the IR beam path [Fig. 6(b)].

The absorbance value was calculated based on the relation, absorbance = $-\log_{10}(I_{sample}/I_{reference})$, where I_{sample} and $I_{reference}$ are the IR intensities of transmitted radiation with and without sample, respectively. Vertical offset has been applied when multiple absorbance curves are illustrated in a single figure.

B. N_2 purge of the beam path

For standard spectroscopic techniques, such as UV–Vis and FTIR, samples are enclosed in the compartment, and the measurements are conducted under vacuum. The evacuation of the optics helps to remove impacts of water vapor and CO_2 on the absorption spectrum. However, mounting the ALD reactor inside the sample compartment necessitates the maintenance of access to the inlet/outlet components of the reactor, and the gate valves thereby limiting the isolation possibilities inside the compartment. Thus, to avoid atmospheric effects, we continuously purge the beam path between the KBr windows and the IR detector/source with N_2. To facilitate this, we machined custom polypropylene caps, fitting exactly in the gap between the gate valve and the FTIR windows. When employing another characterization system or another instrument, the only modification required for integrating the ALD system is the size of the polypropylene caps.

The effect of the N_2 purge of the beam path on the absorbance spectra was measured (supplementary material: Fig. 10). The atmosphere's absorption spectrum was visible in the form of multiple rotationally resolved vibrational absorption peaks. The multiple peaks in the range of 1400–1800 cm^{-1} and from 3600–3800 cm^{-1} are assigned to the bending and stretching modes of the H_2O molecules,

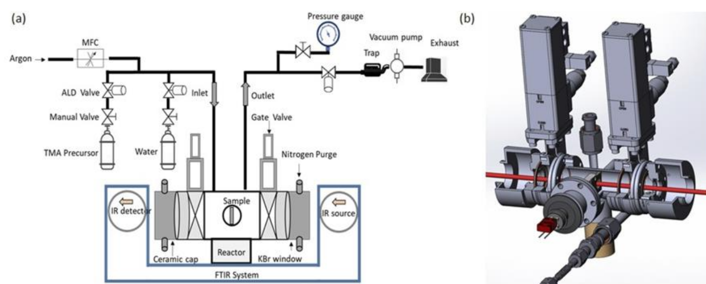

FIG. 6. (a) Schematic of the ALD system integrated with the FTIR spectrometer and (b) 3D representation of the spectrometer and the ALD reactor.

Published under an exclusive license by AIP Publishing

respectively, with rotational fine structure characteristic of gas-phase spectra. The strong absorption peak around 2400 cm^{-1} is assigned to the antisymmetric stretching mode of CO_2. With N_2 purging of the polymeric caps, a flat line in absorption spectra was obtained (supplementary material: Fig. 10), indicating the successful removal of the atmospheric gasses from the beam path.

C. *In situ* ALD-FTIR process

The quality of the *in situ* FTIR absorption measurements in our ALD reactor was verified using the Al_2O_3 ALD process with trimethylaluminum (TMA) and H_2O. These reactants were selected due to their extensively studied reaction mechanism. The manifold, inlet line, and the reactor were heated to 115, 130, and 160 °C, respectively. The sample holder was set at 200 °C. The outlet and exhaust were maintained at 130 and 120 °C, respectively.

With the vacuum system in operation using the Edwards RV5 pump, the ALD system attained a base pressure of 30 mTorr without introducing any gas. High purity argon (5.0) gas was used as a carrier gas, and for purging of unreacted precursor during the ALD process, the flow rate was set at 10 SCCM using an MFC. For the *in situ* ALD study of Al_2O_3, the TMA precursor was pulsed for 0.5 s ten times to ensure complete surface saturation, followed by the FTIR measurement. Subsequently, water was pulsed for 0.1 s ten times, followed by the measurement. Between the reactant pulse and FTIR absorbance measurement, the reactor was purged with Ar gas for 100 s to avoid cross-contamination of surfaces in the beam path.

D. Spectroscopic ellipsometry

The thickness of the ALD Al_2O_3 thin films on the Si substrate was measured using a Woollam M2000 ellipsometer. The angle of incidence of the beam was fixed at an angle of 65°. The thickness was extracted with the optical layer stack (OLS) technique using completeEASE software provided by the same company. The Cauchy dispersion equation achieved a good fit of the ellipsometric data. The optical parameters and absorption coefficient of different materials are selected from the in-built library of the software.

IV. RESULTS AND DISCUSSION

A. Process optimization: ALD of Al_2O_3

Our *in situ* ALD system is designed to minimize the effects of commonplace design constraints.[21] System components are adequately heated, inlet and outlet lines are short, sample positioning is more straightforward, and the purge requirement is minimal. All these improvements contribute to growth behavior that is close to ideal. Ideally, the *in situ* ALD system should have similar conditions to a conventional reactor. Consequently, the relationship between the ALD process parameters and thin-film properties in the *in situ* system can be directly transferred to the conventional industrial system. Here, we investigate the growth of Al_2O_3 and adapt our instrument and process to achieve model growth behavior.

To study the ALD growth behavior in our system, we deposited Al_2O_3 on a Si substrate at 200 °C, keeping the gate valves closed. The TMA precursor and H_2O were pulsed for 25 and 20 ms, respectively. The purge time for each pulse was set at 70 s.

Multiple thickness measurements at various points on the sample were conducted using the ellipsometer; the deposition was found to be spatially uniform, with a deviation of ±0.1 nm. The ALD growth of Al_2O_3 with the number of cycles is shown in Fig. 7. The growth rate showed approximately linear behavior, with an average growth rate of 2.2 Å/cycle.

This is higher than the typical growth rate for Al_2O_3, which is in the range of 1.1–1.3 Å/cycle.[26] However, Al_2O_3 growth rates as high as 2.84 Å/cycle have been observed before.[27] Listed causes are the presence of water molecules in the reactor and other internal surfaces due to inadequate purging, causing CVD-like growth.[28] Another explanation for the high growth rate can be linked to TMA under-dosing conditions.[27]

We increased the TMA pulse from 25 to 50 ms and reduced the H_2O pulse from 20 to 10 ms. As a result, the growth rate decreased from 2.2 to 1.69 Å/cycle. Theoretical study on Al_2O_3 GPC[29] showed that the growth range could be between 0.75 and 1.79 Å/cycle, depending on the surface OH concentration, which may indicate that our process has stabilized within the ALD window, yet, with an unusually high GPC. This led us to investigate the process conditions further.

We followed a published protocol to systematically eliminate causes for higher GPCs and non-uniformity outside the ALD window.[30] All the vacuum components were heated to the necessary temperature, depending on the precursor requirement (TMA and H_2O in this case). Cold spots were systematically eliminated in the vacuum components. The purge time was increased to circumvent the chemical crosstalk between the half cycles.

Finally, to improve evacuation, we introduced a turbopump, leading to a GPC of 1.2–1.25 Å/cycle, similar to what is typically reported for this process.[26] Transmission spectroscopy-based *in situ* ALD setups must provide unrestricted optical access to both sides of the sample's surface, and many, often-conflicting design requirements must be balanced. This certainly increases the complexity of the reaction chamber and the manifold, leading to a relatively large volume needing purging. Furthermore, intricate zones not subjected to the main purge gas flow (such as the compartment housing optical windows) may necessitate pumps, allowing lower base pressure for a complete evacuation. Our system is compact with respect to reported *in situ* spectroscopy systems. Manifold inlets and evacuation outlets are placed in proximity to the sample. One can argue

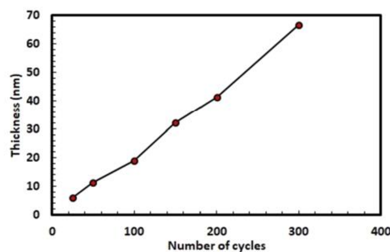

FIG. 7. Al_2O_3 growth with the number of cycles.

that reported purging requirements for conventional *in situ* tools[14] might exceed those reported here.

B. Substrate selection for FTIR studies

The use of single side polished p-type Si wafers as a substrate for the *in situ* ALD study in transmission mode was evaluated. The thickness of the silicon wafer was 279 ± 25 μm. At the Brewster angle, the reflectivity of p-polarized light has a characteristic minimum, thus minimizing reflection losses in transmission geometry, ensuring a well-defined polarization of both reflected and transmitted beam, and increasing sensitivity to absorption from adsorbed species. Our *ex situ* FTIR experiments revealed that for a p-type Si (resistivity: 1–10 Ω cm and crystal orientation: ⟨100⟩ ± 1°) at normal incidence and Brewster angle (Fig. 8), the absorbance of the observed peaks was similar. The two prominent peaks at ~1100 and ~610 cm^{-1} are typically observed in the absorption spectra of silicon.[31,32] Because of its refractive index of ~3.4,[33] reflection losses of ~40% are expected for transmission through silicon, resulting in significantly lower intensity throughput. In addition, free carrier absorption may contribute at sufficiently low wavenumbers.

The use of a material with a lower refractive index minimizes reflection losses. To that end, the IR transparent KBr was used, which has a refractive index of ~1.5[33] in the IR light. Consequently, the reflection loss is minimized to ~10% at normal incidence.[33]

A computational study was conducted (supplementary material) to evaluate the angle dependence of transmission on Si and KBr substrates. Compared to silicon, the use of KBr as a substrate increases the transmission of light and enhances the signal from the absorbance of a thin interfacial layer, here modeled with a dielectric function of a harmonic (Lorentzian) oscillator. With the expected higher signal-to-noise ratio, we argue that KBr as a substrate is attractive for spectroscopic studies in transmission geometry. While the Brewster angle has special significance in reflection experiments, both transmission and absorbance from isotropic thin layers do not show singularities at or around the Brewster angle. As the polarization of the transmitted beam changes at the Brewster angle, the situation becomes more involved for optically anisotropic systems, which have not been investigated here.

C. Effect of inert gas flow during the FTIR measurements

During *in situ* FTIR absorption measurements, it was found that a continuous flow of inert gas (in our case, Ar gas) through the ALD reaction chamber is essential. Discontinuing the inert gas flow after the reactor purge or during the FTIR absorption measurements revealed contamination of the KBr sample surface under study. With no inert gas flowing and without introducing any precursor, absorption peaks were observed in the region 2800–3000 cm^{-1}, as illustrated in Fig. 9. The increased absorption may be attributed to the backflow of unreacted precursors or the desorption from the outlet of the reactor. With a continuous flow of Ar gas, a stable absorption spectrum is observed with only a low amount of surface contamination.

D. Window protection

Introducing the precursor pulse into the reactor without covering the windows will result in condensation of the precursor molecules, thus contaminating the window surface. Although this shortcoming can be partly resolved by conducting a background measurement immediately before each pulse,[16] the measured absorption spectrum can still be misleading, as it will also consider the formation and removal of molecules on the window's surface. In addition, the reaction mechanism will be different when the window and the substrate are at different temperatures.

For the *in situ* ALD spectroscopic studies, the experiments are based on tracking changes in the absorption spectra, and any significant contamination produces erroneous data that will be difficult to analyze. Thus, different strategies have to be implemented to minimize window contamination. The first and the most critical step to protect the windows is installing pneumatically controlled gate valves on the reactor. The gate valves are closed during the precursor and oxidant pulse, thus providing window protection. The second step is reactor purging; it was found that evacuation for at least 100 s

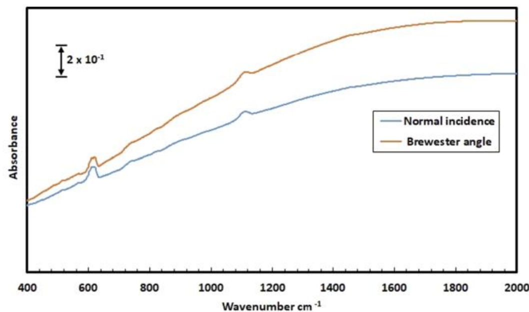

FIG. 8. Absorbance spectra for Si at normal incidence vs at Brewster angle with no sample as background.

Published under an exclusive license by AIP Publishing

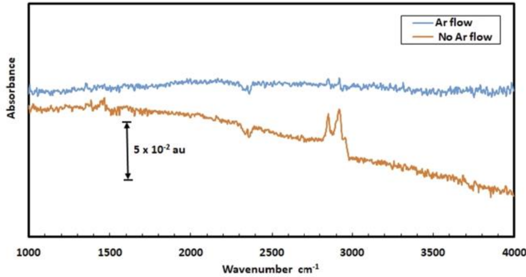

FIG. 9. Absorbance spectra for studying the effect of Ar flow on contamination of KBr substrate (KBr sample as background for no Ar flow and the same measurement as a background for the subsequent Ar flow condition).

after the reactant pulse and prior to opening the gate valves is necessary to protect the windows from contamination through residual gasses; even longer purge times are essential for systems that have a large volume and narrow tubing. Third, all the vacuum components must be heated to avoid any cold spots, as they could lead to the desorption of molecules, thereby contaminating the windows and causing the ALD processes to shift outside of the self-limiting regime.[34]

To characterize contaminations, we conducted a simple experiment. Figure 10 shows differential absorption spectra after the TMA pulse on a pristine Si substrate followed by an H_2O pulse. The FTIR data for the half cycles are presented in the form of differential absorption spectra, i.e., each spectrum is referenced to the previous measurement. Positive peaks represent species that have adsorbed in the current step, while negative peaks are caused by the removal of species present in the reference.

After a TMA pulse (Fig. 10, bottom), the spectrum contains absorption peaks of gaseous CH_4 with maximum absorbance at 1306 and 3016 cm^{-1},[35] the latter with the visible rotational and vibrational lines. As there are no negative peaks from methane in the spectra after the H_2O pulses, we infer that the CH_4 remains present in the gas phase. All spectra, especially the spectrum after the first water pulse, contain contributions from CO_2 (antisymmetric stretching mode in the region 2328–2368 cm^{-1} [35]) and water vapor (bending mode in the region 1620–1680 cm^{-1} and stretching mode in the region 3500–3800 cm^{-1} [36]). Since the CO_2 should not have been introduced in the H_2O pulse, these spectral features most likely stem from residual contributions from the surrounding atmosphere, where they are commonly observed. Strong characteristics of the observed contamination in a different part of the reactor are the peaks at ~2927 and ~1465 cm^{-1}, which can be assigned to CH stretching and bending modes, respectively.[37] The absence of the rotational bands verifies the condensed phase nature of these species. Absorbance from these contaminations does not decrease after the water pulses. Thus, we conclude that adequate system purging and evacuation are critical for window protection.

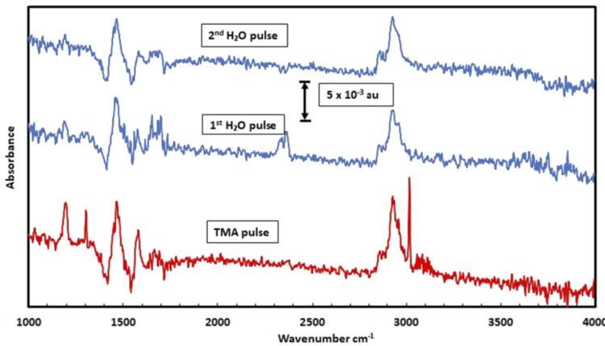

FIG. 10. Absorbance spectra describing contamination of KBr windows after the TMA pulse (KBr substrate as background) followed by first and second water pulse (TMA pulse measurement as background). The absorption measurements are conducted after a 20 s purge.

Published under an exclusive license by AIP Publishing

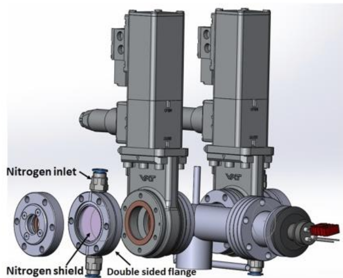

FIG. 11. 3D representation of Argon shield for window protection.

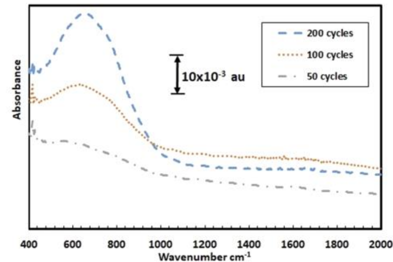

FIG. 12. Comparison of absorbance spectra for 50, 100, and 200 cycles of ALD Al_2O_3 on KBr substrate using DTGS with KBr substrate as background.

Even with great care in the purging steps, it is challenging to avoid window contamination in the long run, as there can be desorption from the walls of the manifold, inlet, and reactor. In addition, there is a high probability that windows are, to some extent, contaminated owing to surface condensation due to lower surface temperatures. To avoid cross-contamination during ALD half cycles, we propose the introduction of the N_2 shielding gas (or similar inert gas) using a double-sided flange mounted between the gate valve and the window flange (Fig. 11). The stream of nitrogen introduced from two sides creates a gas barrier in front of the window, restricting contamination (as used for protecting the interior of transfer chambers or for protecting windows for ellipsometry measurements in existing systems).[38] Furthermore, introducing a turbopump enhances the protection performance of the system. Turbopumps can create a high vacuum, reducing the likelihood of contamination from residual gasses.

E. Detector for FTIR spectroscopy measurements

The two commonly used detectors for FTIR spectroscopy are MCT and deuterated L-alanine doped triglycine sulfate (DTGS). The MCT detector has a faster response time than the DTGS, which is advantageous for samples that change rapidly over a short time. It also has a higher sensitivity, making it useful for applications with low light intensity and weak absorption signals. However, a challenge can be detecting OH-related modes because of the condensation of traces of ice on the detector windows and the associated observation of ice peaks. Furthermore, the MCT baseline often drifts over time. Most MCT detectors are limited to a minimum wavenumber of 600 cm^{-1}, depending on their material composition.

On the other hand, wavenumbers far down to the far-IR can only be detected using a DTGS detector. Measuring the absorption at lower wavenumbers allows us to detect vibrational bands and coordination bonds in metal complexes,[39,40] which is beneficial in ALD studies as for example, in the deposition of metallic films, which currently receives increasing interest. In this case, the optical window materials often limit the available spectral range; with the KBr windows used here, one is typically limited to a spectral range above ~350 cm^{-1}.

Due to the high sensitivity requirements partly due to optical losses, most *in situ* ALD FTIR work reported earlier used the MCT detector,[41] limiting the lower wavenumber to around 600 cm^{-1}. However, MCT detectors come in a wide composition range of Hg doping of the CdTe, giving different responses. Commercially, narrowband MCT detectors have a higher sensitivity and lower spectra window. Thus, the wave number 600 cm^{-1} is not the absolute limit of MCT. On the other hand, the wide bandgap DTGS detector, which we have in our system, can measure down to 30–50 cm^{-1}, using KBr in the beam path limits the spectral range to 400 cm^{-1}. In this work, we want to determine and evaluate our *in situ* system's capability to capture weak signals below 600 cm^{-1} by tracking the chemistry during Al_2O_3 ALD half-cycles using the DTGS detector with higher stability and lower drift than MCTs.[42]

From the point of view of optical throughput, the choice of the same material, both as window and substrate, is beneficial. Generally, higher S/N ratios as enabled by our substrate choice using KBr

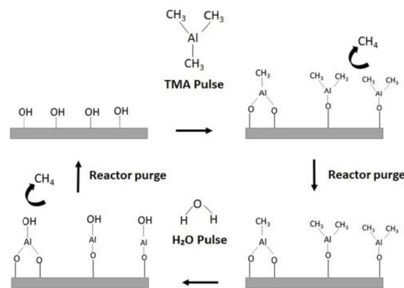

FIG. 13. Schematic representation of the chemistry involved in the cyclic ALD process of Al_2O_3 using TMA and H_2O.

Published under an exclusive license by AIP Publishing

and the opportunity to use both in-built detectors inside the system without needing an external optical beam path allowed us to perform a comparative study, all other factors than the detector being equal. First, *ex situ* measurements were conducted for 50, 100, and 200 cycles of ALD Al_2O_3 deposited on the KBr Substrate with 5 nm Si deposited on one of its sides. The thickness of the Al_2O_3 thin film was ~6, 12, and 24 nm, respectively. The sample was positioned normal to the IR beam. A clear broad absorption band was observed centered at 680 cm^{-1} for the 100 and 200 cycles of Al_2O_3 using a DTGS detector, but a weak shoulder was observed for the 50 cycles process (Fig. 12). This absorption is in the region of the TO phonon of gamma-Al_2O_3.[43] In contrast, with the MCT detector, there was a sharp cut-off in the absorption spectrum around 600 cm^{-1}.

F. *In situ* FTIR Spectra of ALD Al_2O_3 on SiO_2/KBr substrate

The growth mechanism and surface chemistry of ALD-grown Al_2O_3 have been widely studied using IR absorption spectroscopy.[44] Thus, Al_2O_3 growth chemistry allows us to better understand and validate the design and performance of our *in situ* ALD system. The ALD Al_2O_3 growth on –OH terminated SiO_2/Si substrate mainly involves –CH_3 and –OH groups. The chemistry can be illustrated by a schematic, as Fig. 13. The ALD cycle starts with an –OH terminated surface. In the first half-cycle, TMA vapor is pulsed in a controlled way to chemisorb the –OH groups present on the surface. TMA presence initiates a ligand exchange reaction, where the metal

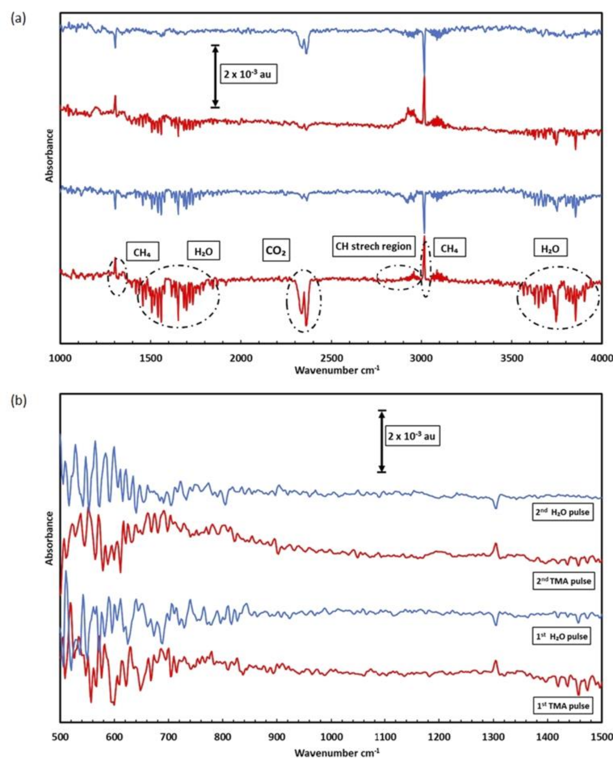

FIG. 14. (a) Absorbance spectra (1000–4000 cm^{-1}) after first, second TMA, and water pulse, respectively, with 5 nm Si/KBr substrate as background for first TMA pulse measurement. Previous measurements are the background for the remaining subsequent measurements. (b) Absorbance spectra (500–1500 cm^{-1}).

component of the precursor attaches with oxygen and simultaneously forms a $–CH_3$ terminated surface. This results in the formation of gas-phase CH_4 molecules as a reaction product. This is followed by a system purge using inert gas to remove the unreacted precursor and reaction by-products, which gives the ALD process its characteristic self-limiting behavior. The second half-cycle consists of an H_2O vapor pulse, which reacts with the $–CH_3$ terminated surface initiating a ligand exchange reaction that results in the formation of an –OH terminated surface. This is then followed by a similar inert gas purge of the reactor as the first half-cycle. The reactions are summarized below in equation form,

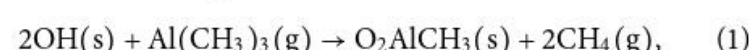

$$2OH(s) + Al(CH_3)_3(g) \rightarrow O_2AlCH_3(s) + 2CH_4(g), \quad (1)$$

$$AlCH_3(s) + H_2O(g) \rightarrow AlOH(s) + CH_4(g). \quad (2)$$

Finally, *in situ* FTIR experiments were conducted to track the reaction mechanism. After the first TMA pulse, also defined as the first half-cycle, positive peaks are observed at 3016 and 1306 cm^{-1} [Fig. 14(a)]. These peaks indicate the presence of gas-phase CH_4, formed as a reaction product during the $Al(CH_3)_3$ (TMA) adsorption half cycle. This behavior has been reported before,[20] where excess TMA precursor was used, and a gas phase IR spectrum was measured with the exhaust valve closed. However, in the absorption spectrum, the rotational–vibrational fine structure of the CH_4 spectrum makes an interpretation of the spectral region with the CH stretching modes (2800–3000 cm^{-1}) of adsorbed methyl groups difficult.

In the subsequent H_2O pulse, the peaks flip at the same position, indicating the molecular species removal. Again, with the second TMA pulse, we see the formation of peaks, and their removal with the next H_2O pulse, thus confirming the cyclic ALD process.[45] The negative peaks are seen from 1400–1800 cm^{-1} and 3500–3900 cm^{-1} after the first TMA pulse, explaining the presence of a rotationally resolved vibrational spectrum of water vapor. The presence of the peaks from CO_2 (2300–2400 cm^{-1}) lets us a reason that at least part of the water vapor contribution originated from residual atmospheric gases in the beam path and slight partial pressure differences between sample and reference measurements.

Low wavenumber absorbance spectra from 500 cm^{-1} are presented in Fig. 14(b). Although the data were measurable, no relevant information was obtained in this case; this could be due to insufficient Al_2O_3. The absorption band in this range could be more distinct with a certain minimum number of cycles, as seen in Fig. 12.

V. CONCLUSION

We present a set of tools and insights for enabling *in situ* ALD-FTIR spectroscopy studies inside an existing characterization instrument. Here, we demonstrate a mechanical design suitable for most conventional spectroscopy compartments and validated inside a Bruker Vertex 80 FTIR spectrometer. Most of our electronic equipment, vacuum components, and electric heaters were off-the-shelf components. However, the substrate was uniformly heated using a specially designed sample holder. This gives us the advantage of using a 4 mm thick KBr disk with sputtered 5 nm Si as a substrate, which increases the IR transmissivity compared to a conventional p-doped Si wafer. In addition, we present insights on the importance of purging and proper vacuum base level to establish self-limiting ALD conditions suitable for investigating the chemistry during nucleation. The reactor windows were successfully shielded from cross-contamination by pneumatic gate valves, uniform reactor heating, and an extended Argon purge of the system. Further protection for the windows and reduced purge time could be achieved by implementing an Argon window shield and installing a turbopump. We compare MCT vs DTGS detectors with *ex situ* studies and portray how respective studies can be instrumental in investigating metal complexes during the early stages of ALD nucleation. Finally, we successfully tracked the ligand exchange reaction for the ALD growth of Al_2O_3 using an FTIR spectrometer, demonstrating the system's capability to conduct *in situ* studies.

SUPPLEMENTARY MATERIAL

See the supplementary material for a computational study comparing angle-dependent optical properties of KBr and Si substrates.

ACKNOWLEDGMENTS

Abdulla Bin Afif was supported by NTNU's Enabling technologies: Nanotechnology. The Research Council of Norway (Norges Forskningsråd) is acknowledged for its support under Project No. 274459, Trånslate, and the Norwegian Micro-and Nano-Fabrication Facility, NorFab, under Project No. 245963/F50. The Norwegian Center for International Cooperation in Education is acknowledged for the funds under Project No. PNA-2017/10077.

The authors acknowledge the help of Hans Olav Vaa and Juan Paulino Perez during this work.

The authors acknowledge the Nanoscale Prototyping Laboratory (NPL) at Stanford University for all the help and support in constructing this system. For the first iterations of the reactor design, Professor Fritz Prinz at Stanford University was instrumental in guidance and support. Stanford employees, colleagues, and friends including Francisco De La Paz, Karen Kim, and Julia Torgersen helped in their free time to assemble parts of the ALD reactor.

AUTHOR DECLARATIONS

Conflict of Interest

The authors have no conflicts to disclose.

Author Contributions

Abdulla Bin Afif: Conceptualization (lead); Data curation (lead); Formal analysis (lead); Investigation (lead); Methodology (lead); Resources (equal); Validation (lead); Writing – original draft (lead); Writing – review & editing (lead). **Anup L Dadlani**: Conceptualization (equal); Formal analysis (supporting); Investigation (supporting); Methodology (supporting); Writing – original draft (supporting); Writing – review & editing (supporting). **Andreas Flaten**: Formal analysis (supporting); Investigation (supporting); Software (lead); Writing – original draft (supporting); Writing – review & editing (supporting). **Markus Joakim Lid**: Investigation (supporting); Writing – review & editing (supporting). **Johannes Ofstad**:

Formal analysis (supporting); Investigation (supporting); Resources (supporting); Writing – review & editing (supporting). **Andreas Erbe**: Data curation (supporting); Formal analysis (supporting); Investigation (supporting); Methodology (supporting); Software (supporting); Supervision (supporting); Validation (supporting); Writing – original draft (supporting); Writing – review & editing (supporting). **Peter Köllensperger**: Investigation (supporting); Project administration (supporting); Resources (supporting); Supervision (supporting). **Jan Torgersen**: Conceptualization (lead); Data curation (lead); Formal analysis (equal); Funding acquisition (lead); Investigation (lead); Methodology (lead); Project administration (lead); Resources (lead); Supervision (lead); Writing – review & editing (lead).

DATA AVAILABILITY

The data that support the findings of this study are available from the corresponding author upon reasonable request.

REFERENCES

[1] R. W. Johnson, A. Hultqvist, and S. F. Bent, "A brief review of atomic layer deposition: From fundamentals to applications," Mater. Today **17**(5), 236–246 (2014).

[2] J. Zhang, G. Zhang, Z. Chen, H. Dai, Q. Hu, S. Liao, and S. Sun, "Emerging applications of atomic layer deposition for lithium-sulfur and sodium-sulfur batteries," Energy Storage Mater. **26**, 513–533 (2020).

[3] S. M. George, "Atomic layer deposition: An overview," Chem. Rev. **110**(1), 111–131 (2010).

[4] O. Sneh, R. B. Clark-Phelps, A. R. Londergan, J. Winkler, and T. E. Seidel, "Thin film atomic layer deposition equipment for semiconductor processing," Thin Solid Films **402**(1–2), 248–261 (2002).

[5] M. Ritala and J. Niinistö, "Industrial applications of atomic layer deposition," ECS Trans. **25**(8), 641–652 (2009).

[6] R. L. Puurunen and W. Vandervorst, "Island growth as a growth mode in atomic layer deposition: A phenomenological model," J. Appl. Phys. **96**(12), 7686–7695 (2004).

[7] P. Schmitt, V. Beladiya, N. Felde, P. Paul, F. Otto, T. Fritz, A. Tünnermann, and A. V. Szeghalmi, "Influence of substrate materials on nucleation and properties of iridium thin films grown by ALD," Coatings **11**(2), 173 (2021).

[8] R. L. Puurunen, "Growth per cycle in atomic layer deposition: A theoretical model," Chem. Vap. Deposition **9**(5), 249–257 (2003).

[9] M. Ylilammi, "Monolayer thickness in atomic layer deposition," Thin Solid Films **279**(1–2), 124–130 (1996).

[10] L. Hu, W. Qi, and Y. Li, "Coating strategies for atomic layer deposition," Nanotechnol. Rev. **6**(6), 527–547 (2017).

[11] P. G. Gordon, A. Kurek, and S. T. Barry, "Trends in copper precursor development for CVD and ALD applications," ECS J. Solid State Sci. Technol. **4**(1), N3188 (2014).

[12] Y. Wang, M. Dai, S. Rivillon, M.-T. Ho, and Y. J. Chabal, "In situ infrared absorption spectroscopy for thin film growth by atomic layer deposition," Proc. SPIE 6325, 36–46 (2006)

[13] Y. Y. Wu and M. Eizenberg, "FTIR and ellipsometry characterization of ultrathin ALD TaN films," Mater. Chem. Phys. **101**(2–3), 269–275 (2007).

[14] J. Kwon, M. Dai, M. D. Halls, E. Langereis, Y. J. Chabal, and R. G. Gordon, "In situ infrared characterization during atomic layer deposition of lanthanum oxide," J. Phys. Chem. C **113**(2), 654–660 (2009).

[15] A. W. Ott, J. W. Klaus, J. M. Johnson, and S. M. George, "Al_3O_3 thin film growth on Si(100) using binary reaction sequence chemistry," Thin Solid Films **292**(1–2), 135–144 (1997).

[16] V. R. Rai, V. Vandalon, and S. Agarwal, "Influence of surface temperature on the mechanism of atomic layer deposition of aluminum oxide using an oxygen plasma and ozone," Langmuir **28**(1), 350–357 (2012).

[17] M. Van Daele, C. Detavernier, and J. Dendooven, "Surface species during ALD of platinum observed with in situ reflection IR spectroscopy," Phys. Chem. Chem. Phys. **20**(39), 25343–25356 (2018).

[18] D. N. Goldstein, J. A. McCormick, and S. M. George, "Al_2O_3 atomic layer deposition with trimethylaluminum and ozone studied by *in situ* transmission FTIR spectroscopy and quadrupole mass spectrometry," J. Phys. Chem. C **112**(49), 19530–19539 (2008).

[19] M. Dai, J. Kwon, E. Langereis, L. S. Wielunski, Y. Chabal, Z. Li, and R. Gordon, "In-situ FTIR study of atomic layer deposition (ALD) of copper metal films," ECS Trans. **11**(7), 91 (2007).

[20] E. Langereis, M. Bouman, J. Keijmel, S. Heil, M. C. Van de Sanden, and W. M. Kessels, "Plasma-assisted ALD of Al_2O_3 at low temperatures: Reaction mechanisms and material properties," ECS Trans. **16**(4), 247 (2008).

[21] J. E. Maslar, W. S. Hurst, D. R. Burgess, Jr., W. A. Kimes, N. V. Nguyen, and E. F. Moore, "*In situ* monitoring of Hafnium oxide atomic layer deposition," AIP Conf. Proc. **931**(1), 121–125 (2007).

[22] E. Levrau, K. Van De Kerckhove, K. Devloo-Casier, S. Pulinthanathu Sree, J. A. Martens, C. Detavernier, and J. Dendooven, "*In situ* IR spectroscopic investigation of alumina ALD on porous silica films: Thermal versus plasma-enhanced ALD," J. Phys. Chem. C **118**(51), 29854–29859 (2014).

[23] R. M. Park, "Thermocouple fundamentals," *Course Chapter, Temp* (Cleveland, OH, 2010), pp. 1–16.

[24] C. V. Madhusudana and C. V. Madhusudana, *Thermal Contact Conductance* (Springer, 1996).

[25] G. G. Gubareff, J. E. Janssen, and R. H. Torborg, *Thermal Radiation Properties Survey: A Review of the Literature* (Honeywell Research Center Minneapolis, MN, 1960).

[26] M. D. Groner, F. H. Fabreguette, J. W. Elam, and S. M. George, "Low-temperature Al_2O_3 atomic layer deposition," Chem. Mater. **16**(4), 639–645 (2004).

[27] H. Salami, A. Poissant, and R. A. Adomaitis, "Anomalously high alumina atomic layer deposition growth per cycle during trimethylaluminum under-dosing conditions," J. Vac. Sci. Technol., A **35**(1), 01B101 (2017).

[28] L. Henn-Lecordier, M. Anderle, E. Robertson, and G. W. Rubloff, "Impact of parasitic reactions on wafer-scale uniformity in water-based and ozone-based atomic layer deposition," J. Vac. Sci. Technol., A **29**(5), 51509 (2011).

[29] A. Philip, S. Thomas, and K. R. Kumar, "Calculation of growth per cycle (GPC) of atomic layer deposited aluminium oxide nanolayers and dependence of GPC on surface OH concentration," Pramana **82**(3), 563–569 (2014).

[30] K.-E. Elers, T. Blomberg, M. Peussa, B. Aitchison, S. Haukka, and S. Marcus, "Film uniformity in atomic layer deposition," Chem. Vap. Deposition **12**(1), 13–24 (2006).

[31] R. J. Collins and H. Y. Fan, "Infrared lattice absorption bands in germanium, silicon, and diamond," Phys. Rev. **93**(4), 674 (1954).

[32] P. Gupta, V. L. Colvin, and S. M. George, "Hydrogen desorption kinetics from monohydride and dihydride species on silicon surfaces," Phys. Rev. B **37**(14), 8234 (1988).

[33] E. D. Palik, *Handbook of Optical Constants of Solids* (Academic Press, New York, 1998).

[34] H. C. M. Knoops, S. E. Potts, A. A. Bol, and W. M. M. Kessels, "Atomic layer deposition," in*Handbook of Crystal Growth* (Elsevier, 2015). pp. 1101–1134.

[35] NIST, N., Standard reference database 69: NIST chemistry WebBook, Natl. Inst. Stand. Technol. (2010).

[36] A. Erbe, A. Sarfraz, C. Toparli, K. Schwenzfeier, and F. Niu, "Optical absorption spectroscopy at interfaces," in *Soft Matter at Aqueous Interfaces* (Springer, 2016), pp. 459–490.

[37] J. Coates, Interpretation of infrared spectra, a practical approach, 2000.

[38] See https://www.veeco.com/products/savannah-thermal-ald-for-rd for Veeco Savannah ALD system.

Published under an exclusive license by AIP Publishing

[39] D. A. Necefoğlu and H. Necefo lu, "Synthesis and characterization of *bis* (nicotinamide) *m*-hydroxybenzoate complexes of Co(II), Ni(II), Cu(II) and Zn(II)," J. Therm. Anal. Calorim. **93**(2), 509–514 (2008).
[40] A. D. Allen and T. Theophanides, "Platinum(II) complexes: Infrared spectra in the 300–800 cm^{-1} region," Can. J. Chem. **42**(7), 1551–1554 (1964).
[41] V. R. Rai and S. Agarwal, "Surface reaction mechanisms during plasma-assisted atomic layer deposition of titanium dioxide," J. Phys. Chem. C **113**(30), 12962–12965 (2009).
[42] K. D. Kempfert, E. Y. Jiang, and J. C. Sherwin Oas, "Detectors for Fourier transform spectroscopy," Application Note (Thermo Nicolet Company, 2001); available at https://mmrc.caltech.edu/FTIR/Nicolet/Nicolet%20Tech%20Notes/DetectorsforFTIR1204.pdf.
[43] P. Brüesch, R. Kötz, H. Neff, and L. Pietronero, "Vibrational properties of Al 2 O 3 films on gold, aluminum, and silicon," Phys. Rev. B **29**(8), 4691 (1984).
[44] A. C. Dillon, A. W. Ott, J. D. Way, and S. M. George, "Surface chemistry of Al_2O_3 deposition using $Al(CH_3)_3$ and H_2O in a binary reaction sequence," Surf. Sci. **322**(1–3), 230–242 (1995).
[45] D. Choudhury, G. Rajaraman, and S. K. Sarkar, "Comparison on atomic/molecular layer deposition grown aluminum alkoxide polymer films using alkane and alkyne organic precursors," J. Vac. Sci. Technol., A **36**(1), 01A108 (2018).

Published under an exclusive license by AIP Publishing

Supplementary material

A toolbox for easy entry low wavenumber *in situ* ALD transmission FTIR spectroscopy studies

Abdulla Bin Afif [1], Anup L Dadlani [1], Andreas Flaten [1], Markus Joakim Lid [1], Johannes Ofstad [2], Andreas Erbe [2], Peter Köllensperger [3], Jan Torgersen [1]
[1] Department of Industrial and Mechanical Engineering, NTNU, Trondheim, Norway
[2] Department of Materials Science and Engineering, NTNU, Trondheim, Norway
[3] Department of Physics, NTNU, Trondheim, Norway

Overview of optical properties of substrates used (Si and KBr)

1. **Definitions and notations**

- Absorbance *Abs* (here used in relation to transmission experiments) $Abs = -log_{10} (T_{sample} / T_{ref})$; ($T_{sample}$ – transmission through a sample to be investigated; T_{ref} – transmission of the reference; can in the simplest case be blank, then $T_{ref} = 1$)
- In the absence of absorption A and scattering S, energy conversion requires that $R + T = 1$. For scattering and absorption, similar "fraction of scattered / absorbed light" can be defined, so that in total, $R + T + A + S = 1$. We will neglect scattering ($S=0$), and A is very small in our system.
- Reflectance absorbance $RA = -log_{10} (R_{sample} / R_{ref})$; ($R_{sample}$ – reflectivity of a sample to be investigated; R_{ref} – reflectivity of the reference belonging to the sample under investigation)
- Angles of incidence are defined against the surface normal. 0°: Normal incidence (perpendicular to the surface), 90° grazing incidence (parallel to the surface).
- Index s: s-polarisation (perpendicular, vertical);
- Index p: p-polarisation (parallel, horizontal).
- Respective quantities Q for unpolarised light can be obtained by averaging the quantities with s- and p-polarisation, i.e. $Q_{unpol} = (Q_s + Q_p)/2$. In the standard FTIR experiment, light in the sample chamber is always partially polarised because of the pass through the beam splitter.
- Reflectivity (reflectance) $R = I_{refl} / I_0$; (I_{refl} – reflected intensity of light; I_0 – incident intensity); $0 \leq R \leq 1$; "fraction of incoming intensity which is reflected"
- Transmission (transmittance) $T = I_{trans} / I_0$; (I_{trans} – transmitted intensity of light; I_0 – incident intensity); $0 \leq T \leq 1$; "fraction of incoming intensity which is transmitted"
- NB: Calculation results contain transmittances which are not normalized for the illuminated area differences; they need to be multiplied by a factor F ; $F = (n_{exit} \cos \vartheta_{exit}) / (n_{inc} \cos \vartheta_{inc})$; n_{exit} – refractive index of exit medium (Si of KBr), n_{inc} – refractive index of incidence medium (air, $n_{inc} = 1$), ϑ_{inc} – angle of incidence, ϑ_{exit} – angle of propagation in exit medium ; ϑ_{exit} follows from the law of refraction, $n_{inc} \sin \vartheta_{inc} = n_{exit} \sin \vartheta_{exit}$.

2. **Method**

Reflectivities were calculated based on the matrix method by Schubert [1]. Transmission and reflection coefficients were calculated based on the equations given by Yeh [2]. The application of the method to IR spectroscopy is described in more detail in [3], an application to analyze angular dependence of IR spectra is given in [4].

The dependence of the refractive index n and absorption coefficient k of organic layers on wavenumber v has been modelled with the dielectric function of a damped harmonic oscillator with

resonance frequency v_0 [5], $(n + I\ k)^2 = n_{inf}^2 + B / (v_0^2 - v^2 - I\ \gamma\ v)$, were I is the square root of -1. The parameters used here were v_0 = 3000 cm^{-1} (corresponding approximately to CH stretch region), damping parameter (width) γ = 20 cm^{-1}, oscillator strength B = 2000 cm^{-2} ; $n_{inf} = 1.5$ (refractive index far away from the resonance frequency, typical value for an organic substance). These parameters are in an order of magnitude that has been used before to describe CH_2 stretching modes [6] but have not been specifically fitted to describe quantitatively the experiments conducted here.

Except noted otherwise, the analyses have been conducted for light passing once through the interface in question. In the experimentally relevant level of approximation, the double interface case can easily be obtained from these results, as can the important trends.

More information on demand.

3. Silicon

3.1 Optical system

Air – Isotropic oscillator layer (1 nm) – SiO_2 layer (1 nm) – Si

Air: Refractive index 1, which in reality corresponds to vacuum and is thus even closer to the experiment.

Oscillator layer: Damped harmonic oscillator with dielectric function as described in section 2.

SiO_2 layer: Refractive index from https://refractiveindex.info/ based on: I. H. Malitson. [7]; used only single wavelength value for 3.333 µm (corresponds to 3000 cm^{-1}), here 1.4107.

Si: Refractive index from https://refractiveindex.info/ based on [8]; used only single wavelength value for 3.333 µm (corresponds to 3000 cm^{-1}), here 3.4333 .

Dispersion (wavelength-dependence) of refractive indices has been neglected. Both dispersion and use of slightly different literature sources will only slightly modify the numbers, but not modify any of the general conclusions. The parameters of the oscillator will affect the exact value of absorbance obtained, but also not the general trends.

For the background needed in the spectrum calculations, the oscillator layer has been removed, and the remaining Air – SiO_2 – Si system used. Computationally, one could also use a "blank" background, which will however lead to a high baseline with a comparatively small peak (challenging to analyse). In first approximation, the trends with angle and sample will be the same as found here.

3.2 Results

3.2.1 Reflectivities from and transmission through silicon

See Fig. 1. Reflectivities follow the well-known curves, with the minimum in reflectivity in p-polarisation at the Brewster angle of 73.76°. The transmission shows a maximum in p-polarisation at the Brewster angle, were a value close to 1 is reached. At normal incidence, the transmission is ca. 70%. Here, values have been estimated for pass through a complete structure twice (once entering silicon and once leaving silicon) by squaring R and T obtained for the single pass. Mimicking approximately the "real" situation, the curve for unpolarised light and two passes through the interface has been estimated, showing a transmission of around 50% from normal incidence up to the

Brewster angle. At higher angles, the transmission drops sharply. Note that for unpolarised light, there isn't any specially sharp feature exactly at the Brewster angle.

These results present the basic optical properties of silicon and determine the intensities detected at

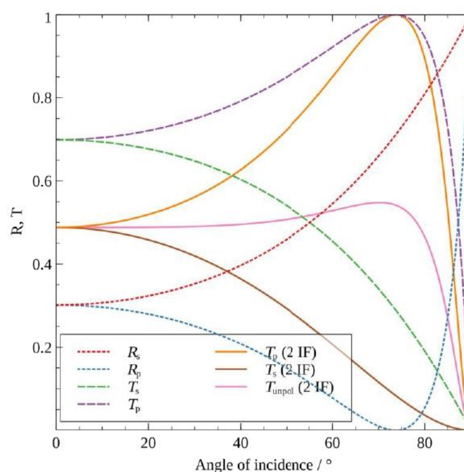

Figure 1: Reflectivities and transmission for silicon at 3000 cm⁻¹ with organic oscillator layer. The basic silicon without the organic oscillator layer will look very similar. 2 IF: Estimation for light passing through two interfaces (once entering silicon, and then leaving it through the second interface). Values for the substrate without the oscillator layer so similar to this that they cannot be distinguished in this type of plot.

a given wavelength. With a weak overall wavelength dependence of the substrate optical properties, the obtained values can be seen as representative for the complete mid-IR range.

3.2.2 Reflection absorbance for the oscillator layer on silicon

For informative reasons, and to be able to compare with reflectance studies from the literature, the reflectance absorbance is included in Fig. 2 (linear scale) and Fig. 3 (logarithmic scale). Both figures show unfortunately numerical problems because of cut-off of digits, visible as numerical noise. While solutions to this problem exist, important trends can still be obtained from the figures. Importantly, the figures show the importance of the Brewster angle in reflection spectroscopy studies, where quite strong absorbance spectra in p-polarisation can be obtained. Note, however, that this high absorbance is caused by the low intensity of the background reflection (see Fig. 1) in p-polarisation, which is why it is also practically difficult to measure. Importantly, at 0° and 90° angle of incidence, the reflection absorbance's are the same (characteristic for an isotropic system; differences can occur for biaxially anisotropic media). At 90°, the reflection absorbance is 0.

Reflection absorbance in s-polarisation is negative at all angles of incidence, characteristic for an IR-transparent substrate. For p-polarisation, the absorbance changes the sign twice. The first change in sign around 25° is presumably a consequence of the sequence of the refractive indices (low in air –

high in oscillator layer – low in SiO_2 – very high in silicon substrate). The second change in sign around the Brewster angle is similar to documented other cases.

Overall, high sensitivity can be obtained to the presence of an absorbing layer near the Brewster angle. However, the exact absorbance and even the direction of the band are very sensitive to the exact angle of incidence. As with a weakly focused beam, there will always be a spread in experiments, this calculation also illustrates the difficulties to interpret the reflectance spectra quantitatively.

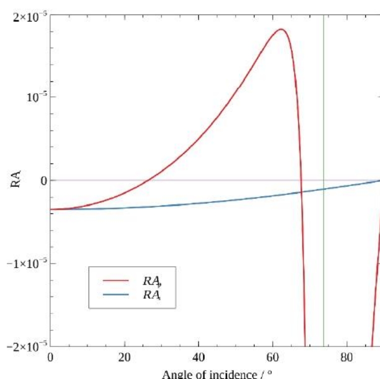

Figure 2: Reflectance absorbance for organic oscillator layer at the absorption maximum at 3000 cm^{-1} on an oxide-covered silicon substrate. Background: Oxide-covered silicon without oscillator layer. Brewster angle marked with vertical line.

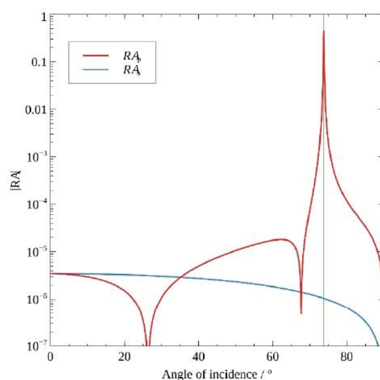

Figure 3: Same data as in Fig. 2, but as absolute value plotted on a logarithmic scale.

3.2.3 Absorbance in transmission geometry on silicon

Fig. 4 shows the calculated angular dependence of the peak absorbance of the oscillator layer in a transmission experiment. Again, as expected, the absorbance is the same in s- and p-polarisation at

normal incidence (0°), because at this angle, the system is invariant towards the two polarizations. For most of the angular range, the absorbance is on a similar order of magnitude as the reflection absorbance. A notable exception is the Brewster angle, which is not special in the transmission experiments. Together with the fact that there are not strong features in the transmission of unpolarised light, it shows thus that it is not extremely important in these experiments to hit the Brewster angle exactly. (This situation is, however expected to change for anisotropic layers, which oriented molecular layers in practice often are). Absorbance is expected to increase with increasing angle of incidence in p-polarisation, but not by orders of magnitude as in reflection experiments.

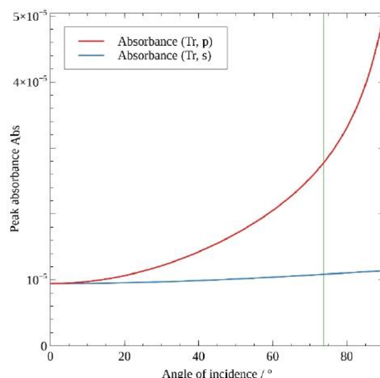

Figure 4: Angular dependence of peak absorbance at 3000 cm^{-1}, the absorption maximum of the oscillator layer, on silicon expected in a transmission experiment. Brewster angle denoted as vertical line. Background: Same system without oscillator layer for red and blue curves.

4 Potassium bromide

4.1 Optical system

Air – Isotropic oscillator layer (1 nm) – SiO_2 layer (5 nm) – KBr

Air: Same as for silicon, see section 3.1.

Oscillator layer: Same as for silicon, see section 3.1.

SiO_2 layer: Same as for silicon

KBr: Refractive index based on: Stephens et al. [9]; used only single wavelength value from the article for ca 3.7 µm, value was 1.5361 and does not change much with wavelength in this region.

As for silicon, dispersion (wavelength-dependence) of refractive indices has been neglected. Background treatment is also the same for silicon. See also section 3.1.

4.2 Results

4.2.1 Reflectivities from and transmission through potassium bromide

Fig. 5 shows the respective values as function of angle of incidence. Reflectivities in both polarisations show the typical expected values: steady increase with angle of incidence for s-polarisation, and

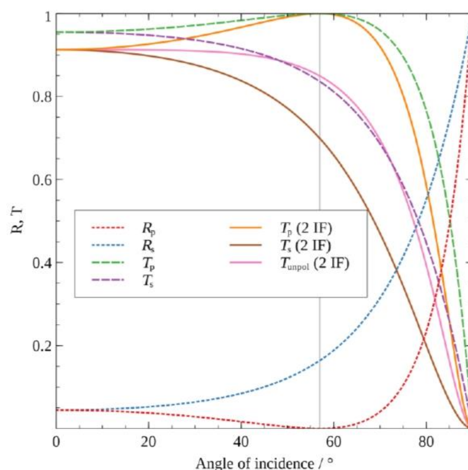

Figure 5 : Reflectivities and transmission for potassium bromide, at 3000 cm⁻¹ with organic oscillator layer that has its peak absorbance at this wavenumber. 2 IF: Estimation for light passing through two interfaces (once entering KBr, and then leaving it through the second interface). Values for the substrate without the oscillator layer so similar to this that they cannot be distinguished in this type of plot. Brewster angle of 56.94° marked as vertical line.

decrease to almost zero at the Brewster angle of 56.94°, and subsequent increase to 1 for p-polarisation. The transmission is the complementary quantity to the reflectivity. For the situation closest to experiment, where the beam is passing through a slab of KBr, the transmission at normal incidence is above 90%, and it remains above 80% until above the Brewster angle. Transmission is thus almost twice as high as for silicon incidence is above 90%, and it remains above 80% until above the Brewster angle. Transmission is thus almost twice as high as for silicon.

4.2.2 Reflection absorbance for the oscillator layer on potassium bromide

The corresponding reflection absorbance for informative purposes is shown in Fig. 6 and 7. This data shows less complexity compared to the silicon substrate. Again, high *RA* is obtained around the Brewster angle in p-polarisation. In s-polarisation, the reflection absorbance decreases with increasing angle of incidence from a given value at normal incidence to 0 at 90°. The negative absorbance in p-polarisation increases to the Brewster angle, and at the Brewster angle, the band changes orientation. This behaviour is exactly as described for water, which has a refractive index closer to that of KBr, and a bit different than silicon. In this system, a measurement exactly at the Brewster angle in p-polarisation is not desirable as the absorbance at the Brewster angle is almost zero. Besides, the intensity reflected is also nearly zero. A measurement in p-polarisation in the vicinity of the Brewster angle (but not exactly at the Brewster angle) would lead the highest absorbance. The overall behaviour is a bit different from silicon. The computed data for the KBr system are also almost free of numerical instabilities.

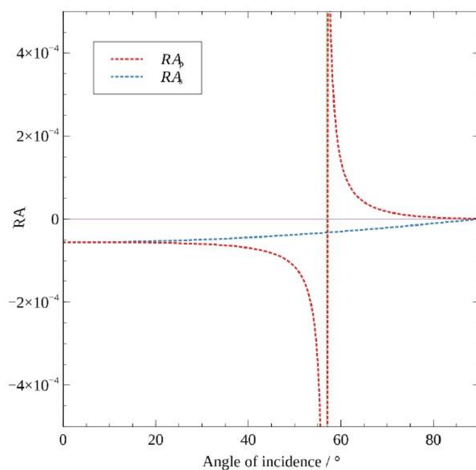

Figure 6: Reflection absorbance for an oscillator layer on SiO2/KBr. Background: Same system without oscillator layer. Brewster angle marked with vertical line.

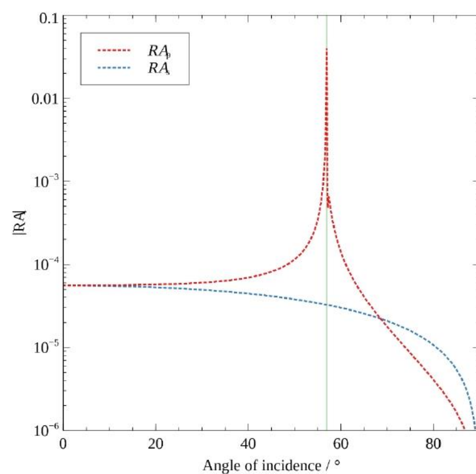

Figure 7: Same data as in Fig. 6, but plotted as absolute value on a logarithmic scale.

4.2.3 Absorbance in transmission geometry on potassium bromide

The absorbance expected in transmission geometry for a thin organic layer on SiO_2-covered KBr is shown in Fig. 8. Again, there isn't a strong angle dependence around the Brewster angle. Numeric problems affect part of the curves; however, the major trends are likely reproduced. Compared to silicon, the interchange of the role of s- and p-polarisation is remarkable, and physically hard to understand. (It is possible that some data columns have been interchanged, however, this has been checked and seems not to be the case). Most likely, the differences are related to the different role of the p-polarisation in the reflectance data, see previous section. When comparing the absorbance at normal incidence to the corresponding quantity for silicon, the KBr value is twice as high; this effect must be related to the differences in the reflectivities and may disappear with a different background.

For both silicon and KBr, the effect of the presence of a second interface (exit of light from KBr through a second interface into air or vacuum) would simply be to double the absorbance value.

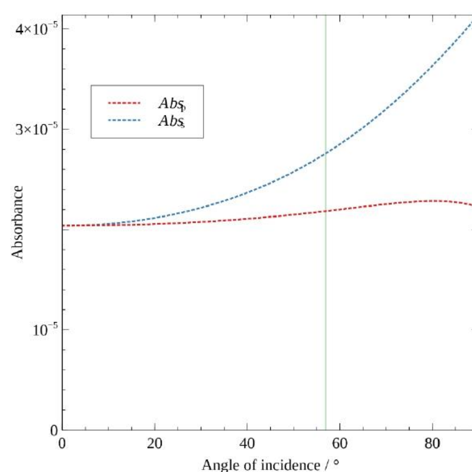

Figure 8: Angular dependence of peak absorbance at 3000 cm-1, the absorption maximum of the oscillator layer, on KBr expected in a transmission experiment. Brewster angle denoted as vertical line. Background: Same system without oscillator layer.

5. Conclusion

Compared to silicon, the use of KBr as a substrate (i) increases the transmission of light through the substrate and (ii) increases the absorbance from a thin interfacial layer, modelled here as an harmonic (Lorentzian) oscillator. With the expected higher signal to noise ratio on KBr, KBr is an attractive substrate for spectroscopic studies in transmission geometry.

While the Brewster angle has special significance in reflection experiments, both transmission and absorbance from isotropic thin layers do not show singularities at or around the Brewster angle. As

the polarisation of the transmitted beam changes at the Brewster angle, the situation becomes more involved for optically anisotropic systems, which have not been investigated here. As many thin films have a domain structure leading macroscopically to uniaxial birefringence with an optical axis perpendicular to the surface, many of the conclusions from these calculations can also be transferred to optically anisotropic layers.

Other data

- **Experimental measurement: Si transmittance measurement at normal incidence and ~ Brewster angle**

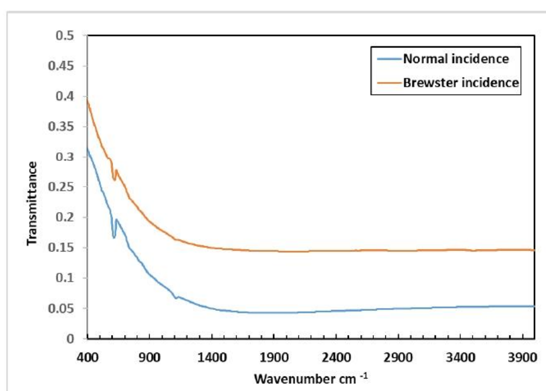

Figure 9: Si at normal incidence and Brewster angle with no sample as background.

- **Effect of nitrogen purging of the beam path**

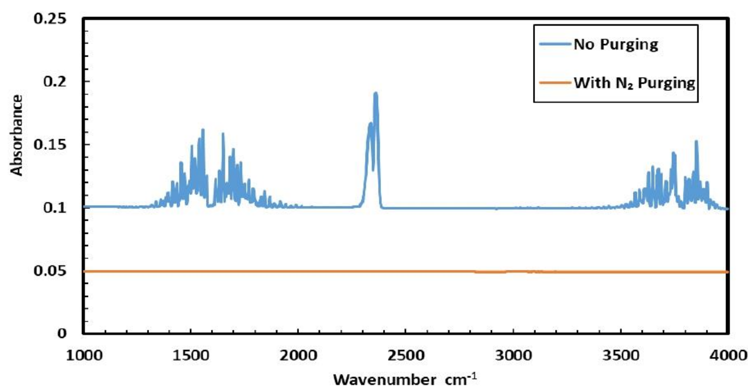

Figure 10: Effect of nitrogen purging of the beam path outside the reactor

References

1. Schubert, M. (1996) Polarization-dependent optical parameters of arbitrarily anisotropic homogeneous layered systems. *Phys. Rev. B*, **53** (8), 4265.
2. Yeh, P. (2005) *Optical waves in layered media*, Wiley.
3. Reithmeier, M., and Erbe, A. (2010) Dielectric interlayers for increasing the transparency of metal films for mid-infrared attenuated total reflection spectroscopy. *Phys. Chem. Chem. Phys.*, **12** (44), 14798–14803.
4. Reithmeier, M., and Erbe, A. (2011) Application of thin-film interference coatings in infrared reflection spectroscopy of organic samples in contact with thin metal films. *Appl. Opt.*, **50** (9), C301–C308.
5. Bohren, C.F., and Huffman, D.R. (1998) Absorption and Scattering of Light by Small Particles, 544 WILEY. *New York*.
6. Erbe, A., Bushby, R.J., Evans, S.D., and Jeuken, L.J.C. (2007) Tethered bilayer lipid membranes studied by simultaneous attenuated total reflectance infrared spectroscopy and electrochemical impedance spectroscopy. *J. Phys. Chem. B*, **111** (13), 3515–3524.
7. Malitson, I.H. (1965) Interspecimen comparison of the refractive index of fused silica. *Josa*, **55** (10), 1205–1209.
8. Edwards, D.F., and Ochoa, E. (1980) Infrared refractive index of silicon. *Appl. Opt.*, **19** (24), 4130–4131.
9. Stephens, R.E., Plyler, E.K., Rodney, W.S., and Spindler, R.J. (1953) Refractive index of potassium bromide for infrared radiant energy. *JOSA*, **43** (2), 110–112.

ISBN 978-82-326-7442-8 (printed ver.)
ISBN 978-82-326-7441-1 (electronic ver.)
ISSN 1503-8181 (printed ver.)
ISSN 2703-8084 (online ver.)

NTNU

Norwegian University of
Science and Technology